Imperial College London

Hexacoordinate Si/Ge Compounds and Their Application in Metal-Organic Frameworks

Shouyi Tian

A Thesis Submitted in Partial Fulfilment of the Requirements for the Degree of

DOCTOR OF PHILOSOPHY

Supervisor: Dr. Rob Davies, Prof. Paul Lickiss

Molecular Science Research Hub

Department of Chemistry

Imperial College London

June 2024

Declaration of Originality

I hereby declare that the work presented in this thesis is my own work conducted between October 2019 and April 2023 in the Department of Chemistry at Imperial College London and has not been submitted for another degree at this or any other university. The usage of other works is cited in the text and the sources are given in the references. Appropriate rights and permissions were acquired where needed.

Copyright Declaration

The copyright of this thesis rests with the author. Unless otherwise indicated, its contents are licensed under a Creative Commons Attribution-NonCommercial 4.0 International Licence (CC BY-NC).

Under this licence, you may copy and redistribute the material in any medium or format. You may also create and distribute modified versions of the work. This is on the condition that: you credit the author and do not use it, or any derivative works, for a commercial purpose.

When reusing or sharing this work, ensure you make the licence terms clear to others by naming the licence and linking to the licence text. Where a work has been adapted, you should indicate that the work has been changed and describe those changes.

Please seek permission from the copyright holder for uses of this work that are not included in this licence or permitted under UK Copyright Law.

Abstract

Metal-Organic Frameworks (MOFs) are porous coordination polymers comprising metal clusters linked by organic linkers, forming intricate framework structures. In recent decades, research on MOFs has gained attention due to their diverse structures and potential applications in gas storage/separation, catalysis, chemical sensing, and drug delivery. The organic connectors impart unique properties to these materials, make the synthesis of new connectors pivotal for exploring MOFs with novel structures and properties. Chapter 1 offers an overview of MOF chemistry, encompassing historical development, design and synthesis, activation, and characterization. The utilization of hexafluoro silicate/germanate anions (SiF_6^{2-}/GeF_6^{2-}) in MOF assemblies and their applications, and examples of COF/MOFs containing SiO_6/GeO_6 units are highlighted. Chapter 2 introduces hydrogen-bonded organic frameworks, and methodologies for synthesizing hexacoordinated Si/Ge connectors. Twenty-one anionic linkers featuring EO_6 centres [E = Si or Ge, **L1-Si/Ge**: tris-oxalate silicate/germanate, **L2-Si/Ge**: tris(3-(3,4-diolatophenyl)acrylic acid) silicate/germanate, **L3-Si/Ge**: tris(3,4-diolato-benzoic acid) silicate/germanate] have been synthesized with different ammonium cations for charge balance, and characterized by NMR and IR spectroscopy and PXRD, and crystals of some compounds have been studied through SCXRD analysis. These structures exhibit H-bond interactions, with some self-assembling into extended networks. Chapter 3 introduces rare earth (RE) MOFs and their applications. Ten RE-MOFs were prepared by treating RE salts (Sc, Y, Gd, Tb, Dy, Ho, Er, Tm, Yb, Lu) with [$(Et_3NH)_2$(**L3-Ge**)]. SCXRD studies revealed that the Y-MOF and all Ln-MOFs are isostructural, comprising bimetallic clusters, while Sc-MOF contains trimetallic clusters. Chapter 4 describes the luminescence mechanisms of f-block elements and applications of Tb-based MOFs. The photoluminescence properties of the Tb-MOF were studied, with characteristics emission under UV excitation. The sensing performance toward metal ions was investigated, showing significant quenching by Pb^{2+} ions with a quench efficiency of 1.80×10^3 M^{-1}, involving a dynamic quench mechanism.

List of Publications

Some of the works in this thesis have been reported in the following co-written published paper:

S. Tian, P. N. Horton, S. J. Coles, A. J. P. White, P. D. Lickiss and R. P. Davies, *J. Mater. Chem. C*, 2024, DOI: 10.1039/d4tc01700e.

Table of Contents

Declaration of Originality 2
Copyright Declaration 2
Abstract 3
List of Publications 4
Table of Contents 5
Acknowledgement 7
List of Abbreviations 8
Chapter 1: Introduction 10
1.1 Background 10
1.1.1 Development of MOFs 11
1.1.2 Design and Synthesis 16
1.1.3 Activation and Characterization 24
1.2 Si/Ge-based Linkers in MOF Construction 31
1.2.1 Synthesis and Structure Overview 43
1.2.2 Applications: Gas Sorption/Separation 45
1.2.3 Applications: Catalyst, Chemical Sensing etc. 52
1.3 Frameworks with XO_6 Type Linkers 53
1.4 Aims and Objectives 57
Chapter 2: Synthesis of Hexacoordinate Linkers 58
2.1 Introduction to Hydrogen-Bonded Organic Frameworks 58
2.1.1 Carboxylic Acid-Based HOF Systems 60
2.1.2 Charge-Assisted H-Bonds in HOF Systems 62
2.2 Synthesis of Si/Ge(ox)$_3$ Type Linkers 66
2.2.1 Synthesis Methods 66
2.2.2 Characterization and Structure Description 67
2.3 Synthesis of Si/Ge(caffeic acid)$_3$ Type Linkers 82
2.3.1 Synthesis Methods 82
2.3.2 Characterization 83
2.4 Synthesis of Si/Ge(3,4-dihydroxybenzoic acid)$_3$ Type Linkers 84
2.4.1 Synthesis Methods 84
2.4.2 Characterization and Structure Description 84
2.5 Synthesis of Ti(3,4-dihydroxybenzoic acid)$_3$ Linkers 91
2.5.1 Synthesis Methods 91
2.5.2 Characterization and Structure Description 91
2.6 Synthesis of 4,5-Dihydroxyphthalic Acid 98
2.7 Conclusions 103
Chapter 3: Metal-Organic Frameworks Constructed using a Hexacoordinate Ge Linker 110
3.1 Introduction 110

3.2 Rare Earth Metal-Organic Frameworks (RE-MOFs) 112
3.3 Synthesis of IMP-RE Series MOFs 122
3.3.1 A Y-MOF (IMP-33-Y) Built from L3-Ge with *flu*-3,6-*C*2/*c* Topology .. 122
3.3.2 Lanthanide MOFs (IMP-33-Ln) Built from L3-Ge with *flu*-3,6-*C*2/*c* Topology 127
3.3.3 A Sc-MOF (IMP-34-Sc) Built from L3-Ge with *flu*-3,6-*C*2/*c* Topology 133
3.4 Other Attempted Syntheses..... 137
3.5 Conclusions..... 141
Chapter 4: IMP-33-Tb for Metal Sensing..... 143
4.1 Introduction..... 143
4.2 Tb-MOF as a sensing agent to detect Pb^{2+}..... 152
4.2.1 Photoluminescence Properties of IMP-33-Tb..... 152
4.2.2 IMP-33-Tb for Aqueous Pb^{2+} Sensing 153
4.2.3 Mechanism Discussion 156
4.3 Conclusions..... 159
Chapter 5: Conclusions..... 160
Chapter 6: Experimental 163
6.1 Materials and General Methods..... 163
6.2 L1 type linkers 165
6.3 L2 type linkers 172
6.4 L3 type linkers 174
6.5 MOF synthesis 178
6.5 Other compounds..... 179
List of References 182
Supplementary Information 199

Acknowledgement

First and foremost, I wish to express my deepest thanks to my supervisors Dr Rob Davies and Prof. Paul Lickiss for their excellent supervision and support throughout my PhD journey. They have provided countless ideas, discussions, and proofreading, which are essential in every step of my study. I appreciate the understanding and support during my challenge times.

Thanks to Dr Andrew White and Dr Peter Horton (NCS at University of Southampton) for their assistance on X-ray crystallography and solving crystal structures, Dr Lisa Haigh and Malgorzata Puchnarewicz for the help on mass spec services, Peter Haycock for the help on NMR service, Dr Mike Ray and Doris Pappoe for the help on administrative matters, Jiewen Wei for the training and discussion on photoluminescence and quantum yield measurement.

Thanks to Sherry, Nudrat, and Nas for their invaluable help on lab induction, and safety training, and allow me to get familiar with everything in the lab and ensure the lab is running smoothly. Thanks to Dr Luke Delmas for the help on lab demonstrations and useful advice. Thanks Tania, Lenka, Mohammad, Angelina, Rupa, Shuo, Jiayin, Mariam, Ziyuan, Chengkai, Liyuan, Saeed, Tom, Sonal, Jero, Ruichen, Zhaolong, and Irene for creating a vibrant and fun environment made my lab experiences colourful. Also, thanks to my friends Xin, Yu, Jianfeng, Xiantao, Qisi, Tianyou, Rabia, Yujie for being supportive and enjoying the fun time together.

I would like to thank my parents for their endless love and support. Special thanks to my mother-in-law who has greatly helped me with daily household chores and taking over everything so that I can focus on my study. Thanks to the presence of my daughter in my life, every time I look on her face I am filled with hope. Finally, thanks to my wife for her love, encouragement, and mental support, without whom I cannot reach here.

List of Abbreviations

BET	Brauner-Emmet-Teller
Bipy	4,4'-Bipyridine
Bu	Butyl
cat	Catechol
CCDC	Cambridge Crystallographic Data Centre
CCS	Carbon capture and storage
COF	Covalent-organic framework
CP	Coordination polymer
CSD	Cambridge Structural Database
DCM	Dichloromethane
DEF	N,N-Diethylformamide
DMA	N,N-Dimethylacetamide
DMAE	2-(Dimethylamino)ethanol
DMAP	3-(Dimethylamino)propanol
DMF	N,N-Dimethylformamide
DMSO	Dimethyl sulfoxide
DSC	Differential Scanning Calorimetry
EC	Electrochemical
EnT	Energy transfer
Et	Ethyl
Gu	Guanidine
HOF	Hydrogen-bonded organic framework
ICP-AES	Inductively coupled plasma atomic emission spectroscopy
iPr	Iso-propyl
IR	Infrared
IRMOF	Isoreticular MOF

Ln	Lanthanide
MC	Mechanochemical
Me	Methyl
MeCN	Acetonitrile
MOF	Metal-organic framework
MS	Mass spectrometry
NIR	Near-Infrared
MW	Microwave-assisted
NMR	Nuclear magnetic resonance
OMS	Open metal site
pip	piperazine
PXRD	Powder X-ray diffraction
RE	Rare earth
RT	Room temperature
SBU	Secondary building unit
SC	Sonochemical
SCXRD	Single-crystal X-ray diffraction
T_g	Glass transition temperature
T_m	Melting point
TGA	Thermogravimetric analysis
THF	Tetrahydrofuran
TMBDA	N,N,N',N'-tetramethyl-1,4-butanediamine
TMEDA	N,N,N',N'-tetramethylethylenediamine
TMPDA	N,N,N',N'-tetramethyl-1,3-propanediamine
UV-vis	Ultraviolet-visible
XRF	X-ray fluorescence spectrometer

Chapter 1: Introduction

1.1 Background

Metal-organic frameworks (MOFs) are crystalline porous materials assembled from metal-based nodes (usually called secondary building units, SBUs) and organic linkers through coordination bonds.[1] They are a subclass of coordination polymers (CPs) due to their polymeric features and are often termed porous coordination polymers (PCPs). Usually, MOFs are synthesized through the reaction of metal salts with organic linkers in a solvent (Figure 1.1) to give 2D layered or 3D framework structures. The void space among linkers and metal nodes is initially occupied by solvent molecules which can be subsequently removed through an activation process.[2] The activated frameworks can exhibit permanent porosities, thus giving MOFs high porosity (up to 91.1% of unit cell volume) and extremely large surface area (up to 9100 m^2/g).[3, 4] The empty spaces allow guest molecules to enter and have interactions with the framework. The functional diversity of MOF materials can be achieved through 1) modification of functional groups in the organic linkers; 2) adjusting the length and structure of the organic linkers; 3) incorporating open metal sites (OMS); 4) adjusting the type of metal ions.[1, 5] As a result, MOFs have been applied to various areas such as gas storage and separation, catalytic reactions, chemical sensing, drug delivery, optical materials etc.[6]

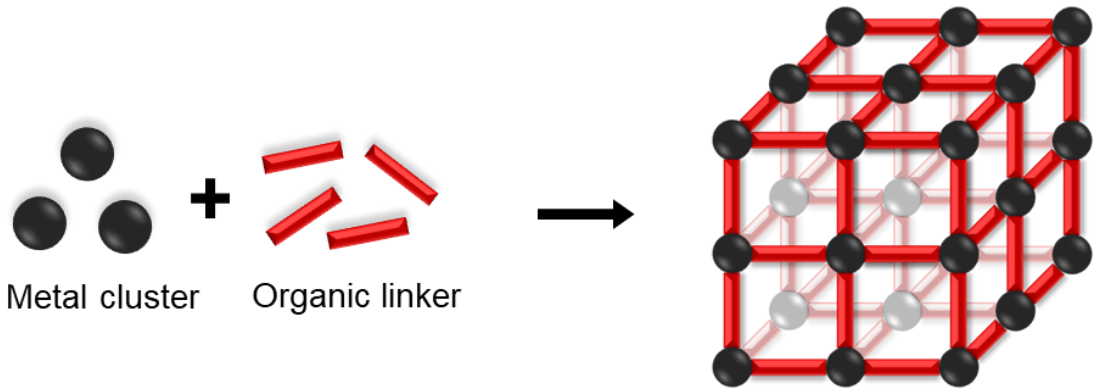

Figure 1.1 Demonstration of MOF synthesis and general structures.

1.1.1 Development of MOFs

Back in early 1989, Hoskins and Robson synthesized an infinite framework from the reaction of $Cu(I)(NCCH_3)_4$ units with 4,4,'4'',4'''-tetracyanotetraphenylmethane.[7] The design of this CP was driven by the connection of tetrahedral centres with appropriate rod-like connection units, which could potentially generate infinite networks and a regular array of cavities. Such structure-directing strategies of designed materials were widely used in the field of zeolite materials by synthetic chemists.[8] Later, they further synthesized and explored some 3D frameworks using such structure-directing methods with Zn, Cd and Cu metal centres.[9] As proposed by Kitagawa,[10] these examples illustrated the 1st generation of MOFs (or PCPs), which were recognized through their organic linker-bridged frameworks rather than conventional inorganic clusters. This type of PCP usually exhibits a closed-framework feature: although the nano-sized pores were visible through X-ray diffraction studies, the pores were filled by solvent molecules leaving no spaces for guest molecules to enter, and the removal of the solvent molecules caused the collapse of the framework.[11]

The term 'metal-organic frameworks' was initially introduced by Yaghi and co-workers in 1995.[12] They reported the hydrothermal synthesis of a crystalline 3D Cu-MOF using $Cu(NO_3)_2 \cdot 2.5H_2O$ and 4,4'-bipyridine. The resulting rectangular orange crystals were found to be $[Cu(4,4'\text{-bipy})_{1.5} \cdot (NO_3)(H_2O)_{1.25}]$, exhibiting six interpenetrated framework structures. In the same year, Yaghi *et al.* reported a Co-MOF using BTC (1,3,5-benzenetricarboxylate) as the linker.[13] Unlike the 3D Cu-MOF, this Co-MOF comprises Co ions linked by BTC linkers as well as H-bond interactions between adjacent carboxylate groups to form a 2D layered structure. In addition, each Co ion is coordinated by two perpendicular bipyridine molecules, and each layer is held closely through π-π interactions between the bipyridine molecules.

In the following years, research on MOFs gained more interest with a shift from adopting N-based neutral linkers to charged carboxylate linkers. The establishment of permanent porosity in MOFs led to the introduction of 2nd generation MOFs.[14, 15] These MOFs can maintain their structure after the removal of solvent molecules. This also promoted research

on the surface area and topology of the frameworks. The report on the synthesis of MOF-5 with permanent porosity and a large surface area stands out as a landmark in MOF chemistry.[16] The reaction of zinc nitrate with H_2BDC (BDC = 1,4-benzenedicarboxylate) in DMF and chlorobenzene afforded MOF-5 (Figure 1.2) with a formula of $[Zn_4O(BDC)_3 \cdot (DMF)_8(C_6H_5Cl)]$. Upon activation, this framework remained stable with an experimental accessible void space of 55-61%. The Langmuir surface area was then determined through gas sorption studies to be about 2900 m^2/g, which exceeded most of the conventional zeolite materials at the time. The discovery of ultra-high surface area and permanent porosity features in MOF materials significantly advanced MOF chemistry. Subsequently, extensive research has been conducted on the synthesis and potential applications of MOFs, as outlined below.

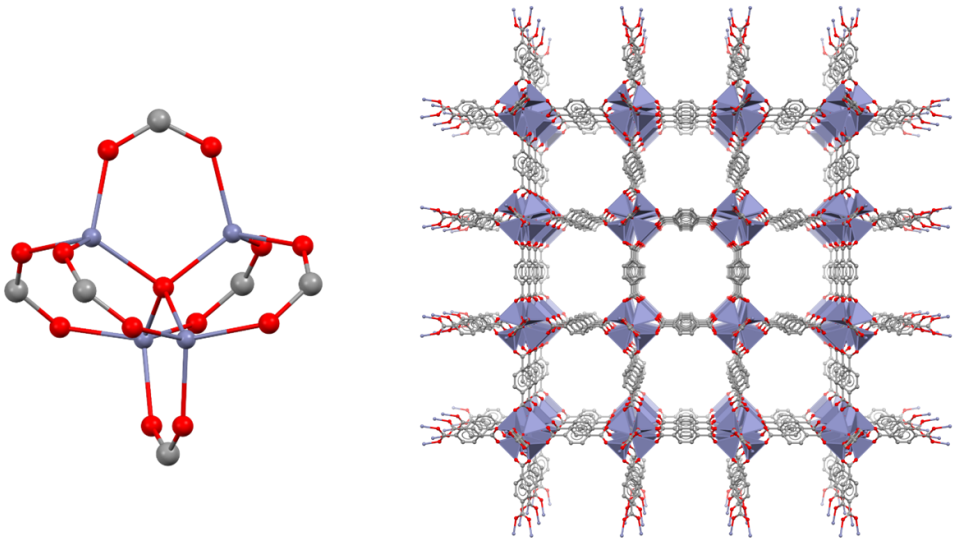

Figure 1.2 Crystal structure of MOF-5 left) SBU; right) packing diagram showing *pcu* topology. C: grey, O: red, Zn: purple. H atoms are omitted for clarity. Figure redrawn using published crystal data from Yaghi and co-workers (CCDC refcode SAHYIK).[16]

Apart from the prototype MOF-5, another well-studied MOF was reported in the same year, namely HKUST-1 (HKUST = Hong Kong University of Science and Technology).[17] The combination of a paddlewheel cluster $[Cu_2(COO)_4(H_2O)_2]$ (Figure 1.3) with 1,3,5-benzene-tricarboxylate ligand generates an interesting 3D framework with a 3D channel size of 1 nm (diameter), giving a total accessible void space of 40% of the cell volume.

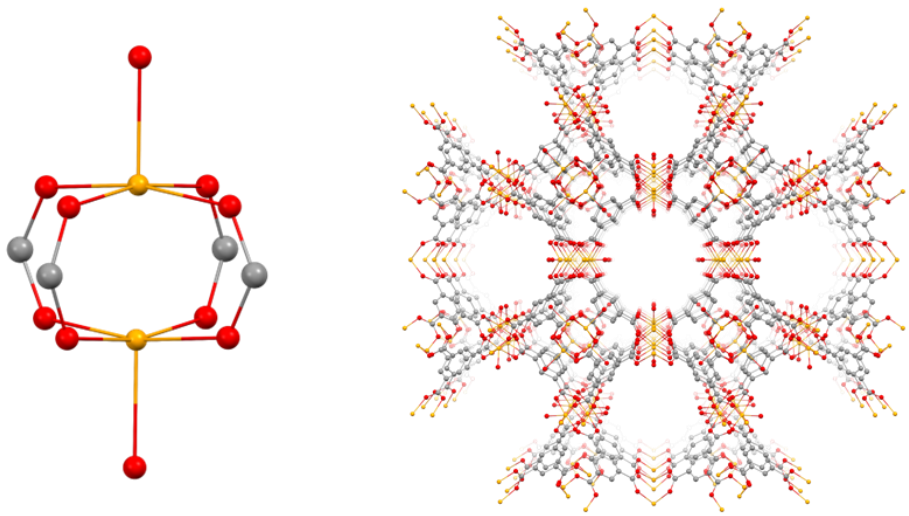

Figure 1.3 Crystal structure of HKUST-1 left) Cu paddle wheel SBU with two axial water molecules; right) packing diagram showing pore spaces. C: grey, O: red, Cu: orange. H atoms are omitted for clarity. Figure redrawn using published crystal data from Williams and co-workers (CCDC refcode FIQCEN).[17]

The 3rd generation of MOFs distinguished itself by its 'flexible' features, thus endowing dynamic properties to the frameworks (Figure 1.4). The earliest report on guest-induced framework expansion was found in a Cu-based CP, as reported by Kitagawa and co-workers.[18] The observation of a shift in peak positions towards higher angles in PXRD plots for thermally activated samples indicated that this Cu-CP underwent a decrease in the crystal lattice distance, and that such a change was reversed by soaking the activated sample in water or methanol. This example successfully demonstrated the capability of MOFs to exhibit reversible structural changes. Later, the exploration of the MIL-53 series of MOFs (MIL = Matériaux de l'Institut Lavoisier) by Férey and colleagues demonstrated the breathing-effect of the frameworks caused by solvent-host interactions.[19-21] The PXRD pattern of the dried form of MIL-53 significantly differed from the as-synthesized samples, indicating the change in pore size between the drying and hydrating process. Computational studies were then applied to investigate the reversible breathing effect of MIL-88, which showed a ~85% increase in the cell volume after absorbing water. In subsequent works, both MIL-88B and MIL-88D exhibited cell contractions when water molecules were

removed from the frameworks.[22] The successful synthesis and characterization of these flexible MOFs showing reversible pore expansion or contraction significantly promoted the research on gas sorption/separation applications.

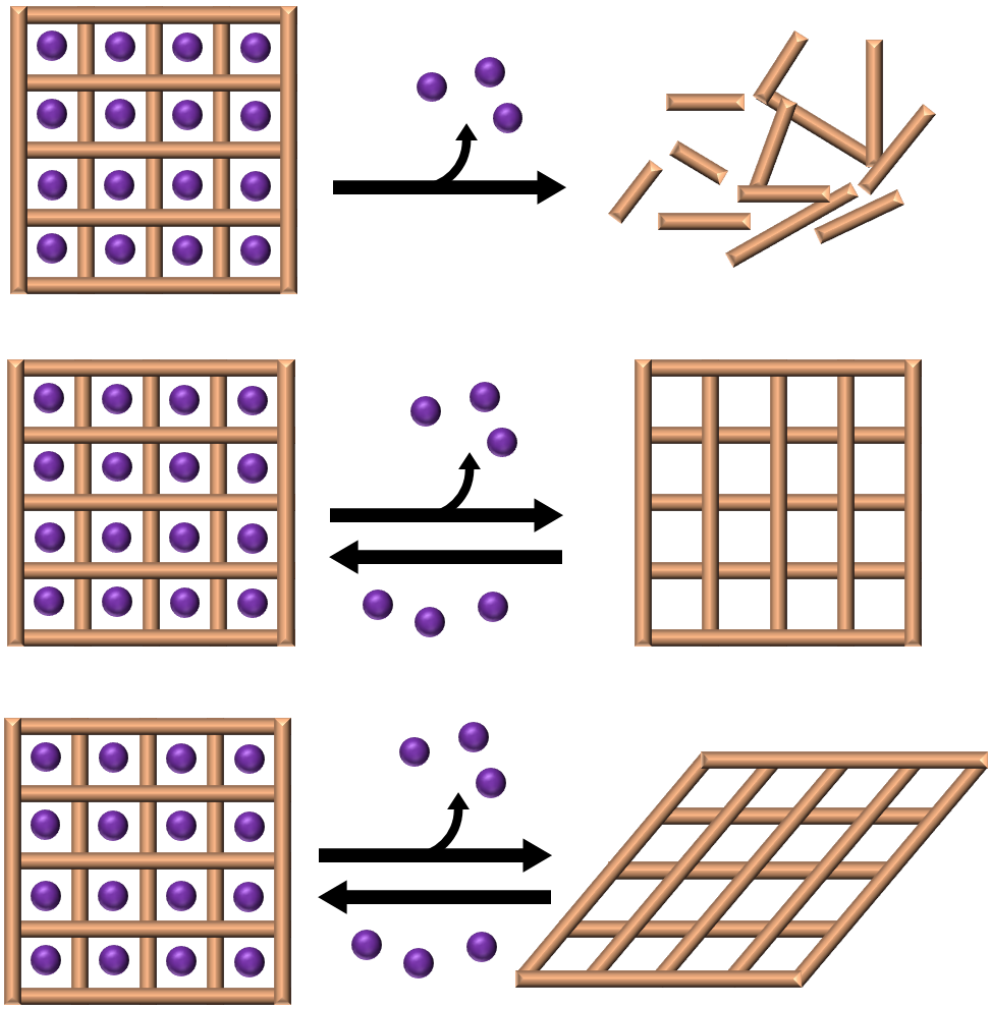

Figure 1.4 Overview of 1st (top), 2nd (middle), and 3rd (bottom) generation of MOFs. Top) breakdown of MOF framework on activation; middle) reversible activation of pores; bottom) 'breath of lattice', change in framework shape on activation.

Crystalline materials can undergo a phase change to a non-crystalline state, either to a glass or liquid state. Compared to their solid crystalline state, the non-crystalline state may display new properties and promote their usage in fabricating new materials.[23] While scientists have been working on obtaining ordered frameworks in the past few decades, the presence of disorder in the framework may also trigger novel features in MOFs. Despite

MOFs being well-ordered crystalline materials that possess a melting point (T_m) at a certain temperature, the frameworks usually undergo thermal decomposition before turning to a liquid state. Hence it is challenging to turn ordered MOFs into disordered liquids due to the intrinsic thermal instability, and this feature further limited the preparation of the glass state of MOFs through quenching of melts which have already been applied in preparing other glass systems, such as metallic, oxide.[24]

In 2012, Kitagawa and co-workers reported a Zn-CP possessing a low T_m (168°C).[25] The reaction of ZnO with imidazole (ImH) and H_3PO_4 afforded crystalline product Zn-CP with a formula of $[Zn(HPO_4)(H_2PO_4)_2](ImH_2)_2$. As suggested by TGA results, the framework remained stable up to 200°C before undergoing decomposition, thus indicating stability during the phase change from solid to liquid state. The differential scanning calorimetry (DSC) results revealed that the liquid phase of the Zn-CP underwent a phase change to the glass state upon cooling to 25°C, as indicated by PXRD measurement showing no diffraction peak. There have been more studies on MOFs showing reversible crystal-liquid-glass phase changes in the following years,[26-28] and the successful demonstration of the formation of glass MOFs (gMOF) led to the development of 4th generation of MOFs (Figure 1.5).[23] Various features of gMOFs were then explored, such as glass transition temperature (T_g), mechanical properties, and conductivities, and gMOFs have been gradually applied in various fields, such as energy storage, electronic devices, photocatalysis etc.[29]

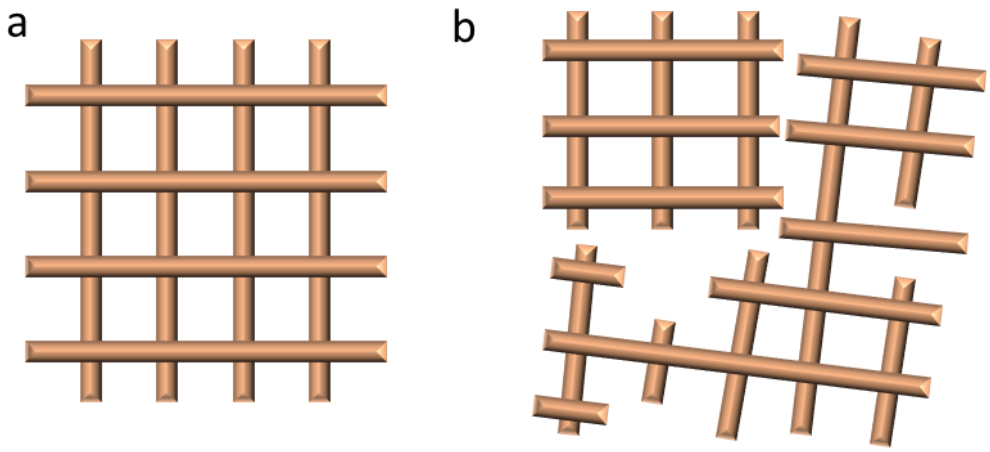

Figure 1.5 Schematic structures of a) crystalline MOFs; b) glass MOFs.

1.1.2 Design and Synthesis

1.1.2.1 MOF Design

Traditional MOF synthesis involves the mixing of metal salts and organic ligands in a solvent or solvent mixture at high temperatures to allow the formation of crystals. However, the lack of direction and size control of the crystal structure in this process has been a major challenge in the pre-designing of structures. MOF chemists have been exploring rational design strategies to achieve structure control while obtaining robust frameworks. A preliminary attempt involved isoreticular design, in which the MOFs are synthesized using different linkers displaying the same connectivity, but of different lengths or sizes (see below), to increase pore size and surface area, based on a known MOF structure.[30]

Yaghi and co-workers successfully demonstrated the feasibility of isoreticular synthesis by adopting different di-topic carboxylate linkers in the synthesis of the MOF-5 series.[4] By using linkers possessing different lengths (Figure 1.6), the IRMOF (Isoreticular MOF) series had identical topology compared to MOF-5 (IRMOF-1), while exhibiting various pore sizes (diameter) ranging between 3.8 and 28.8 Å. Such synthesis strategies have fulfilled the requirements, in which the starting building unit possesses similar features compared to the original linker, and the obtained frameworks exhibit the same connection mode while displaying various functionalities and dimensions. In addition, the resultant products are required to exhibit high levels of crystallinity to ease their characterization through XRD techniques. As a successful demonstration, IRMOF-6 (R6-BDC as linkers, Figure 1.6) exhibited methane uptake up to 240 cm^3/g under 298 K and 36 atm, which is promising as a candidate to be used in automobile fueling.[31]

Apart from the variation of organic linkers in isoreticular synthesis, the isoreticular approach also encompasses the variation of metal ions within the coordination network. Although the change in synthesis conditions or metal species often results in variations in the size, shape, or coordination environment of the metal cluster thus leading to the formation of a different topology, in some cases the use of different metal sources can result

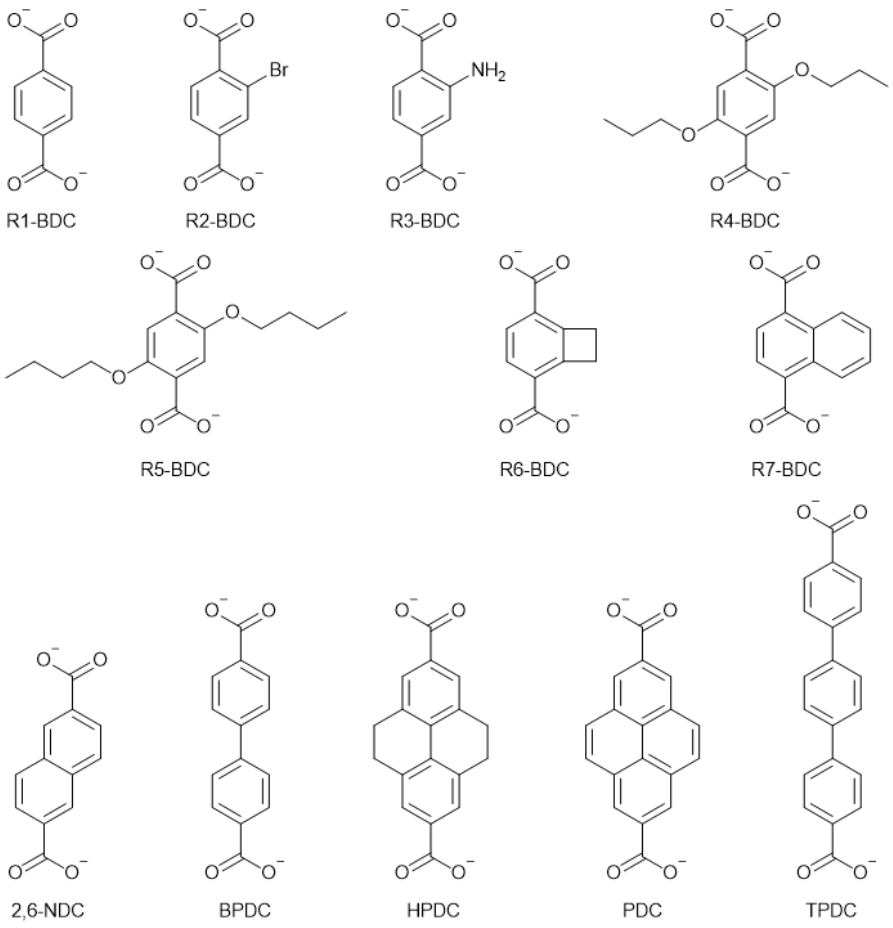

Figure 1.6 Linkers used for the synthesis of the IRMOF series.[4]

in the generation of isostructural metal cluster and same topology. This can be found in HKUST-1 where Zn^{2+}, Fe^{2+}, and Cr^{2+} were applied in the MOF synthesis,[32-34] and the obtained frameworks exhibited identical metal clusters and topology compared to the original Cu-based frameworks.

It should be noted that with the increasing linker lengths, the frameworks are more likely to collapse, a good example of this being the stability difference observed between UiO-66 and UiO-67 (UiO = University of Oslo).[35] The longer BPDC linker used in UiO-67 (compared to the shorter BDC ligand in UiO-66 construction) resulted in a less stable framework towards water and acid. The longer linkers also increase the chance for framework interpenetration which can, to some extent, increase the stability of the frameworks, but the porosity of the framework will decrease simultaneously. In addition,

the reduction in the availability of active sites can further hamper the applications in which large molecules are involved, such as catalysis, drug delivery, gas storage or separation.

An approach avoiding interpenetration and maximising the internal porosity can involve changing synthesis methods or introducing a sterically hindering group on the original linker.[4, 30, 36] To obtain the same topology, the connection mode of the metal cluster and the organic linkers should be identical, and the presence of a sterically hindering group in the ligand may force the framework to arrange in a non-interpenetrated arrangement. For example, this strategy was used in the synthesis of PCN-228, PCN-229 and PCN-230 (PCN

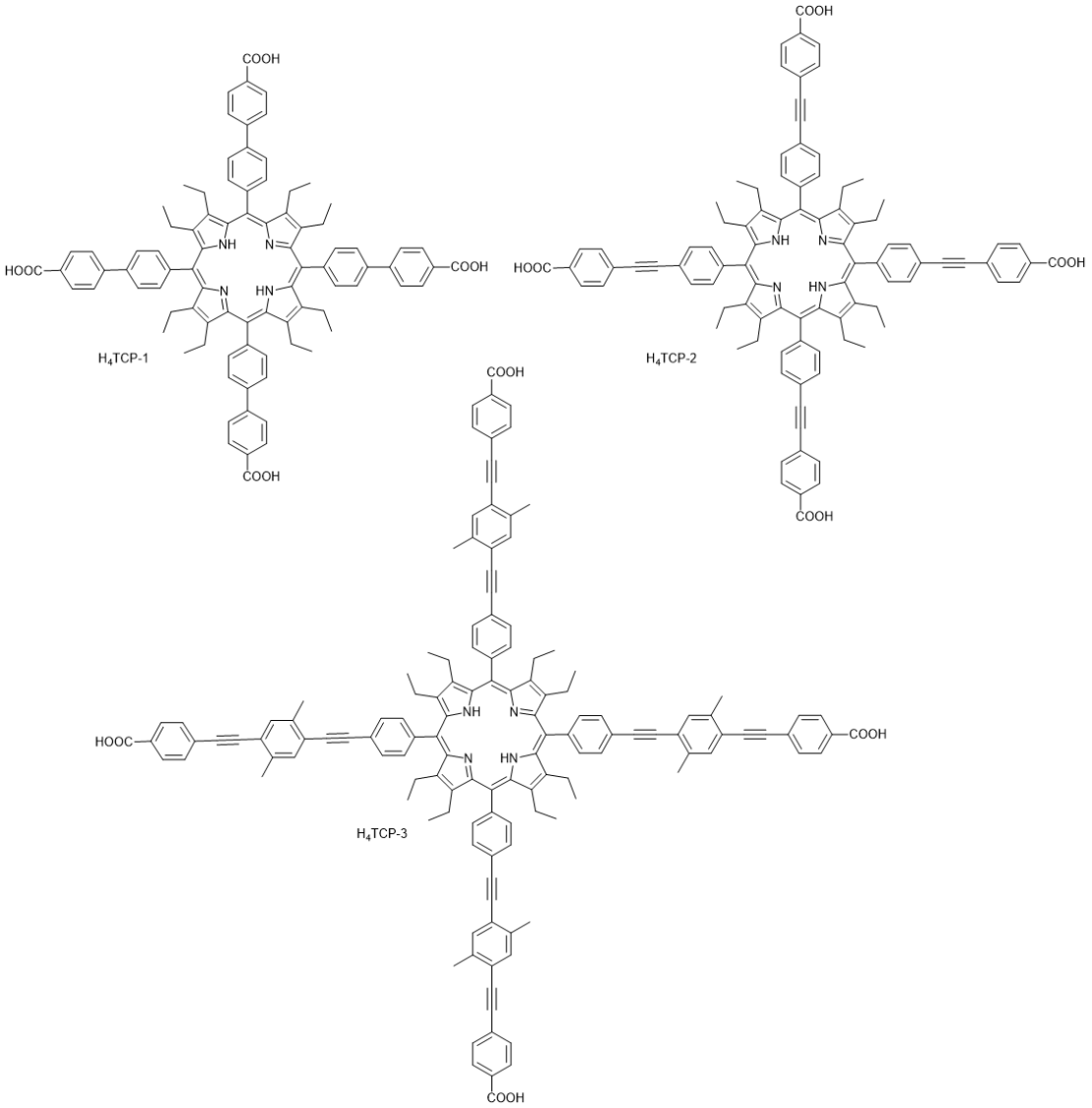

Figure 1.7 Linker used in the construction of PCN MOFs; H_4TCP-1 was used for PCN-228, H_4TCP-2 was used for PCN-229 and H_4TCP-3 was used for PCN-230.

= porous coordination network) by introducing a carbon triple bond between neighbouring phenyl rings in the organic linker (Figure 1.7).[37] Although the pore size ranges from 2.5 to 3.8 nm, no interpenetration was observed in these three MOFs due to the presence of the porphyrin centre in the organic linker. Additionally, the adoption of a topology that cannot translate in all directions without overlapping upon itself, such as *flu*, is a feasible approach to avoid interpenetration.[30]

The methods mentioned above are effective in synthesizing MOFs based on known MOF structures. However, these approaches generally lack directional control when aiming to synthesize MOFs with entirely new structures. Reticular synthesis is defined as the arranging of designed rigid molecular building blocks into predefined organised structures that are interconnected by strong bonds,[38] and such a process is important in establishing a robust correlation between the resulting MOF and its starting materials. While it is difficult to directly incorporate metal ions with organic ligands into pre-designed shapes due to the lack of directional control, the chelation of metal ions with carboxylate groups offers the

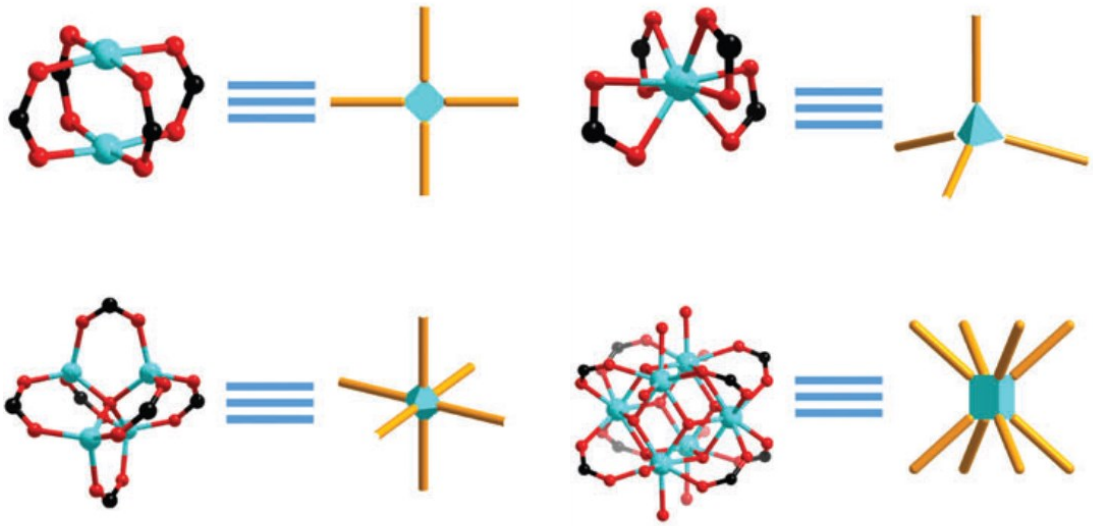

Figure 1.8 Different SBUs exhibiting various connectivity and directions. Cu paddle wheel cluster: top left; Zn tetrahedral cluster: bottom left; Ln cluster: top right; Zr cluster: bottom right.[39]

chance to control the geometry and connectivity of the cluster (termed SBU, Secondary Building Unit) more rigidly. For example, the Zn tetrahedral cluster can be regarded as a rigid 6-connected octahedral node, the Cu paddle wheel cluster is regarded as a 4-connected square planar node etc (Figure 1.8). These clusters are then connected by predesigned organic ligands through strong bonds (C-C) to generate the required framework structure.

The implementation of reticular synthesis opens new avenues for the deliberate design of MOF materials. By understanding the target network 'blueprint' and identifying the required building blocks, researchers can achieve precise control over the synthesis process. This approach holds great promise in the synthesis of MOFs and other extended structures, offering a level of predictability and reproducibility that is crucial for advancing the field of materials science.

1.1.2.2 Synthesis Methods

Conventional MOF synthesis methods usually involve direct heating of metal salts and organic ligands in a solvent or solvent mixture. Based on the temperature employed, it can be classified as solvothermal or non-solvothermal synthesis,[40] where the former is usually conducted in an autoclave at the temperature above the boiling point of the solvent with autogenous pressure, and the latter takes place at or below the boiling point of the solvent under ambient pressure. During the synthesis process, solvent molecules can bind to metal cations and can be removed later through thermal vacuum treatment (known as thermal activation) to allow the exposure of open metal sites while maintaining the framework integrity. The coordination reactions between the metal cations and ligands are reversible, thus allowing the self-correction of defects throughout the synthesis process.[30]

A modulator is defined as a monodentate chemical species, such as benzoic acid or formic acid, that can bind to metal cations in the MOF synthesis reactions with a lower affinity compared to the ligands making up the target MOF.[30] Usually acid reagents are used as the modulator, which can not only reduce the pH in the reaction system to slow the deprotonation process of the ligand but also competitively coordinate with the metal ions

or cluster to slow the nucleation rate. All these interactions contribute to the reduction of defects in the crystals and an increase in the crystallinity and size of the crystals.[41] For example, by the addition of benzoic acid in the synthesis of UiO-66 MOFs, the product changes from intergrown to individual crystals, and the crystal size can be adjusted through the variation of modulator concentrations.[42]

It should be noted that, although the increasing concentration of modulator allows the growth of larger crystals, the presence of excess modulator can completely stop the nucleation of metal ions with the organic linker, thus leading to the absence of framework formation.[30] It is also worth mentioning that the variation of modulator acid can cause the formation of different metal clusters, thus yielding impure products.[43] Hence it is vitally important to find the optimized type and concentration of modulator in MOF synthesis to achieve targeted goals.

Apart from conventional solvothermal synthesis, it is important to explore novel synthesis methods for the discovery of new materials. As MOFs are a versatile platform for various applications, in each case the requirement on the size and shape of MOF materials is different. Sub-millimetre-sized MOF crystals are ideal for crystallography studies to explore the relationship between structure and functionality, while nano-sized MOF particles can be used for drug delivery in the biomedical field. The shape and size of the crystal have significant impacts on the diffusion rate of the guest molecules when a MOF is adopted for gas absorption or separation applications, or catalytic reactions. Thus, MOF chemists have developed various methods to explore the synthesis parameters.

Microwave-assisted (MW) synthesis has been widely applied in synthetic chemistry but mainly focused on organic chemistry.[44] MW synthesis is based on the interaction between electromagnetic waves and reactants with induced mobile electric charges, which can be polar solvents in solutions or ions in a solid. The high-frequency nature of the microwave forces the molecules to change their orientation rapidly, thus increasing the temperature as well as the kinetic energy of the molecules. The introduction of MW in MOF synthesis has several advantages, such as short reaction time, and high energy efficiency.[45] MW synthesis

is mainly used for the fast synthesis of nanoscale MOFs, due to the higher nucleation rate caused by the direct heating of the solvent. Several micro/nano-sized MOFs have been successfully prepared through MW synthesis, such as MOF-5, HKUST-1, Cr-MIL-101, Fe-MIL-88A.[46-49]

Electrochemical (EC) synthesis as an alternative synthesis method to obtain MOF materials was first reported by researchers at BASF in 2005.[50] In this method, the metal source is generated through the dissolution of an anode into the reaction medium, which contains dissolved linker molecules and a conducting salt. Notably, the avoidance of metal deposition on the cathode is achieved by employing protic solvents, and the continuous generation of H_2 can be avoided by the adoption of compounds in the electrolyte that can be reduced in this process such as acrylonitrile, acrylic, or maleic esters. EC synthesis is considered suitable for large-scale synthesis of MOFs because of the elimination of anions such as nitrate, perchlorate, or chloride. In addition, this route allows the continuous running of the synthesis process and achieves higher solids content compared to conventional batch reactions. A few Cu- and Zn-based MOFs have been successfully prepared using this method, such as a Zn-based nano-MOF [Zn(1,3-bdc)$_{0.5}$(bzim)] (bzim = benzimidazole) exhibiting adsorption ability towards ibuprofen, and the preparation of Cu-based MOF films [Cu_3(HHTP)$_2$] (HHTP = 2,3,6,7,10,11-hexahydroxytriphenylene).[51, 52] The general concern associated with EC is the presence of ligand molecules or conducting salts in the pores, which may result in an inferior quality of the MOFs,[53] hence the reaction conditions should be precisely adjusted to obtain optimized results and minimize the side effects.

Sonochemical (SC) synthesis has been widely applied in the preparation of nanomaterials and organic synthesis, and this method was applied in MOF synthesis in 2008, in which a nano-sized Zn-based MOF [$Zn_3(BTC)_2 \cdot 12H_2O$] was obtained and applied in selective sensing of organoamines.[54] As the length of the ultrasound wavelength is much longer than the molecule size, there is no direct interaction between the ultrasound wave and the reactant molecules. When ultrasound (usually 35 - 50 kHz) interacts with liquids, repeating

rarefactions and compressions occur, promoting the growth and collapse of the bubbles respectively. The collapse of the bubbles formed results in a rapid change of the pressure and temperature within the bubble, typically around 1000 bar and 5000 K respectively. The presence of these 'hot spots' releases energy to the reactant and promotes the formation and growth of MOFs. SC synthesis has the advantage of being simple, low-cost, efficient and environmentally friendly compared with conventional solvothermal synthesis. For example, it only takes 90 mins to synthesize the nanosized Zn-MOF [$Zn_3(BTC)_2 \cdot 12H_2O$] with high yield (85.3%), however hydrothermal synthesis of the same Zn-MOF requires 24 h reaction time under high pressure and 140°C.[54] More studies on the influence of reaction time, temperature, and concentration of initial reagents and solvents were conducted in subsequent years.[55-57] While the method yields promising results, there have been concerns about the reproducibility of the results. Different apparatus may generate different powers of ultrasound in the synthesis process. Additionally, the reaction temperature will increase when the reactor is placed in the ultrasound bath for a long time without other intervention, which may invalidate comparisons.

Mechanochemical (MC) synthesis refers to the process of breaking intramolecular bonds through mechanical forces, usually in a ball milling process, followed by chemical transformation.[58] MC synthesis has been widely applied in obtaining materials such as solid catalysts, nanoparticles, polymers, small organic molecules etc.[59-62] The first study on MC synthesis of MOFs was reported by James and colleagues in 2006, in which a 3D MOF [$Cu(INA)_2$] (INA = isonicotinic acid) was synthesized through a ball milling solvent-free process.[63] There have been several further reports of MC synthesis of MOFs, such as MOF-74, MOF-5, MIL-101 etc., in subsequent years.[64-67] MC synthesis is usually conducted in solvent-free conditions, or sometimes with small amounts of solvent added, which facilitates the use of an insoluble metal source in the synthesis, such as metal oxide.[68] Additionally, the byproducts are usually water or acetic acid when metal oxide, hydroxide or acetate are used, which is environmentally friendly and can be easily removed through thermal activation.[40] MC synthesis is considered a green approach, although there are

concerns about possible impurities from the milling reactors or amorphous products.[68, 69]

In addition to the above commonly used methods for MOF synthesis, other methods such as spray drying, flow synthesis, template, atomic layer deposition etc. can be found in the literature.[70-74]

1.1.3 Activation and Characterization

1.1.3.1 Activation

During the synthesis process, the guest molecules, which are usually solvent, unreacted linker or modulator molecules, may become trapped in the pores. It is then necessary to remove these molecules to access the pore spaces in the framework. However, solvents with high surface tension/high boiling point, such as water or DMF, may cause a higher capillary force during the liquid-to-gas phase change, which will devastate the framework when they are being removed.[75, 76] Care is needed to avoid such problems, especially when aiming to achieve the highest possible surface area and porosity. Several commonly used activation methods are discussed below.

Conventional thermal activation involves the process of applying heat and vacuum to the as-synthesized MOF samples to remove the solvent. This method has been applied in some MOFs with high stability, such as Cr-MIL-101 and UiO-66,[77, 78] which have BET surface areas of ~4100 m^2/g and 1070 m^2/g respectively. These two MOFs both exhibited remarkable thermal and chemical stabilities due to the strong Cr-O/Zr-O bonds, thus allowing direct activation to be applied. However, in most cases, direct activation of MOF samples leads to partial or total loss of crystallinity, as the coordination bonds presented in the frameworks are not strong enough to offset the high surface tension and capillary forces.[79] Thus, alternative milder activation methods should be considered to keep the framework intact.

As the reason for the collapse of the framework during activation is associated with the high surface tension and capillary forces generated during the liquid-to-gas phase change

process of solvent molecules, the easiest strategy to minimize this problem is to exchange for a solvent exhibiting low surface tension/boiling point, known as the solvent-exchange method. Such solvents, for example, MeOH, DCM or acetone, possess weaker intermolecular interactions and can generate less surface tension and capillary force during the activation process. The first attempt of the solvent-exchange method to activate MOF was demonstrated by Yaghi and coworkers in the activation of MOF-5.[16] The as-synthesized framework was soaked in $CHCl_3$ to replace DMF and chlorobenzene prior to activation, and the resulting activated MOF exhibited a Langmuir surface area of 2900 m^2/g. Similarly, Matzger and colleagues reported the use of perfluoropentane as the solvent to activate DUT-23(Zn) (DUT = Dresden University of Technology), a Zn-based MOF with paddle-wheel type SBU $[Zn_2(CO_2R)_4]$.[80] When n-hexane was used as the exchange solvent, the BET surface area was only ~100 m^2/g, whereas when DUT-23(Zn) was exchanged with perfluoropentane which has lower surface tension than n-hexane, the activated sample exhibited a BET area of 4890 m^2/g. As the solvent-exchange method is an effective way to activate MOF materials, this process should be carried out with care to minimize the potential loss of surface area due to incomplete activation. The MOF sample should be washed thoroughly using the reaction solvent to remove any unreacted linkers or other impurities. It is then recommended that the MOF sample is soaked in the exchange solvent overnight or for a prolonged time to allow the complete exchange, which can be later verified through NMR studies.[81] The exchanged sample can be activated with vacuum and applied heat, and the temperature should be higher than the boiling point of the exchanged solvent but far below the decomposition temperature of the frameworks, to allow complete activation.

An extension of the solvent-exchange method is to use supercritical carbon dioxide ($scCO_2$), namely supercritical activation.[82] Instead of liquid-to-gas phase change which may produce capillary force, the use of $scCO_2$ has eliminated the negative effect in this process through the supercritical phase. Thus, the fragile framework can remain intact and allow the measurement of surface area. Numerous reports have demonstrated the feasibility of $scCO_2$

activation, such as for NU-100, MOF-210 and SNU-70 (NU = Northwestern University, SNU = Seoul National University), which have BET surface areas of 7140, 6240 and 5290 m^2/g respectively, after $scCO_2$ activation.[82-84] Additionally, $scCO_2$ has advantages such as being non-flammable and inexpensive compared to other organic solvents. Usually before activation, the as-synthesized MOF is soaked in a solvent that is miscible with liquid CO_2, such as methanol or ethanol. Next, the MOF sample is exchanged with liquid CO_2 several times, and then the sample is heated to the supercritical temperature and pressure (31°C and 73 atm) to allow the 'fluid' to evacuate from the MOF sample. After completing this process, the sample is treated with mild heat and vacuum to remove any remaining CO_2 before conducting gas sorption measurements.

Alternative methods such as freeze-drying can be conducted to retain the framework structure as well. The MOF sample is exchanged with a compatible solvent that has a high freezing point and then cooled to freeze the solvent. By applying a vacuum, the solvent undergoes sublimation and turns into the gas phase without the occurrence of liquid-to-gas transformation. Such a process avoids the presence of deconstructive liquid surface tension and capillary force and can therefore keep the framework intact. Examples can be found in the report by Lin and colleagues,[85] where they soak the Cu-MOF $[Cu_2(L)(H_2O)_2]$, L = tetra(*p*-benzoic acid)methane, in benzene and the suspension was frozen at 0°C. After three freeze-thaw cycles, the sample was treated with a dynamic vacuum at 0°C to allow the benzene to sublime, followed by vacuum treatment at elevated temperatures for another 40 h. The resulting activated MOF has an increased BET surface area of 1560 m^2/g, nearly three times larger than the sample activated by the solvent-exchange method (526 m^2/g).

Other activation methods such as microwave activation and chemical activation have been reported as well.[86-89] However, these methods have not been as widely used due to the limitations in the activation process. For example, in the microwave activation method, the MOF sample (UiO-66, DUT-84 or MOF-808) is placed in water and the mixture is heated by microwave at 150°C to remove the modulators involved in the synthesis process.[86] This method is only applicable to those MOFs that are stable in water and high temperatures and

may not be efficient in completely removing the guest molecules. In the chemical activation method, hydrochloric acid is used to remove the linker and modulator in NU-1000,[89] then the MOF sample was treated using the solvent-exchange method before activation. The introduction of acid in the system may potentially cause the collapse of the framework, hence only acid-stable MOFs such as Zr-based MOFs are suitable for this method.[90, 91]

1.1.3.2 Characterization

X-ray diffraction (XRD) analysis is a powerful tool in characterising MOF structures because MOFs are crystalline porous materials with highly ordered atoms. Single crystal X-ray diffraction (SCXRD) and powder X-ray diffraction (PXRD) are the most used characterization techniques for MOFs. SCXRD can provide structure information at atom levels, with corresponding bond lengths and angles in sub-Angstrom precision.[92] Data are often collected at low temperatures to minimize the thermal motion of the atoms to obtain high-resolution data. After data collection from a single crystal, the well-arranged atoms can be localized to determine the framework structure, although it is also common to observe some disordered atoms from guest/solvent molecules in the pore spaces. Alternatively, an increase in data collection temperature may promote the disordered molecules to tumble rapidly, thus minimizing their diffraction peaks to give a better result of the data set.[81] Additionally, SCXRD also enables the possibility of studying MOF structures after 'post-treatment', such as gas sorption, guest exchange or structure change induced by a breathing effect,[93-96] provided that the crystal remains intact. It should be pointed out that SCXRD analysis has high requirements on the size, shape and quality of the crystal, which is challenging for some series of MOFs. Nevertheless, there are no universal guidelines for the growth of large crystals suitable for SCXRD analysis, and efforts must be made to adjust the reaction conditions such as temperature, time, concentration etc. to determine the optimized conditions in each case.

PXRD is an alternative way to obtain the fingerprint of a crystalline material, especially when there is a lack of large crystals from the product. The sample should be prepared as a

fine powder to distribute the crystal orientation evenly before conducting measurement. In some cases when the crystals are in a needle or plate shape, they tend to stay in a preferred orientation, hence it is necessary to continuously rotate the sample holder during the measurement process to eliminate such effects. By comparing PXRD results with the calculated powder pattern from SCXRD data, the phase purity of the bulk crystals can be verified. It is also possible to calculate the lattice constant according to the powder pattern, and sometimes full structure through computational modelling,[77, 97] although this process remains challenging. PXRD measurement is also a convenient approach to check the integrity of the MOF sample after activation or post-treatment process and can indicate the occurrence of phase change in some flexible MOFs.[98, 99]

One of the fascinating features that make MOFs attract tremendous research interest is the high surface area, which surpasses most conventional porous materials. Hence it is of great importance to measure their surface area, which is usually conducted through gas adsorption isotherm experiments. The analysis of these isotherms offers opportunities to determine not only surface area but pore size distribution and pore volume of MOFs. After the activation process, the N_2 adsorption measurement at 77 K is the most used method to evaluate the surface area of MOFs. Failure to activate the MOF samples properly may result in invalid results, hence extra care should be taken in these processes. Usually, the surface area results are considered to be reliable when the amount of sample used (in grams) multiplied by the specific surface area (in m^2/g) is higher than 100 m^2.

Currently, there are two main theorems used to calculate surface areas, Brauner-Emmet-Teller (BET) theory and Langmuir theory.[100, 101] The BET surface area is calculated based on the multilayer gas adsorption model, which is widely used in calculating the surface area of MOF materials, whereas the Langmuir theory assumes that gas molecules are distributed as a monolayer on the surface of the materials, and this theory tends to overestimate the surface area of the MOFs.[81]

The BET equation is shown below,

$$\frac{p/p_0}{n(1-p/p_0)} = \frac{1}{n_m C} + \frac{C-1}{n_m C}(p/p_0)$$

where n is the amount of N_2 gas adsorbed, p is the pressure, p_0 is the saturation pressure of N_2, n_m is the monolayer capacity, and C is the BET constant. The BET surface area can be calculated through the plot of $[(p/p_0)/n(1-p/p_0)]$ vs p/p_0. Rouquerol *et al.* stated that a linear region must be selected in this plot to meet the criteria, where (i) the BET constant C must be positive, (ii) $n(1-p/p_0)$ should exhibit a monotonic increase with p/p_0, (iii) the pressure corresponding to the monolayer capacity (n_m) should fall within the range of the data, and (iv) the calculated value for monolayer formation $(1/(\sqrt{C}+1))$ should be approximately equivalent to p/p_0 at the monolayer capacity.[102] From the slope and intercept of this linear region, the BET area (apparent surface area), n_m, and C can be determined. In practice, it is sometimes difficult to select a region from experiment isotherms that meet all four criteria, care should be taken to minimize the standard deviation.[103] Nevertheless, BET surface area is widely accepted and regarded as a valuable fingerprint of MOF materials. It should be noted that when micropores are presented, in most cases of MOFs, it is difficult to distinguish between monolayer adsorption and multilayer adsorption, making it difficult to identify a linear range for BET calculations. Therefore, it is advisable to use terms such as 'apparent BET surface area' or 'estimated BET surface area' to address this issue.[104]

Density functional theory (DFT) is a widely accepted method for the analysis of MOF pore size, although other methods such as the Barrett-Joyner-Halenda (BJH) method and Grand canonical Monte Carlo (GCMC) models can be used in the simulation as well.[92] It should be noted that, due to potential structural change, improper activation or model limitation, the simulated pore size distribution may not represent the actual situation, and MOF crystals may possess different pore distribution. Caution is required when calculating pore size distribution information from the isotherms, and comparisons between each model should be made before obtaining an acceptable fitting result. Pore volume can be calculated through the volume of total gas adsorbed when p/p_0 approaches 1.0.

Apart from the above basic X-ray diffraction characterizations to obtain structural

information, and N_2 adsorption/desorption isotherms to evaluate porosity and surface area, other techniques are often used to characterize different properties based on the demand of the application. They can be categorized into several aspects, such as morphology characterization including scanning electron microscopy (SEM) or transition electron microscopy (TEM) for a higher resolution; element analysis such as inductive coupled plasma atomic emission spectroscopy (ICP-AES), X-ray photoelectron spectroscopy (XPS) and energy dispersive X-ray spectroscopy (EDS); stability tests such as aqueous stabilities (various pH) and thermal stabilities through thermogravimetric analysis (TGA); nuclear magnetic resonance (NMR) spectroscopy to study the impurities in the frameworks using digested MOF samples; particle size distribution studies through dynamic light scattering (DLS) measurement in the case of nano-MOFs; photoluminescence (PL) studies for chemical sensing applications etc. Information on these methods can be found in the literature.[92, 104, 105]

1.2 Si/Ge-based Linkers in MOF Construction

The organic linker plays an important role in MOF materials, as it can be fine-tuned to generate novel structures and bring novel properties to the MOF. The most utilised linker types are aromatic carboxylate-based planar linkers such as BDC, BTC and their derivatives (Figure 1.9). Undoubtedly, the combination of these planar linkers with metal clusters can generate 3D frameworks, but this usually involves the judicious choice of appropriate metal clusters.[106]

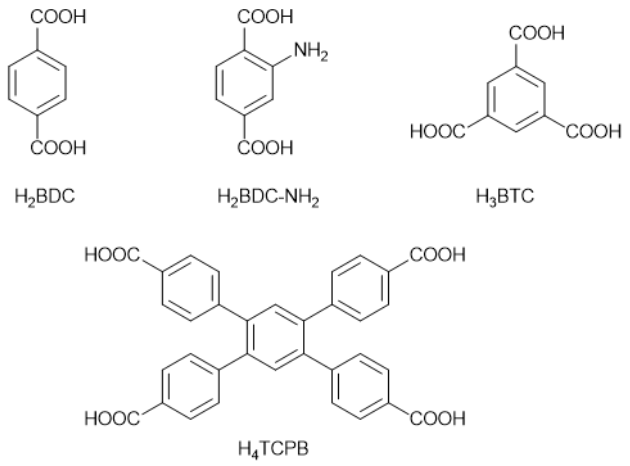

Figure 1.9 Structure of some commonly used aromatic carboxylate-based linkers.

The use of non-planar connectors offers a direct approach to generate 3D structures, for example, tetraphenylmethane-based linkers,[96] although there are still challenges remaining in the linker synthesis process.[107] Alternatively, tetravalent silicon, and to a lesser extent germanium, centred linkers have shown promise in MOF construction in recent years, and some of the resulting MOFs have exhibited good performance in gas storage and separation, catalysis and luminescence sensing.[108-110] Si-based linkers exhibit unique characteristics compared to their carbon analogues. These linkers are more synthetically accessible than their carbon analogues, making them more suitable for building novel structures and easy to modify. The increased E-C bond (E = Si or Ge) length has contributed to the conformation flexibility as well as reduced rigidity, allowing the formation of novel topologies in some cases. Typically, these linkers are based on tetrahedral silicon centres or

siloxanes with carboxylic acid or tetrazole functional groups (Figure 1.10).

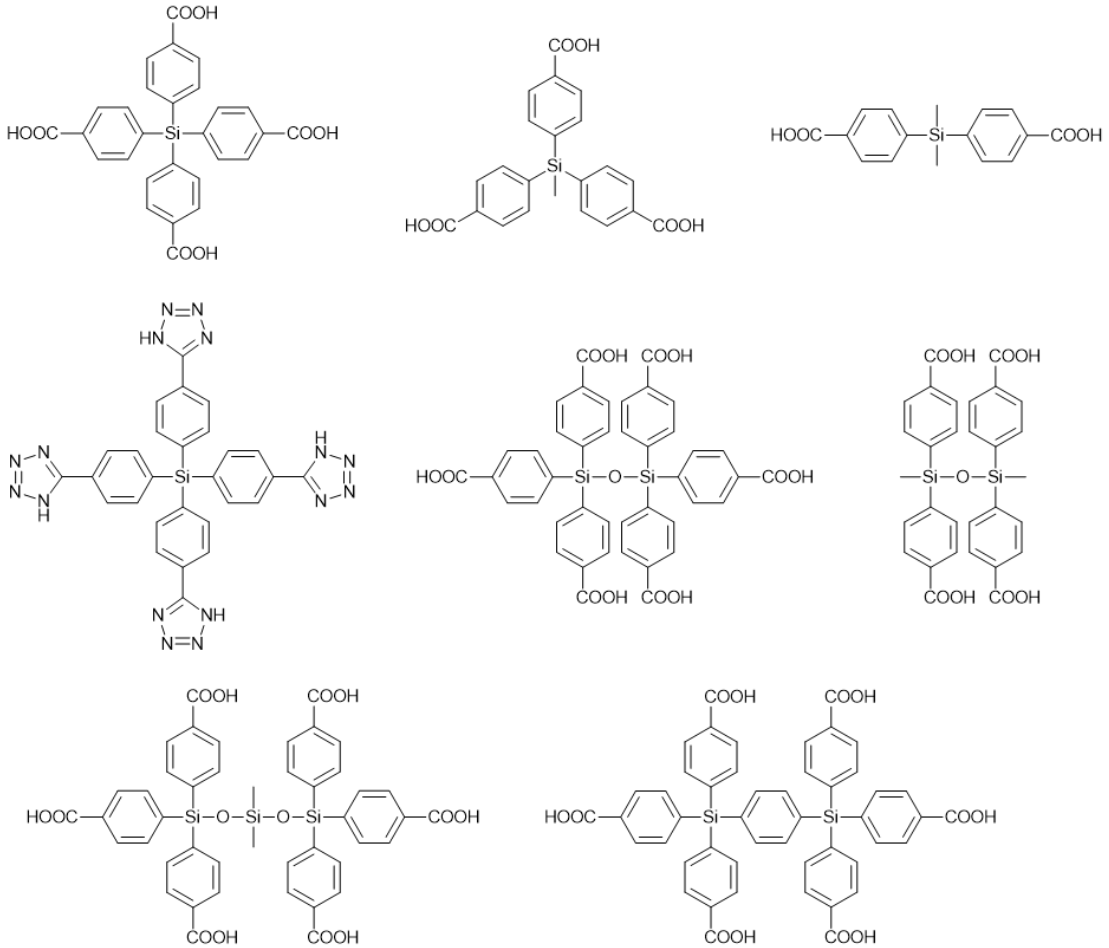

Figure 1.10 Structure of some tetravalent silicon or siloxane linkers used in IMP MOFs (IMP stands for Imperial College London).

The first study involving the use of tetrahedral organosilicon-based linkers in the construction of CPs was reported by Tilley and colleagues in 1997.[111] Tetrakis(*p*-cyanophenyl)silane was used to construct two structures using AgO_3SCF_3 or $AgPF_6$ as metal precursors, and the resulting frameworks consisted of interpenetrated double layers through the combination of Ag ions and tetrahedral Si connectors. These results demonstrated the feasibility of adopting organosilicon compounds as building blocks to construct 3D frameworks, although these two structures suffered from poor stability. The syntheses of tetrakis(*p*-carboxyphenyl)silane (TCPS),[112] and tetrakis(*p*-carboxyphenyl) germanium (TCPG)[113] were reported separately by Lambert and co-workers, and both

TCPS and TCPG reacted with various metal cations to yield different MOFs.

Later, Davies and colleagues reported MOF synthesis using tetravalent Si-based linkers [$Me_nSi(p\text{-}C_6H_4CO_2H)_{4-n}$, n = 0, 1, 2, shown in Figure 1.10].[114] These linkers provide versatile platforms for reaction with various metal sources for the construction of novel 2D or 3D MOFs. For example, a Cu-based MOF (IMP-9) was constructed from the reaction of copper (II) nitrate with TCPS,[107] and the resulting 3D framework comprises square planar paddlewheel SBUs and TCPS linkers exhibiting *pts* topology (Figure 1.11).

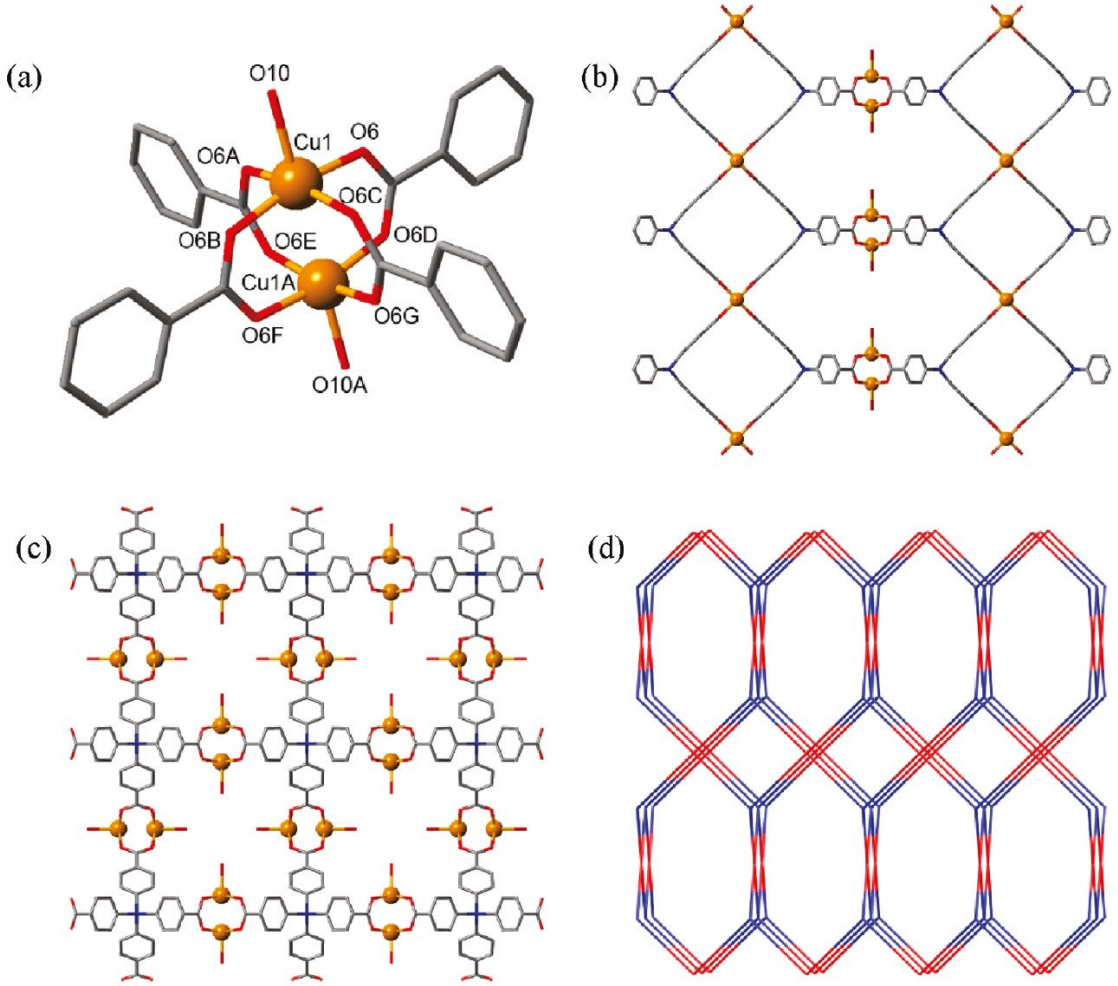

Figure 1.11 Crystal structure of IMP-9, a) square planar paddlewheel binuclear SBU; b) packing diagram from (1 0 0) view; c) packing diagram from (0 0 1) view; d) *pts* topology. C: grey, O: red, Cu: orange, Si: blue. H atoms and uncoordinated solvent molecules are omitted for clarity.[107]

The incorporation of hydrophobic groups in the siloxane linkers can increase the hydrophobicity, such as IMP-32-Zr reported by Davies and co-workers.[115] The reaction of $ZrOCl_2$ with 1,3-dimethyltetrakis(p-carboxyphenyl) disiloxane in DMF and formic acid afforded needle crystals of IMP-32-Zr which consisted of eight-connected Zr_6O_8 nodes and four-connected siloxane liners (Figure 1.12). Due to the presence of the Si-CH_3 groups, IMP-32-Zr exhibited low water uptake (≤ 15 wt%) at 95% relative humidity.

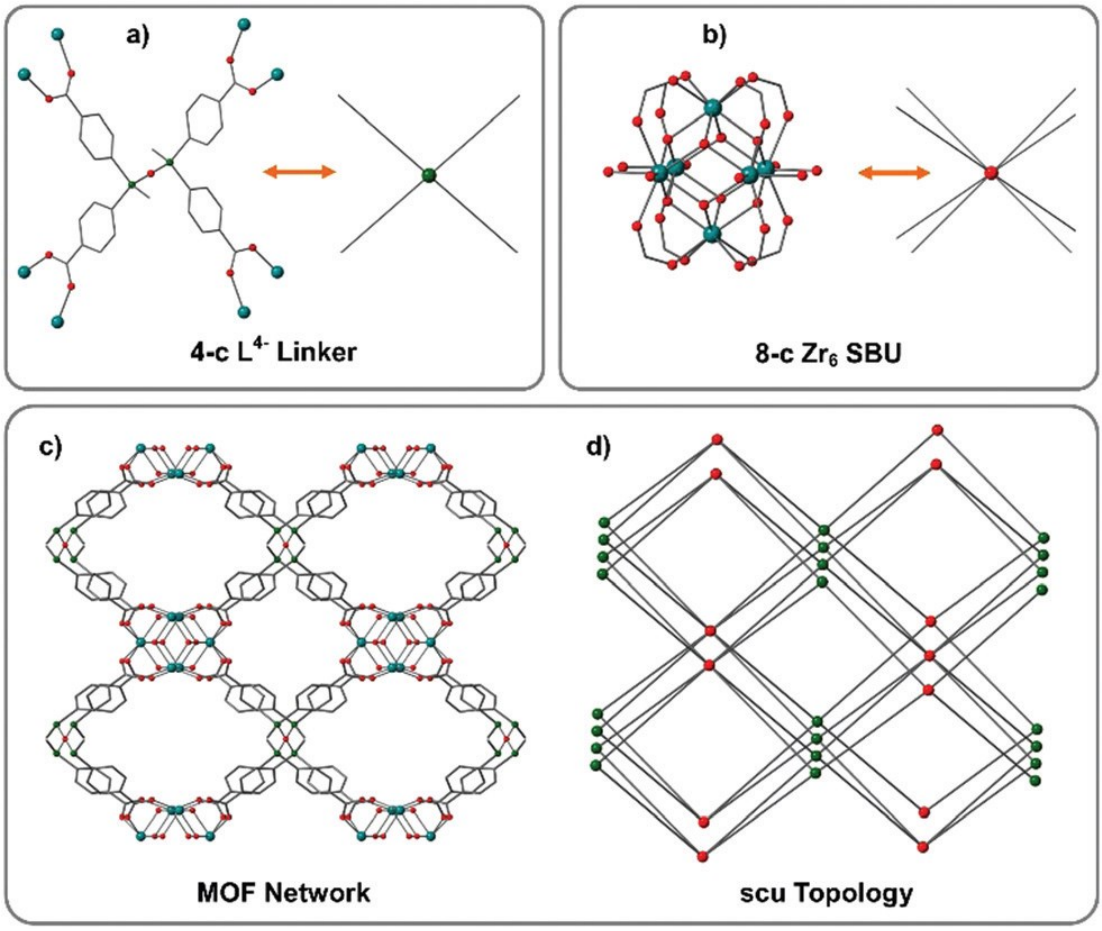

Figure 1.12 Crystal structure of IMP-32-Zr, a) coordination environment of the siloxane linkers; b) Zr_6O_8 SBU; c) packing diagram from (1 0 0) view; d) *scu* topology. C: grey, O: red, Zr: turquoise, Si: green. H atoms and solvent molecules are omitted for clarity.[115]

Xue *et al.* reported a Cu-MOF with 5,5',5'',5'''-silanetetrayltetraisophthalic acid as the linker.[116] This MOF comprises Cu paddlewheel SBUs and octadentate linkers to yield a *scu* topology. Furthermore, this Cu-MOF possesses permanent porosity and exhibits good

selectivity for CO_2 over CH_4 (6.2 in molar ratio), and a relatively high H_2 storage capacity (211 cm^3/g). Gao *et al.* reported a Cd-MOF constructed using TCPS as the linker.[117] The large rectangular channels (7 × 8 $Å^2$) allow the absorption of organic dyes, and this Cd-MOF exhibited high methylene blue uptake capacity (~1008 mg/g) which could mainly be attributed to the size fit of the dye molecules as well as the π···π and p···π interactions between the linker phenyl rings and dye molecule. Such high absorption capacity suggests that this Cd-MOF can be applied to separate organic dyes from wastewater and thus reduce their harmful effect on the aquatic environment.

Although these silane/siloxane-based linkers have been adopted in MOF synthesis, it should be noted that many MOFs possess poor stability upon activation, such as some IMP MOFs.[118-120] As a result, their gas capture capacities have only been calculated theoretically, such as PCN-12-Si which has a calculated 4.8 wt% H_2 capacity at 30 bar but an experimental value of 0 after activation.[121] In addition, there is a lack of research on using tetravalent Ge-based linkers for MOF construction, with only a few reported examples.[113]

Alternatively, the use of hexacoordinated Si connectors such as SiF_6^{2-} for MOF construction

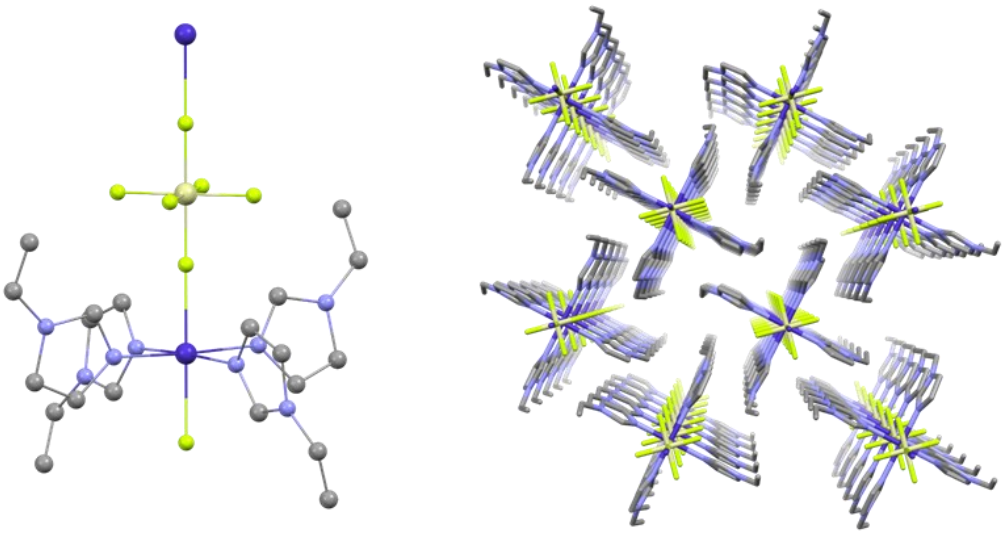

Figure 1.13 Left) coordination environment of the Co^{2+} ion; Right) packing diagram from (0 0 1) view, showing infinite 1D linear chains. C: grey, N: night blue, F: green-yellow, Si: pale yellow, Co: indigo. H atoms are omitted for clarity. Figure redrawn using published crystal data from Reedijk and colleagues (CSD refcode: BOHFAF).[122]

may overcome some of these challenges. In 1982, Reedijk and colleagues reported the use of this anion in the construction of coordination compounds as an anionic counterpart to metal cations.[122] The reaction of N-vinylimidazole (viz) with $CoSiF_6$ afforded pink crystals which were analysed by SCXRD to be $[Co(viz)_4SiF_6]$. Each Co^{2+} cation is coordinated by four N atoms from the viz group and two F atoms from two SiF_6 units in the apical direction to give an octahedral geometry. While there is only one coordination point in each viz group, no further coordination was observed in the viz group or Co^{2+} cations, and such arrangement generates indefinite 1D linear chain structures with the repeat unit of -F-Si-F-Co-F-Si-F- (Figure 1.13).

The incorporation of the SiF_6^{2-} anion in the construction of 3D CPs was reported by Zaworotko and colleagues in 1995.[123] The cooling of a 1,4-dioxane and DMF solvent mixture containing $ZnSiF_6$ and 4,4'-bipyridine (Bipy) afforded colourless crystals with a formula of $[Zn(Bipy)_2SiF_6]\cdot xDMF$ revealed by SCXRD analysis. In the crystal structure, each Zn^{2+} cation coordinates with four Bipy N atoms, and each Bipy ligand coordinates

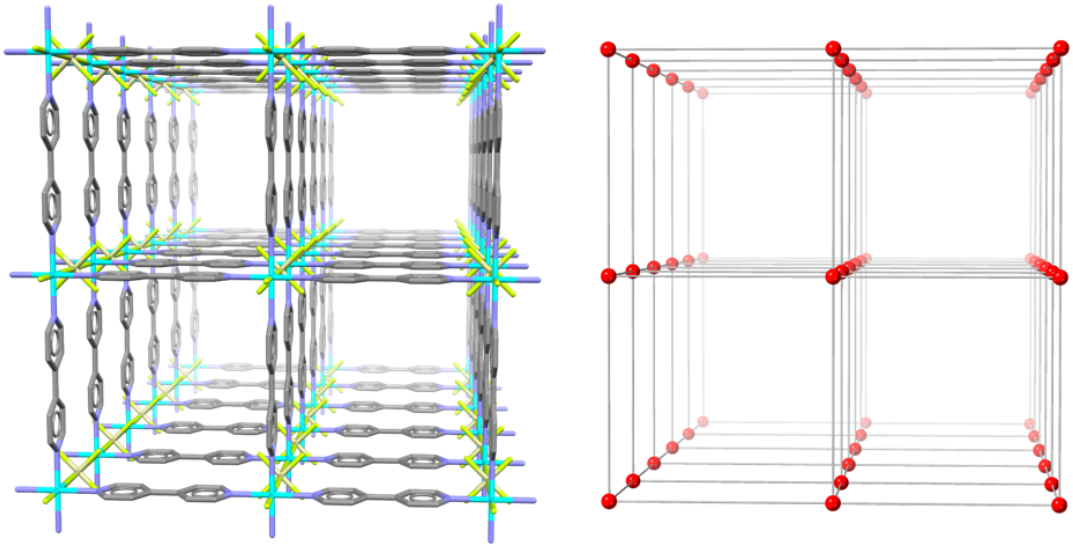

Figure 1.14 Left) Crystal structure of $[Zn(Bipy)_2SiF_6]$ along (0 0 1), right) simplified *pcu* network topology. C: grey, N: night blue, F: green-yellow, Si: pale yellow, Zn: pale blue. H atoms are omitted for clarity. Figure redrawn using published crystal data from Zaworotko and colleagues (CSD refcode: ZESFUY).[123]

with two Zn^{2+} cations to generate a square-grid planar net. Each layer is linked by the bridging SiF_6^{2-} anion coordinating with Zn^{2+} cations in the apical directions to generate 3D structures with *pcu* topology (Figure 1.14). Although this CP was not stable upon exposure to air or water, it offered a platform to precisely design the dimensions of the pore through the variation of the organic linkers.

In 2000, Kitagawa and co-workers reported a Cu-based CP $[Cu(Bipy)_2]SiF_6$ which was prepared by the reaction of $Cu(BF_4)_2 \cdot 6H_2O$, $(NH_4)_2SiF_6$ and 4,4'-bipyridine in a mixture of water and ethylene glycol.[124] The resulting framework exhibited an identical structure compared to the Zn-CP, and the increased stability of the framework allowed the complete removal of solvent molecules from the pore to expose guest-accessible spaces, with a BET surface area of 1337 m^2/g through Ar adsorption measurement. In addition, this CP exhibited a large methane uptake capacity (6.5 mmol/g at 36 bar), higher than that of zeolite 5A (3.7 mmol/g at 36 bar). This prototype successfully demonstrated the feasibility of adopting this type of CP in gas adsorption applications. In the following decades, numerous studies on this type of CP have been reported with the bridging ligand extended to GeF_6^{2-}, TiF_6^{2-}, SnF_6^{2-}, NbF_6^{2-}, PF_6^{-}, VF_6^{2-}, GaF_6^{3-}, ReF_6^{2-}, SbF_6^{-} and AlF_6^{3-} (XFSIX).[125-133] In addition, the SiF_6^{2-} anion has also been applied in HOF synthesis.[134, 135]

In the following section, SiF_6^{2-} and GeF_6^{2-} type MOFs are summarized and listed. As there are fewer reports on MOFs with other hexafluoro-based anions, these MOFs are not listed but instead are mentioned in subsequent discussions where relevant. Table 1.1 below only includes MOFs with crystal data available from the CCDC (November 2023). Frameworks with the same linker and net topology but with different uncoordinated solvent molecules are merged into one entry.

Table 1.1 List of SIFSIX and GeFSIX type MOFs. For structures of the linkers see below.

Entry	Formula	Crystal growth method	Topology	Properties & References
1	$Cu(bipy)_2SiF_6$	Layer diffusion	*pcu*	CH_4 uptake,[124, 130] CO_2 uptake over CH_4,[136] C_2H_2/C_2H_4 separation,[137] SO_2 uptake, SO_2/N_2 and SO_2/CO_2 selectivity[138]
2	$Cu(bipy)_2GeF_6$	Layer diffusion	*pcu*	CH_4 uptake[130]
3	$Cu(dpm)_2SiF_6$	Layer diffusion	2D	C_2H_2/CO_2 separation[139]
4	$Cu(dpm)_2GeF_6$	Layer diffusion	2D	C_2H_2/CO_2 separation[139]
5	$Co(viz)_4SiF_6$	Slow crystallization	1D	Structure report only[122]
6	$[Zn_2(pdte)_4SiF_6]SiF_6$	Layer diffusion	1D	Structure report only[140]
7	$Cu(bipy)_2SiF_6$	Solvothermal	*kgm*	Magnetic properties[141]
8	$Zn(tpyp\text{-}Fe)SiF_6$	Layer diffusion	*fsc*	CO_2 uptake over N_2/CH_4, oxygen reduction reaction[142]
9	$Zn(bpmhaz)_2SiF_6$	Layer diffusion	*pcu*	Structure report only[143]
10	$Cu(bpb\text{-}CF_3)_2SiF_6$	Layer diffusion	*pcu*	C_2H_2 and CO_2 uptake over CH_4/N_2[144]
11	$Cu(dpt)_2SiF_6$	Layer diffusion	*pcu*	Analogues $Cu(dptz)TiF_6$: CO_2 uptake, CO_2/N_2 separation;[131] CO_2 uptake from CO_2/N_2 or CO_2/CH_4[145]
12	$Ni(pyaz)_2SiF_6$	Layer/grinding	*pcu*	CO_2 uptake, H_2S tolerance,[146] C_3H_4 remove from C_3H_6,[147] Mechanism studies on Ke adsorption[148]
13	$Cu_2(abtaz)_2SiF_6$	Electrochemical	/	First Cu^+-SiF_6^{2-} bond[149]
14	$Cu(dpac)_2SiF_6$	Layer diffusion	*pcu*	C_2H_2 uptake, C_2H_2 removal from C_2H_4,[137] SO_2 uptake, SO_2/N_2 and SO_2/CO_2 selectivity,[138] CO_2 uptake from N_2, H_2 or CH_4[150]
15	$Cu_3(tpa)_4(SiF_6)_3$	Layer diffusion	*Ith-d*	C_2H_2 uptake, C_2H_2/CO_2 separation,[151]
16	$Ni(pypz)_2SiF_6$	Layer diffusion	*pcu*	C_2H_2/CO_2 separation[152]
17	$Cu(pypz)_2SiF_6$	Layer diffusion	*pcu*	Structure report only[152]
18	$Zn(tepb)SiF_6$	Layer diffusion	*fsc*	C_2H_2/CO_2 separation,[153] C_2H_2/C_2H_4 separation[154]

19	$Cu_3(tmtpb)_4(SiF_6)_3$	Layer diffusion	/	C_2H_2 and C_3H_4 uptake, C_2H_2/C_2H_4 and C_3H_4/C_3H_6 separation[155]
20	$Zn(dpndi)_2SiF_6$	Layer diffusion	*pcu*	Prevent interpenetration, photochromic properties[156]
21	$Cu(pyaz)SiF_6(H_2O)_2$	Layer diffusion	1D	Structure report only[157]
22	$Cu(pyaz)_3SiF_6(H_2O)_2$	Layer diffusion	2D	Structure report only[157]
23	$Zn(pyaz)_2SiF_6$	Layer diffusion	*pcu*	H_2 uptake[157]
24	$Cu(dpmo)_2SiF_6$	Slow crystallization	2D	Structure report only[158]
25	$Zn(bpp)_2SiF_6$	Layer diffusion	2D	Structure report only[159]
26	$Cu(pyina)_2SiF_6$	Layer diffusion	*pcu*	C_2H_2/CO_2 uptake over CH_4[160]
27	$Zn(dpydmbp)_2SiF_6$	Layer diffusion	2D	Structure report only[161]
28	$Cu(bpye)_2SiF_6$	Solvothermal	*pcu*	CO_2 uptake over CH_4[136]
29	$Cu(pyac)_2SiF_6$	/	*sql*	Metalloligand, water vapour stability, CO_2 uptake over CH_4[162]
30	$Zn(dpytm)_2SiF_6$ + 3 similar	Layer diffusion	2D	Structure report only[163]
31	$Cu(azpy)_2SiF_6$	Layer diffusion	*pcu*	CO_2/CH_4 separation,[164] CO_2 uptake,[165] C_2H_2 remove from C_2H_4[166]
32	$Cu(ppzh)_4SiF_6$	Slow crystallization	1D	Structure report only[167]
33	$Cu(dimbza)_2SiF_6$	Solvothermal	*dia*[168]/*scu*[169]	TiF_6 analogues C_2H_2/C_2H_4 separation,[168] C_2H_2/CO_2 sepration[169]
34	$Cu(sdi)_2SiF_6$	Layer diffusion	*nbo*	CO_2/CH_4 and C_2H_2/CH_4 separation[170]
35	$Cu(pyaoh)_4SiF_6$	Slow recrystallization	1D	Structure report only[171]
36	$Cu_3(R\text{-}trisn)_4(SiF_6)_2$	Layer diffusion	1D	Structure report only[172]
37	$Cd_2(Me_4bpz)_4SiF_6(NCS)_2$	Layer diffusion	*noz*	Structure report only[173]
38	$Cd(Me_4bpz)_2SiF_6$	Solvothermal	*pcu*	Structure report only[173]
39	$Cu(dpso2)_2GeF_6$	Layer diffusion	*sql*	C_2H_2/CO_2 separation[174]
40	$Cu_2(sahdz)_2SiF_6$	Layer diffusion	1D	Structure report only[175]
41	$Cu_2(btdda)SiF_6(H_2O)_2$	Layer diffusion	1D	Structure report only[176]
42	$Cd(imppy)_2SiF_6$	Slow evaporation	/	Luminescent properties[177]
43	$Zn(pds)_2SiF_6$	Layer diffusion	*cds*	Structure report only[178]

44	$Zn(bpyna)_2SiF_6$	Layer diffusion	*pcu*	Structure report only[179]
45	$Zn(bipydp)_2SiF_6$	Layer diffusion	*pcu*	Structure report only[179]
46	$Cu/Zn(bienpyb)_2SiF_6$	Layer diffusion	*pcu*	Offset interpenetration[180]
47	$Zn(bienpybp)_2SiF_6$	Layer diffusion	*pcu*	Structure report only[180]
48	$[Cu_2(bdmpysie)_4SiF_6]SiF_6$	Slow crystallization	1D	Structure report only[181]
49	$Cu(dps)_2GeF_6$	Slow crystallization	/	C_3H_4/C_3H_6 and C_2H_2/C_2H_4 separation[182]
50	$Zn(dps)_2GeF_6$	Slow crystallization	/	C_3H_4/C_3H_6 and C_2H_2/C_2H_4 separation[182]
51	$Fe(pyaz)_2SiF_6$	Slow evaporation	*pcu*	Xe uptake over Kr[148]
52	$Cu(dpac)_2GeF_6$	Layer diffusion	*pcu*	C_4H_6 uptake, C_4H_6/iso-C_4H_8 spearation[132]
53	$Cd(pyba)_2SiF_6$	Layer diffusion	*neb*	Luminescence property[183]
54	$Zn(bpybz)_2SiF_6$	Layer diffusion	*pcu*	Enhanced thermal stability[184]
55	$Zn(bpyacna)_2SiF_6$	Layer diffusion	*pcu*	Enhanced thermal stability[184]
56	$Cu(na)_2SiF_6$	Slow crystallization	*1D*	Structure report only[185]
57	$Cu(bimbz)_2SiF_6$	Layer diffusion[186, 187] Solvothermal[188]	*pcu*	Phase change during gas adsorption, CO_2 uptake,[186] CO_2 and C_2H_2 uptake over C_2H_4,[187] C_2H_4 uptake from $C_2H_2/CO_2/C_2H_4$[188]
58	$Zn(bpye)_2SiF_6$	Layer diffusion	*pcu/sql*	3D/2D through different solvent, C_2H_2 uptake over CO_2 and CH_4[189]
59	$Zn(dpc)_2SiF_6$	Slow evaporation	*sql*	CO_2 uptake[190]
60	$Cu(2,4'\text{-}bipy)_4SiF_6$	Slow crystallization	1D	Structure report only[191]
61	$Cu(phpyr)_4SiF_6$	Slow crystallization	1D	Structure report only[191]
62	$Zn(tpe)SiF_6$	Layer diffusion	*fsc*	C_2H_2 capture from C_2H_2/C_2H_4[192]
63	$Cu(dps)_2SiF_6$	Layer diffusion	*sql*	C_2H_2 capture (remove) from C_2H_2/C_2H_4[193]
64	$Zn(dps)_2SiF_6$	Slow crystallization	*sql*	C_2H_2 uptake from C_2H_2/CO_2 and C_2H_2/C_2H_4[194]
65	$Zn(bpybzr)_2SiF_6$ + 2 similar	Layer diffusion	*pcu*	Structure report only[195]
66	$Cu(azpy)_2GeF_6$	Layer diffusion	*pcu*	C_4H_6 uptake over n-C_4H_8 and iso-C_4H_8[132]
67	$Cu(dpso2)_2GeF_6$	Layer diffusion	2D	C_2H_2 uptake over C_2H_4[196]

68	$Zn(an2py)_2SiF_6$	Layer diffusion	*pcu*	Two-photon excited fluorescence[197]
69	$Cu(nppfba)_4SiF_6$	/	1D	Structure report only[198]
70	$Cu(dpio)_2SiF_6$	Layer diffusion	*pcu*	Nitroxyl radicals catalyse aerobic oxidation of alcohol[199]
71	$Cu(inicam)_4SiF_6$	Slow crystallization	1D	Structure report only[200]
72	$Cu(tripp)SiF_6$	Layer diffusion	/	Structure report only[201]
73	$Zn(pytec)SiF_6$ + 1 similar	Layer diffusion	1D	Structure report only[202]
74	$Cu(azpy)_2SiF_6$	Layer diffusion	*pcu*	CO_2 uptake[203]
75	$Zn(bpy)_2SiF_6$	Layer diffusion	*pcu*	Structure report only[204]
76	$Zn(pyac)_2SiF_6$	Layer diffusion	*pcu*	Structure report only[204]
77	$Zn(bpybz)_2SiF_6$	Layer diffusion	*pcu*	Structure report only[204]
78	$Cd(bib)_2SiF_6$	Layer diffusion	*pcu*	Sensing arginine[205]
79	$Cu(bydo)_2SiF_6$	Layer diffusion	*bcu*	Structure report only[133]
80	$Cu(pyazole)_4SiF_6$	Layer diffusion	1D	Structure report only[206]
81	$Cu_2(dpya)_2F_2SiF_6$	Solvothermal	1D	Antiferromagnetic properties[207]
82	$Cu(tpbda)SiF_6$	Layer diffusion	*wly*	C_2H_2 uptake and separation from C_2H_2/CO_2 or C_2H_2/C_2H_4[129]
83	$Cu(methsca)(H_2O)SiF_6$	Slow evaporation	1D	Structure report only[208]
84	$Cd(pmntd)_2SiF_6$	Layer diffusion	*pcu*	Structure report only[209]
85	$Cu_3(pyarc)_4SiF_6$	Layer diffusion	*sql*	CO_2 uptake over N_2 and CH_4[210]
86	$Ni(pyaz)_2GeF_6$	Heating	*pcu*	Mechano-assisted synthesis, CO_2 uptake and CO_2/CH_4 separation[211]

Full topology figure and description can be found in the RCSR website: https://rcsr.anu.edu.au/nets.

List of linkers (with entry below the structure).

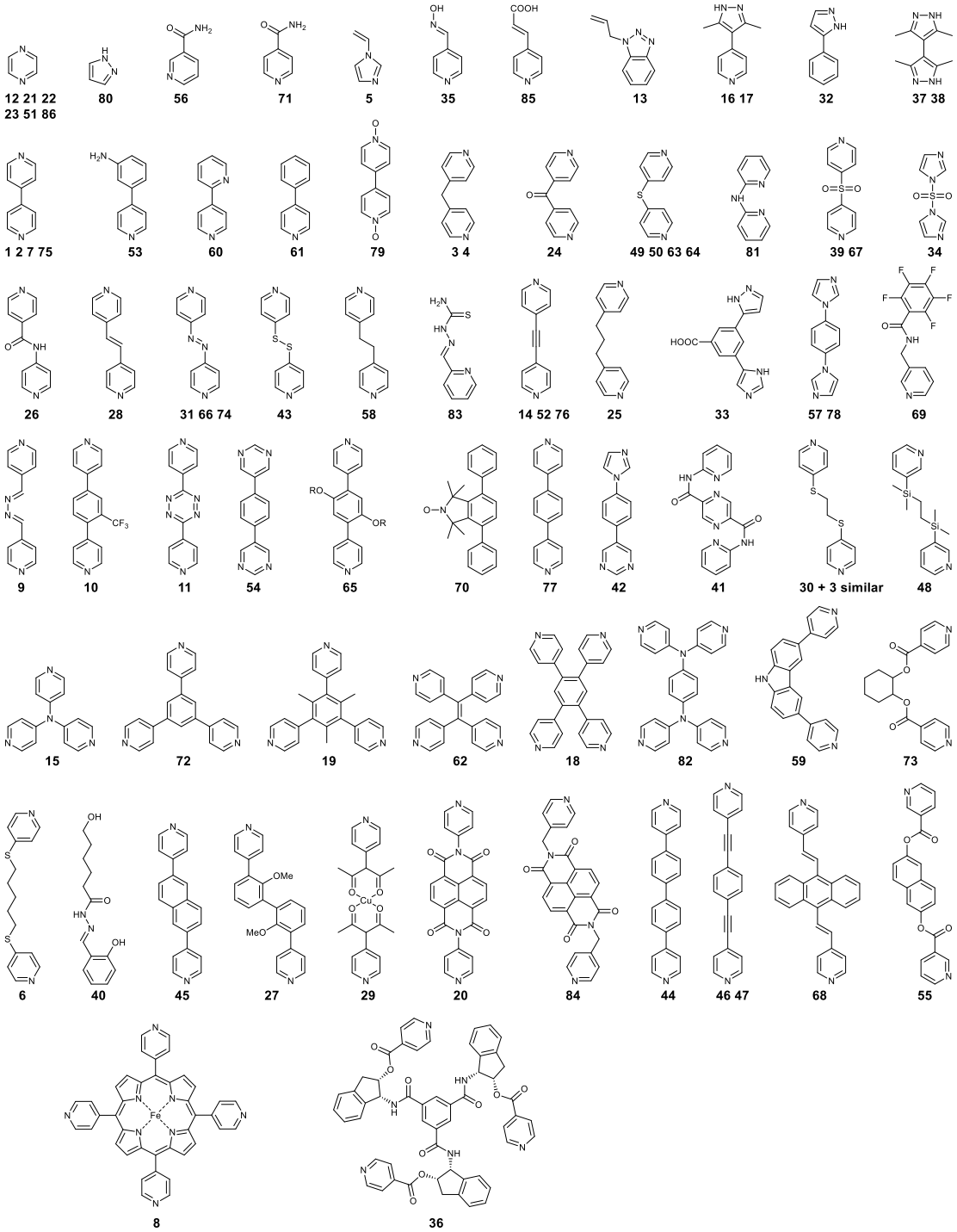

1.2.1 Synthesis and Structure Overview

As can be seen from Table 1.1, layer diffusion is the most commonly used method to synthesize SIFSIX type MOFs, while other approaches such as solvothermal,[141] electrochemical,[149] mechanochemical,[146, 211] sonochemical methods,[212, 213] have been reported as well. In a typical layering diffusion process, the organic ligand is dissolved in an alcohol solvent and carefully layered on a DMSO/alcohol/chloroform solution of metal hexafluorosilicate salts in a thin glass tube. Usually, there is a buffer layer of the solvent between these two layers to slow the mixing rate, and large crystals can often be obtained after a few days (Figure 1.15). Alternatively, direct mixing of linker and metal salt solutions leads to a fast reaction and yields the powder form of the products in a few minutes or hours.

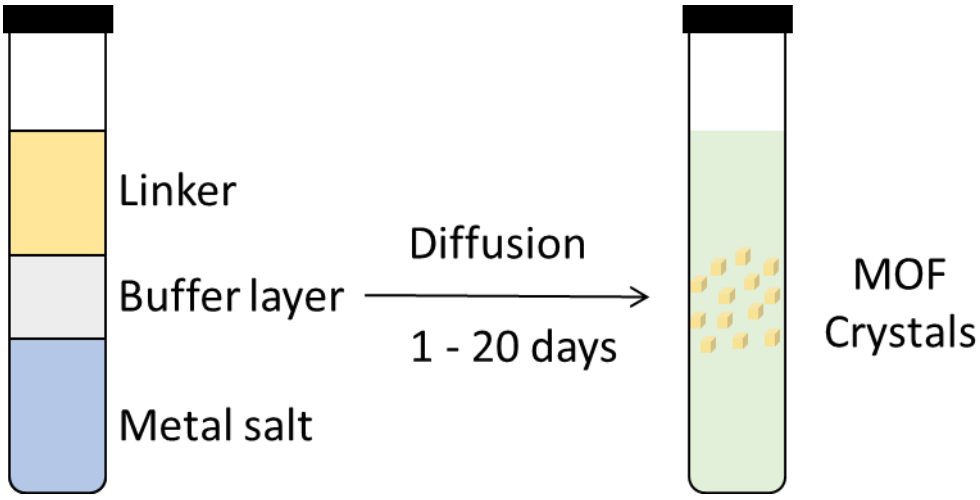

Figure 1.15 The layer diffusion method.

An alternative approach is to use metal tetrafluoroborate as the reagent and allow the reaction to occur in a glass container. The partial hydrolysis of BF_4^- anion leads to the formation of HF which then reacts with SiO_2 in the glass to generate H_2SiF_6. For example, Wu and colleagues reported the synthesis of Cu-TPA-SiF_6 [$Cu_3(TPA)_4(SiF_6)_3$, TPA = tri(pyridin-4-yl)amine] through the slow diffusion of a TPA solution (in MeOH) into an aqueous solution of $Cu(BF_4)_2$.[214] The crystals of Cu-TPA-BF_4 underwent a colour change from blue to violet after staying in a glass tube for 6 weeks, resulting in the formation of Cu-TPA-SiF_6, as confirmed by SCXRD studies.

The structures of XFSIX-type MOFs can exhibit 1D linear chains, 2D networks or 3D frameworks, depending on the type and geometry of the organic ligand. When there is only one coordinating point in the N-based ligand or the N atoms in a ditopic ligand point in the same direction, these arrangements usually yield 1D chain structures. The use of non-linear ditopic ligands may facilitate the formation of 2D sheet structures, and the adoption of a rigid linear ditopic ligand should afford 3D cubic frameworks with *pcu* topology (Figure 1.16). The 3D MOF can be simplified into a formula $[M(L)_2(XF_6)]$, where M is a metal cation such as Cu(II), Zn(II), Co(II), Ni(II), X = Si, Ge or other species stated in the preceding text, and L is usually a bipyridine or pyrazine based derivative linker which has two binding sites.

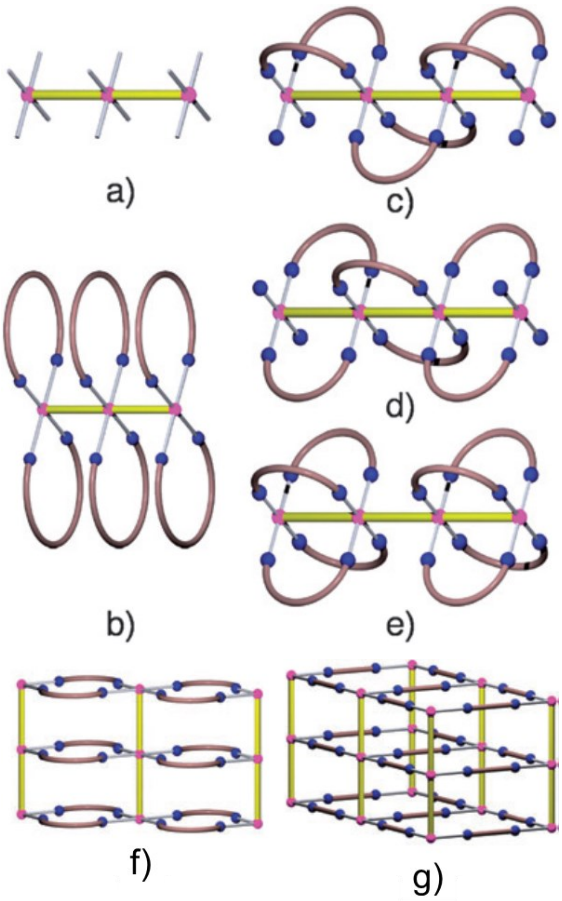

Figure 1.16 Schematic representation of a-e) 1D chain, f) 2D sheet, g) 3D framework structures. The yellow pillars represent -F-Si-F-M(pink)-F-Si-F- chain and organic ligands are shown in purple rods with two blue coordinating points.[140, 163]

The square grid of XFSIX MOFs allows the modification of the framework channel to different pore sizes through the variation of organic linkers. A typical example demonstrated by Chen *et al.* shows that the pore size of UTSA-200a (UTSA = University of Texas at San Antonio) is controlled by changing 4,4'-dipyridylacetylene (dpa) to 4,4'-azopyridine (azpy) (Figure 1.17), resulting in the slightly reduced pore diameter from 4.4 Å to 3.4 Å.[166] Similar examples were also prepared by Xing *et al.*, but with a GeF_6^{2-} or TiF_6^{2-} anion as the bridging ligand instead of SiF_6^{2-} to achieve precise pore size control.[132, 215, 216]

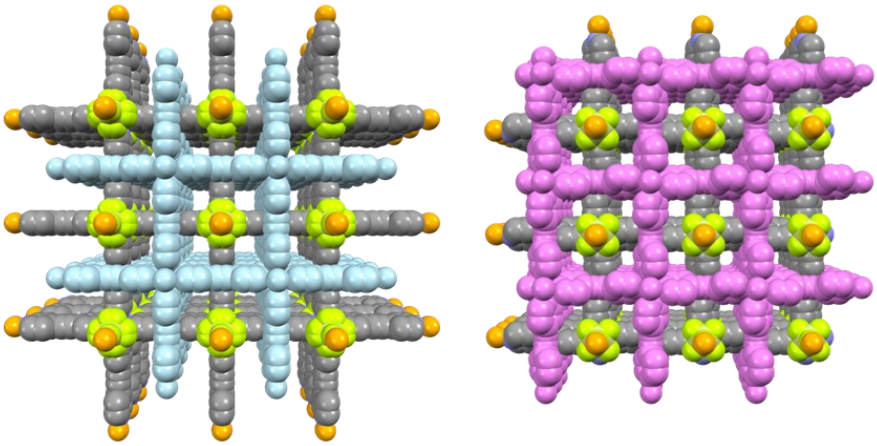

Figure 1.17 Structure comparison of SIFSIX-2-Cu-i (left, i stands for interpretation) and UTSA-200a (right) showing slightly decreased channel size when using azpy as ligands. Interpenetrated frameworks are drawn in light blue and violet colours. C: grey, F: bright green, Cu: orange, Si: pale yellow, N: night blue. H atoms are omitted for clarity. Figure redrawn using published crystal data (CSD refcode: YEMTIV (left), YEPTIZ (right)). [150, 166]

1.2.2 Applications: Gas Sorption/Separation

Gas sorption, separation and purification are basic but crucial issues in industry. Porous materials such as zeolites have long been utilized for these purposes. However, limitations within these materials such as poor tuneability of the pore size have obstructed further development. MOFs constructed from inorganic fluorinated anions (SiF_6^{2-}, GeF_6^{2-} or TiF_6^{2-} etc.) provide a platform to achieve these aims because these MOFs usually possess

permanent porosities with guest accessible spaces, and the fine tuneability of their pore size allows precise control for specific gas separations. The judicious choice of linkers to control pore size and functionality illustrates the power of the isoreticular principle in designing these MOFs.[217]

1.2.3.1 CO_2 Sorption/Separation

CO_2 capture from flue gas by porous materials is of great interest due to global climate change. Traditional amine-based absorbents which allow the direct reaction of flue gas with the absorbents to form chemical compounds suffer from several drawbacks, such as high energy costs for separation and purification, and oxidative degradation of the absorbents.[218] Research on MOFs has demonstrated their potential as promising materials for solving these problems. Several MOFs with XF_6^{2-} anions have been reported to exhibit excellent CO_2 adsorption performance.[131, 136, 145, 219, 220] For example, Zaworotko and co-workers reported the synthesis of [Cu(bpy-1)$_2$(SiF$_6$)] and its expanded analogue [Cu(bpy-2)$_2$(SiF$_6$)] [bpy-1 = 4,4'-bipyridine, entry **1**, bpy-2 = 1,2-bis(4-pyridyl)-ethene, entry **28**].[136] These two PCPs provide ideal platforms to evaluate the gas adsorption performance from the perspective of pore size. [Cu(bpy-1)$_2$(SiF$_6$)] exhibited a CO_2 uptake capacity of 23.1 wt% at 298 K and 1 atm, which exceeds most MOFs containing OMS and is comparable with Mg/DOBDC at 296 K (24.4 wt%).[221] [Cu(bpy-2)$_2$(SiF$_6$)] exhibited a CO_2 uptake capacity of 12.1 wt%. Although this value is lower than that of [Cu(bpy-1)$_2$(SiF$_6$)], the CH_4 uptake is only 0.71 wt%, and this led to a relatively high CO_2 uptake (selectivity) of 8:1 to CH_4.

Apart from physisorption, the presence of OMS, fluorine atoms or functional groups in the frameworks may also favour interactions with CO_2 molecules, therefore further enhancing the CO_2 capacity in these MOF materials. Considering the fact that N_2 makes up the majority of many emitted gas streams, and the concentration of emitted CO_2 is low in comparison, it is important to investigate the adsorption performance in low CO_2 pressure regions, as well as the selectivity for CO_2 over N_2.

In 2019, Zaworotko *et al.* reported the synthesis of SIFSIX-18-Ni [Ni(L)$_2$SiF$_6$, L =

3,3',5,5'-tetramethyl-1H,1'H-4,4'-bipyrazole, entry **37**/**38**] exhibiting high selectivity for CO_2 from wet CO_2/N_2.[219] This MOF not only shows almost full loading of CO_2 (2.2 mmol g^{-1}) at 0.01 bar and 298K but also exhibits extremely low water and N_2 uptake. Further investigations revealed that unlike other MOFs with OMS or amine groups which provide binding sites or reaction points for CO_2, the high CO_2 affinity and uptake in SIFSIX-18-Ni can be attributed to both C···F interactions between CO_2 and the SiF_6^{2-} anion and C-H···O interactions between the organic linker's methyl group and CO_2. Moreover, the methyl group decorated frameworks provide hydrophobicity at the same time, which excludes absorption of water molecules. The strong binding affinity towards CO_2 molecules makes the SIFSIX-18-Ni a partial sieve for CO_2 over N_2.

A similar adsorption mechanism was also demonstrated by Chen and co-workers using UTSA-120 [$Cu(dpt)_2SiF_6$], dpt = 3,6-di(4-pyridyl)-1,2,4,5-tetrazine, entry **11**).[145] The presence of functional tetrazine groups in the ligand in UTSA-120 greatly enhanced the CO_2 adsorption capacity in the low-pressure region (<0.5 bar) compared to SIFSIX-2-Cu-i [$Cu(dpac)_2SiF_6$, i = interpenetrated frameworks] in which bipyridine acetylene is used as ligand. At 0.15 bar, UTSA-120 exhibits a CO_2 uptake capacity of 3.56 mmol/g, which is comparable to other top-performing MOFs. Neutron powder diffraction was conducted to investigate the origins of enhancement in CO_2 capacity. As anticipated, the interactions between CO_2 molecules and SiF_6^{2-} anions are observed with a C···F distance of 2.741 Å. In addition, weak C···N interactions between CO_2 molecules and the tetrazine rings are also observed, with a longer distance of 3.701 Å than the C···F distance. It is also worth mentioning that the interpenetration of this framework leads to dense packing and hence, more pore channels are created due to the splitting of a single channel into four by the interpenetrated framework, which promotes the interaction between CO_2 molecules and the framework. Thus, the enhanced CO_2 uptake capacity can be attributed to the synergistic effects of the dual functionalities and the size sieve effect. Furthermore, based on ideal adsorbed solution theory (IAST), the calculated selectivity of CO_2/N_2 mixtures (15:85, v/v) is around 600 at 296 K, and the gas separation performance of UTSA-120 was verified by

column breakthrough experiments, which proves its outstanding CO_2 uptake capacity and selectivity.

Pore size control is considered a powerful approach to give high selectivity for CO_2 in gas separations and is not only applicable to CO_2/N_2 mixtures but also to other gas mixtures. An example of this is CO_2/CH_4 using ZU-36-Ni [GeFSIX-3-Ni, $Ni(pyaz)_2GeF_6$, pyaz = pyrazine, ZU = Zhejiang University, entry **86**] which was reported by Xing and co-workers in 2020.[211] The precise control of pore size through judicious choice of both metal cation and N-type ligand gives ZU-36-Ni a pore size of 3.35 Å, which is slightly larger than the kinetic diameter of CO_2 molecule (3.3 Å) but smaller than that of N_2 (3.6 Å) and CH_4 (3.8 Å). The selectivity of CO_2/N_2 (15/85) and CO_2/CH_4 (50/50) was calculated to be 4200 and 930 respectively, based on IAST, and the selectivity was verified by column breakthrough experiments. ZU-36-Ni also exhibited high CO_2 uptake capacity (1.07 mmol/g at 298 K and 400 ppm) which can be attributed to the strong interactions between the F atoms in the framework and the C atoms in CO_2.

1.2.3.2 Light Hydrocarbon Separation

Light hydrocarbons such as ethene (C_2H_4), acetylene (C_2H_2) or propene (C_3H_6), are important industry materials to produce polymer-based products.[137] Traditional separation methods such as cryogenic distillation are energy-consuming and inefficient because of the similarities in molecular sizes, shapes and physical properties of these hydrocarbons.[166, 194] MOFs may provide adsorption-based separation solutions due to their highly porous nature, especially when the pore size is precisely tuned to achieve the maximum sieve effect.

In this regard, Chen and co-workers reported a series of SIFSIX-MOFs that have excellent separation performances to these light hydrocarbon gases as well as obtaining single components with high purity.[144, 194, 222] A typical example of separating C_2H_2 from C_2H_4 is illustrated by UTSA-200a.[166] By judiciously choosing a shorter linker of 4,4'-azopyridine instead of 4,4'-dipyridylacetylene, the interpenetrated frameworks exhibited a pore size of 3.4 Å which is slightly larger than the kinetic diameter of C_2H_2 (3.3 Å) but smaller than

that of C_2H_4 (4.2 Å). Hence, this MOF exhibits high C_2H_2 uptake capacity and excellent separation ability. This was confirmed by column breakthrough experiments: A mixture of C_2H_2/C_2H_4 (1/99) was allowed to pass the column and the outlet gas was analysed by gas chromatography, with a high C_2H_4 purity of >99.9999%. It is also worth mentioning that the adsorbed C_2H_2 could be easily recovered with a 97% purity.

Another example (UTSA-300a) with a similar separation mechanism has also been reported by the same group.[194] In this UTSA-300a, the pore size shrank after activation, and crystallographic analysis reveals that the shrank pore only allows C_2H_2 molecules to enter and interact with binding sites while completely blocking CO_2 and C_2H_4 molecules. Thus, this MOF exhibits high C_2H_2/CO_2 and C_2H_2/C_2H_4 selectivity of up to 19 and 83 respectively at 1 bar, which can be potentially applied to gas separation applications.

In addition to utilising pore size to achieve high gas selectivity, the addition of functional groups to the linker is also an effective approach to enhance selectivity. In this regard, Wang *et al.* reported a MOF (UTSA-48) [$Cu(pyina)_2SiF_6$], pyina = N-(pyridine-4-yl)isonicotinamide, entry **26**, with high selectivity for C_2H_2 and CO_2 over CH_4 through decorating the pore surface with -CONH- groups.[160] An enhanced Henry's law selectivity of this MOF for C_2H_2/CH_4 (53.4) and CO_2/CH_4 (13.2) at 296 K, was obtained due to the presence of the amide groups which facilitated the dipole-quadrupole interactions between the amide group and CO_2, as well as H-bonds interactions between N(H) and CO_2.

A combination of sieve effects and host-guest interactions may further improve the separation performance. In this regard, Qian and colleagues reported ZJU-300a, (ZJU = Zhejiang University) from the combination of TPE ligand (1,1,2,2-tetra(pyridin-4-yl)ethene, entry **62**) and $ZnSiF_6$ (Figure 1.18).[192] There are three types of cavities present in the framework, with different pore sizes ranging from 3.2 to 4.0 Å. The size sieve effect contributes to a high selectivity towards C_2H_2 while excluding C_2H_4, with an IAST selectivity of 1672 at 296 K and 1 bar (C_2H_2/C_2H_4 = 1/99, v/v). In addition, the presence of multiple F atoms in the pore as well as the dense pore cavities provide ultra-strong binding affinity and allow dense packing of C_2H_2 molecules, with an improved C_2H_2 uptake

capacity of 3.23 mmol/g at 296K and 0.01 bar, comparing to SIFSIX-14-Cu-i.

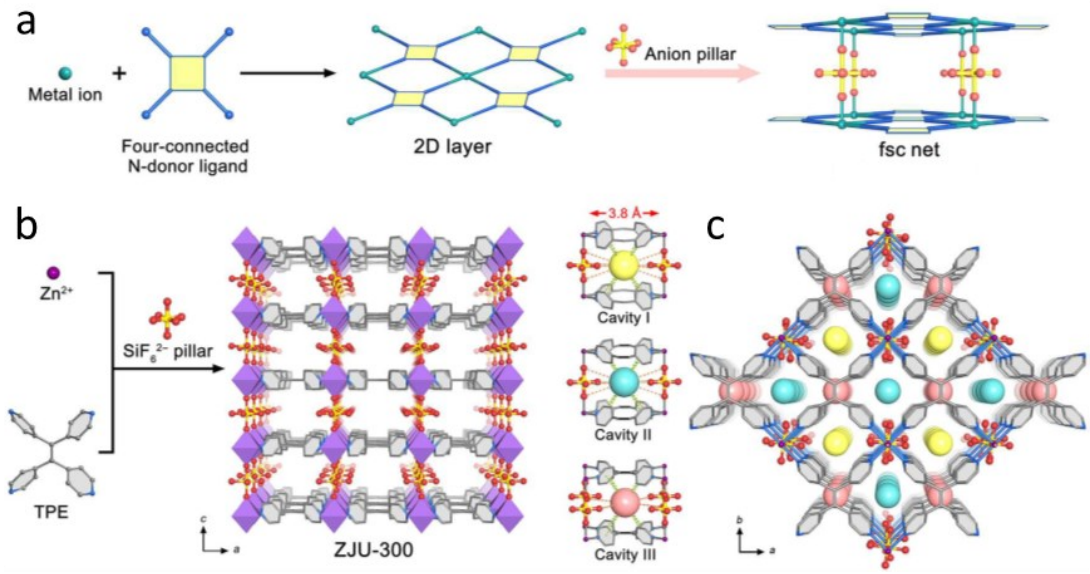

Figure 1.18 a) Demonstration of *fsc* net built from four-connected nodes and rhombic pores containing parallelly adjacent SiF_6^{2-} nodes; b) Crystal structure of ZJU-300 along *b* axis with three types of cavities; c) Packing diagram showing different cavities.[192]

1.2.3.3 Other Gas Capture/Separations

High-purity xenon and krypton gases are widely used in lasers, electric light sources, semiconductors etc. These gases are mainly obtained as by-products from air separations or from used nuclear fuel.[135] Conventional methods for the separation of these two gases mainly involve cryogenic distillation or fluorocarbon-based absorption. However, these processes are expensive and require high-energy input and complex engineering control.[223] Porous materials may provide an alternative approach to achieve the separation of Xe and Kr. For example, Li and co-workers reported a series of SIFSIX-type MOFs (SIFSIX-3-M, M = Zn, Cu, Ni, Co or Fe, pyrazine as the ligand) for applications in this area.[224] The Cu-MOF in particular exhibited good stability towards β and γ radiation, hence it was selected for breakthrough adsorption studies. The separation of Xe and ^{85}Kr from their mixtures in dry air (400 ppm Xe and 40 ppm Kr) was achieved through two beds: in the first bed Xe and CO_2 were absorbed by the MOF due to their strong affinity with the frameworks, and

Kr, N_2 and O_2 were passed into the second bed where Kr was absorbed by the MOF to achieve the separation (Figure 1.19).

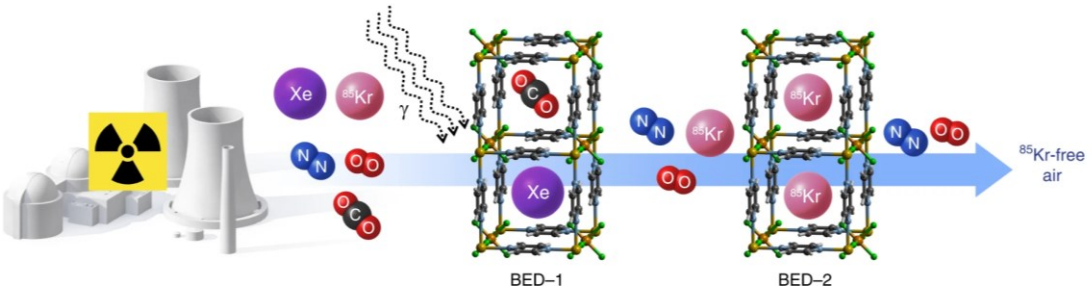

Figure 1.19 Schematic demonstration of the two-bed technique for ^{85}Kr separation from used nuclear fuel.[224]

Separation of hydrogen isotopes (D and T) are of great importance as they play a pivotal role in many scenarios such as nuclear fusion reactors, lighting, isotopic tracing etc. SIFSIX-type MOF can also offer a platform for the separation of these gases. For example, Zhong and colleagues reported the utilization of SIFSIX-3-Zn [Cu(pyrazine)$_2$SiF$_6$] as a molecular sieve to achieve the separation of hydrogen and deuterium.[225] This MOF exhibited a high selectivity for D_2/H_2 mixtures through a quantum sieving effect, with a record value of 53.8 at 25 kPa and 20 K. This performance can be attributed to the differences in the zero-point-energy (ZPE) between H_2 and D_2, where D_2 has a lower ZPE thus promoting its absorption in the framework over H_2.

Mixed-matrix membrane-based gas separations have attracted research interest due to the easier fabrication of membranes and low energy consumption.[226] Incorporating MOF materials may bring novel properties to the membrane. In this regard, Eddaoudi and colleagues have reported a SIFSIX-3-Cu based membrane for CO_2 capture.[227] A liquid-phase epitaxy (LPE) method was used to prepare continuous, homogeneous and defect-free MOF membranes based on a porous alumina substrate. The obtained mixed-matrix membrane containing SIFSIX-3-Cu exhibited good CO_2 selectivity over H_2 (CO_2/H_2: 30/70) and CH_4 (CO_2/CH_2: 50/50), with a favourable CO_2 selectivity of 27 and 14.6 at 308 K and 2 bar.

1.2.3 Applications: Catalyst, Chemical Sensing etc.

Although SIFSIX-type MOFs have been commonly reported for gas separations, these MOFs can also be applied to other fields such as catalysis and chemical sensing. For example, Kitagawa and colleagues reported the synthesis of $[Cu(DPIO)_2SiF_6]$ [DPIO = 4,7-bis(4-pyridyl)-1,1,3,3-tetramethylisoindolin-2-yloxyl, entry **70**] and its catalytic performance in oxidation reactions.[199] The framework has an identical arrangement to SIFSIX-1-Cu with a narrowest pore cross-section size of 7.6 Å, and the pore spaces are decorated with the isoindoline moieties which allows direct exposure of nitroxyl radicals. This MOF was then applied in alcohol oxidation reactions, with results showing that substituted benzyl alcohols were oxidized to the corresponding aldehydes in almost quantitative yields. In addition, the catalyst can be easily separated from the reaction mixture by filtration, and the by-products can be removed by evaporation under reduced pressure to obtain the pure product.

In addition, Zhao *et al*. have reported the synthesis of two Cd-based MOFs; $[Cd(bib)_2SiF_6]$ (Cd-MOF **1**) [bib = 1-(4-imidazol-1-ylphenyl)imidazole, entry **78**] and its interpenetrated analogue $[Cd(bib)_2SiF_6]\cdot DMF\cdot 3H_2O$ (Cd-MOF **2**).[205] Both MOFs were suspended in aqueous solutions (1.0 mg/mL) and exhibited fluorescence properties with emission wavelengths at 309 and 310 nm (excitation at 260 and 265 nm for Cd-MOF **1** and **2** respectively). The luminescence behaviour of both MOFs was studied on exposure to different amino acids. There was a significant enhancement in the emission intensity when arginine was added to the MOF suspension, while other amino acids had negligible effects on the fluorescence behaviour. The enhanced efficiency was then calculated, with values of 1.39×10^4 and 1.50×10^4 /M for **1** and **2** respectively, with both R^2 higher than 0.99. The possible mechanism for the enhancement was attributed to the interactions between the guanidine group in arginine and the frameworks, such as F···(H)N, C=N···H or C-H···N/O, as confirmed by FT-IR, UV-vis spectroscopic and PXRD studies. These MOFs also exhibited good anti-interference performance, suggesting potential applications as arginine sensors.

1.3 Frameworks with XO_6 Type Linkers

Although a large number of SIFSIX-type MOFs have been successfully prepared and characterized, research on building porous organic frameworks (MOFs or COFs) with SiO_6 or GeO_6-containing linkers has been less studied, with only a few examples reported.

In 2017, Thomas and colleagues reported the synthesis of anionic silicate COFs built from SiO_6 centres.[228] The reaction of tetramethyl orthosilicate (TMOS) with 9,10-dimethyl-2,3,6,7-tetrahydroxyanthracene (DMTHA) and alkali-metal methoxide (Li, Na or K) in a Teflon-lined steel autoclave at 180°C for four days afforded the pale-brown precipitates (SiCOF, Figure 1.20). The product was analysed by FT-IR and NMR spectroscopies with a Si-O stretching band observed at 665 cm^{-1} and a ^{29}Si NMR signal at -143 ppm. These results suggested that a single component Si-COF had been successfully prepared with no sign of defects or incomplete coordination. The presence of counterions was confirmed by NMR

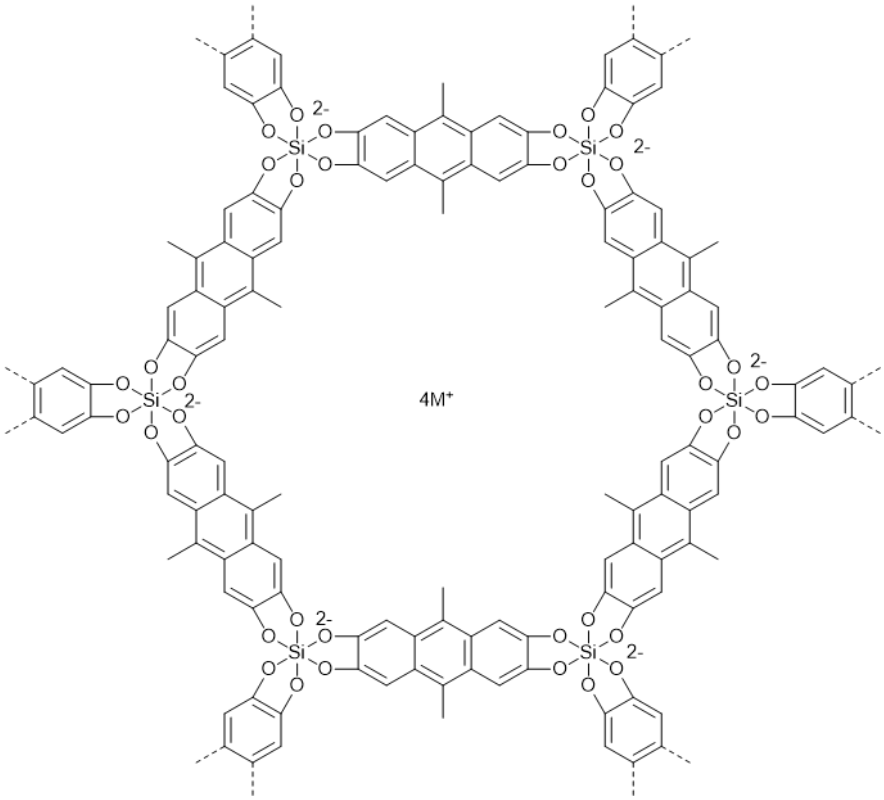

Figure 1.20 Structure of SiCOF. M = Li, Na or K.

spectroscopy (Li^+ and Na^+) and EDX (Na^+ and K^+) analysis and their ratio to the anionic frameworks were studied by ICP-AES. Although single crystals of the SiCOF were not obtained, a calculated PXRD pattern obtained from the simulated structure fitted with the measured pattern, indicating the high phase purity of the product. In addition, the permanent porosity of these frameworks was confirmed through N_2 and Ar sorption studies, with calculated BET surface areas of 1153, 1276 and 1067 m^2/g for SiCOF-Li, Na and K respectively.

This example demonstrated the feasibility of making porous frameworks with a SiO_6 octahedral component. Roeser and colleagues reported the synthesis of SiCOF-5 through the reaction of methyltrimethoxysilane (MTMS) with 2,3,6,7,10,11-hexahydroxy-triphenylene (HHTP) and sodium methoxide.[229] Although single crystals of SiCOF-5 were not obtained, FTIR, NMR, EDX and ICP-AES analysis was consistent with the proposed chemical formulation of the framework [$Na_2(Si(C_{18}H_6O_6))$]. The structure was predicted from the high-resolution PXRD measurement results, suggesting the framework has a *srs-c* topology (Figure 1.20). The BET surface area was calculated to be 370 m^2/g through N_2 sorption isothermals at 77 K, proving the permanent porosity of SiCOF-5.

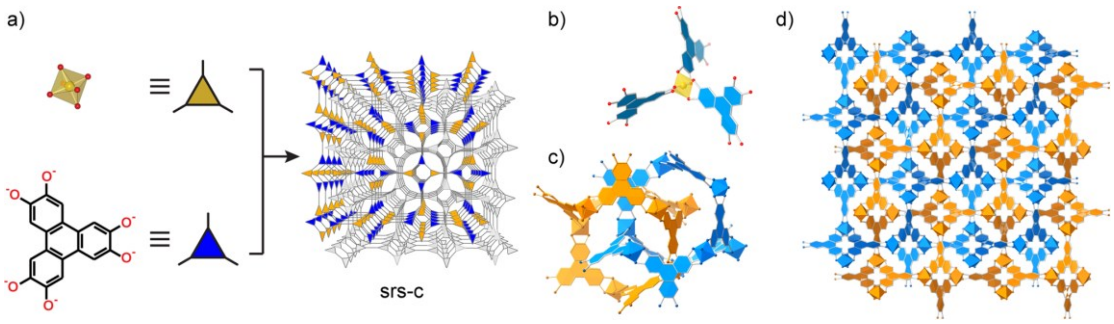

Figure 1.21 a) Structure of the octahedral SiO_6 unit and HHTP ligand and resulting *srs-c* net of the SiCOF-5; b) arrangement of the SiO_6 nodes and ligands; c) interpenetrated structures; d) structure of the SiCOF-5 framework without guest molecules.[229]

Wang and colleagues reported the synthesis of Ge-COF-1 through microwave-assisted heating of DMTHA with lithium methoxide and germanium oxide.[230] The product was characterized by IR and NMR spectroscopies and XPS to confirm its chemical formulation

$[M_2(Ge(C_{16}H_{10}O_4)_{1.5})]$ (M = Li, Na or K). and the measured PXRD pattern fitted well with the calculated pattern from the structural model. The permanent porosity of Ge-COF-1 was tested through N_2 sorption studies at 77 K, with a calculated BET surface area of 808 m^2/g, and the pore size distribution was calculated with a major peak at around 1.5 nm. The Li-ion conductivity was also studied with a value of 1.1×10^{-6} S/cm at 30°C and 1.0×10^{-5} S/cm at 100°C. In a later study, Ge-COF-1 with different counterions (Na^+ and K^+) were synthesized using the same method (Figure 1.22).[231] The Ge-COF-1-K exhibited a BET surface area of 1252 m^2/g, and CO_2 uptake of 247.4 mg/g at 273 K and 1 bar, with CO_2/N_2 IAST selectivity of 140. This K-based COF also exhibited a high SO_2 uptake capacity of 154 mg/g at low SO_2 concentrations and good stability after a few cycles of breakthrough tests.

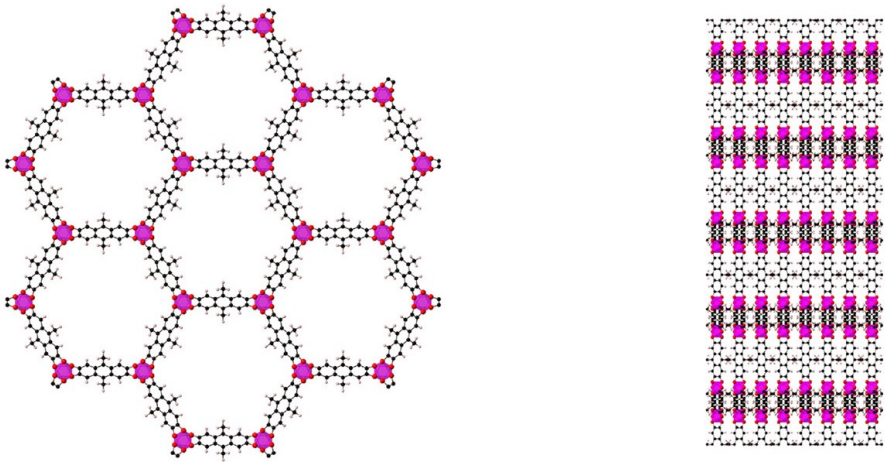

Figure 1.22 Left) The honeycomb structure of the Ge-COF-1 with *hcb* topology from (0 0 1) view; right) packing diagram from (1 0 0) direction.[231]

Triscatechol-type compounds containing hexaoxosilicon centres have also been applied to the synthesis of porous organic polymers, and these polymers have been applied to the adsorption of cationic dyes or used as solid electrolytes for lithium metal batteries.[232-234]

Martsinko, Seifullina and co-workers reported the combination of critic acid (H_4Cit) with GeO_2 to afford the $[Ge(\mu\text{-}HCit)_2]^{2-}$ cluster, and the cluster was then treated with metal (Cu or Ba) salt to generate the extended networks (Figure 1.23).[235, 236] In these two examples,

metal cations are coordinated by carboxylate groups presented in the Ge ligand. In the Cu-CPs, the Ge ligand coordinates with four Cu^{2+} ions, exhibiting a tetradentate coordination mode, whereas the Ge ligand in the Ba-CPs coordinates with two Ba^{2+} ions as a bidentate ligand. The Ba-CPs have a 1D structure owing to the connection mode of the bidentate ligand with bilateral Ba^{2+} cations, while the Cu-CPs form 3D frameworks by incorporating a bridging ligand, iso-nicotinic acid hydrazide, with the Ge ligand, and exhibit cavities volume of 26.7% of the unit cell along (1 0 0) direction.

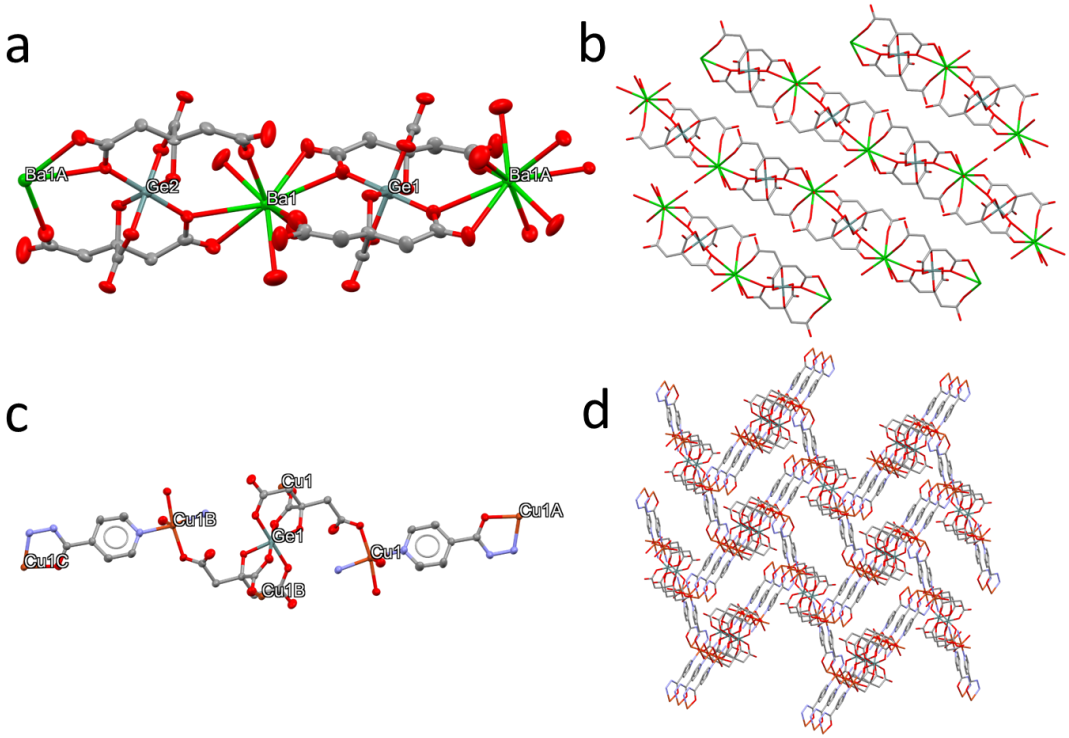

Figure 1.23 a) coordination environment of the Ge ligand in Ba-CPs; b) packing diagram showing 1D linear chain structure; c) coordination environment of the Ge and co-ligand in the Cu-CPs; d) packing diagram showing 3D framework structures of the Cu-CPs. C: grey, O: red, N: light blue. Structures are drawn using published crystal data from E. E. Martsinko and co-workers (CSD refcode: Ba-CP: APIREX, Cu-CP: RIGYOY).[235, 236]

1.4 Aims and Objectives

In the sections above, the historical development of MOFs, as well as their design, synthesis, activation and characterization methods have been illustrated. The use of hexacoordinated Si/Ge in MOF constructions has currently been mainly focused on hexafluoro silicate/ germanate type compounds, while the field of building MOFs using SiO_6/GeO_6 type linkers is still under exploration. Different from carbon-centred tridentate linkers which usually exhibit planar structure, the use of SiO_6/GeO_6 octahedral-containing linker in MOF synthesis may allow the direct formation of 3D frameworks. The negatively charged SiO_6/GeO_6 unit is expected to yield anionic frameworks, which may have interactions with cationic species to afford applications in catalysis, chemical sensing etc. The aim of this current work mainly focuses on the synthesis of tridentate linkers with hexaoxo silicon/germanium centres and the study of the structures and stabilities of these new molecules. In addition, their solid-state packing will be studied using XRD techniques to explore if they can form H-bonded networks or HOFs. Then, these linkers will be applied to MOF synthesis with a range of metal centres for multiple potential applications. The obtained MOFs will be fully characterised to determine any novel structures and properties. The negative charge present at the hexavalent Si or Ge centre makes these ligands particularly amenable to the synthesis of anionic MOFs and any examples of these will be studied for their sensing ability of cationic metal ions.

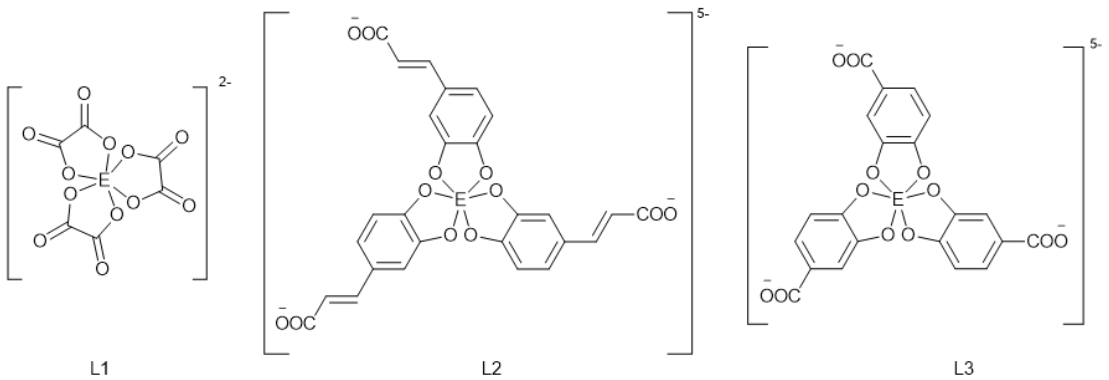

Figure 1.24 Proposed structure of **L1**, **L2**, and **L3** type linkers. (E = Si/Ge)

Chapter 2: Synthesis of Hexacoordinate Linkers

2.1 Introduction to Hydrogen-Bonded Organic Frameworks

Hydrogen-bonded organic frameworks (HOFs) are crystalline porous materials formed through the self-assembly of organic molecules via intermolecular H-bond interactions.[237] These materials exhibit diverse structures, ranging from 1D chains to 2D networks or 3D frameworks, depending on the geometric characteristics and interconnectivity of the organic molecules.[238-240] The use of H-bonds to regulate molecular aggregation for 3D framework growth was first proposed in the 1990s.[241] Subsequently, research interest in these frameworks began to expand, and the establishment of the microporosity of HOFs in 2010 significantly accelerated the research on this type of framework.[242] In the following year, Chen *et al.* demonstrated the permanent porosity of HOF-1 which exhibited high selectivity of C_2H_2 over C_2H_4, whilst highlighting the potential of HOFs as a microporous platform for gas storage and separation applications.[243]

In the following decade, research on HOF synthesis has been extensively studied. Typically, HOFs are synthesized in their crystal form through slow crystallization in a solvent/solvent mixture.[244] Commonly used methods for HOF synthesis include liquid/vapour diffusion of an anti-solvent into the HOF precursor solvent or evaporation/cooling of a hot solution containing organic building blocks. Other methods, such as electrophoretic deposition, can be used for the preparation of HOF thin films.[245] However, challenges arise in terms of the applications of HOFs, because the frameworks often collapse upon the loss of solvent during the activation process.[237, 246] Such instability originates from the weakness of H-bonds: compared to MOFs and COFs, which are constructed through coordination bonds and covalent bonds respectively, H-bond energies are usually low, typically 10-40 kJ/mol (Figure 2.1). Although in some extreme cases, this value can extend to 1-170 kJ/mol, it is still lower than that of the coordination bonds in MOFs (90-350 kJ/mol) and covalent bonds in COFs (300-600 kJ/mol).[247] Strategies to improve the stability and robustness of HOF

frameworks include applying organic molecules with multiple H-bonding sites during synthesis, introducing π-π interactions and van der Waal's forces in HOF design.[248, 249] In addition, the implementation of longer molecules in the HOF assembly process may promote the formation of interpenetrated structures which will also increase the overall stability of the framework.[248]

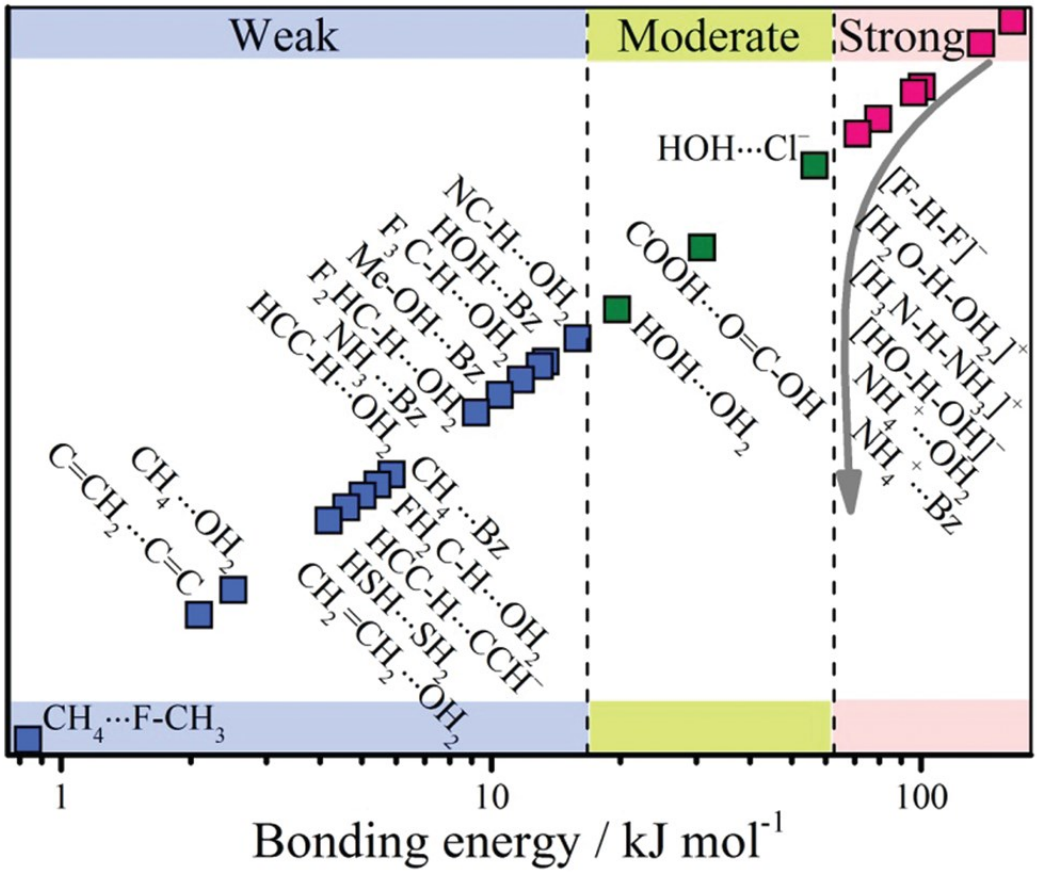

Figure 2.1 Hydrogen bond energy in different types of compounds.[237]

The inherent weakness of H-bonds, in turn, endows HOFs with novel features. Their synthesis can be achieved under mild conditions due to the weak H-bond energies. The good solution processability of the organic molecules, and the flexible and reversible nature of H-bond interactions allow easy regeneration and recycling of HOFs. Additionally, the absence of the metal element promotes HOFs' suitability as biocompatible materials. The presence of a π-π conjugated system in some HOFs also facilitates their utilization in ion conduction applications. Moreover, the presence of accessible void space allows guest molecules to enter and interact with the framework. Benefiting from these features, HOFs

have been applied in different scenarios such as gas storage and separation, chiral molecule separation, catalysis, sensing, membrane-based applications etc.[250-255]

To date, several types of H-bonding motifs have been explored, including those based on carboxylic acid, pyrazole, boronic acid, amide, diaminotriazine, diaminopurine and so on.[256-261] This chapter centres on the exploration of HOFs based upon carboxylic acids and selected charge-assisted H-bonds, such as ammonium-carboxylate and pyridinium-carboxylate.

2.1.1 Carboxylic Acid-Based HOF Systems

HOFs constructed from carboxylic acid compounds are well known for forming dimers through H-bonding between pairs of carboxylic acid groups.[244, 262] The self-assembly of carboxylic acid groups in solutions usually forms H-bonds with the structure illustrated in Figure 2.2. The O-H···O angle typically ranges between 170-180°, creating a linear linkage between the molecules.[263]

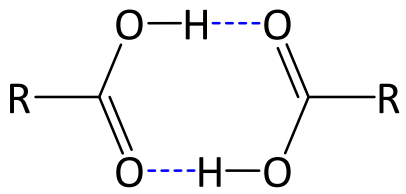

Figure 2.2 Dimeric hydrogen bonding between two carboxylic acids. H-bonds are shown in blue dashed lines.

Many HOFs constructed from poly-carboxylic acids which exhibit sheet structures have been reported over the past decades. For example, Miyata and colleagues synthesized a hexagonal network using dodecadehydrotribenzo[18]annulene (DBA, Figure 2.3).[264] The structure of the Phenylene Triangle (PhT) was confirmed through SCXRD studies. Upon crystallisation in DMF and methyl benzoate, carboxylic acid groups in the neighbouring molecules formed dimers, generating a 2D-sheet structure with three types of triangular voids. The staggered packing of the 2D sheets led to a solid with a calculated void space of 58% by *PLATON*.[265]

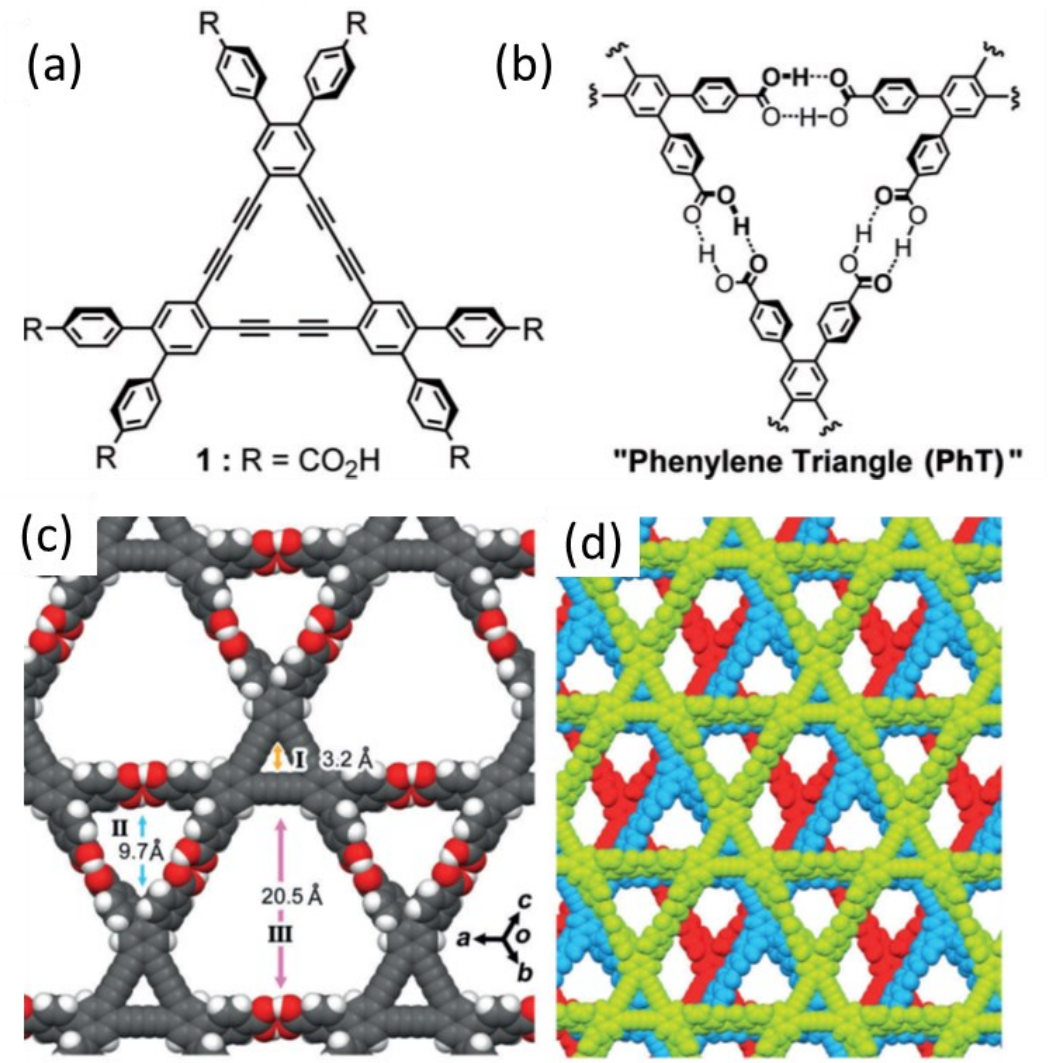

Figure 2.3 a) Structure of DBA; b) COOH dimer between molecules; c) single layer of the DBA HOFs showing three different void sizes; d) packing diagram of the staggered layer structure, three different layers shown in red, blue and green.[264]

The direct construction of 3D HOFs with highly branched carboxylic acid compounds can be achieved through conformation control of the organic molecules. For example, Douhal and co-workers designed a hexaazatriphenylene-based molecule with six terminal COOH groups (CPHAT).[266] The six COOH groups in CPHAT (Figure 2.4) are not in the same plane as the central ring. Instead, the dihedral angle between the peripheral phenylene groups and the centre HAT ring is about 30°, distinguishing this molecule from the planar structure of the triphenylene centre. The 3D extended HOF (CPHAT-1) was obtained through the slow evaporation of a DMF/1,2,4-trichlorobenzene solution and exhibited an

infinite three-fold helical structure with a pitch of 14.4 Å. Moreover, SCXRD studies on the HOF crystal revealed that the framework remained intact on activation and that the exposure of empty channels allowed gas sorption studies to be carried out. Gas uptake studies showed that this HOF had a CO_2 uptake value of 137 cm^3/g at 0.99 bar, and a calculated BET surface area of 649 m^2/g.

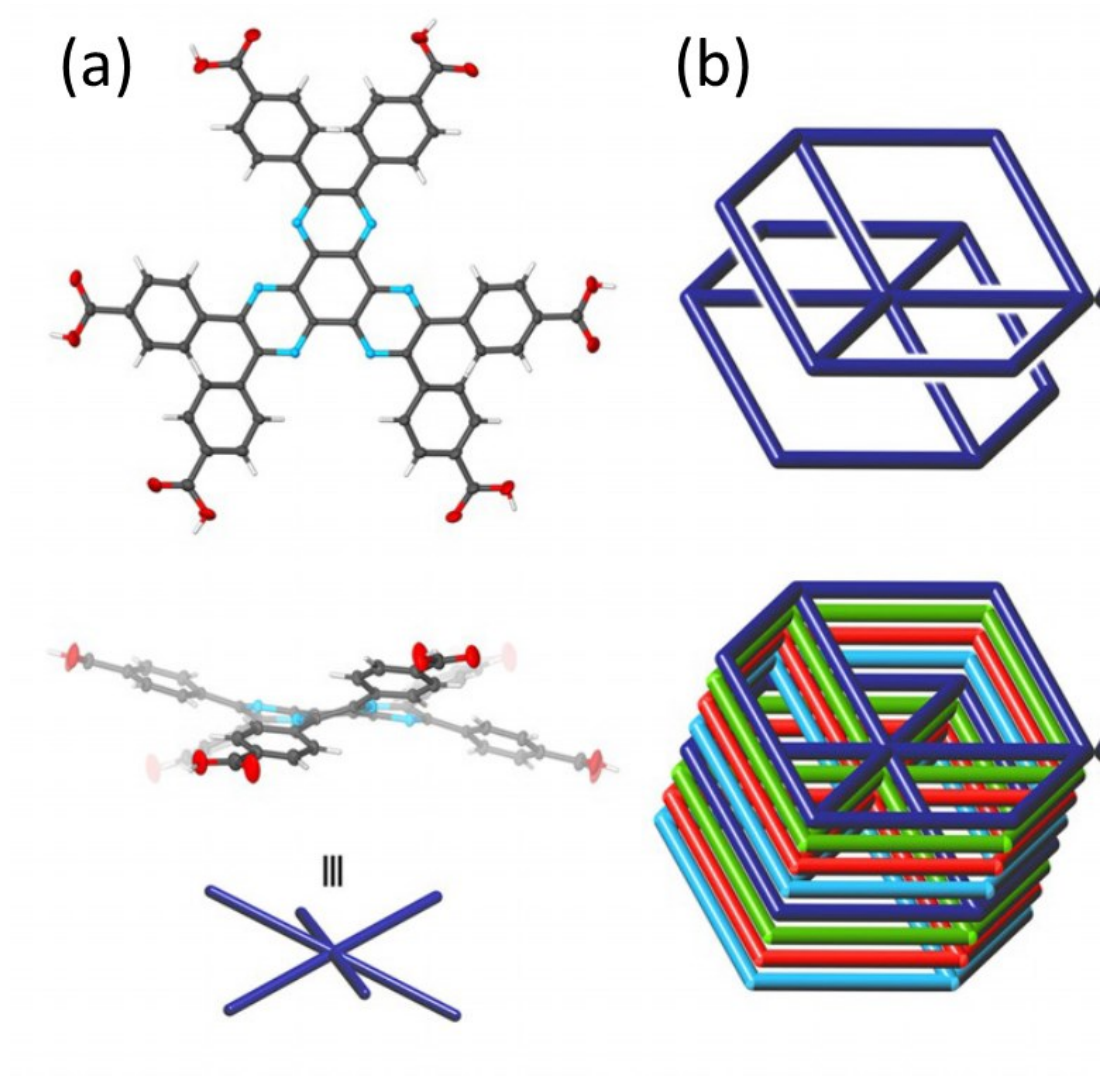

Figure 2.4 a) non-planar structure of the CPHAT molecule, top view and side view; b) single (top) and 4-fold interpenetrated HOFs structure (bottom) with ***pcu*** topology. C: grey, O: red, N: sky blue, H: white.[266]

2.1.2 Charge-Assisted H-Bonds in HOF Systems

The limited strength of H-bonds has restricted the utility of HOF materials. One strategy to

enhance the robustness of the framework is to adopt charged components which provide additional electrostatic attractions between the components.[267] Charged components, such as guanidinium-sulfonate, ammonium-sulfonate, and amidinium-carboxylate (Figure 2.5), have been employed in HOF construction. These ionic HOFs usually exhibit enhanced thermal and chemical stability compared to HOFs constructed from neutral motifs.[268]

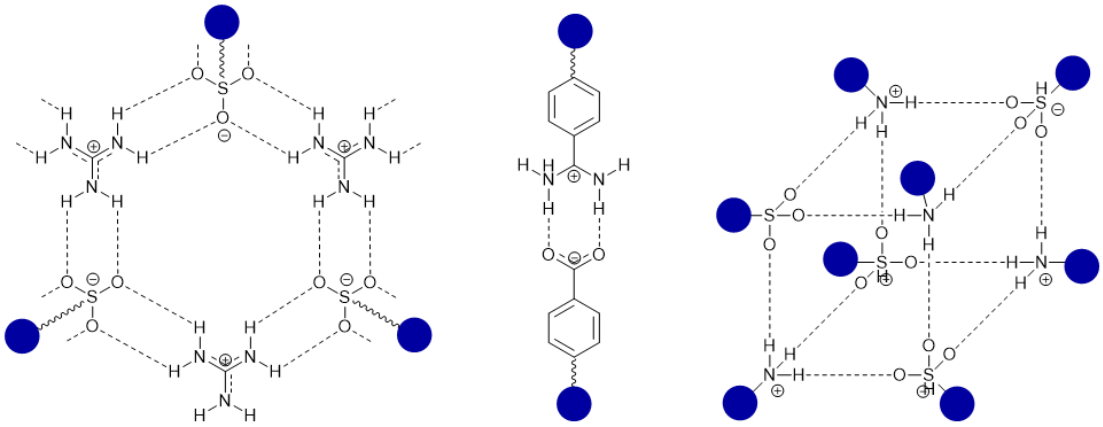

Figure 2.5 Examples of H-bonding motifs with charge-assisted H-bonds.

For example, Hong *et al.* synthesized a HOF with the combination of guanidinium chloride (Gua-HCl) and tetrakis(4-sulfophenyl)methane (H_4SPM).[269] The slow diffusion of CH_2Cl_2 into the above mixture in a solvent blend of MeOH and acetone led to the formation of single crystals of **KUF-1** (KUF = Korea University Framework). The activated HOF (**KUF-1a**, Figure 2.6) exhibit an NH_3 absorption value of 6.67 mmol/g at 298 K and 1 bar. After the gas adsorption process, PXRD results revealed that the unit cell volume reduced from 2005.7 $Å^3$ to 1898.1 $Å^3$, while after degassing the cell volume returned to 2002.1 $Å^3$. These processes demonstrated that the framework changes during the NH_3 sorption/desorption process were reversible. It was speculated that the H-bonds between the guanidinium cations and SPM^{4-} anions can maintain the framework during the gas sorption process. After NH_3 molecules enter the framework, the formation of additional H-bonds between NH_3 molecules and frameworks leads to the structure change, resulting in a reduction in cell volume. The easy degassing process under mild conditions endows this HOF with potential applicability in NH_3 adsorption.

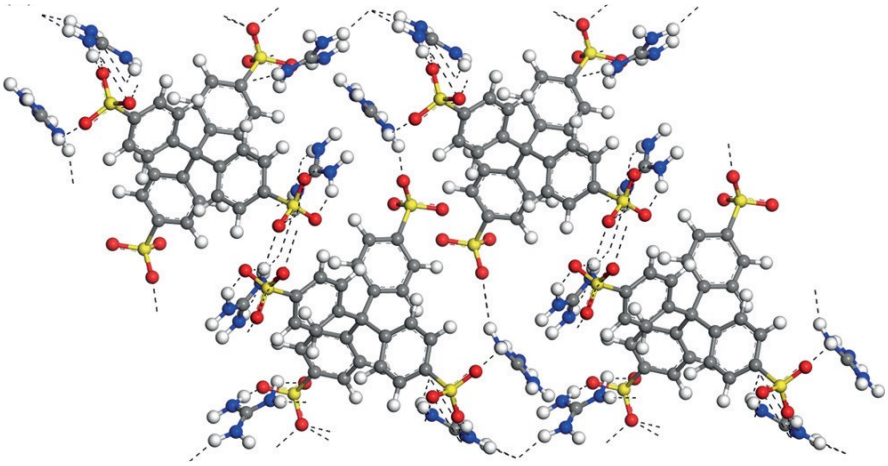

Figure 2.6 Structure of KUF-1a showing H-bonds (dotted lines) among $GuaH^+$ cations and SPM^{4-} anions. N: blue, S: yellow, O: red, C: grey, H: white.[269]

Xiao and co-workers synthesized two HOFs (**E1** and **E2**) based on TTF-benzoate (H_4L, TTF = tetrathiafulvalene) and bipyridine type compounds.[270] The crystals of HOF **E1** (H_4L with 4,4'-bipyridine, bipy, Figure 2.7) and **E2** (H_4L with trans-1,2-bis(4-pyridyl)ethane, bipy-ete) were obtained through a similar procedure from the slow evaporation of a THF solution containing H_4L and bipy or bipy-ete respectively. Both frameworks exhibited a 2D layer structure: HOF **E1** was constructed through the connection of N-H···O and O-H···O type H-bonds, whereas the pyridine is not protonated in HOF **E2**, resulting in N···H-O and O-H···O type H-bonds. Additionally, both **E1** and **E2** exhibited photoelectric response properties upon irradiation with Xe light, suggesting their potential application in photocurrent materials.

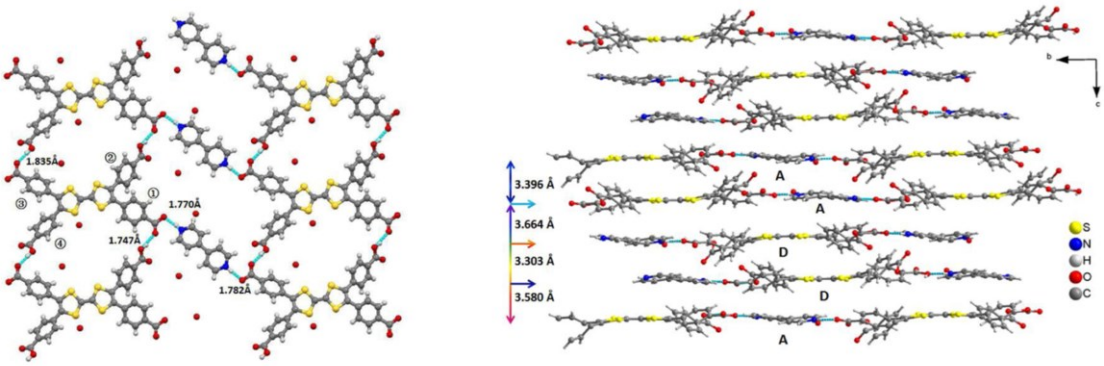

(a) (b)

Figure 2.7 a) Crystal structure of **E1**; b) 2D layer structure of **E1**.[270]

An overview of HOFs, including their synthesis, diverse structure, properties, and potential applications has been outlined in the preceding text. In this chapter, various anionic linkers paired with different ammonium cations have been synthesized, with the anticipation that negatively charged Si/Ge oxalate compounds with ammonium counterions (L1-type linker), and linkers with carboxyl groups (L3-type linker) may self-assemble into novel strongly-bound HOF materials (Figure 2.8). To explore the potential of such networks as HOFs, efforts have been made to grow single crystals of these salts for full structural analysis using XRD methods.

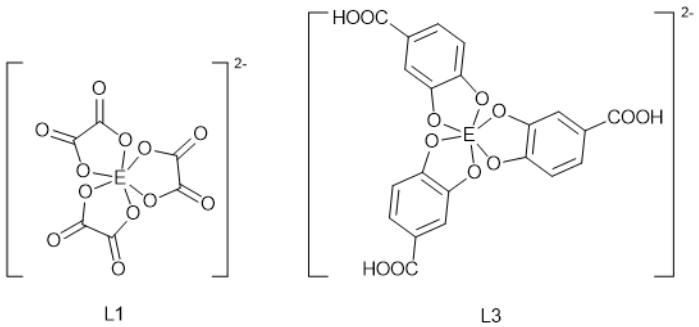

Figure 2.8 Structure of L1 and L3 type linkers.

2.2 Synthesis of Si/Ge(ox)$_3$ Type Linkers

2.2.1 Synthesis Methods

Two different methodologies have been applied in this work for the synthesis of tris-oxalate silicate. In the first approach, $SiCl_4$ was treated with silver oxalate. The negative charge of the Si linker anion was balanced by adding a quaternary ammonium salt. This method was used to synthesize $[Et_4N]_2$[**L1-Si**] (**1**) and $[n\text{-}Bu_4N]_2$[**L1-Si**] (**2**). An excess of silver oxalate (3.1 equiv.) was added, to sufficiently provide 3 equivalents of oxalate anion due to the photosensitivity of silver oxalate.[271] Ammonium bromide and $SiCl_4$ were added to the mixture, hence it was possible to readily separate the silver halide by-product as a precipitate, and the remaining ammonium cation acts to balance the charge of the **L1-Si**.[272] After the removal of the precipitate, the isolation of the product from the solvent mixture was achieved by adding an anti-solvent in which the product is less soluble, in this case Et_2O, thus leading to precipitation of the product.

In the second method, $Si(OMe)_4$ was used as the Si source and treated with oxalic acid and an amine. This method was conducted to synthesize $[Et_2NH_2]_2$[**L1-Si**] (**3**), $[Et_3NH]_2$[**L1-Si**] (**4**), and a diamine was used in the syntheses of $[H_2TMEDA]$[**L1-Si**] (**5**), $[H_2TMPDA]$[**L1-Si**] (**6**) and $[H_2TMBDA]$[**L1-Si**] (**7**). Products **3** and **4** can be purified by recrystallization in EtOH, while diammonium products **5-7** were insoluble in the reaction solvent (MeOH) and came out from the reaction mixture as precipitates.

The synthesis of tris-oxalate germanate was similar to the second method for the silicate linker, but $Ge(OMe)_4$ was used in place of $Si(OMe)_4$. Products containing the Ge linker, $[Et_3NH]_2$[**L1-Ge**] (**8**), $[H_2TMEDA]$[**L1-Ge**] (**9**) and $[H_2TMPDA]$[**L1-Ge**] (**10**), can be obtained using a simple workup procedure by either recrystallization in EtOH (compound **8**) or gravity filtration (**9** and **10**). The synthesis methods with the methoxide reagents are shown below in scheme 2.1.

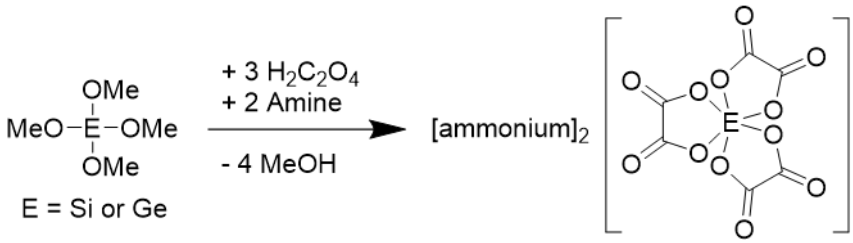

Scheme 2.1 The second synthesis method of L1-type linker, amine = Et_2NH, Et_3N, TMEDA, TMPDA or TMBDA. 1 equiv. with diamine (TMEDA, TMPDA or TMBDA).

Alternatively, GeO_2 was used as the precursor in the second method to synthesize [H_2Bipy][**L1-Ge**] (**11**) and [Gu]$_2$[**L1-Ge**] (**12**). In this method, water was used as the solvent due to the low solubility of GeO_2 in common organic solvents. The increased solubility of GeO_2 at higher temperatures allowed the formation of $[Ge(ox)_3]^{2-}$. After thermal annealing (see 6.2 experimental section), the mother liquid was transferred to a glass vial and the product was obtained after removal of the water in vacuo.

2.2.2 Characterization and Structure Description

The defining characteristic of the L1-type linker is the hexacoordinate chemical environment of the central Si/Ge atom. The coordination mode of the Si linker was confirmed using ^{29}Si NMR, with all these **L1-Si** linkers (compounds **1**-**7**) displaying a single peak at around -174 ppm which is consistent with the literature-reported value for similar compounds.[273] The presence of ammonium cations and their ratio to the anions in the linkers was confirmed by ^{1}H and ^{13}C NMR. MS-ESI studies for compounds **4**, **5**, **8** and **9** confirmed the presence of the expected [**L1-Si**+H]$^-$ (**4**, **5**) and [**L1-Ge**+H]$^-$ (**8**, **9**) ions. (Table 2.1)

parameters	**4**	**5**	**8**	**9**
^{29}Si NMR (ppm)	-174.04	-173.99	-	-
MS (found)	292.9250	292.9240	338.8694	338.8697
MS (calcd.)	292.9237	292.9237	388.8680	388.8680

Table 2.1 Comparison of L1-type linker (^{73}Ge NMR was not available).

PXRD result indicates that **1** is crystalline (see Supplementary Information, SI), hence attempts to grow single crystals of **1** were conducted. Unfortunately, although it was possible to obtain some needle crystals the scattering was too weak during SCXRD analysis, and a full structure solution for **1** could not be obtained. Although compound **2** was obtained as a solid, its hygroscopic nature makes it unsuitable for PXRD measurement.

The PXRD patterns of compounds **3-10** were recorded. It is expected that compounds that possess different centre atoms (Si/Ge) in the anions but have the same ammonium cations (such as triethylammonium cations in compounds **4** and **8**) might exhibit similar diffraction data (Figure 2.9). Compound **8** has been reported in the literature,[274] hence the simulated PXRD pattern was generated using Mercury[275] software from the published data to make comparisons. Such peak overlay reveals that compounds **4** and **8** have high levels of crystallinity and form the same structure as in the literature.

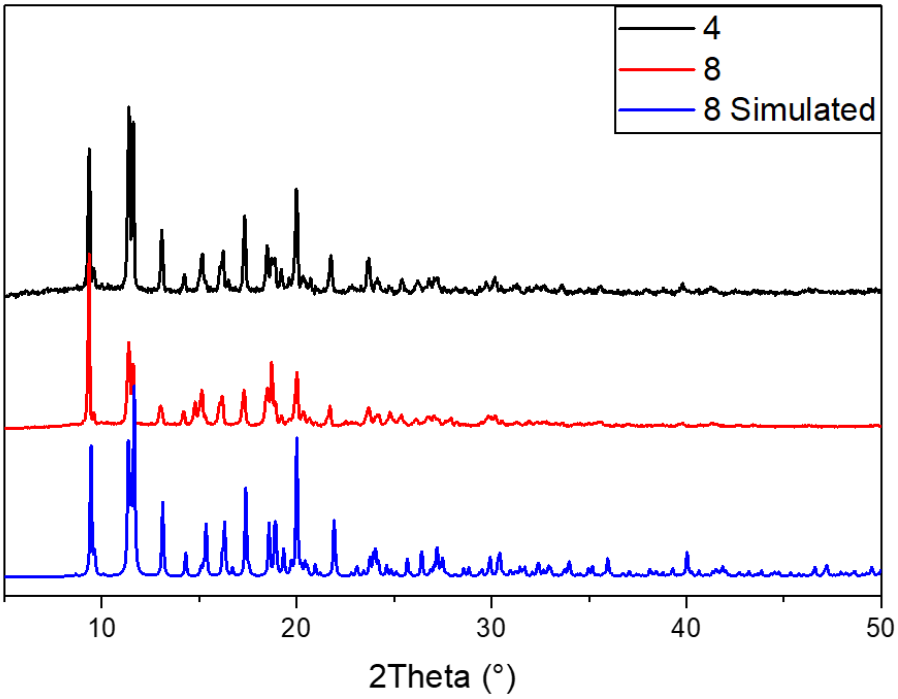

Figure 2.9 PXRD pattern of compounds **4**, **8** and simulated **8**. The simulated pattern was generated using published data from Tacke and co-workers (CSD refcode: IGUJOJ).[274]

The presence of N-H protons in ammonium cations enables the formation of H-bonds in these compounds. However, in each triethylammonium cation, there is only one proton that

forms a one-direction H-bond. The two ammonium cations in compound **8** form isolated aggregates with the germanate anion through intermolecular N(H)···O H-bonds, and no further extensions were observed.

The use of diamine, such as N,N,N',N'-tetramethylethylenediamine (TMEDA), offers an opportunity of generating an extended network through H-bond interactions from two N-H protons when they are protonated. In order to explore the H-bonded network, single crystals of compound **5** were obtained through the vapour diffusion method,[276] by dissolving **5** in DMF prior to the slow diffusion of Et_2O to afford yellow, needle-shaped crystals.

Single crystal X-ray diffraction studies revealed that compound **5** crystallised in the monoclinic *C*2/*c* space group. Each asymmetric unit contains half a cation and half an anion, and there are four formula molecules $[(C_6O_{12}Si)(C_6H_{18}N_2)]$ in each unit cell. The central Si atom coordinates with six O atoms from three oxalate groups to give an octahedral geometry (Figure 2.10 a), with Si-O bond lengths ranging from 1.7749(11) to 1.7770(11) Å, and adjacent and opposite O-Si-O angles between 87.63(5)-94.65(5)° and 174.78(8)-175.14(5)° respectively. These values are in good agreement with other reported compounds with SiO_6 cores.[277, 278] There are two types of C-O bond lengths which range from 1.2032(19) to 1.2088(19) Å and 1.3075(19) to 1.3093(19) Å. These two types of bonds are therefore characteristic of double C=O and single C-O bonds respectively.[272] In addition, the dianion is chiral at the Si centre, with a racemic mix of Λ and Δ isomers observed in the solid-state structure.

As anticipated, intermolecular H-bonds can be observed between the amine N-H and terminal O atoms on the oxalate groups (Figure 2.10, with N(H)···O=C distances between 2.855 and 2.893 Å (donor to acceptor)). Each silicon-based dianion is connected by four H-bonds from four different H_2TMEDA cations: two bonds are observed from two O atoms in one oxalate group which are O6···H11 and O7···H11, while another two bonds are found from two different oxalate groups (O2···H11 and O10···H11). Each H_2TMEDA cation is connected to four linker anions, hence, both the ammonium cation and the linker anion can be regarded as 4-connected nodes to yield a 2-D layered structure with *sql* net.

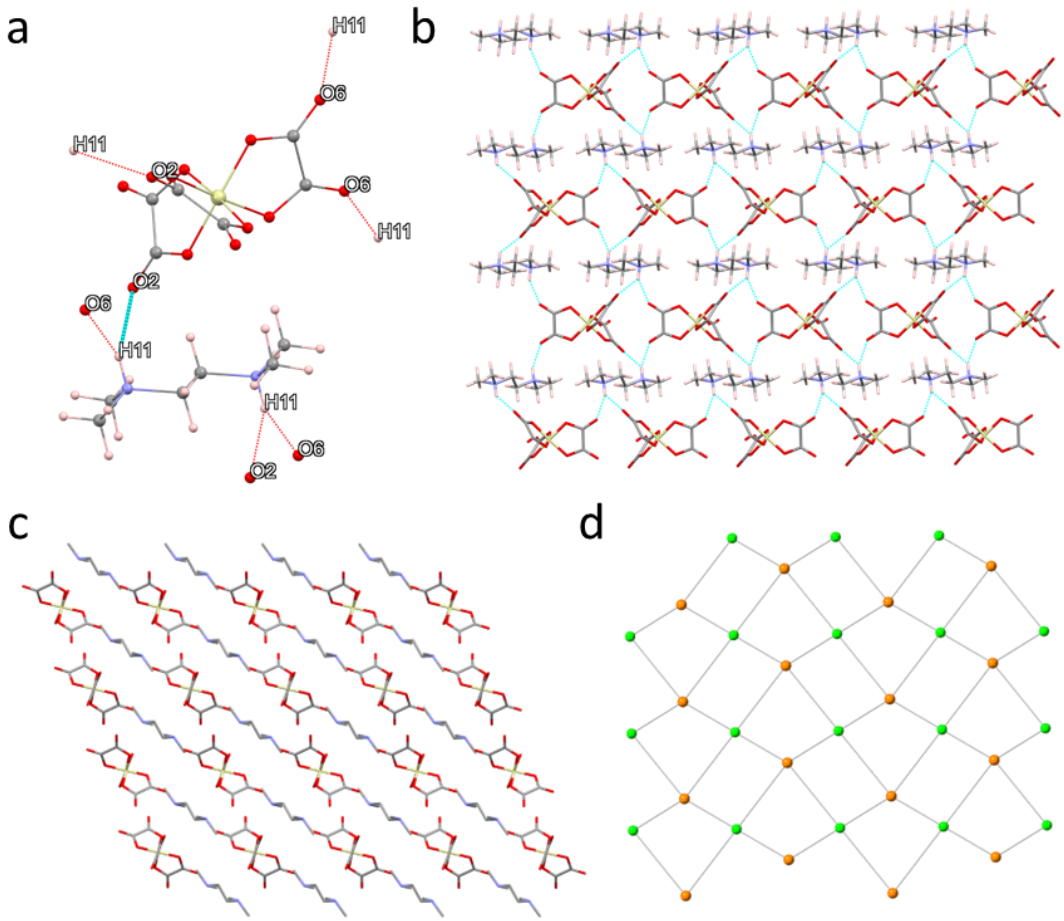

Figure 2.10 Crystal structure of compound **5**, a) intermolecular H-bonds; b) H-bonded networks; c) 2D layered structures along (0 1 0) direction; d) simplified *sql* net (anion and cations are shown in orange and green dots respectively). C: grey, O: red, N: night blue, Si: pale yellow, H: pale pink, H-bonds are shown in red/blue dotted lines. H atoms are not shown in c for clarity.

Treatment of $Ge(OMe)_4$ with oxalic acid and TMEDA afforded compound **9** as a white powder. It was predicted that compound **9** would be iso-structural with **5**, due to the only difference being the replacement of Si with Ge in the dianion. To verify this, colourless block crystals of **9** were obtained by slow cooling hot aqueous solution of compound **9**. Subsequently, SCXRD analysis was carried out to obtain detailed structural information.

As anticipated, compound **9** crystallized in the monoclinic *C*2/*c* space group. The unit cell is slightly larger than that of compound **5**, and this difference can be attributed to the larger

atomic radius of Ge compared to Si (Table 2.2). The C-O bond lengths are also consistent with those observed in compound **5**, lying in the ranges 1.204(2) Å to 1.207(2) Å and 1.301(2) Å to 1.313(2) Å. Ge-O bond lengths lie in the range 1.8784(11) Å to 1.8827(11) Å which is slightly longer than the analogues Si-O bonds. The bond angle within adjacent and opposite O-Ge-O units are between 85.78(7)-96.46(5)° and 172.06(7)-172.56(5)°, which is close to the ideal octahedral geometry. Despite crystals of compound **9** being obtained under different conditions to those of **5**, the overall H-bonded network is identical (Figure 2.11), with the N(H)···O=C distance between 2.850 and 2.922 Å. Additionally, the overall topology is identical with compound **5** to yield 4-connected *sql* layered nets.

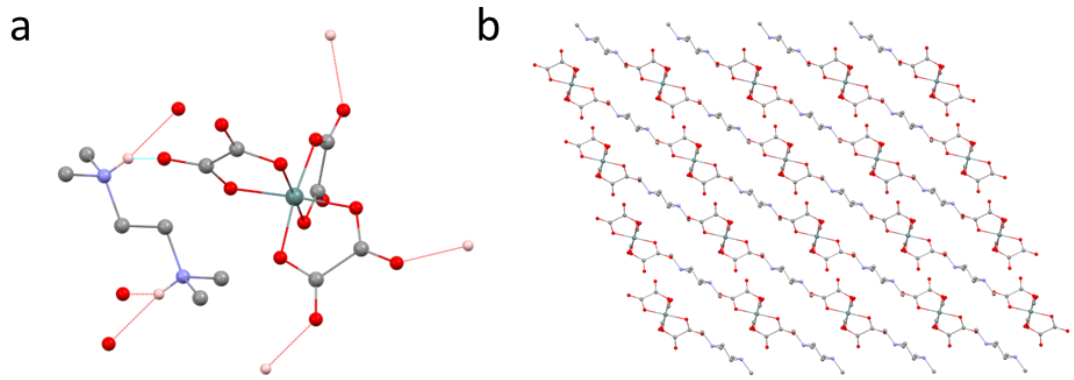

Figure 2.11 a) crystal structure of compound **9** showing intermolecular H-bonds; b) packing diagram along (0 1 0) view of compound **9**. C: grey, O: red, N: night blue, Ge: grey blue. H-bonds are shown in red/blue dotted lines. Non-H-bonded H atoms are omitted for clarity.

parameters	Compound **5**	Compound **9**
a	15.9360(10) Å	15.9823(3) Å
b	8.0111(4) Å	8.04505(12) Å
c	14.4195(11) Å	14.5077(3) Å
β	111.531(8)°	111.711(2)°
V (Å^3)	1712.4(2)	1733.05(6)
E-O bond length (mean, Å)	1.7762	1.8809
Atom radius	Si(IV): 0.4 Å	Ge(IV): 0.67 Å

Table 2.2 Crystallography data of compounds **5** and **9**.

PXRD studies on compounds **5** and **9** revealed that the traces for the as-synthesized products were in good agreement with the calculated patterns from their single crystal data (Figure 2.12), thus demonstrating good phase purity of the products. The presence of H-bonded networks suggests that there might be pores suitable for guest molecules to access similar to previously reported HOFs. However *PLATON*[265] was used to calculate the potential void space from the crystallographic *cif* file, and this gave a value of zero for possible solvent-accessible area due to the dense packing of the molecules.

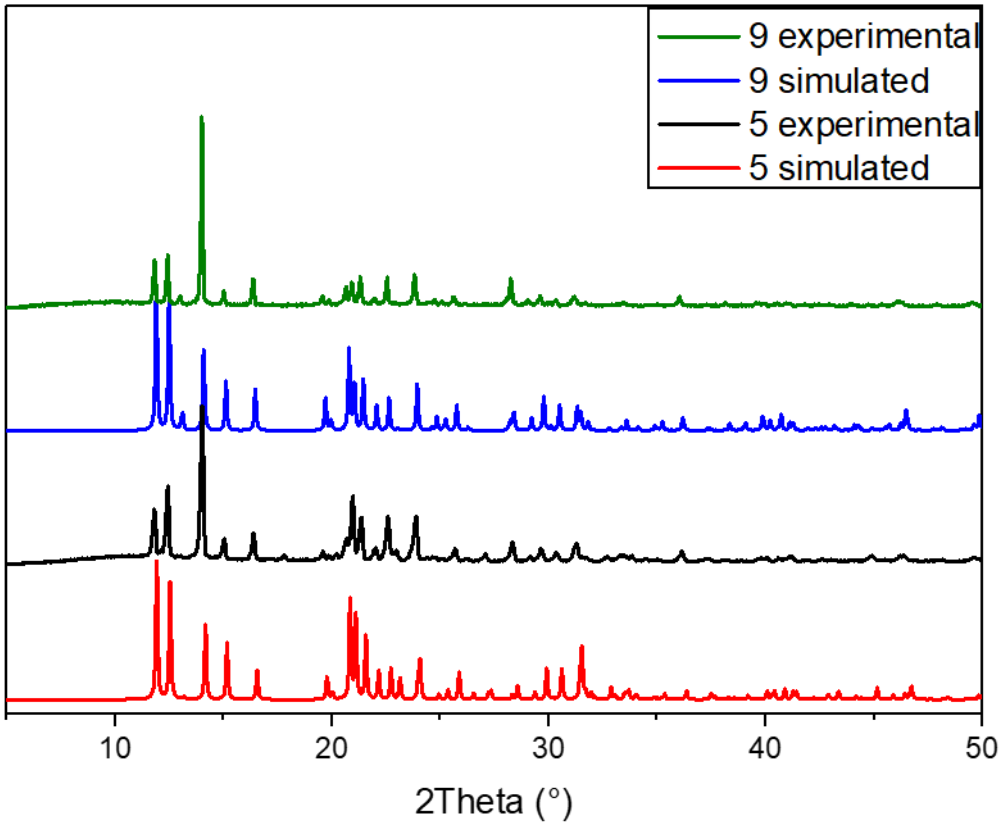

Figure 2.12 Experimental PXRD patterns of **5**, **9** and their simulated patterns from SCXRD data.

One way to increase the pore size, in this situation, might be to use longer reach cations. TMPDA and TMBDA (N,N,N',N'-tetramethylpropanediamine and N,N,N',N'-tetramethylbutanediamine respectively) were therefore selected because the extra carbon atom(s) would extend the length of the cations and thus might facilitate the formation of void spaces.

Treatment of $Si(OMe)_4$ with oxalic acid and the longer diamines yielded compounds **6** and **7** as white powders (**6** from TMPDA, **7** from TMBDA). ^{29}Si NMR studies reveal that the central Si atoms in compounds **6** and **7** are in hexacoordinate environments, with chemical shift values of -173.99 and -174.01 ppm, respectively. Single crystals of **6** and **7** were obtained through the vapour diffusion method and were used for SCXRD analysis. The crystal of compound **6** comprises a structure of the formula $[(C_6O_{12}Si)(C_7H_{20}N_2)_2(C_2O_4)]$. It crystallized in the triclinic *P*-1 space group. Each asymmetric unit contains two H_2TMPDA cations, one linker anion and one independent oxalate anion. The Si-O bond lengths are in the range of 1.7644(11) to 1.7864(10) Å, and the bond angles of adjacent and opposite O-Si-O are between 87.27(5)-94.30(5)° and 175.59(5)-176.05(5)° respectively. These values are consistent with other SiO_6 containing compounds. The C-O bond lengths in the free oxalate group lie in the range 1.2334(19) to 1.2593(17) Å indicating complete charge delocalisation and therefore differ from the C-O bond lengths in the linker anion which are 1.202(2) to 1.2092(19) Å for C-O single bonds, and 1.3033(19) to 1.3126(18) Å for C=O double bond.

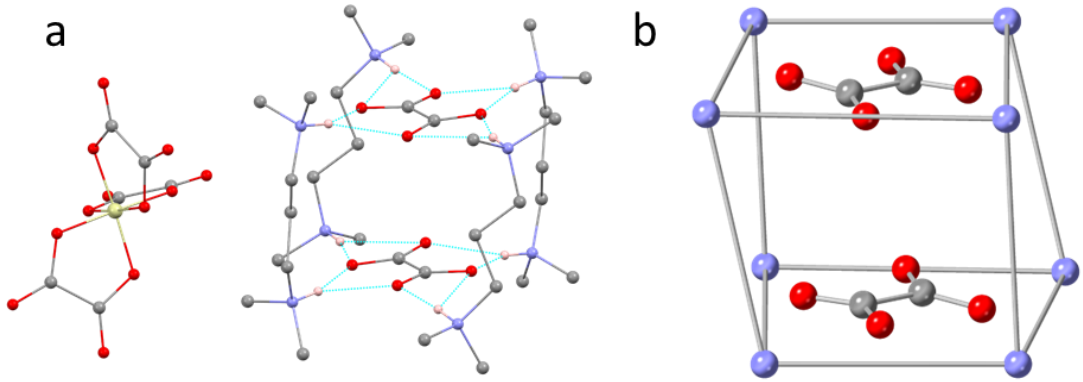

Figure 2.13 Crystal structure of compound **6**, a) H-bonds between H_2TMPDA cations and oxalate anions forming a cube-cage (with additional one oxalate group and two H_2TMPDA cations shown to exhibit the cage structure); b) simplified cube-shaped cage. C: grey, O: red, N: night blue, Si: pale yellow, H: pale pink. Only H-bonded (blue dotted lines) H atoms are shown.

Intermolecular H-bonds were observed between H_2TMPDA cations and the free oxalate

anion only, with N(H)···O distances between 2.663 and 3.171 Å. Two oxalate anions are located in parallel planes and these two planes are vertically connected by four H_2TMPDA cations situated at corners to form a distorted cube-like cage (Figure 2.13). There is no H-bond observed between the linker anion and H_2TMPDA cations, and the reason for the presence of an unexpected free oxalate anion is unclear.

The Ge analogue compound **10** was collected as a white powder through a similar procedure to **6**, using $Ge(OMe)_4$ as the starting material instead of $Si(OMe)_4$. It can be seen from Figure 2.14 that most of the peaks of compound **10** align with the peak position in compound **6**, suggesting that **10** may have a similar structure compared to **6**, while the extra peaks suggest that **10** contains products with different phases. The difference between the as-synthesized compound **6** and the simulated pattern might be due to the breakdown of the H-bonded structure during the sample thermal vacuum drying procedure, which may further affect the overall structure arrangement and lattice constant.

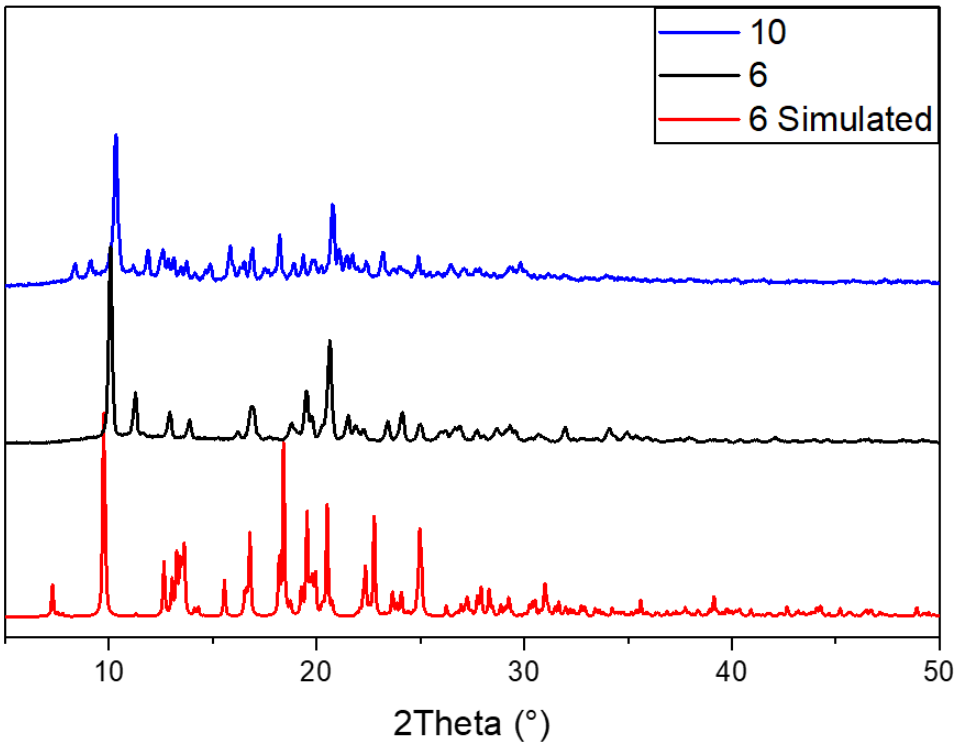

Figure 2.14 PXRD pattern of compounds **6** (simulated and measured) and **10** (measured).

The structures of the H_2TMBDA containing solids were then studied: The slow diffusion

of Et_2O into a DMF solution of compound **7** afforded colourless plate crystals. Crystals of compound **7** have a formula of $[(C_6O_{12}Si)(C_8H_{22}N_2)_2(C_2O_4)\cdot DMF]$ as confirmed by SCXRD studies and crystallise in the monoclinic $P2_1/n$ space group. Each asymmetric unit contains two H_2TMBDA cations, one linker anion, one free oxalate group and one disordered DMF molecule. The Si-O bond lengths fall in the range 1.7679(11) to 1.7813(10) Å, and adjacent and opposite O-Si-O bond angles are found between 87.55(5)-93.88(5)° and 174.19(5)-177.34(5)° respectively. These values match those of other SiO_6 type compounds, and the Si centre atom is in a slightly disordered octahedral geometry.

H-bonds are only present between H_2TMBDA cations and the free oxalate anion. However, due to the zigzag chain structure of the H_2TMBDA molecule, the presence of the extra carbon atom changes the N-H orientation compared to H_2TMPDA in compound **6**, which significantly affects the overall structure. The two N-H protons are arranged in an antiparallel fashion, allowing each H_2TMBDA cation to form H-bonds with neighbouring oxalate groups laterally. Each oxalate group is connected to four H_2TMBDA cations, and such an arrangement gives a 2D layered structure with a wave-like pattern (Figure 2.15). Free oxalate anions can be regarded as 4-connected nodes to yield a *sql* net.

The presence of the DMF molecule and the formation of H-bonds in the crystal growth process is likely to affect the overall lattice parameters. Thermal vacuum treatment of compound **7** could result in the breakdown of H-bond interactions, thus leading to the generation of a new phase, as reflected in the difference between the simulated powder pattern from single crystal data and as-synthesized compound **7** (Figure 2.16).

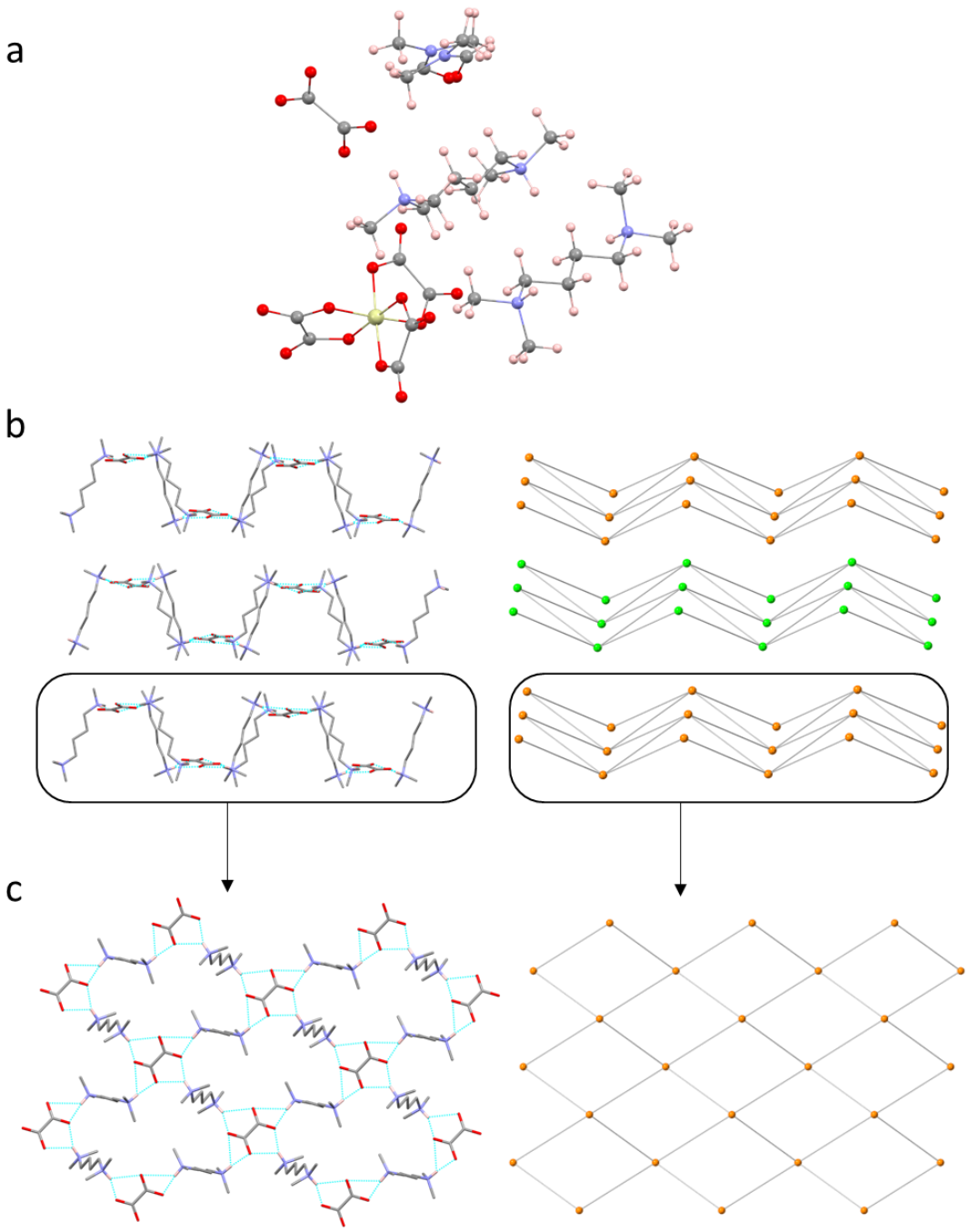

Figure 2.15 a) Crystal structure of compound **7** containing L1-Si anion, two H_2TMBDA cations, one oxalate anion and disordered DMF molecules; b) wavy 2D H-bonded network constructed by H_2TMBDA cations and oxalate anions, (0 1 0) view; c) vertical view of a layer with *sql* net. C: grey, O: red, N: night blue, Si: pale yellow, H: pale pink. Only H-bonded (blue dotted lines) H atoms are shown in b, c, and linker anions are not shown for clarity.

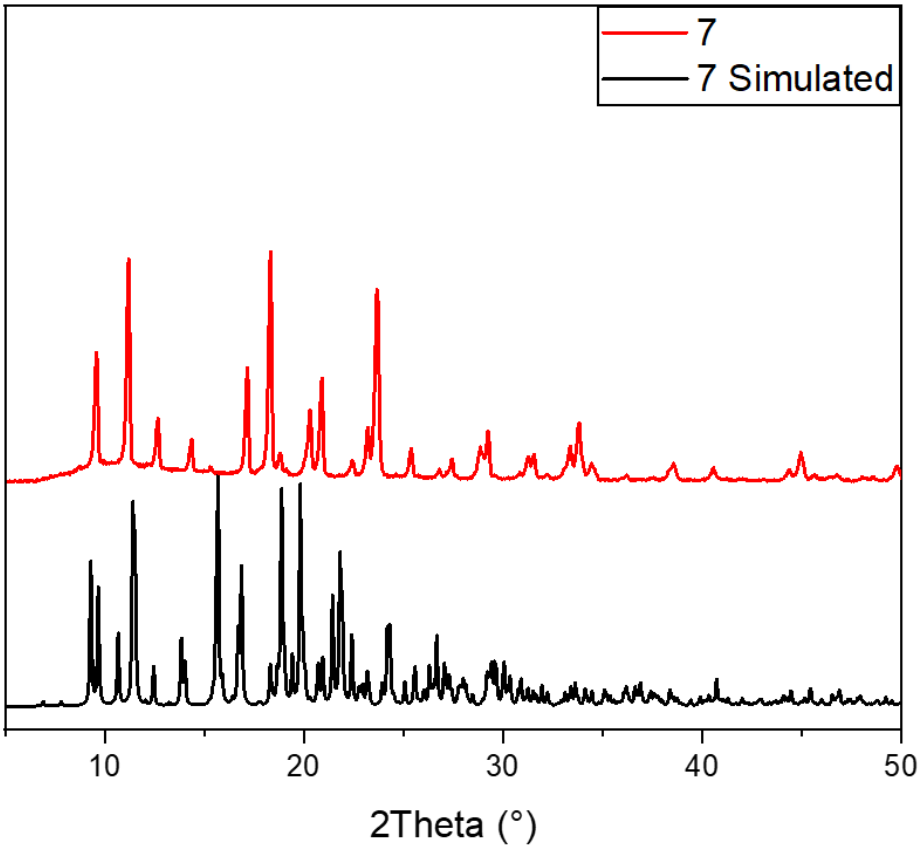

Figure 2.16 PXRD pattern of compound **7** (simulated and measured).

Alternatively, **L1-Ge** type linkers can be synthesized from GeO_2 in an aqueous environment. This method was similar to the synthesis of [2,2'-Hbipy]$_2$[Ge(C_2O_4)$_3$] with a GeO_2, oxalic acid and 2,2'-bipyridine ratio of 3:4:2.[279] The hydrothermal reaction of GeO_2 with oxalic acid and 4,4'-bipyridine afforded colourless block crystals. However, SCXRD analysis revealed that these crystals were the known compound [H_2bipy][Ge(C_2O_4)$_2$(OH)$_2$] (CSD refcode: BIWWEK). Consequently, the ratio of the above chemicals was modified to 1:3:1 (GeO_2:$H_2C_2O_4$:4,4'-bipy) while the reaction conditions remained unchanged. Hydrothermal treatment of the above mixture in a PTFE autoclave afforded colourless needle crystals. Then the mother liquid was transferred into a clean glass vial, and the liquid was left in the open air. Colourless tablets crystals (crystal of compound **11**) were obtained after 3 days, and these crystals were analysed and found to be [(H_2Bipy)(Ge(C_2O_4)$_3$)·H_2O] through SCXRD studies. Compound **11** crystallized in the monoclinic space group $P2_1/c$,

and there are four formula molecules in each unit cell. The centre Ge atom coordinates with three oxalate linkers as expected, forming a slightly disordered octahedral geometry with adjacent and opposite O-Ge-O angles in the ranges 86.74(7)-96.58(8)° and 173.28(7)-174.04(7)° respectively. The Ge-O distances are in the range 1.8657(17)-1.8933(17) Å, and the structural features observed from the GeO_6 skeleton in **11** are similar to those of **9** and other reported [$Ge(ox)_3$] complexes.[274, 279]

The pyridinium cations form H-bonds with O atoms from linker anions and water molecules. H-bond interactions are also observed between O atoms in the GeO_6 centre and water molecules. Each linker anion forms six H-bonds in total (Figure 2.17 a): two terminal O atoms from one oxalate group form H-bonds with pyridinium cations which are O5···H31 and O6···H31, forming a five-member ring. Another two terminal O atoms from the second oxalate group form two H-bonds with two pyridinium cations, which are O26···H31 and O25···H40. There is an H-bond observed between Ge-O21 and H50A from the water molecule, while the last H-bond originates from the O16 in the third oxalate group and H50B from the water molecule. Interestingly, three H-bonds among O25···H40, O21···H50A and O50···H40 form a six-membered ring. Each linker anion and bipyridinium cation are linked by H-bonds to form a 2-D layered structure (Figure 2.17 b), and each layer is connected by H-bonds in the (1 0 0) direction to generate a 3-D framework structure (Figure 2.17c). However, the dense packing excludes any large pores within the structure for guest molecules to be absorbed, as shown by calculations using *PLATON*.[265]

The PXRD pattern of bulk compound **11** from the tablet crystals fits the simulated pattern from the SXCRD data well (Figure 2.18). However, the measured peak intensity of the needle crystals is different from that in **11**, which may result from the preferred orientation of the needle crystals or the difference in crystal growth conditions.

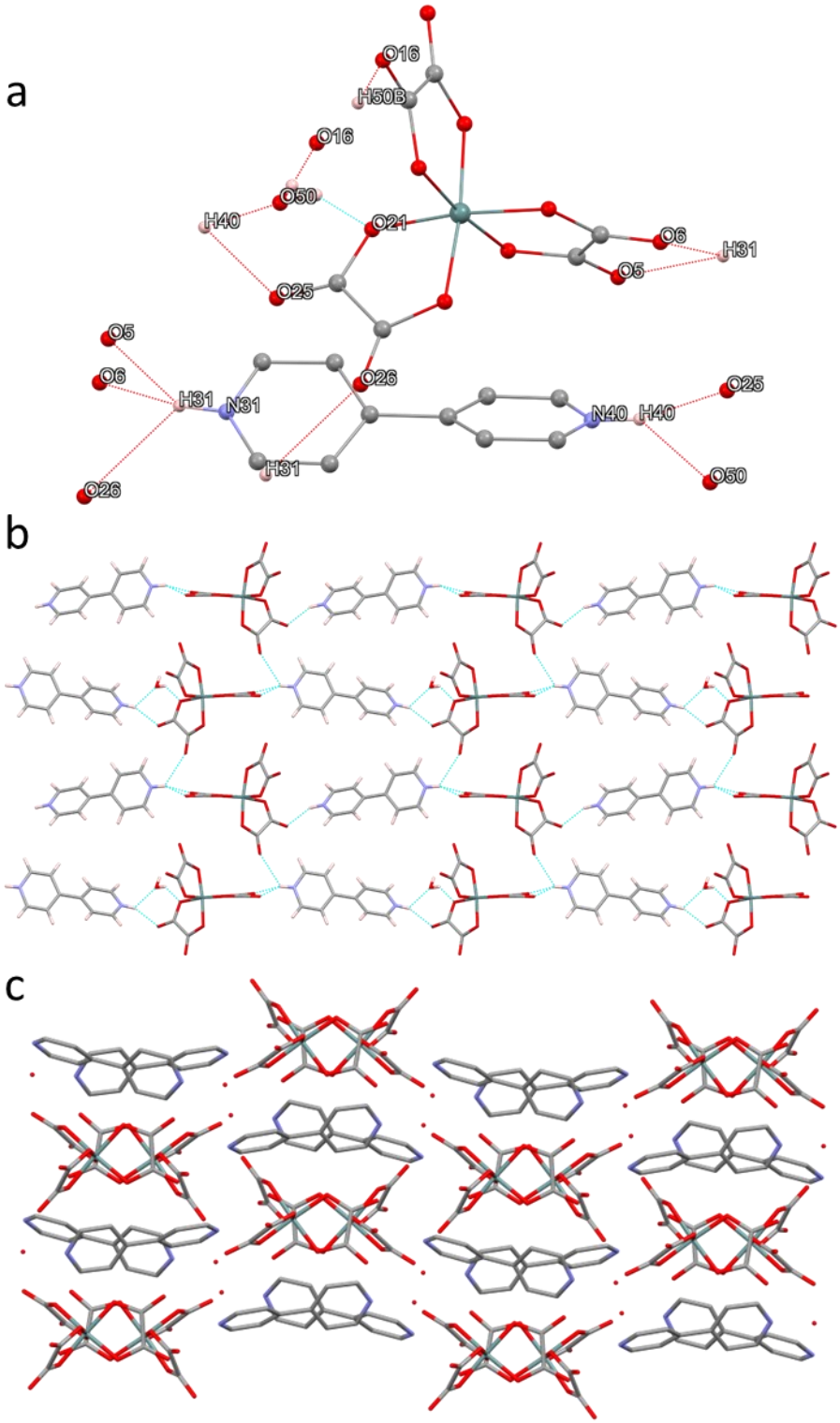

Figure 2.17 a) Crystal structure of compound **11** showing H-bonding interactions; b) 2D layered structure built from H_2bipy cations and linker anion along (1 0 0) direction; c) packing diagram of the layered structure along (0 0 1) view. C: grey, O: red, N: night blue, Ge: grey blue, H: pale pink. H atoms are omitted in the packing diagram for clarity.

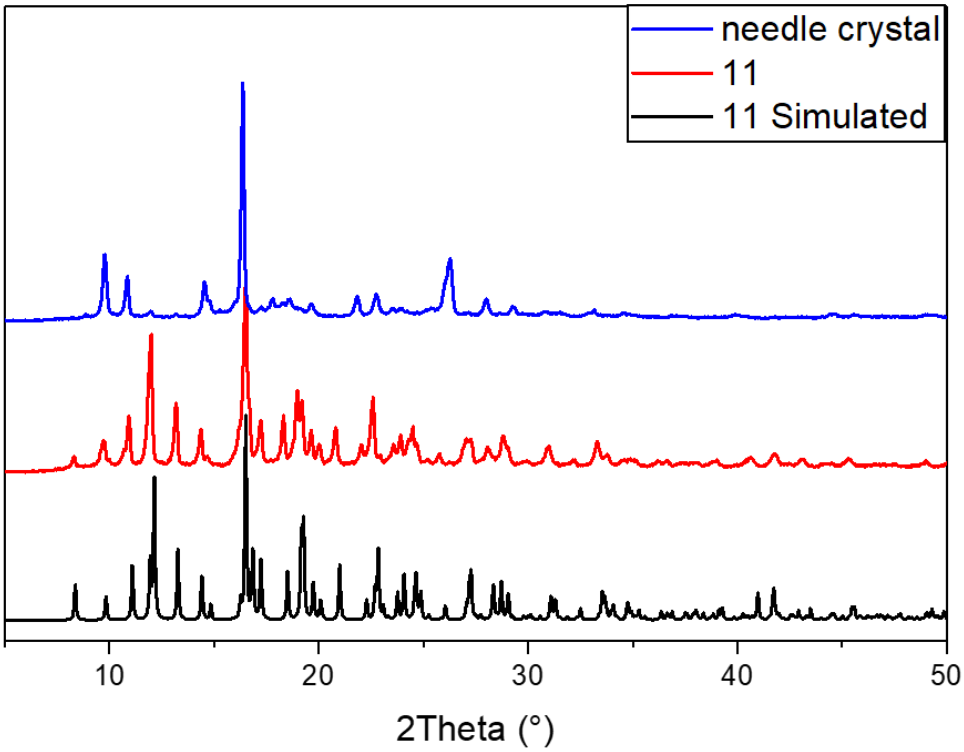

Figure 2.18 PXRD patterns of compound **11** (simulated and measured), and the measured pattern of the needle crystal by-product.

It is anticipated that guanidinium (Gu) cations may form multiple H-bonds with the O atoms in the linker oxalate group, hence guanidinium oxalate was prepared as a precursor for linker synthesis. $Gu_2C_2O_4$ was found to be insoluble in most organic solvents, therefore the synthesis was carried out in water, following the same conditions used in compound **11**. Treatment of $Gu_2C_2O_4$ with GeO_2 and oxalic acid (ratio 1:1:2) in a PTFE autoclave at 100°C for 3 days yielded a clear solution. Colourless block-like needle crystals (compound **12**) were obtained after the solution was left in an open atmosphere for 1 month. The formula of the crystal was confirmed through SCXRD studies to be $[(Gu)_2(Ge(C_2O_4)_3)\cdot 2.5H_2O]$, however, the preliminary results revealed that the structure was heavily disordered (water molecules and Gu cations). Compound **12** crystallised in the monoclinic $P2_1/n$ space group. Each unit cell contains 12 linker anions and 24 guanidinium cations, which equals twelve of the formula units. The Ge-O bond lengths are in the range between 1.8678(17) and 1.8935(18) Å, and adjacent and opposite O-Ge-O bond angles range from 85.61(8) to

95.10(8)° and 172.87(8) to 175.43(8)°, and these results match the values in other GeO_6 type compounds. It should be noted that the C-N bond length in all guanidinium cations spans from 1.290(4) to 1.324(4) Å, and such bond lengths are in line with other guanidinium compounds.[280, 281] Compared to the C-N bond length in the neutral guanidine molecule, the uniform C-N bond length in **12** suggested that the positive charge is evenly distributed on the cation due to its resonance structure.[282] H-bonds are presented between cations and O atoms in the anion (Figure 2.19), however the dense packing of the molecules excludes the formation of any void space for guest molecules to be absorbed.

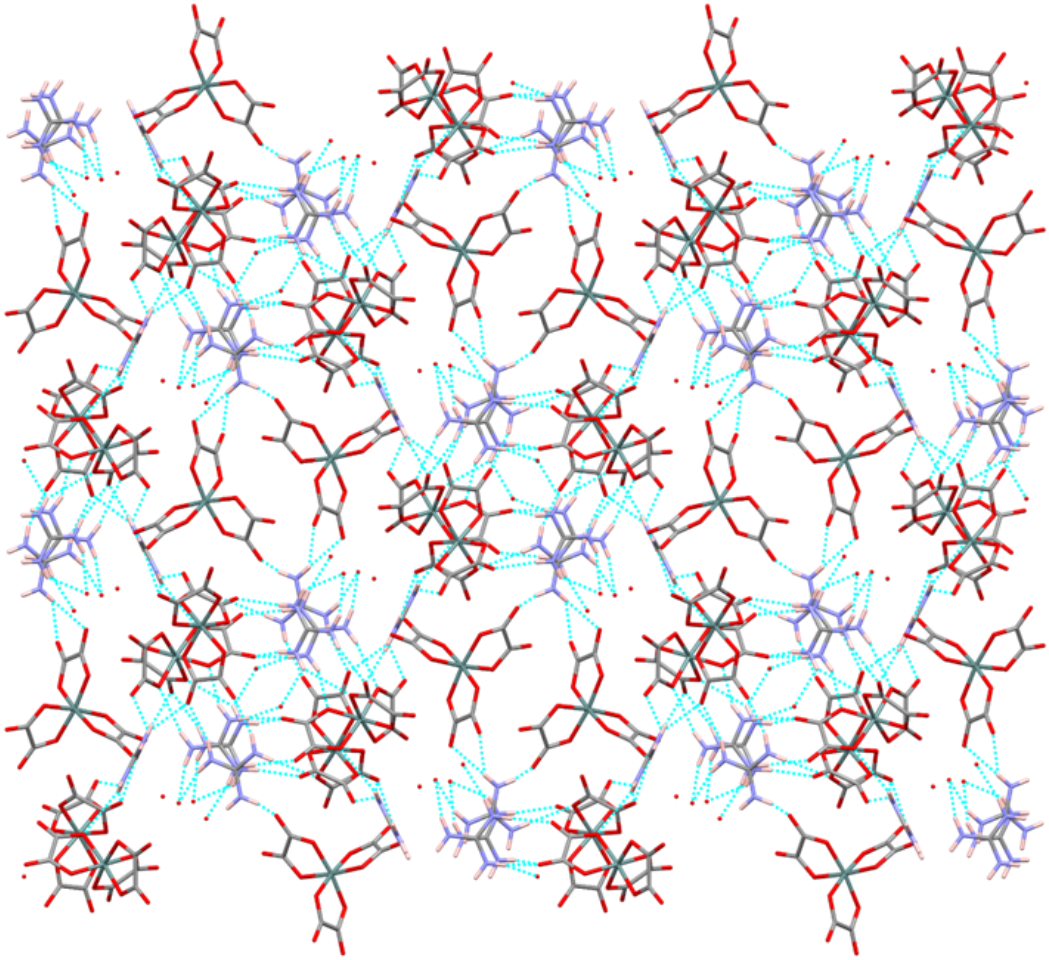

Figure 2.19 Packing diagram of compound **12** along (1 0 0) direction. C: grey, O: red, N: night blue, Ge: grey blue, H: pale pink. H-bonds are shown in dotted blue line.

2.3 Synthesis of Si/Ge(caffeic acid)$_3$ Type Linkers

2.3.1 Synthesis Methods

L2-type compounds (shown in Scheme 2.2) were prepared through a similar procedure for the synthesis of known tris-catechol type compounds,[283] but a change in the starting material of catechol to its derivatives was adopted in the synthesis process. Thus tris[3-(3,4-diolatophenyl)acrylic acid] silicate/germanate compounds were prepared through the reaction of caffeic acid with amine and $Si(OMe)_4$ or $Ge(OMe)_4$ in MeCN. All L2-type compounds are new compounds and the additional COOH groups can provide coordination points for MOF construction. This procedure was employed for the synthesis of $[Et_3NH]_2$[**L2-Si**] (**13**), $[HDMAE]_2$[**L2-Si**] (**14**) and $[Et_3NH]_2$[**L2-Ge**] (**15**), as illustrated below in scheme 2.2.

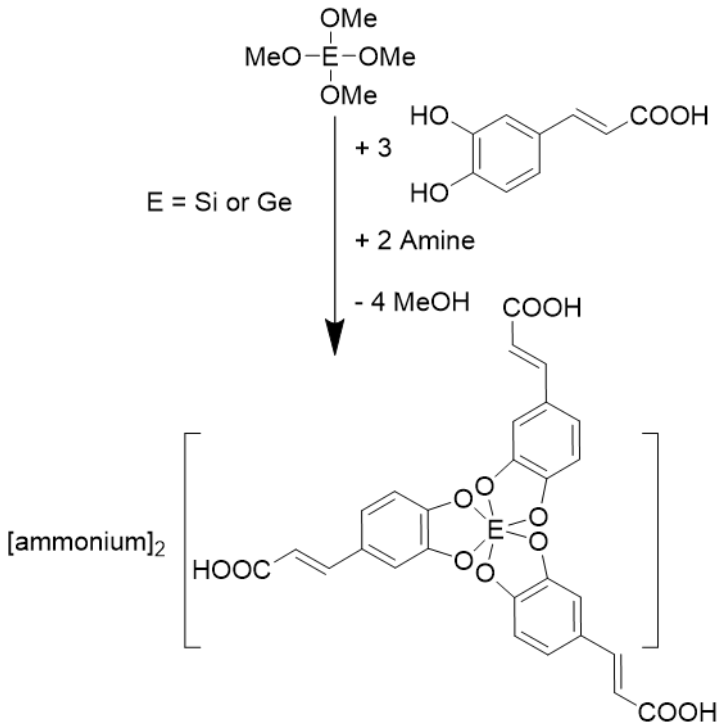

Scheme 2.2 Synthesis of L2 type linker. Amine = Et_3N, DMAE, DMAP.

2.3.2 Characterization

L2 is considered a desirable target linker due to the presence of terminal COOH groups which are ideal for metal coordination to form extended networks. The long side arm may facilitate the formation of large pores and provide additional points for modification to achieve different functions.

Treatment of caffeic acid with $Si(OMe)_4$ and amine afford compounds **13** and **14** as yellow powders (triethylamine for **13** and dimethylamino ethanol for **14**). Both compounds were characterized by ^{29}Si NMR spectroscopy to confirm the SiO_6 environment, and the chemical shift values were close to the reported value for tris-catechol silicate, which are -138.37 (**13**), -138.58 (**14**) and -139.3 ppm (tris-catechol silicate).[273, 283] the presence of the **L2-Si** dianion in compound **13** was confirmed through MS-ESI studies which showed the expected peak for [**L2-Si**+H]$^-$. Unexpectedly, ^1H NMR spectroscopy of **13** and **14** showed that the anion to cation ratio was 1:3, and the presence of the extra ammonium cation might be attributed to the reaction between the amine with one COOH to give ammonium carboxylate.

Treatment of caffeic acid with $Ge(OMe)_4$ and Et_3N afforded compound **15** as a yellow powder. ^1H NMR spectroscopic results revealed that the ammonium cation and linker anion were in a ratio of 2:1. MS-ESI studies for compound **15** showed that the expected [**L2-Ge**+H]$^-$ (**15**) ion was observed. To have an in-depth study on the structure of L2-type linkers, especially the presence of H-bond interactions, attempts to grow single crystals of **13** were carried out. Despite compound **13** exhibiting some crystallinity as shown by PXRD results, attempts to grow single crystals of **13** were not successful. Compounds **14** and **15** are non-crystalline, hence attempts to grow single crystals were not conducted.

2.4 Synthesis of Si/Ge(3,4-dihydroxybenzoic acid)$_3$ Type Linkers

2.4.1 Synthesis Methods

In line with the method discussed above for the synthesis of L2 linkers, 3,4-dihydroxy-benzoic acid was chosen, instead of caffeic acid, for the synthesis of L3 linkers. The products can be readily obtained through filtration from the reaction mixture, and this method was carried out for the production of $[Et_3NH]_2$[**L3-Si**] (**16**), $[Et_2NH_2]_2$[**L3-Si**] (**17**), $[HDMAE]_2$[**L3-Si**] (**18**), $[HDMAP]_2$[**L3-Si**] (**19**), $[Et_3NH]_2$[**L3-Ge**] (**20**), and $[Et_2NH_2]_2$[**L3-Ge**] (**21**). All of these are new compounds and the synthesis is shown in Scheme 2.3 below.

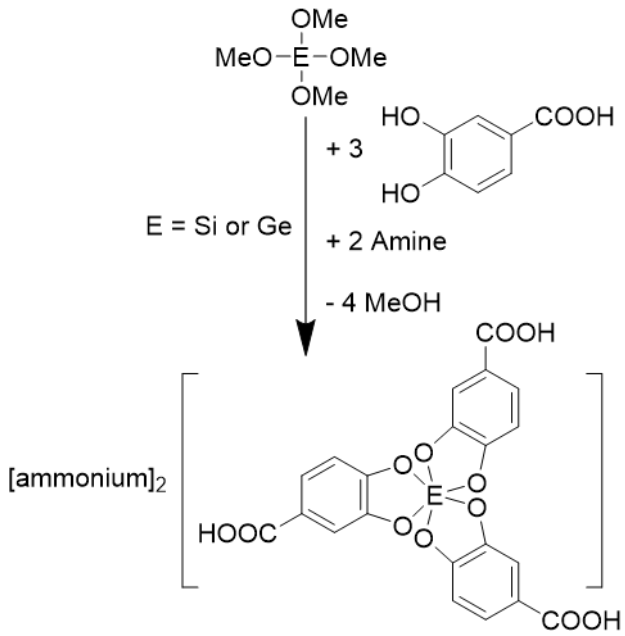

Scheme 2.3 Synthesis method of L3 type linker. Amine = Et_3N, Et_2NH, DMAE or DMAP.

2.4.2 Characterization and Structure Description

Compound **16** was obtained through a similar method to **13** to give a white powder. The SiO_6 environment was confirmed by ^{29}Si NMR spectroscopy with a chemical shift value of -138.17 ppm, and this value was in good agreement with the L2 linkers and tris-catechol silicate. The ratio of cation to anion was confirmed by ^{1}H NMR spectroscopy with a value

of 2:1. MS-ESI studies showed that the expected [**L3-Si**+H]$^-$ ion was observed.

	13	**15**	**16**	**20**
^{29}Si NMR (ppm)	-138.37	-	-138.17	-
MS (found)	563.0655	609.0099	485.0198	530.9626
MS (calcd.)	563.0646	609.0088	485.0182	530.9624

Table 2.3 Comparison of L2 and L3 linkers.

PXRD results indicated that compound **16** was crystalline hence attempts to grow single crystals of **16** were carried out. The slow diffusion of Et_2O into a DMF solution of **16** afforded colourless tablet crystals. As revealed from SCXRD studies, crystal **16** crystallised in the triclinic *P*-1 space group. Each molecule contains two triethyl ammonium cations and one linker anion, with the formula $[(C_{21}H_{12}O_{12}Si)(C_6H_{16}N)_2]$. The central Si atom in the anion coordinates with three deprotonated phenol di-hydroxy groups from the dihydroxybenzoic acid to give an octahedral geometry (Figure 2.20). The Si-O bond lengths lie in the range 1.767(3) to 1.798(3) Å, and adjacent and opposite O-Si-O bond angles are in the ranges 87.10(14) to 94.67(14)° and 174.50(16) to 177.24(16)° respectively. There are only small differences between the above angle values and the ideal octahedral geometry, and these bond length and angle values are consistent with tris-catechol silicate.[283] Both ammonium cations and one of the benzoic acid rings were disordered. In addition, the dianion is chiral at the Si centre, with a racemic mix of Λ and Δ isomers observed in the solid-state structure.

Intermolecular H-bonds are observed between the N-H group on the ammonium cation and three facially positioned oxygen atoms in the SiO_6 group, with N(H)···O-Si distances between 2.867 and 3.355 Å (mean 3.146 Å). Two of the carboxylic acid groups in each dianion formed hydrogen bonding dimers with adjacent COOH groups, resulting in the formation of a zigzag H-bonded chain (Figure 2.20). The O(H)···O distances are between 2.573 and 2.605 Å, which are consistent with similar structures in HOFs built from poly-carboxylic acids.[119] No H-bonding interactions were observed in the third COOH group.

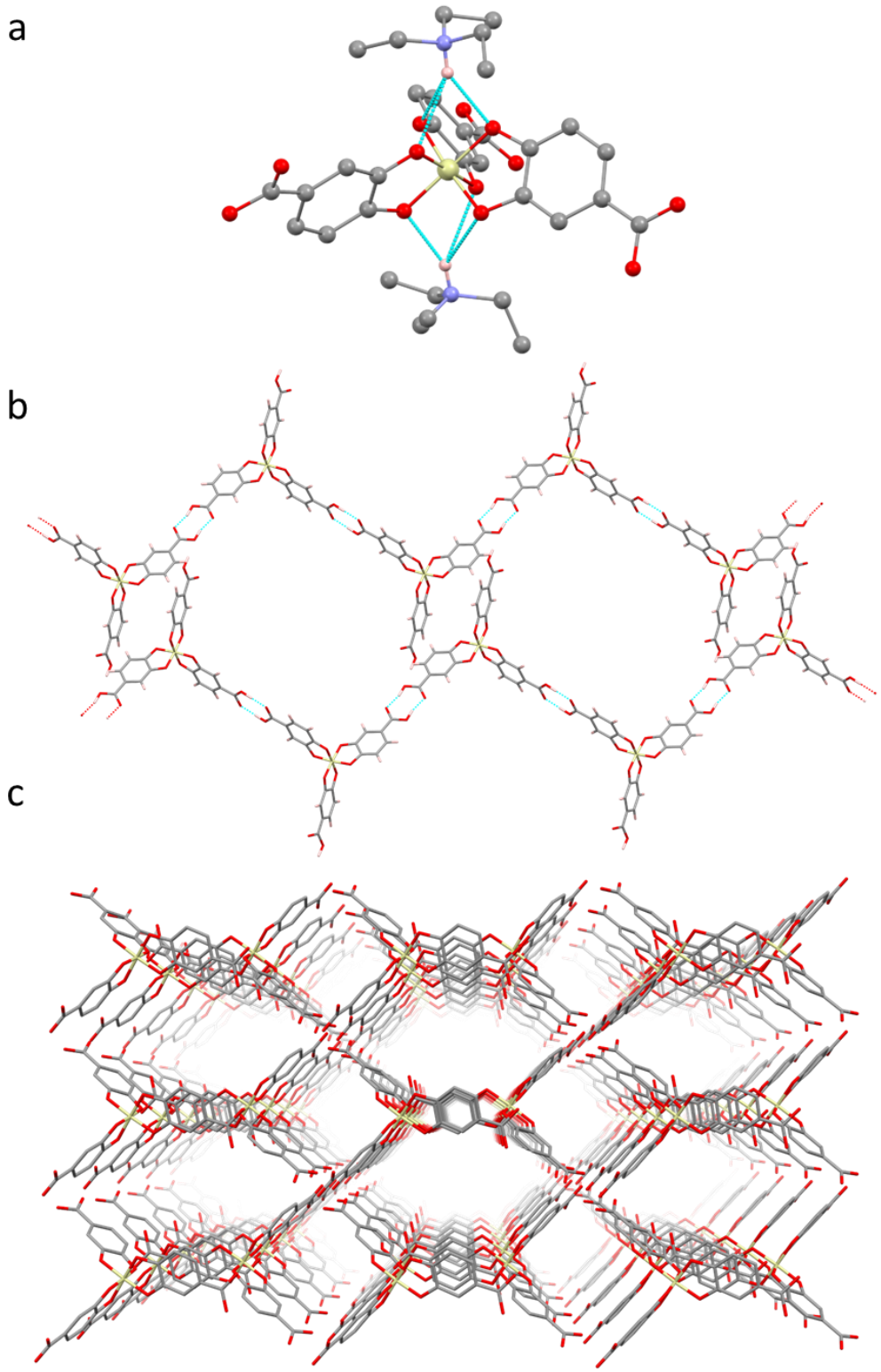

Figure 2.20 a) Crystal structure of compound **16** (single unit); b) Zigzag chain structure; c) packing diagram viewed along (0 1 0). C: grey, O: red, N: night blue, Si: pale yellow, H: pink. H-bonds: blue dotted lines; ammonium cations are omitted in b and c for clarity.

Void space is observed along the (0 1 0) direction due to the arrangement of the antiparallel 1D chains with channels of diameter 3.4 Å,[284] and the void space is initially occupied by solvent molecules (DMF). It was calculated by *PLATON*[265] that the solvent-accessible space is about 36%. However, thermal activation of the compound under vacuum led to its structural change, as indicated by PXRD results (Figure 2.21). The difference between the simulated and experimental patterns might originate from the breaking of the H-bond interactions during activation.

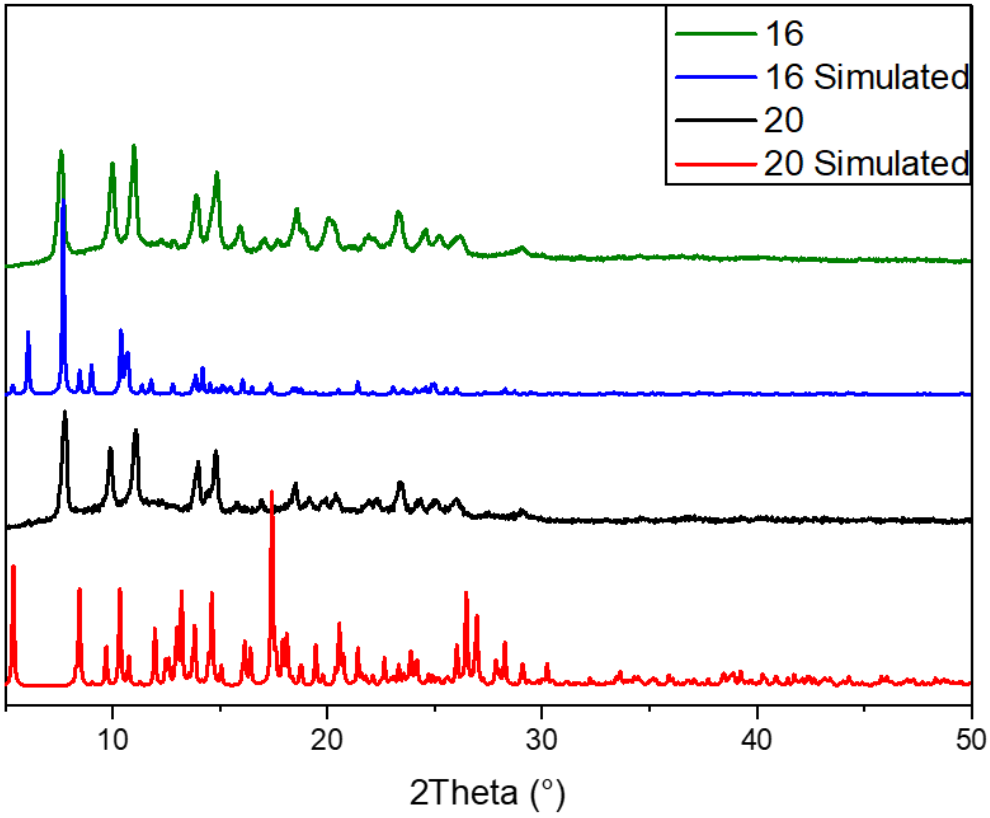

Figure 2.21 Simulated and measured PXRD pattern of compounds **16** and **20**.

Treatment of $Si(OMe)_4$ with 3,4-dihydroxybenzoic acid and different amines afforded compounds **17-19** (diethylamine for **17**, dimethylamino ethanol for **18** and dimethylamino propanol for **19**). All these compounds exhibited single peaks in ^{29}Si NMR spectra showing similar values at around -138.4 ppm, and ^{1}H NMR results revealed that the ratio of ammonium cations to linker anion is 2:1 in these compounds. A single N-H donor group in the ammonium cation could be expected to form H-bonds with one donor molecule, while

there is a strong possibility that the presence of multiple H-bond donors in the cation, such as in diethyl ammonium or dimethylammonium alcohol, may link other molecules to generate more extended H-bonded networks.[283, 285-287] However, PXRD results revealed that these compounds were non-crystalline, therefore attempt to grow single crystals of the above compounds was not carried out.

Compounds **20** and **21** (from triethylamine and diethylamine respectively) were obtained via a similar method compared to that of **16**, but instead, $Ge(OMe)_4$ was used as the precursor. These two compounds were analyzed by ^{1}H NMR studies, revealing the expected linker-to-ammonium ratio to be 1:2. MS-ESI studies of compound **20** confirmed the presence of [**L3-Ge**+H]$^-$ ion with a peak located at 530.9626 (calcd. 530.9624).

To conduct an in-depth investigation into their structure, attempts to grow single crystals of compound **20** were implemented. Single colourless blade-shaped crystals were obtained by slow evaporation of an aqueous solution of compound **20**. Compound **20** crystallized in the monoclinic $P2_1/c$ space group, with a formula of $[(C_{21}H_{12}O_{12}Ge)(C_6H_{16}N)_2 \cdot 3.5H_2O]$. Each asymmetric unit contains two linker anions, four ammonium cations and seven water molecules, which are equal to two formula units, and there are four formula molecules in one unit cell. The observed Ge-O bond length falls in the range 1.8803(17) to 1.9056(17) Å, and the angle of the adjacent and opposite O-Ge-O units are 86.01(7) to 96.17(7)°, and 172.24(7) to 176.64(8)° respectively. These values are in close agreement with other GeO_6-type compounds. The dianion exhibits chirality at the germanium centre, presenting a racemic mixture of Λ and Δ isomers as evidenced by the solid-state structure analysis. Due to the presence of water molecules, several H-bonds are observed among the ammonium cations, linker anions and water molecules (Figure 2.22). However, the dense packing has excluded the presence of any large pores.

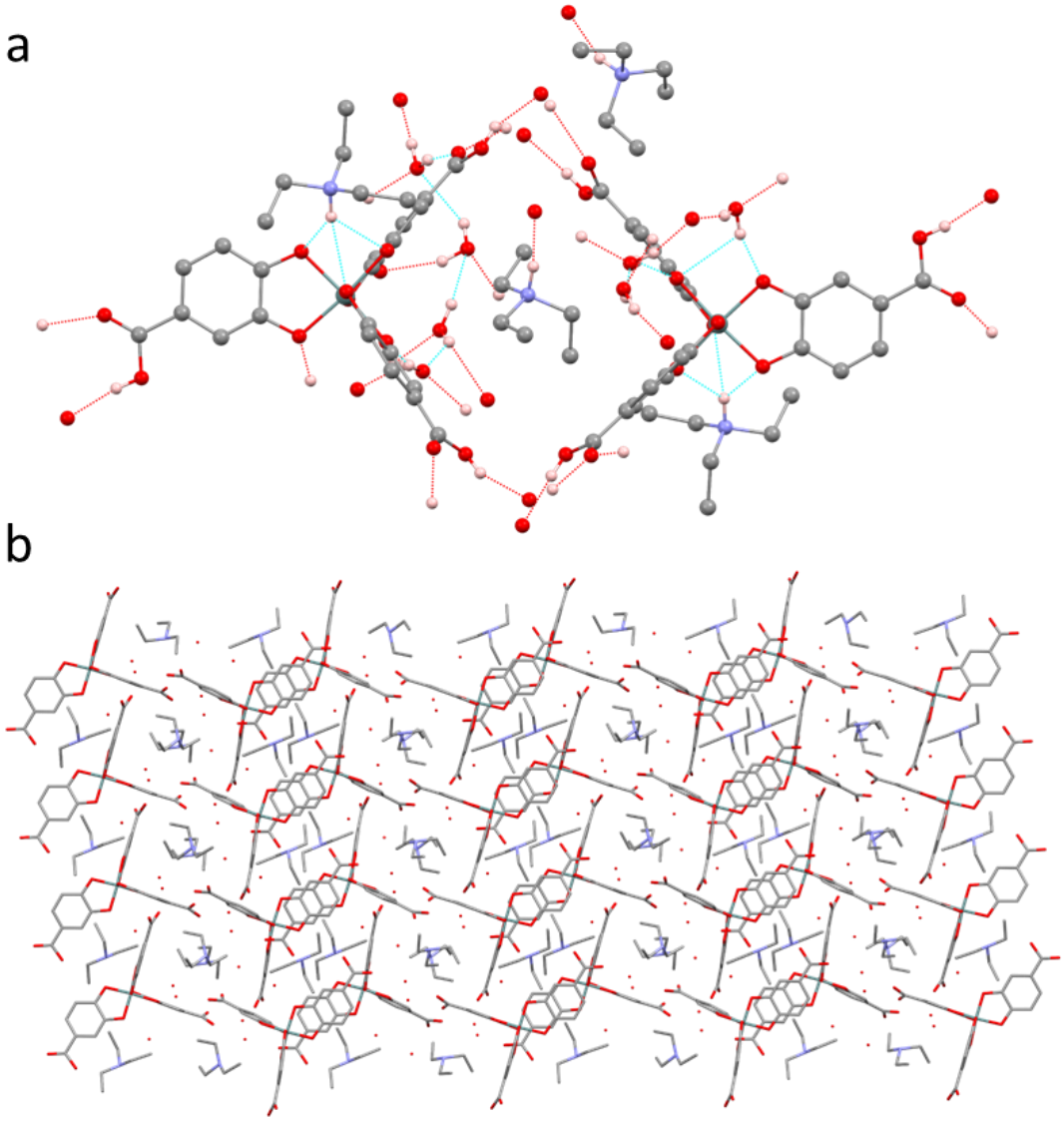

Figure 2.22 a) crystal structure of compound **20** showing H-bonds; b) packing diagram along (0 1 0) view. C: grey, O: red, N: night blue, Ge: grey blue, H: pale pink. Only H-bonded H atoms are shown for clarity.

Compound **20** is expected to exhibit a similar PXRD pattern compared to **16**, as the only difference between these two compounds is the central atom in the linker anion. It was observed from the PXRD results that the powder patterns of compounds **16** and **20** were almost identical (Figure 2.21). This finding matches with the identical PXRD pattern observed from compounds **4** and **8**, as well as **5** and **9**, confirming that the overall structure of the Si/Ge compounds is not affected by the variation in the central atoms. The presence

of water molecules in the crystal of **20** led to the formation of extensive H-bonds, thus generating a different crystal structure compared to bulk **20** in powder form. Such differences were reflected in the calculated and experimental PXRD pattern, as shown in Figure 2.21.

TGA results revealed that both compounds **16** and **20** (as-synthesized powder products without further treatment before TGA measurement) exhibited similar thermal stability up to approx. 200 and 220°C respectively before decomposition (Figure 2.23). Compound **16** exhibited a 4.5% weight loss between 30-150°C due to the loss of solvent molecules used in the work-up process (MeCN and Et_2O) which were not completely removed during the drying process.

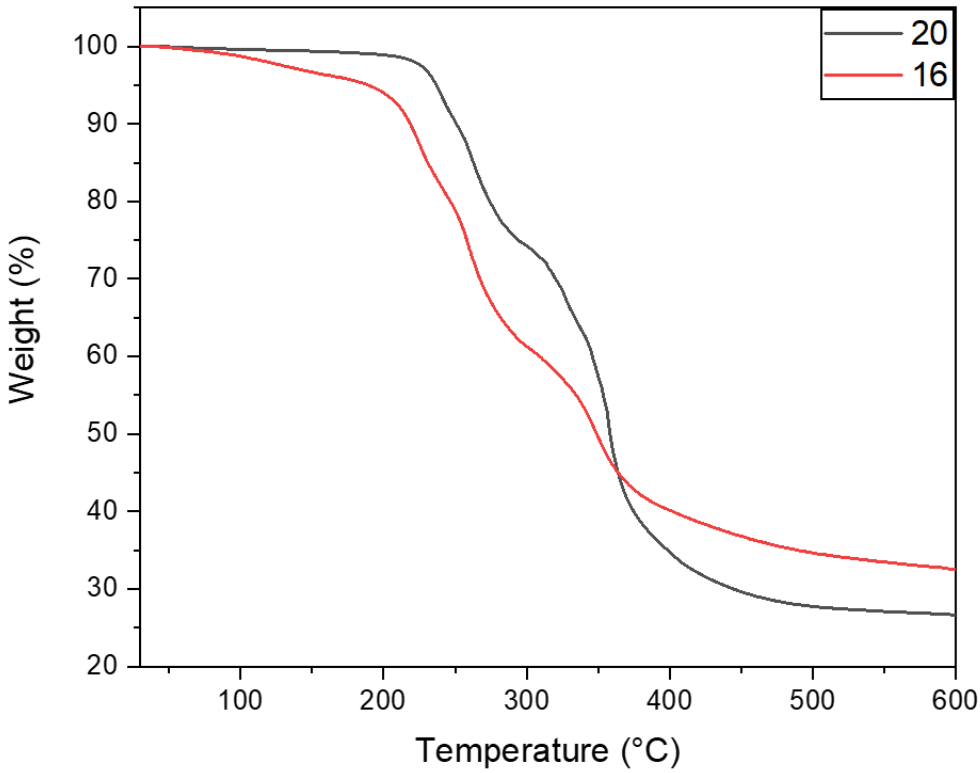

Figure 2.23 TGA curve of compounds **16** and **20** (as-synthesized powder products).

2.5 Synthesis of Ti(3,4-dihydroxybenzoic acid)$_3$ Linkers

2.5.1 Synthesis Methods

The synthesis of the tris-(3,4-dihydroxybenzoic acid) titanium complex is similar to the synthesis of **L3-Si/Ge**. The titanium source was from $Ti(OiPr)_4$ to give $[Et_3NH]_2$[**L3-Ti**] (**22**) through the reaction with 3,4-dihydroxybenzoic acid and Et_3N. The product can be readily obtained by simple filtration, and the synthesis procedure is listed in Scheme 2.4 below.

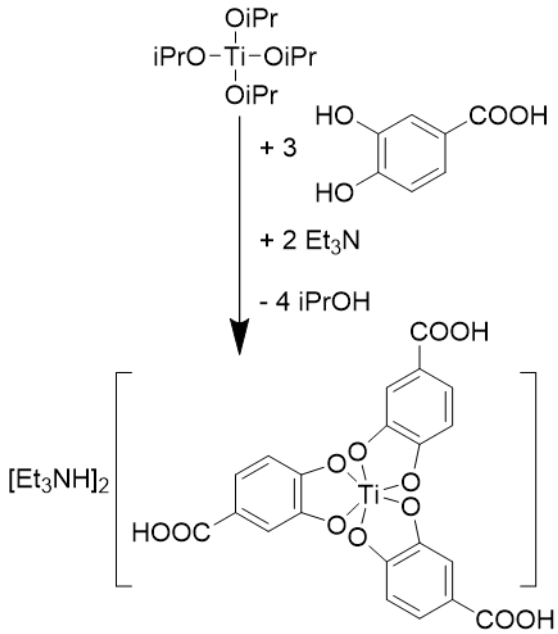

Scheme 2.4 Synthesis procedure of $[Et_3NH]_2$[**L3-Ti**].

2.5.2 Characterization and Structure Description

Treatment of $Ti(OiPr)_4$ with Et_3N and 3,4-dihydroxybenzoic acid affords compound **22**. ^{1}H NMR studies revealed that **22** displayed five sharp peaks from triethyl ammonium cations (1.17 and 3.09 ppm) and the anion (6.03, 6.56, and 7.07 ppm). Two broad peaks at 8.85 and 11.59 ppm from N**H** and COO**H** respectively, were observed as well, and the ratio of the Ti anion to ammonium cations was 1:2. MS-ESI study showed the $[L3\text{-}Ti+H]^-$ ion was observed at 504.9891 (calcd. 504.9892).

In order to study the detailed structure, dark brown plate-shaped single crystals of **22** were obtained through the vapour diffusion method by slow diffusion of Et_2O into a DMF solution containing **22**. SCXRD studies revealed that compound **22** crystallized in the monoclinic *C*2/*c* space group, with a formula of $[(C_{21}H_{12}O_{12}Ti)(C_6H_{16}N)_2]$. Each asymmetric unit contains half of the formula, and each unit cell contains four formula molecules. The central Ti atom in the anion forms a distorted octahedral geometry by coordinating with three deprotonated phenol di-hydroxy groups originating from three catechols. The Ti-O bond lengths are in the range 1.947(3) to 1.989(3) Å, with the bond angle of adjacent and opposite O-Ti-O units spanning from 78.96(17) to 100.84(13)° and 163.2(2) to 163.57(13)° respectively. These values are slightly different from SiO_6/GeO_6 type compounds but align consistently with the values found in other reported TiO_6 type compounds.[288-290] One COOH group is disordered over two different positions (50:50 occupancy).

Intermolecular H-bonds were found between the O1, O2 atoms from the TiO_6 centre and ammonium N-H21, with N(H)···O-Ti distances between 3.023 and 3.067 Å. H-bonds were also observed between the O atoms on the TiO_6 centre and adjacent COOH groups, with O(H)···O-Ti distances ranging from 2.647 to 2.812 Å [O4(H4)···O11 and O13(H13)···O2]. The extension of such H-bond arrangements leads to a H-bonded metal-complex framework, with a 2D layered structure (Figure 2.24). However, *PLATON*[265] estimates that there is no solvent-accessible void space due to the dense packing of the molecules.

The phase purity of the bulk powder was checked through PXRD studies, revealing a close match with the simulated pattern (Figure 2.25). TGA results (as-synthesized powder product without further treatment before TGA measurement) suggested that compound **22** remained stable until about 240°C before decomposition (Figure 2.26). This decomposition temperature is similar to that found for compounds **16** and **20** (see Chapter 2.4).

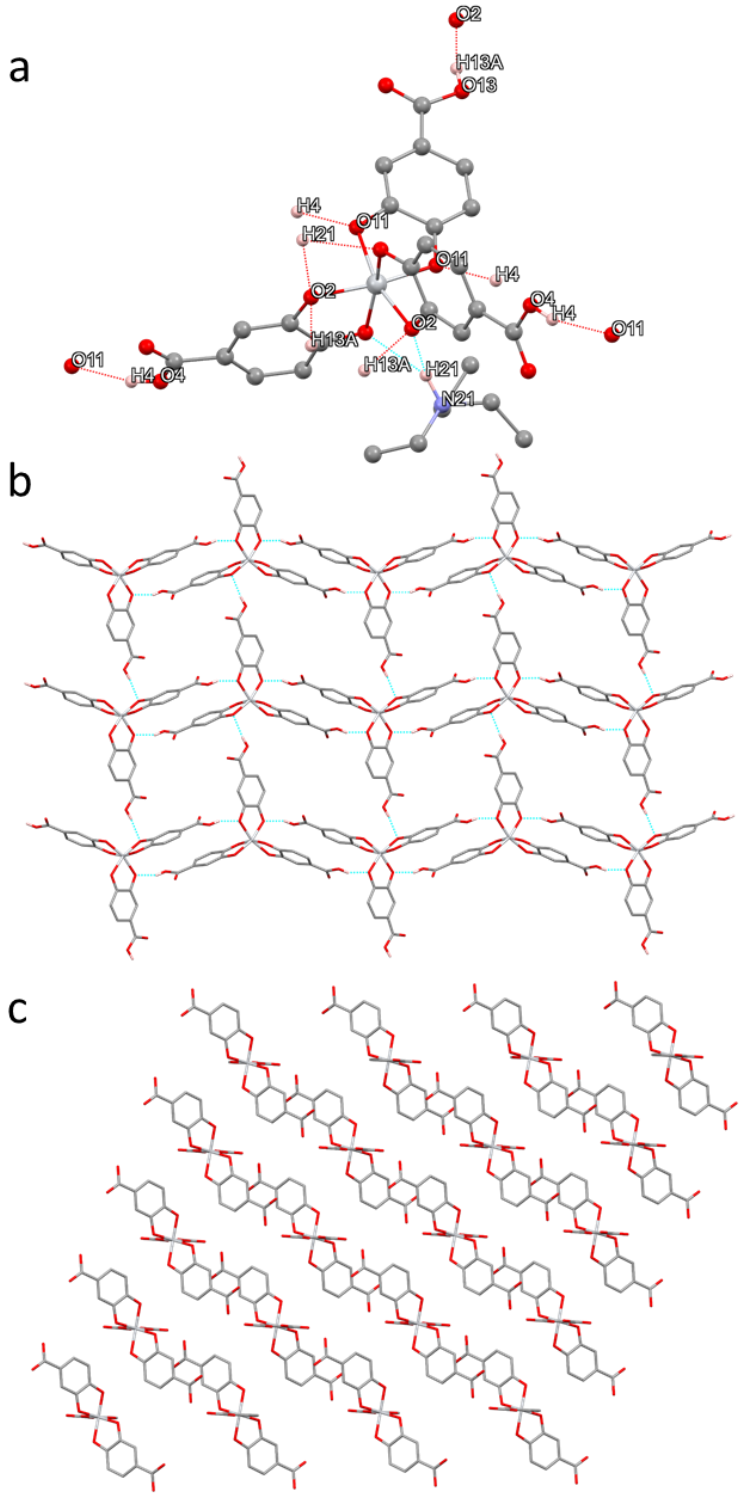

Figure 2.24 a) crystal structure and H-bonds' environments of compound **22**; b) H-bond linked 2D layered structure; c) packing diagram from (0 1 0) view. C: grey, O: red, N: night blue, Ti: light grey, H: pale pink. Only H-bonded H atoms are shown for clarity; ammonium cations are not shown in b and c.

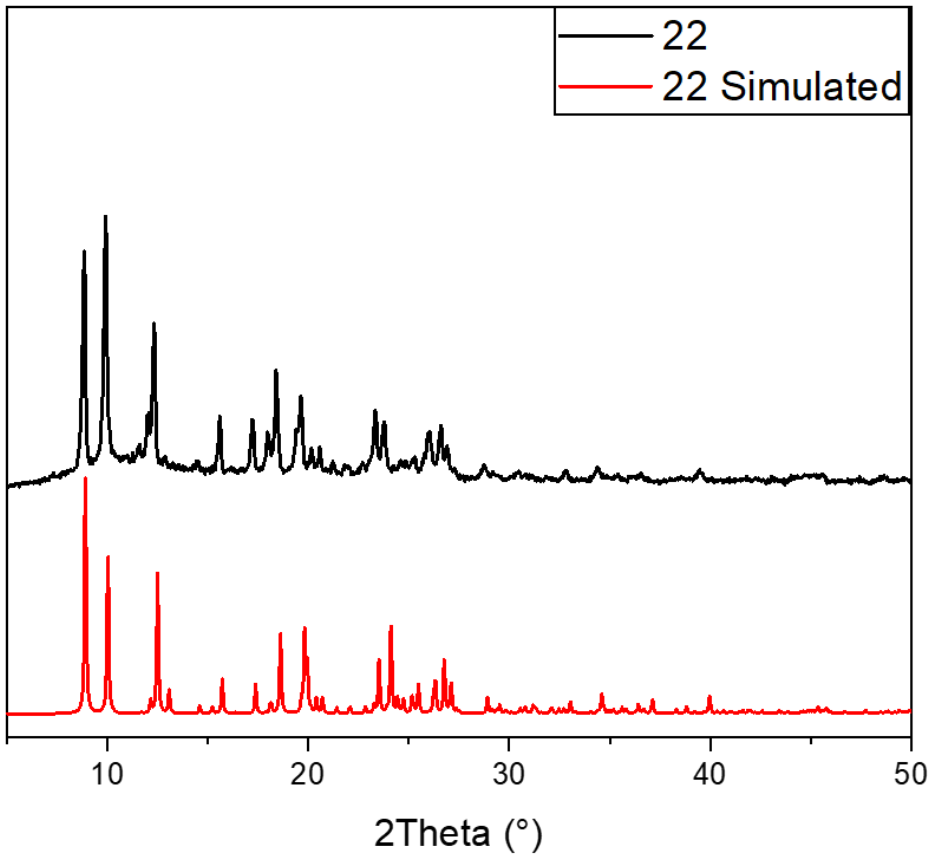

Figure 2.25 PXRD pattern of compound **22** (simulated and experimental).

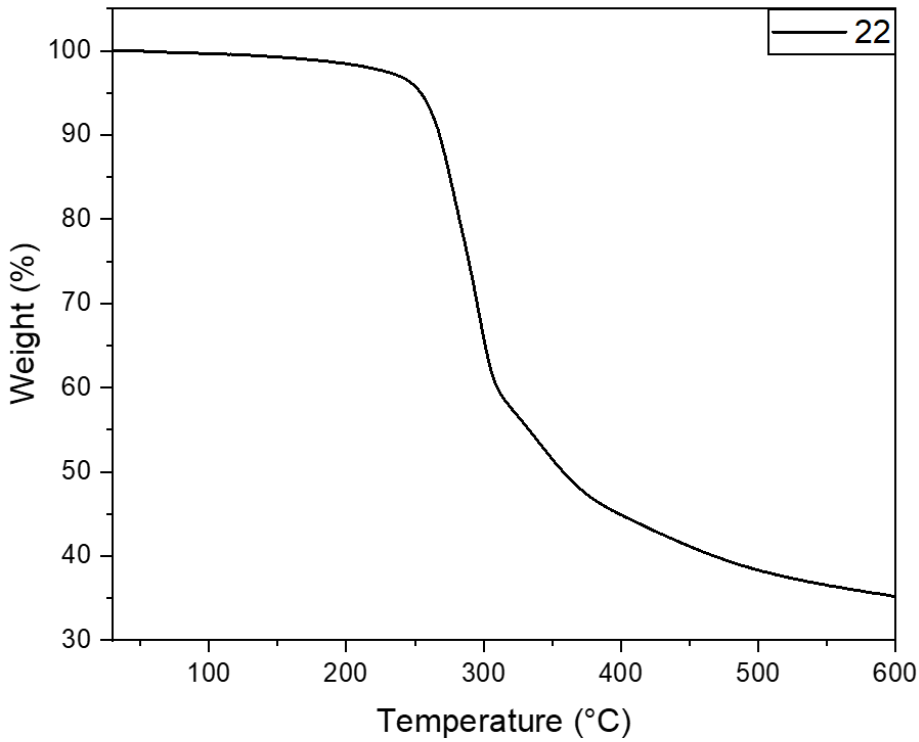

Figure 2.26 TGA curve of compound **22** (as-synthesized powder product).

Attempts to synthesize a tris-(3,4-dihydroxybenzoic acid) titanium complex were carried out following the protocol reported by Zhang and co-workers.[291] The hydrothermal reaction of the acid with piperazine (pip) and $Ti(OiPr)_4$ afforded compound **23** as dark brown blade-shaped crystals. ^{1}H NMR spectra indicated that there are only two types of protons in the benzene ring, and the ratio of the linker to the pip cations was 2:1. In order to investigate the structure further, a single crystal of compound **23** was selected for SCXRD analysis. The results indicated that there is no COOH group presented on the benzene ring. Mechanisms involved in this decarboxylation process are not clear, but it could originate from the catalytic reaction using TiO_2 which may be generated from the hydrolysis of $Ti(OiPr)_4$.[292]

Compound **23** crystallized in the triclinic *P*-1 space group. Each asymmetric unit contains one $Ti(cat)_3^{2-}$ anion (cat = catechol), one diammonium cation and one water molecule, which equals one formula $[Ti(cat)_3 \cdot H_2pip \cdot H_2O]$, and there are two formula molecules in each unit cell. The Ti atom in the anion sits in a distorted octahedral geometry with Ti-O bond lengths falling between 1.9332(18) and 2.003(2) Å, and the adjacent and opposite O-Ti-O angles sit in the ranges79.49(8)-103.04(8)° and 163.00(9)-165.91(9)°. These values are in good agreement with those for compound **22** and other TiO_6-type compounds.[288-290]

Intermolecular H-bonds were observed in the structure between ammonium cations, linker anions and water molecules. The 2D sheet structure extended across the crystallography *boc* plane through the H-bonds among O atoms from the linker central TiO_6 group, N-H from pip cations, and water molecules (Figure 2.27). However, *PLATON*[265] calculated that there is no solvent-accessible void space in compound **23**, which is due to the dense packing of the structure. The PXRD pattern of **23** matched the calculated pattern well, indicating that the bulk product was a pure phase. (Figure 2.28).

The composition of compound **23** is similar to the previously reported compound $[Ti(cat)_3 \cdot H_2pip \cdot 8H_2O]$ (CSD refcode LEXQUD, Table 2.4),[291] but the difference in the total number of water molecules in the unit cell significantly affects the packing. This distinction can be recognized through the calculated PXRD results of the two compounds (Figure 2.28).

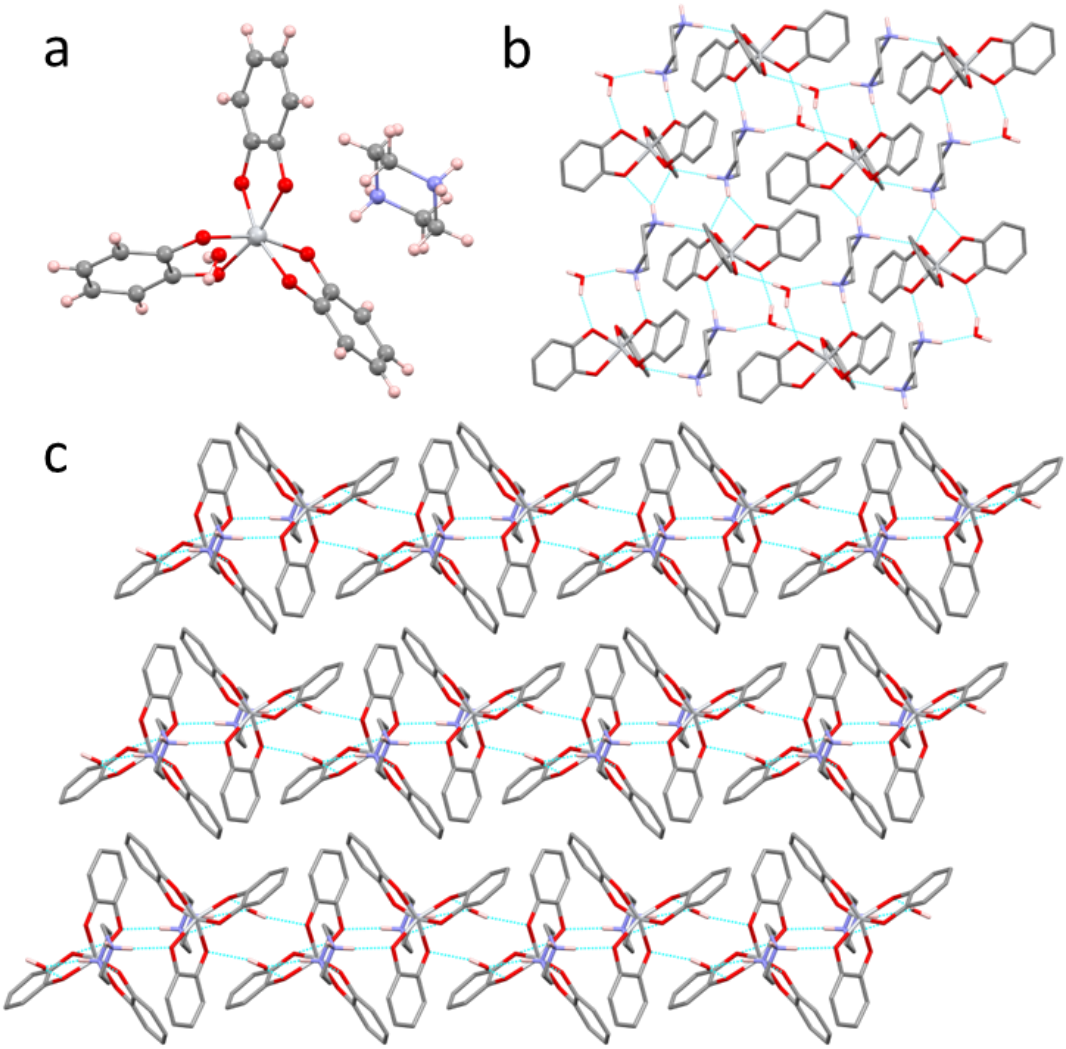

Figure 2.27 a) crystal structure of compound **23**; b) H-bond linked 2D layered structure; c) packing diagram from (0 1 0) view. C: grey, O: red, N: night blue, Ti: light grey, H: pale pink. Only H-bonded H atoms are shown in b and c for clarity.

parameters	Compound **23**	**LEXQUD**
Crystal system	Triclinic	Monoclinic
Space group	*P*-1	*I* 2/*a*
a/Å	10.3771(3)	11.8798(6)
b/Å	10.3813(2)	14.7918(10)
c/Å	10.6564(3)	16.3248(8)
α/°	94.673(2)	90

β/°	103.798(2)	95.779(5)
γ/°	100.929(2)	90
V/Å^3	1084.94(5)	2854.07
Z	2	4
Z'	1	0.5

Table 2.4 Crystallography data of compound **23** and **LEXQUD**.

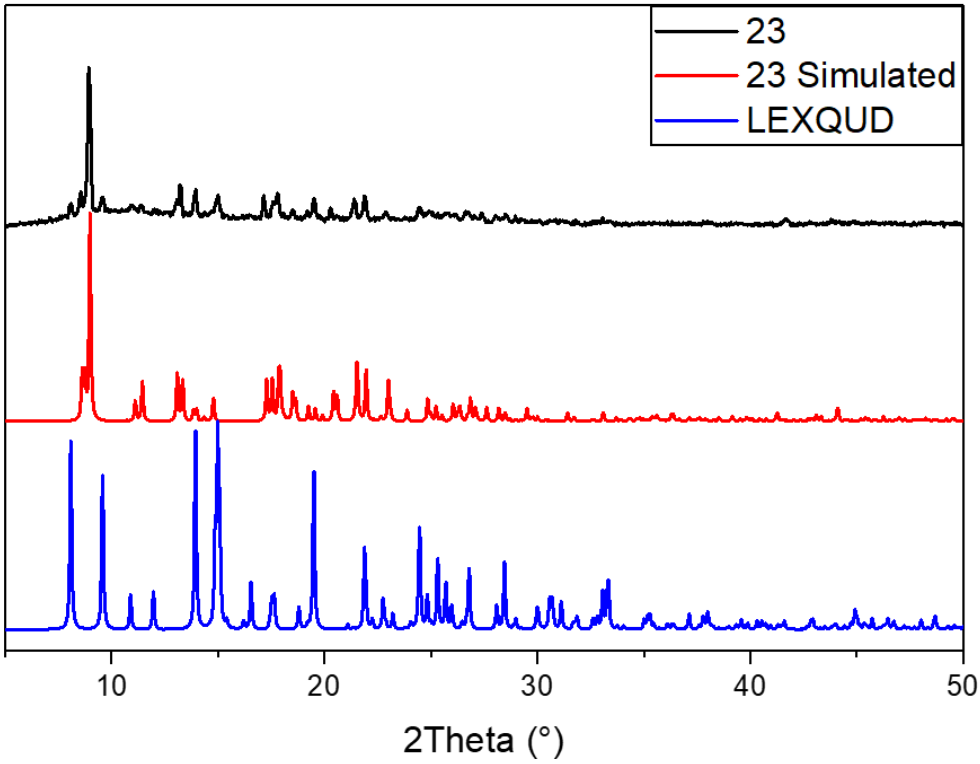

Figure 2.28 PXRD pattern of compound **23** (simulated and experimental) and LEXQUD.

2.6 Synthesis of 4,5-Dihydroxyphthalic Acid

The use of dihydroxybenzoic acid in linker synthesis has been proven feasible, as demonstrated in the preceding text. It is then assumed that the linker anions with high symmetry may reduce the disorder in the crystal system, for example, the presence of two COOH groups on the catechol ring may reduce the overall disorder in compound **16**. Such a compound, 4,5-dihydroxyphthalic acid (**24**), was first reported in 1891 and was prepared from the demethylation reaction of 4,5-dimethoxyphthalic acid (**25**) using concentrated hydroiodic acid.[293] Although various methods can be employed to synthesize compound **24**, in most cases the intermediate compound involves terephthalic acid derivatives. The heteroatoms or functional groups are replaced with OH through a substitution reaction in the final step to give **24** (using acetic acid, HI or PCl_5).[293-295] Considering all these methods, a dimethoxybenzene-based compound was chosen as the starting material, because it can be oxidized in a feasible large-scale reaction to yield compound **25**. Therefore, the first step aims to prepare 4,5-dimethoxy benzene derivatives as illustrated below in Scheme 2.5.

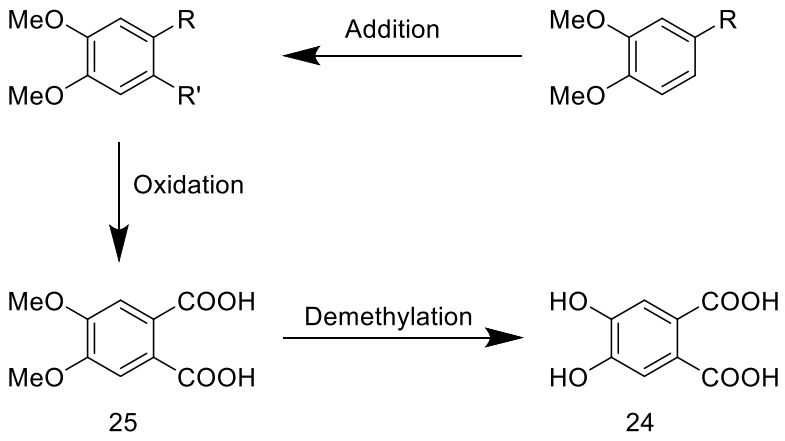

Scheme 2.5 Proposed synthesis method for compound **24**.

The formylation reaction is a powerful way to introduce a formyl group onto a phenyl ring. Formylation agents, such as dichloromethyl methyl ether, are normally used as the source of the aldehyde group, and electrophilic aromatic substitution is often involved in such reactions.[296] 3,4-Dimethoxytoluene was first chosen in an attempt to produce 4,5-

dimethoxy-2-methyl benzaldehyde (**26**, Scheme 2.6). The methoxy group can act as an electron-donating group, which will facilitate the reaction. Treatment of 3,4-dimethoxytoluene with dichloromethyl methyl ether in the presence of $SnCl_4$ affords **26**. Compound **26** was analysed by ^{1}H NMR spectroscopy and shown to exhibit six peaks (see SI) which are consistent with the literature.[297] This compound was then treated with K_2CO_3 and $KMnO_4$ in an aqueous solution to yield compound **25**. However, the oxidation reaction was not complete when carried out under the literature conditions, resulting in a mixture containing the product **25**, mono-oxidized compound and other unidentified compounds as revealed by ^{1}H NMR studies. It should also be noted that the mixture was obtained on a small scale, hence further operations were not conducted.

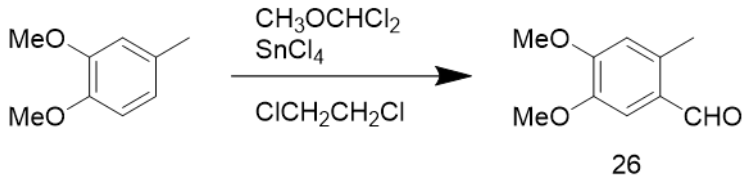

Scheme 2.6 Synthesis procedure for compound **26**.

An alternative reaction involved the treatment of 3,4-dimethoxy benzoic acid with paraformaldehyde in a hot concentrated HCl solution to afford 5,6-dimethoxyphthalide (**27**).[298] Compound **27** was confirmed by ^{1}H NMR spectroscopy showing five peaks (see SI) due to the unsymmetric structure of the phthalide. This product was obtained on a gram scale with high purity, hence it was used directly in the second oxidation step. A slightly modified condition was utilized by the reaction of **27** with $KMnO_4$ in an aqueous solution containing NaOH.[298] The crude product was isolated, and ^{1}H NMR spectra indicated that the crude product contained **27**, **25**, and other minor impurities. The mixture was then treated with $NaHCO_3$ solution to dissolve acidic compounds (**25**). The unreacted **27** and other impurities were insoluble and then removed by extraction with EtOAc, and the aqueous solution containing deprotonated **25** was then acidified with HCl and extracted by EtOAc. This organic solvent was then removed under reduced pressure to yield compound **25**.

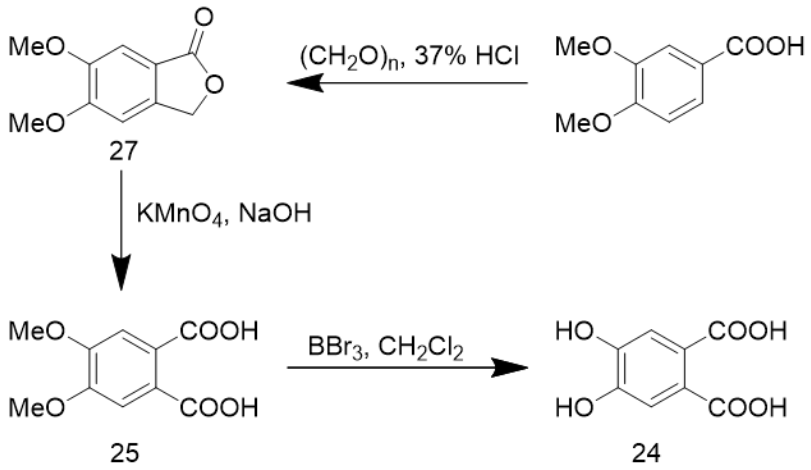

Scheme 2.7 Synthesis procedure of **24** using paraformaldehyde.

The slow evaporation of an acidified solution of **25** (1M HCl) afforded colourless block-like needle crystals which were then studied using SCXRD. Compound **25** crystallises in the monoclinic $P2_1/c$ space group. Each unit cell contains four molecules sitting in parallel planes, with a distance of approx. 3.6 Å between each layer. The presence of neighbouring COOH groups facilitates the formation of both intermolecular and intramolecular H-bonds (Figure 2.29). The intramolecular O(H)···O distance is 2.450 Å, with an almost linear O-H-O angle of 177.10°. The intermolecular H-bond length between O(H)···O is slightly longer than the intramolecular one with a distance of 2.621 Å, while the O-H-O angle is slightly smaller (170.48°). The extension of the H-bonds between adjacent molecules led to the formation of a linear chain along the crystallographic (0 1 0) direction.

PXRD results indicated that compound **25** exhibits a high level of crystallinity and was in good agreement with the simulated pattern generated from the single crystal data (Figure 2.30). The slight peak shift may be due to the temperature difference in the data collecting process, where the crystal data was collected at 173 K, and experimental data was obtained at RT (298 K). The lower temperature may cause a decrease in the cell length, thus causing the peak positions to shift to higher 2Theta values.[299]

The final step to convert **25** to **24** involves a demethylation reaction. Several different methods were attempted, including the use of LiCl and pTSA in a solvent of NMP, a dry

method involving $AlCl_3$ and NaI, reflux with AcOH and HBr, and BBr_3 in CH_2Cl_2.[300-303] After several attempts, the product was only identified through the reaction with BBr_3 in CH_2Cl_2. The presence of compound **24** was confirmed by ^{1}H NMR spectroscopy with peaks located at 7.01, 9.79 and 12.82 ppm (Figure 2.31). However in practice, the product was a viscous liquid and contained numerous impurities, further purification procedures were not carried out.

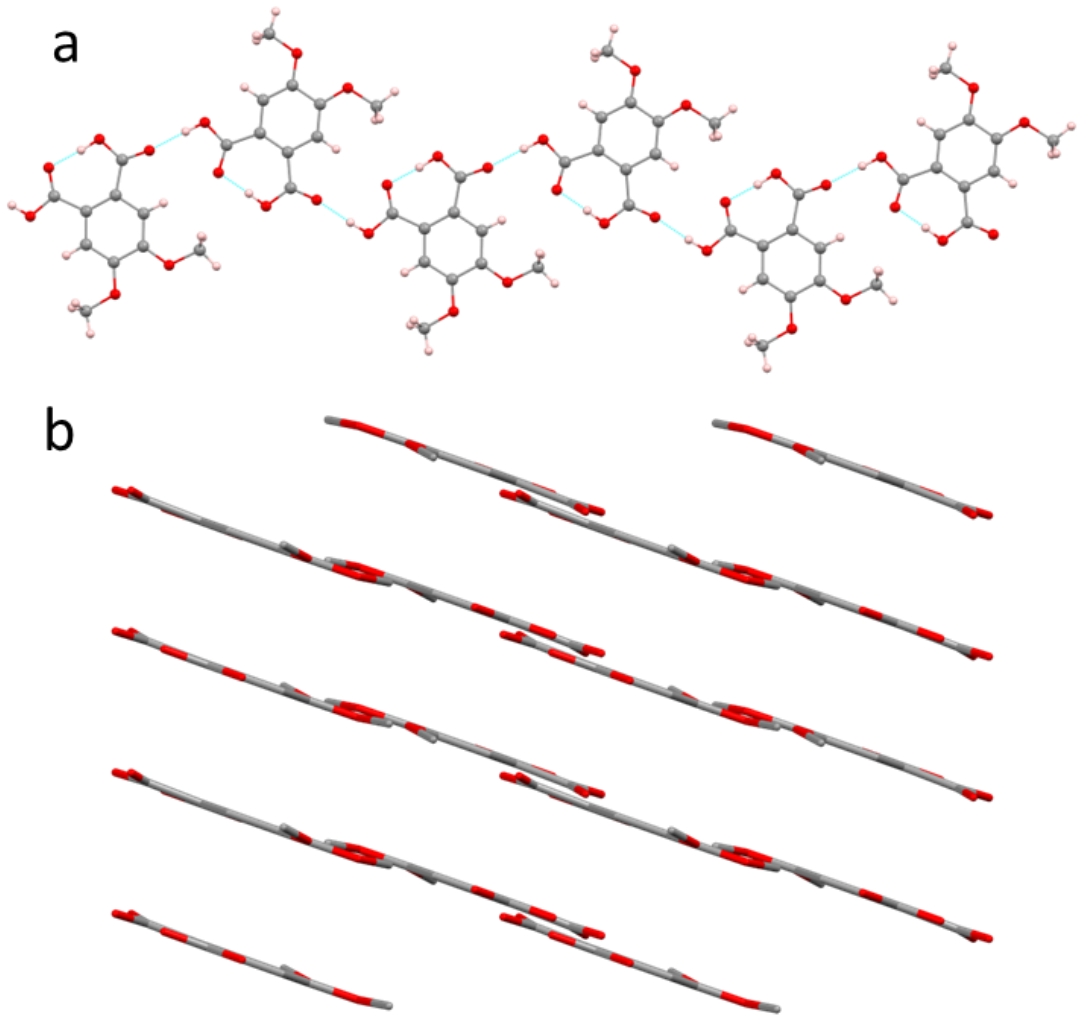

Figure 2.29 a) Crystal structure of compound **25** showing both intra and intermolecular H-bonds and 1D chain; b) packing diagram along (0 1 0) view, showing parallel planes. C: grey, O: red, H; pale pink. H atoms are not shown in b for clarity.

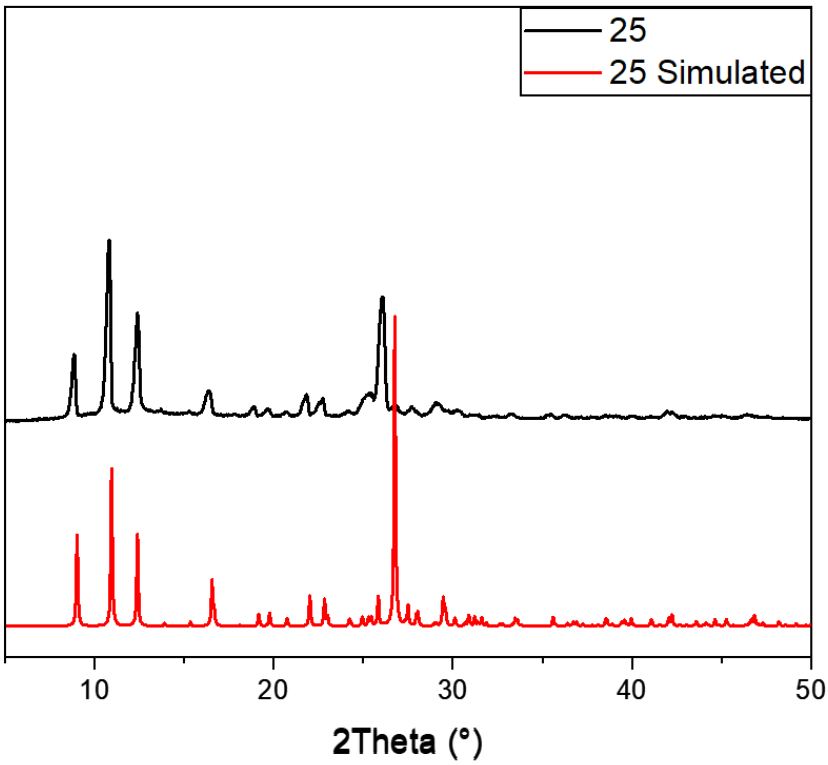

Figure 2.30 PXRD pattern of compound **25** (simulated and experimental).

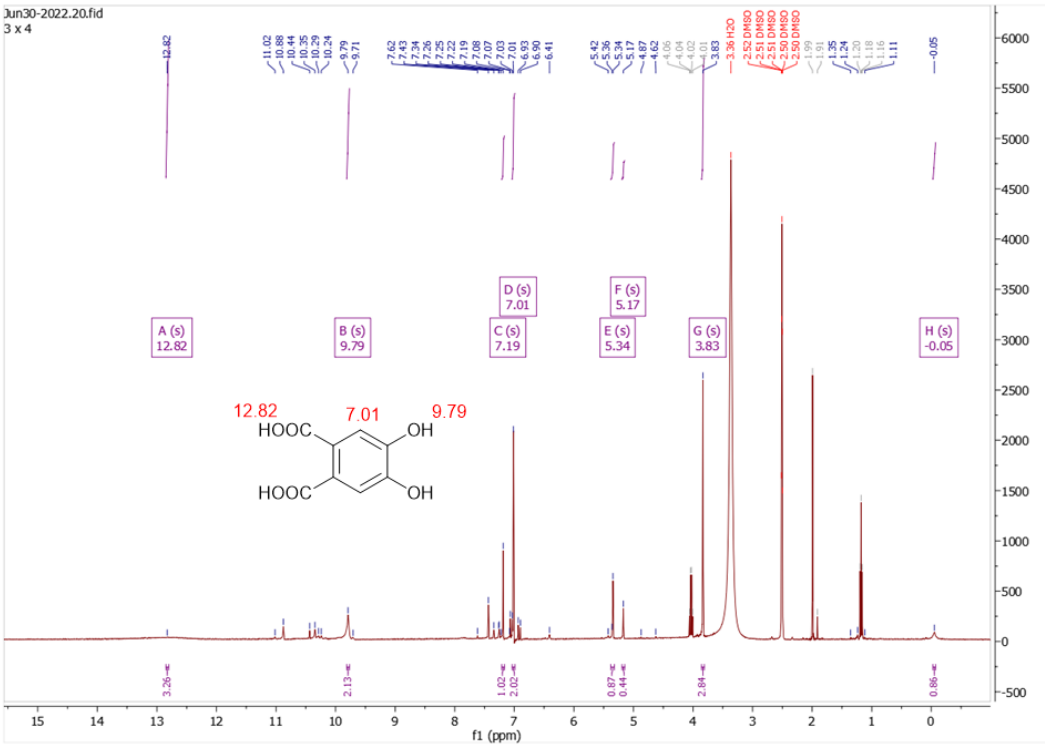

Figure 2.31 ^{1}H NMR (DMSO-D_6) spectra confirming the presence of compound **24** along with impurities.

2.7 Conclusions

In summary, three types of potential linkers have been successfully prepared (Table 2.5). The L1 linker was prepared following the same method as the literature but with a different range of ammonium cations, while the methods for L2 and L3 synthesis were slightly modified compared to the known tris-catechol compound. A total of twenty-two compounds have been prepared and characterized using various techniques, such as NMR, PXRD. All Si compounds exhibit characteristic peaks in their ^{29}Si NMR spectra. PXRD results indicate that the difference in the anion central atom (Si/Ge) does not affect the overall structure when an identical ammonium cation is present. Crystals of some complexes were obtained, and their structures were analysed through SCXRD. H-bonds are formed between the ammonium cation and linker anion, and the presence of multiple H-bond donors in L1, such as TMEDA cations in compounds **5** and **9**, and neighbouring carboxylic acid group in L3, such as compounds **16**, **20**, and **22**, facilitates the formation of extended H-bonded networks. The introduction of a metal ion in the H-bond motif may allow the formation of 3D frameworks when the metal complex combines with other H-bond acceptors or donors. In addition, the replacement of the COOH group with the CHO group (3,4-dihydroxybenzoaldehyde) in L3-type linkers makes the new compounds promising candidates for the formation of imine bonds,[232] thus facilitating the formation of novel 3D COF when reacting with primary amine compounds,[304] and these works could be further explored.

While the L1- compounds were synthesized following the literature procedure, L2- and L3-compounds have not been reported before. Therefore, this work contributes to the field of hexacoordinate Si/Ge/Ti families. All three types of anions are identified as potential building blocks for MOF synthesis due to the chelating ability of the oxalate or carboxylate groups. In the next chapter, MOF synthesis using the linkers described above will be demonstrated and discussed.

Compound number	Anion	Cation	X-ray structure	Figure
1	L1-Si	Et_4N	-	-
2		n-Bu_4N	-	-
3		Et_2NH_2	-	-
4		Et_3NH	-	-
5		H_2TMEDA	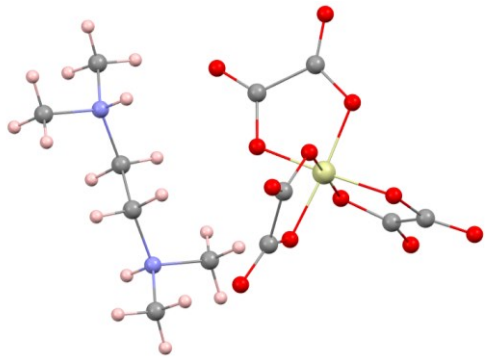	2.10
6		H_2TMPDA	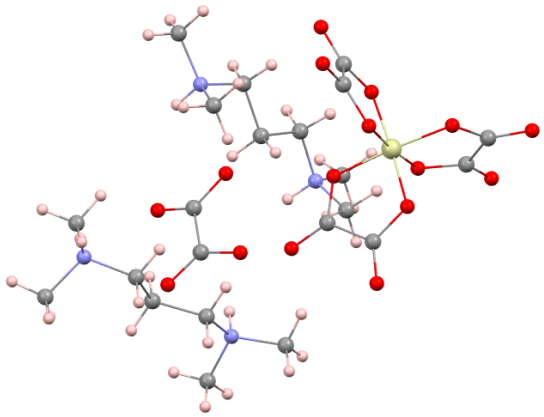	2.13

7		H_2TMBDA	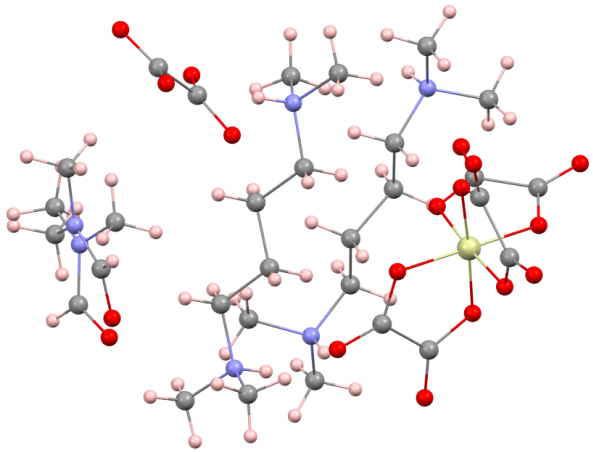	2.15
8	L1-Ge	Et_3NH	-	-
9		H_2TMEDA	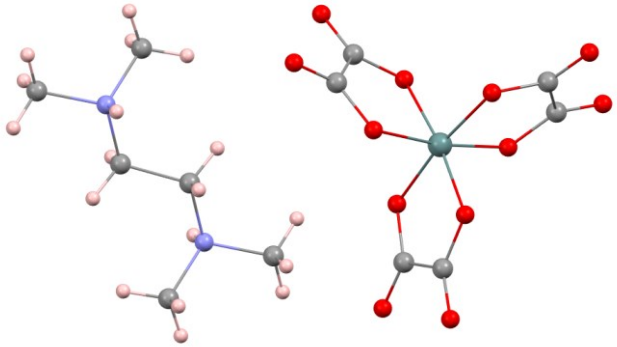	2.11
10		H_2TMPDA	-	-

11		H_2Bipy	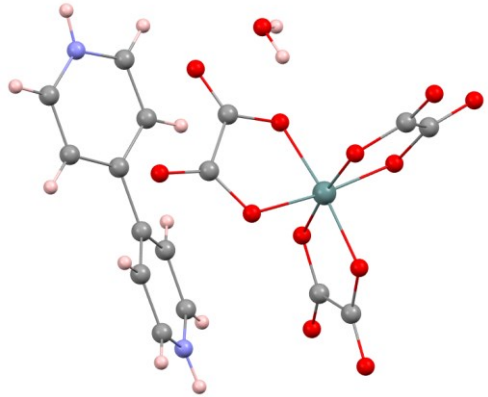	2.17
12		Gu	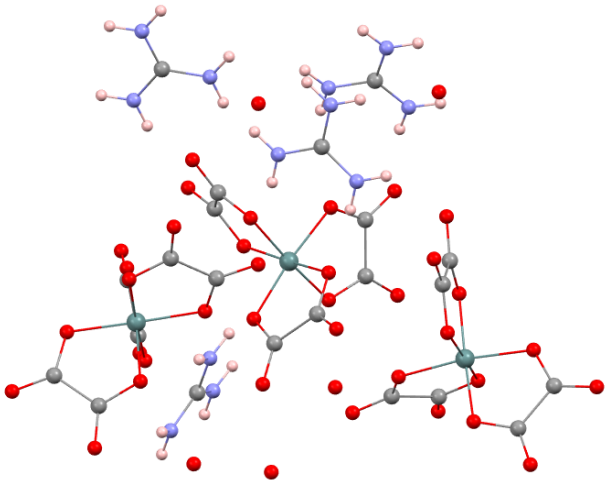	2.19
13	L2-Si	Et_3NH	-	-
14		HDMAE	-	-
15	L2-Ge	Et_3NH	-	-

16	L3-Si	Et_3NH	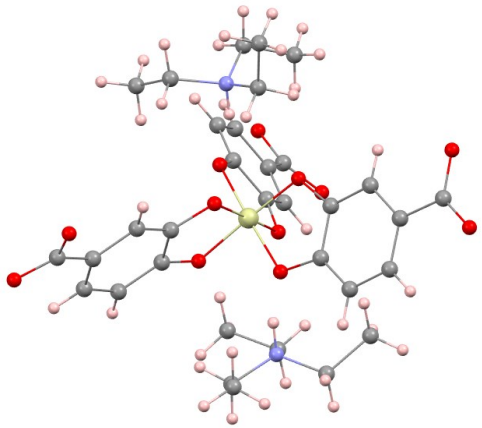	2.20
17		Et_2NH_2	-	-
18		HDMAE	-	-
19		HDMAP	-	-
20	L3-Ge	Et_3NH	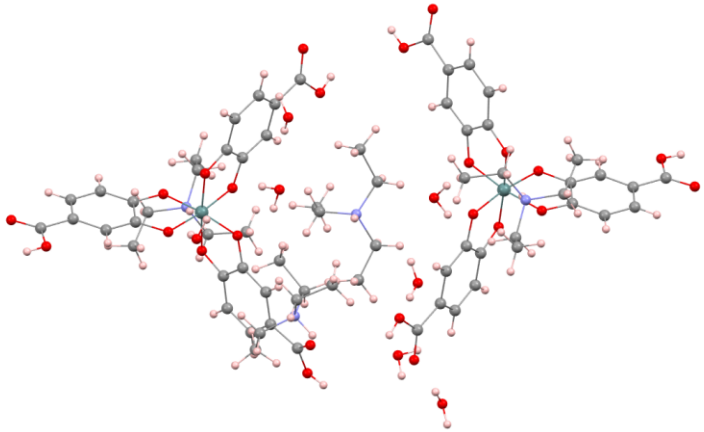	2.22
21		Et_2NH_2	-	-

22	L3-Ti	Et_3NH	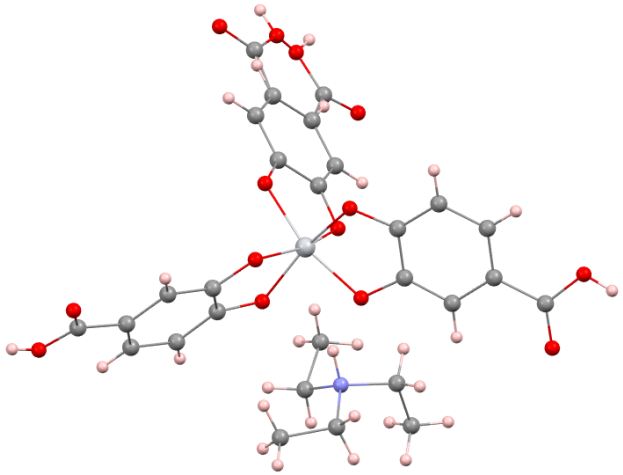	2.24
23	$Ti(cat)_3$	H_2pip	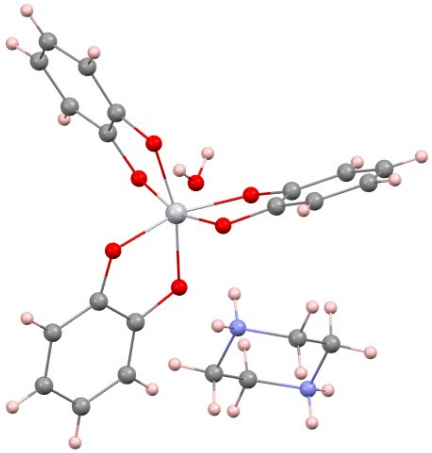	2.27
24	4,5-dihydroxyphthalic acid		-	-

25	4,5-dimethoxyphthalic acid	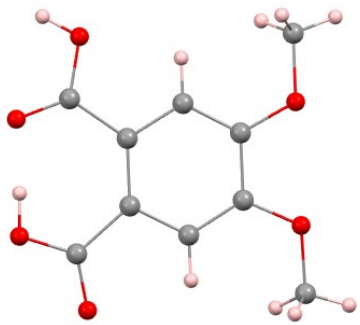	2.29
26	4,5-dimethoxy-2-methyl benzaldehyde	-	-
27	5,6-dimethoxyphthalide	-	-

Table 2.5 Summary of all compounds synthesized in this chapter.

Chapter 3: Metal-Organic Frameworks Constructed using a Hexacoordinate Ge Linker

3.1 Introduction

The utilisation of hexacoordinate Ge ligands in MOF construction remains a rare occurrence in the literature. There are 216 hits for MOF structures containing Ge ligands, as recorded under the CCDC MOF subset (up to November 2023), among them only 47 structures feature a GeX_6 unit. In these instances, the Ge atom coordinates with either six neighbouring atoms to form GeO_6,[235, 236, 305] GeF_6,[132, 211, 306] or $GeNO_5$[307] units, or with other Ge or heteroatoms to form clusters, such as Ge_7,[308] Ge_9,[309] Ge_3O_6,[310] Ge_9O_{18},[311] or $GeW_{12}O_{40}$[312] clusters. In addition, these reports mainly focus on structure characterisation, with only a few MOFs being further applied in applications such as gas separation. Despite MOFs being a subclass of CPs, there are still differences between them in terms of synthesis method, porosity, and structural regularity.[313, 314] Generally, the linker used in MOF construction can be either neutral N-based linkers such as bipyridine, or charged carboxylate linkers such as BDC or BTC and their derivatives. Moreover, the presence of void space in MOF structures enables guest molecules to access their interiors and any functional sites in the framework. However, most of the GeX_6 complexes are non-porous, except for the GeF_6-based MOFs. Furthermore, MOFs typically exhibits infinite framework structures, while some of the GeX_6 complexes manifest cluster structures rather than infinite frameworks. Considering all these factors, most of the examples in the CCDC search results are more appropriately classified as CPs, whereas only a few examples feature independent GeF_6 or GeO_6 nodes and are suitable to be categorised as MOFs. The application of hexacoordinate Ge ligands in MOF construction is therefore still limited.

The GeF_6 node has been demonstrated to be a good co-ligand in MOF construction, particularly in the field of gas separation as discussed in Chapter 1. The F atoms in the GeF_6 node tend to bind with metal cations, forming 1D linear -F-Ge-F-M-F-Ge-F-M- chain

structures. The metal cations are then coordinated by pyridine-based ligands to connect these chains, depending on the orientation, generating 2D or 3D frameworks. However, only a limited variety of metals, Co, Ni, Cu and Zn, have been applied in these MOFs.[132, 174, 211, 215, 306, 315] The limited range of metals used and their rigid structures further limit the functional diversities of this type of MOF.

GeO_6-type nodes have been applied in the synthesis of CPs, although examples remain rare. The two examples discussed in section 1.3 have successfully illustrated that the GeO_6-type compound containing carboxylate groups is suitable for MOF construction. The presence of three carboxylate groups in the **L3-Ge** type linker might facilitate the formation of 3D MOFs because the linker can bind to different metal nodes (Figure 3.1) across different chains/layers to generate 3D frameworks. Therefore, the structure of the **L3-Ge** type linker might eliminate the need for a co-ligand and simplify the synthesis process, while yielding novel 3D MOFs.

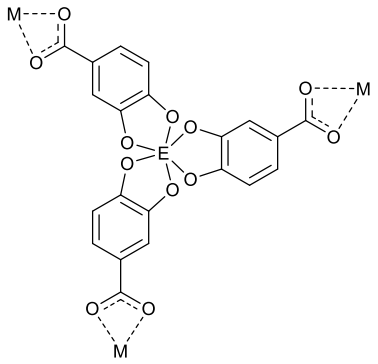

Figure 3.1 Possible coordination mode for L3-type linker (E = Si/Ge).

3.2 Rare Earth Metal-Organic Frameworks (RE-MOFs)

Research on MOF synthesis has extensively covered metals in the -s, -p, -d and -f blocks. These metals exhibit different coordination numbers, potentially resulting in diverse coordination geometries and imparting novel structures and properties to the MOFs. MOFs constructed with Group IIIB metals, which refer to scandium, yttrium, and lanthanide series MOFs (RE-MOFs), have gained attention due to their unique properties and their potential applications.[316] However, previous research has been predominantly focused on lanthanide series MOFs (Ln-MOFs), whereas Sc-MOFs and Y-MOFs are not well explored. There are only 249 and 606 reported structures for Sc-MOF and Y-MOF respectively in the CCDC MOF subset (up to November 2023), which is far less than Ln-MOFs (16168 hits).

The Sc^{3+} cation has a high positive charge, small ionic radius and empty valence orbitals, hence it can be regarded as a hard Lewis acid. Typically, Sc^{3+} cations tend to form six coordinated complexes to give an octahedral geometry, although the coordination number can range from 3 to 9. Sc^{3+} cations tend to coordinate with O-donor ligands such as carboxylate, oxalate or hydroxy groups to form stable complexes.[317] As the lightest transition metal, Sc-MOFs are promising candidates as highly stable materials for gas sorption and catalytic applications.

For example, Zhai and co-workers reported the synthesis of two Sc-soc-MOF: Sc-EBTC and Sc-ABTC, by incorporating carboxylate ligands derived from H_4EBTC (1,1'-ethynebenzene-3,3',5,5'-tetracarboxylic acid) or H_4ABTC (3,3',5,5'-azobenzenetetra-carboxylic acid) respectively in MOF synthesis.[318] As illustrated in Figure 3.2, two types of SBU are observed in Sc-EBTC. SBU1 comprises typical trinuclear $[Sc_3O(COO)_6]$ nodes which are located at six vertices of a cubic cage, whereas the remaining two vertices are occupied by two SBU2 clusters each consisting of a mononuclear ScO_6 unit linked by six monodentate carboxylate groups. Although only SBU1 is presented in Sc-ABTC, the framework connectivity is identical to Sc-EBTC, and both MOFs adopt *soc* topologies. The Sc-EBTC and Sc-ABTC MOFs exhibit permanent porosity, with reported BET surface

areas of 842.5 and 864.1 m^2/g respectively. Both Sc-soc-MOFs have good gas uptake capacities for C_2H_2, C_2H_4 and CO_2, and the selectivity of these gas over CH_4 are 12.5, 11.3, 3.8 for Sc-EBTC, and 14.7, 11.7, 4.3 for Sc-ABTC respectively. These values indicate that these Sc-soc-MOFs are promising candidates for the purification of natural gas.

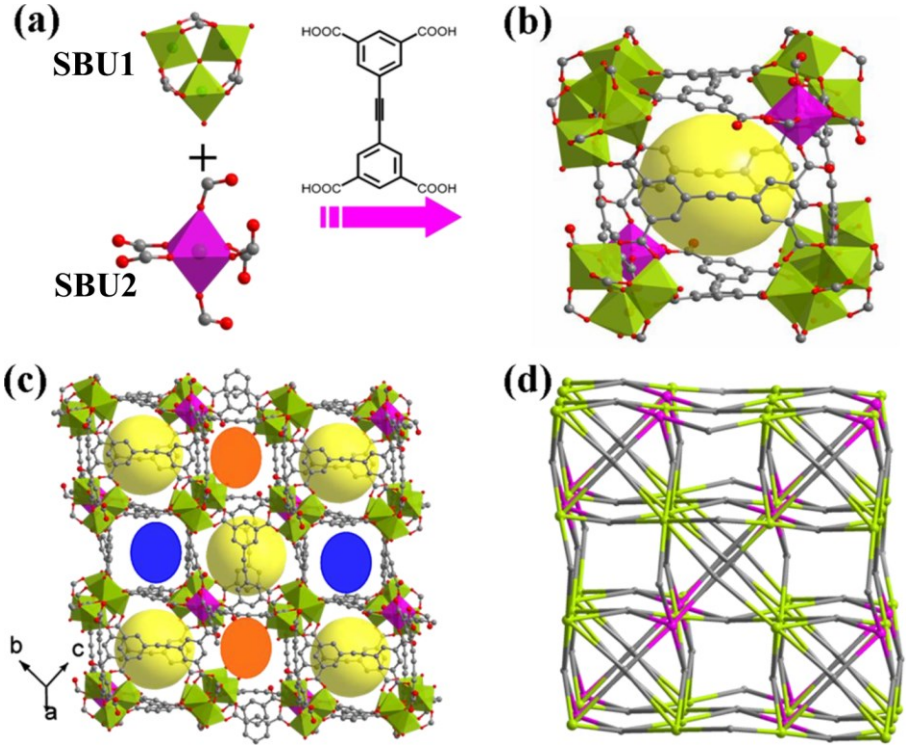

Figure 3.2 Structure of Sc-EBTC, a) two types of SBU and H_4EBTC; b) the cubic cage constructed from six ligand anions, six SBU1 and two SBU2; c) 3D structure of the framework, orange: channel containing coordinating molecules, blue: guest-free channel; d) (4,6)-connected ***soc*** topology framework.[318]

Zhai and co-workers have reported two Sc-MOFs (SNNU-5-Sc and SNNU-150-Sc) through solvothermal reactions of scandium nitrate with H_3TTCA (3,5-bis(4'-carboxylphenyl)benzoic acid, for SNNU-5-Sc) or H_3NTB (4,4',4''-nitrilotribenzoic acid, for SNNU-150-Sc).[319] The same SBU [$Sc_3O(COO)_6$] was observed in these two MOFs, while the difference in linker species resulted in the variation in structures and topologies in each MOF (Figure 3.3). Both MOFs exhibited permanent porosities, wherein the SNNU-5-Sc displayed good C_2H_2 uptake capacity (211.2 cm^3/g), and the SNNU-150-Sc demonstrated outstanding selectivity for C_2H_2 over CH_4 (80.65). Notably, these two MOFs

can retain their structures under harsh conditions in both acidic and basic environments (pH 2 - 12), which can be attributed to the strong coordination bonds between the Sc^{3+} cations and carboxylate groups.

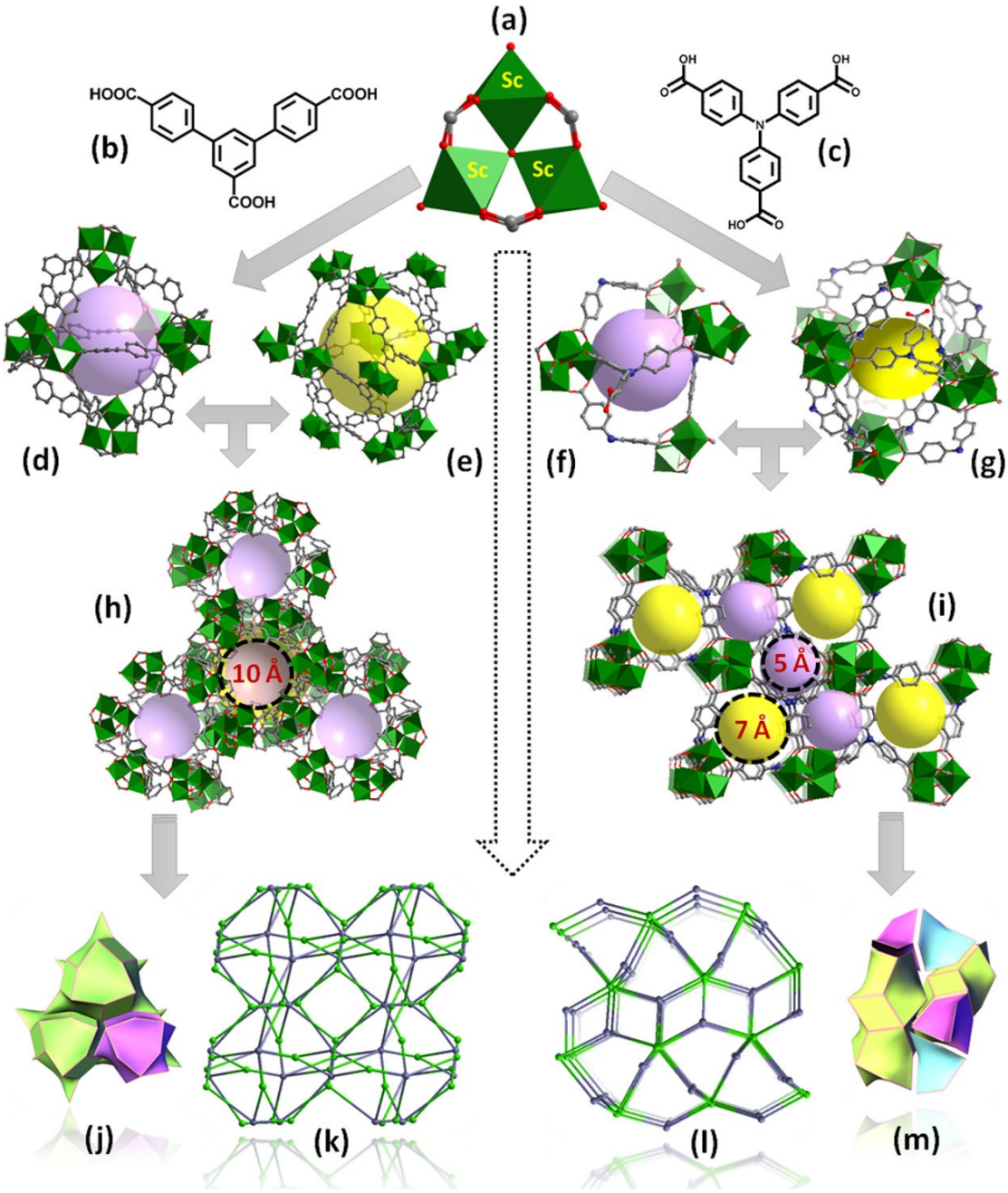

Figure 3.3 Structure of SNNU-5-Sc (left) and SNNU-150-Sc, a) SBU; b,c) H_3TTCA and H_3NTB; d-g) four types of pores; h,i) 3D frameworks of the two MOF; j-m) topology nets and tilings.[319]

A Sc-MOF has also been applied in the field of catalytic reactions. Xu *et al.* reported a Sc-MOF built from the TDC linker (H_2TDC = 2,5-thiophenedicarboxylic acid).[320] The Sc^{3+} cations formed 1D linear chains with adjacent Sc^{3+} cations linked by three di-monodentate carboxylate groups (Figure 3.4). The framework retained its original structure after thermal and vacuum activation, and then the activated Sc-MOF was employed in Strecker-type reactions to produce α-aminonitriles. In the reaction of N-benzyl benzaldimine and trimethylsilyl cyanide, the yield could exceed 99% after 75.5 h when the Sc-MOF was used as the catalyst, whereas it required more than seven times the reaction time with a low conversion yield of 35% without the catalyst. This Sc-MOF showed excellent catalytic performance and can be utilized as a reusable heterogeneous catalyst.

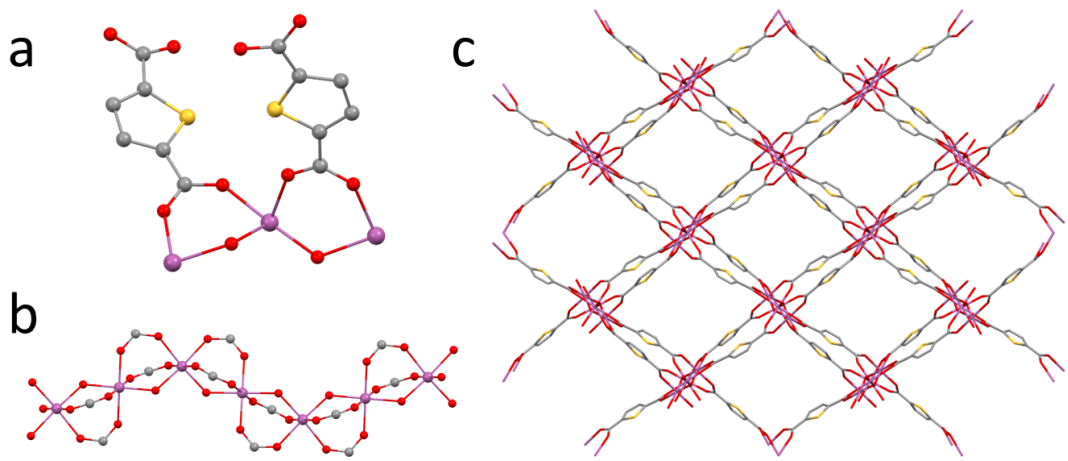

Figure 3.4 a) crystal structure of the Sc-MOF built from TDC linker (asymmetric unit); b) 1D linear chain; c) packing diagram along *a* axis. C: grey, O: red, S: yellow, Sc: pink. Figure drawn using published crystal data from Xu and co-workers (CSD refcode: VUCHEJ).[320]

Despite the relatively greater number of reported Y-MOF than Sc-MOF, research on Y-MOF based applications is still limited compared to other d-block and lanthanide MOFs. The Y^{3+} ion is also classified as a hard Lewis acid and favours the formation of higher coordination number complexes with N- or O-based donor groups, ranging from 3 to 10.[321] Y-MOFs exhibit good performance in gas sorption and separation, catalysis, and in some cases can be used as sensors when integrated into specialised devices.[322]

The purification of methane in natural gas is of great importance. Wang and co-workers synthesized a microporous Y-MOF using H_6TDPAT [H_6TDPAT = 2,4,6-tris(3,5-dicarboxylphenyl-amino)-1,3,5-triazine] as the ligand source.[323] The resulting Y-MOF (Y-H_3TDPAT) exhibited open channels after activation (Figure 3.5), with a selectivity of 77.2 for C_2H_2 over CH_4 77.2 at 298 K and 1 bar, according to Henry's Law. Such high affinity towards C_2H_2 molecules originates from the π-π stacking interactions between C_2H_2 molecules and the triazine groups in the framework, while such interactions were not observed for CH_4 molecules. The outstanding performance in C_2H_2/CH_4 selectivity makes this Y-MOF a promising candidate in natural gas purification applications.

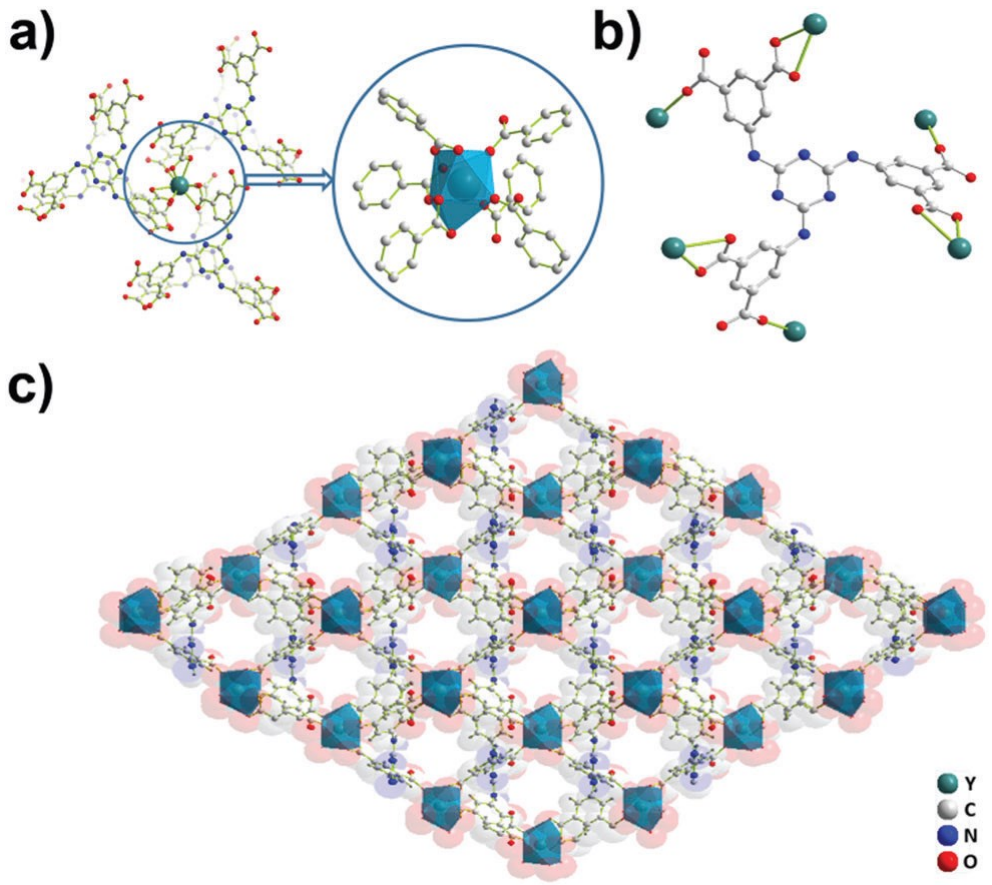

Figure 3.5 Coordination environment of the Y^{3+} cations (a) and ligand anions (b) in Y-H_3TDPAT; c) packing diagram of the Y-H_3TDPAT along *b* axis.[323]

Yttrium-based MOFs are good candidates for catalysis, benefiting from the higher coordination number of Y^{3+} cations. The potential higher coordination numbers provide

extra space, allowing the coordination of Y^{3+} cations with solvent molecules during MOF synthesis. After removing coordinated solvent molecules through activation, the OMS can be accessed by guest molecules. For example, Rodrigues-Dieguez and co-workers designed a Y-MOF (MOF **1**) by combining yttrium nitrate and 3-amino-4-hydroxybenzoic acid.[324] The exposure of OMS was achieved through the removal of coordinated DMF molecules, thus allowing the coordination of guest molecules to the metal cation. In the cyanosilylation reaction of carbonyl compounds, this Y-MOF exhibited remarkable catalytic performance across a broad range of substrates, with conversion yields exceeding 99% (Figure 3.6). These values are far more than those reported values for Ln-MOFs as catalysts which often gave reduced yields. Two possible mechanisms were proposed for this process, and both involved the coordination of carbonyl substrates to the Y^{3+} cations in the first step.

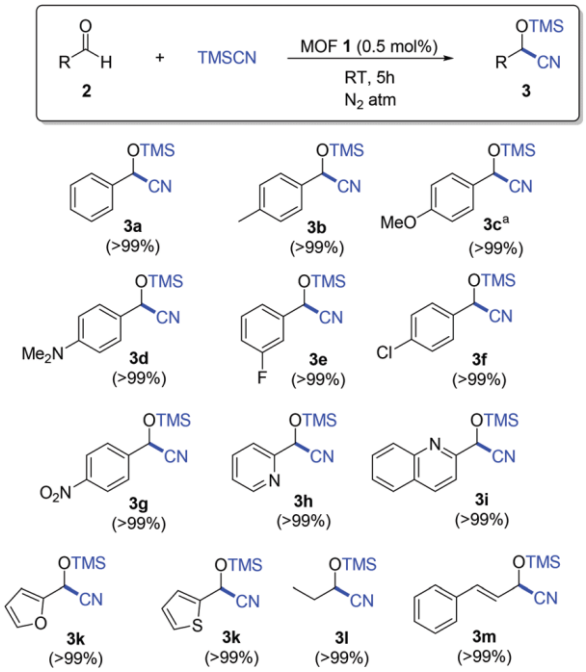

Figure 3.6 Cyanosilylation reactions of some aldehydes with TMSCN (trimethylsilyl cyanide), under optimized conditions (aldehyde **2**: 0.25 mmol, TMSCN: 0.275 mmol, MOF **1**: 2.3 mg, 0.5 mol%, N_2, RT, 5 h).[324]

Research on Ln-MOFs has attracted tremendous interest due to their unique structures and properties arising from the use of lanthanide ions. The higher coordination number facilitates the formation of polynuclear metal clusters, such as hexanuclear, heptanuclear,

and even nonanuclear metal clusters, which are much less commonly observed in d-block MOFs.[325-330] The electron 4f orbital is well shielded by the outer 5s and 5p orbitals, resulting in their properties being unaffected by the surrounding chemical environment. As a result, their unique features remain unchanged when they are integrated into MOF materials, distinguishing themselves through their optical and magnetic properties, in addition to the common applications shared with other MOFs, including gas sorption and separation, and catalysis.

One way to design white light-emitting devices is to combine red, green and blue light emitters.[331] An example can be found in the report by Qian and co-workers.[332] The doping of Tb-MOF and Eu-MOF, which emit green and red light respectively, into the blue-emitting La-MOF [ZJU-1, $Na_3(Ln(PDA)_3)(H_2O)_x$, Ln = La (x = 12), Eu (x = 10) or Tb (x = 9), PDA = tris(pyridine-2,6-dicarboxylate)] gave a white light emission under UV excitation. By finely adjusting the ratio of Tb-MOF and Eu-MOF, this MOF mixture gave white lights with CIE coordinate (0.3269, 0.3123) or (0.3109, 0.3332) when ZJU-1 was dopped with 1.0% Tb-MOF and 2.0% Eu-MOF, or 1.5% Tb-MOF and 2.0% Eu-MOF respectively (Figure 3.7). These values are very close to the pure white light coordinate (0.3333, 0.3333), which could be potentially adopted in light emitting applications.

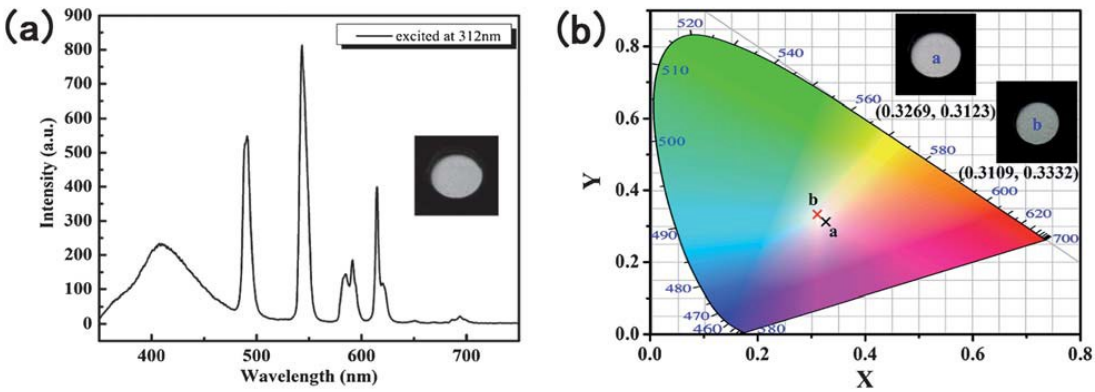

Figure 3.7 a) Emission spectra of ZJU-1 under UV-excitation at 312 nm; b) CIE coordinate of the MOF doped with different ratios of Tb-MOF and Eu-MOF.[332]

NIR luminescent Ln-MOFs can be widely applied in optical telecommunication devices, lasers, invisible inks, barcodes etc.[333-336] For example, Rosi and co-workers designed a Yb-

MOF using H_2-PVDC [4,4'-((2,5-dimethoxy-1,4-phenylene)di-2,1-ethenediyl)bis-benzoic acid] as the linker precursor.[337] Benefiting from the antenna effect of the ligand, the Yb-MOF (Yb-PVDC-1) was found to exhibit NIR at λ_{em} = 980 nm under UV excitation between 370 and 470 nm. It is worth noting that the free di-acid requires higher energy to be excited (310 to 415 nm), while after being incorporated into the frameworks, the presence of neighbouring linker-to-linker interactions in the frameworks leads to the redshift of the excitation range, thus reducing the excitation energy needed.

In a later work, Rosi and co-workers added Er^{3+} ions into the synthesis process of Yb-PVDC-1.[338] The resulting MOF (Er_xYb_{1-x}-PVDC-1) gave two sharp signals (980 and 1530 nm from Yb^{3+} and Er^{3+} respectively) under excitation (Figure 3.8). The emission intensity of these two peaks can be quantitively adjusted through the variation of the Yb^{3+} to Er^{3+} ratio. A spectroscopically readable barcode was then generated using Er_xYb_{1-x}-PVDC-1 luminescent materials.

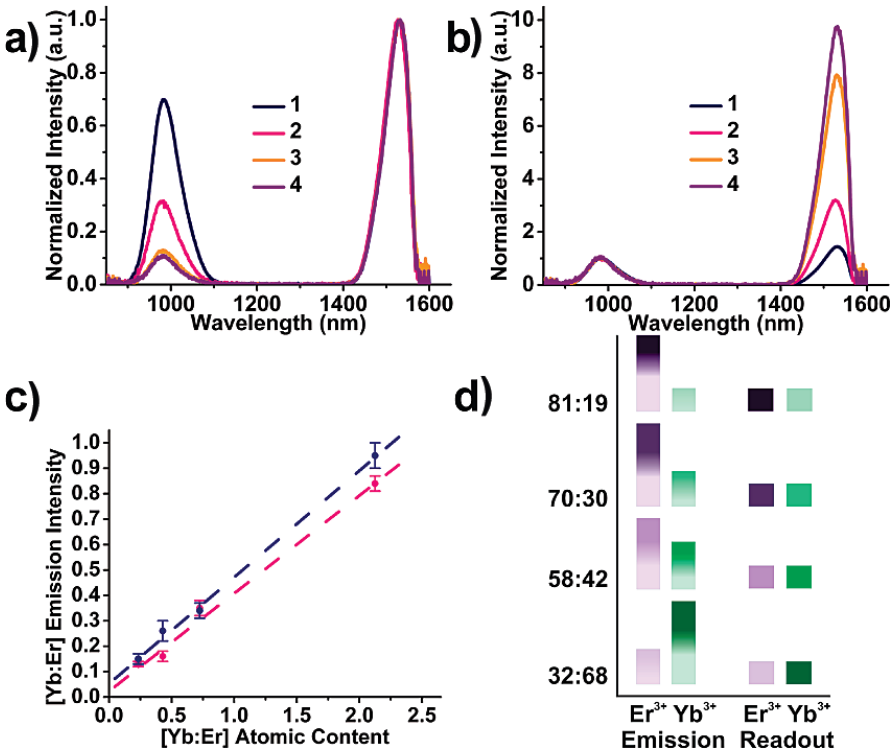

Figure 3.8 a,b) Emission spectra of Yb^{3+} and Er^{3+} (λ_{ex} = 490 nm); c) the ratio of integrated emission intensities and atomic ratio (measured by EDS, blue, λ_{ex} = 370 nm; pink, λ_{ex} = 490 nm); d) Colour-coded schematic of the barcode readout.[338]

Gadolinium-based materials are often used as magnetic resonance imaging (MRI) contrast agents. Lin *et al.* reported a nanosized particle Gd-MOF by stirring a mixture of $GdCl_3$ and bis(methylammonium)benzene-1,4-dicarboxylate in a cetyltrimethylammonium bromide (CTAB)/isooctane/1-hexanol/water system.[339] The obtained Gd-MOF nanorods (NMOF) were characterised by SEM with a rod size of ~100 × 40 nm, and the bulk phase purity was confirmed through PXRD measurement. This NMOF exhibits higher longitudinal (R1) and transverse (R2) relaxivity than the clinically used OmniScan® agent, demonstrating the potential to be applied in MRI contrast agents.

Nanosized MOFs are good candidates in the field of drug delivery for cancer therapy. Compared to traditional chemotherapy and radiotherapy, nanotherapeutic approaches are considered to have benefits such as low system toxicity, increased drug accumulation in tumour tissue, and the capability for surface functionalisation.[340] For instance, Lin and co-workers synthesized a nanoscale Tb-MOF (NCP-1) to deliver a Pt(IV) species as the active drug.[341] These nanoparticles were then coated with a silica shell (NCP-1') to ensure the stability of the MOF upon dissolution in water (Figure 3.9), and the thickness of the silica shell can be controlled by varying the coating time, resulting in NCP-1'-a and NCP-1'-b (silica thickness 2 and 7 nm respectively). The surface of the NCP-1' was then decorated with c(RGDfK) which is a small cyclic peptide sequence known for its strong binding affinity to $\alpha_V\beta_3$ integrin. NCP-1'-a and NCP-1'-b exhibited IC_{50} (50% Inhibitory Concentration) values of 9.7 and 11.9 mM respectively, comparable to the 13 mM IC_{50} observed for cisplatin under identical *in vitro* conditions.

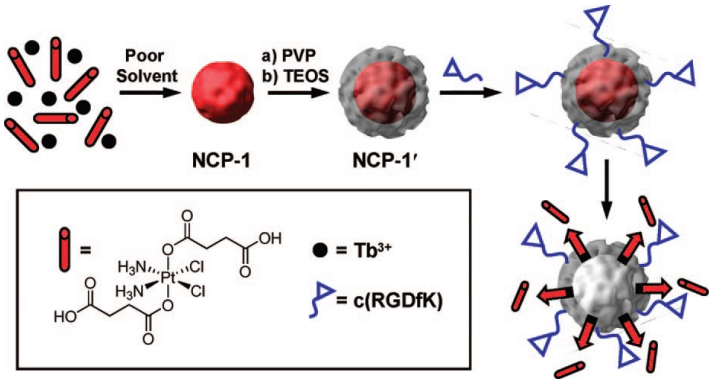

Figure 3.9 Synthesis and decoration process of NCP-1, and Pt release process.[341]

The combination of the novel hexacoordinate Ge ligand together with RE ions may generate novel MOF structures, giving rise to interesting properties that could be applied in various areas, as illustrated by the above examples. MOF synthesis using RE metal salts and the Ge linker was therefore carried out to explore the structures, properties, and potential applications of the novel RE-MOFs.

3.3 Synthesis of IMP-RE Series MOFs

A series of metal nitrate salts (Na, Mg, K, Ca, Sc, Cr, Mn, Fe, Co, Ni, Cu, Zn, Ga, Sr, Y, Cd, In, Ln, Pb) have been used in MOF synthesis with L1, L2 and L3 type linkers. Most of the reactions were carried out using 0.05 mmol of the linker with two molar equivalents of metal salts (3 equiv. for divalent metals and 6 equiv. for monovalent metals). The solvent used in those reactions were water, DMF, DMA, MeOH, MeCN or their combinations. Reaction temperature varies from 60 to 150°C and time last from 1 day to 5 days. However, most of the reactions yield no product, amorphous dark precipitation or gel-like product, with only a handful of reactions yielding reproducible crystals discussed in the following text.

3.3.1 A Y-MOF (IMP-33-Y) Built from L3-Ge with *flu*-3,6-*C*2/*c* Topology

Compound **20** ($[Et_3NH]_2$[**L3-Ge**]) was identified as a suitable linker for MOF construction because the three terminal carboxylate groups can potentially bind to three or more different metal cations to form infinite frameworks. Treatment of **20** with $Y(NO_3)_3 \cdot 6H_2O$ (molar ratio 1:2) in a mixture of water and MeCN at 80°C in a sealed glass vial for 1 day afforded colourless blade-shape crystals of **IMP-33-Y**. The crystals were analysed by SCXRD to be $[[Y_2(\mathbf{L3\text{-}Ge})_2(H_2O)_4][Y(H_2O)_8] \cdot (Et_3NH) \cdot 3H_2O]$ and the phase purity of bulk crystals was checked by PXRD measurement and was shown to be consistent with the calculated pattern from the SCXRD data (Figure 3.10). **IMP-33-Y** crystallises in the monoclinic *C*2/*c* space group. Each asymmetric unit contains one fully deprotonated ligand anion, one Y^{3+} cation coordinating with the ligand, two water molecules coordinating with the Y^{3+} cation, one disordered independent Y^{3+} cation, and eight water molecules coordinating with the disordered Y^{3+} cation ($[Y(H_2O)_8]^{3+}$: take 50% occupancy due to symmetric disorder). Each unit cell contains eight ligand molecules, eight bridging Y^{3+} cations and four disordered $[Y(H_2O)_8]^{3+}$ cations. Hence overall **IMP-33-Y** comprises an anionic $[Y_2(\mathbf{L3\text{-}Ge})_2(H_2O)_4]^{4-}$ framework, with the negative charge balanced by $[Y(H_2O)_8]^{3+}$ and $[Et_3NH]^+$ cations within its pores (Figure 3.11). H-bond interactions were also observed between the oxygen atoms

on the ligand carboxylate groups and water molecules from solvent and SBU. The disordered Y^{3+} counter cation was located in the solid-state structure, however the ammonium cations were not observed due to disorder although their presence was confirmed using ^{1}H NMR spectroscopy of the digested MOF in aqueous NaOD which showed a germanate ligand to ammonium cation ratio of 2:1.

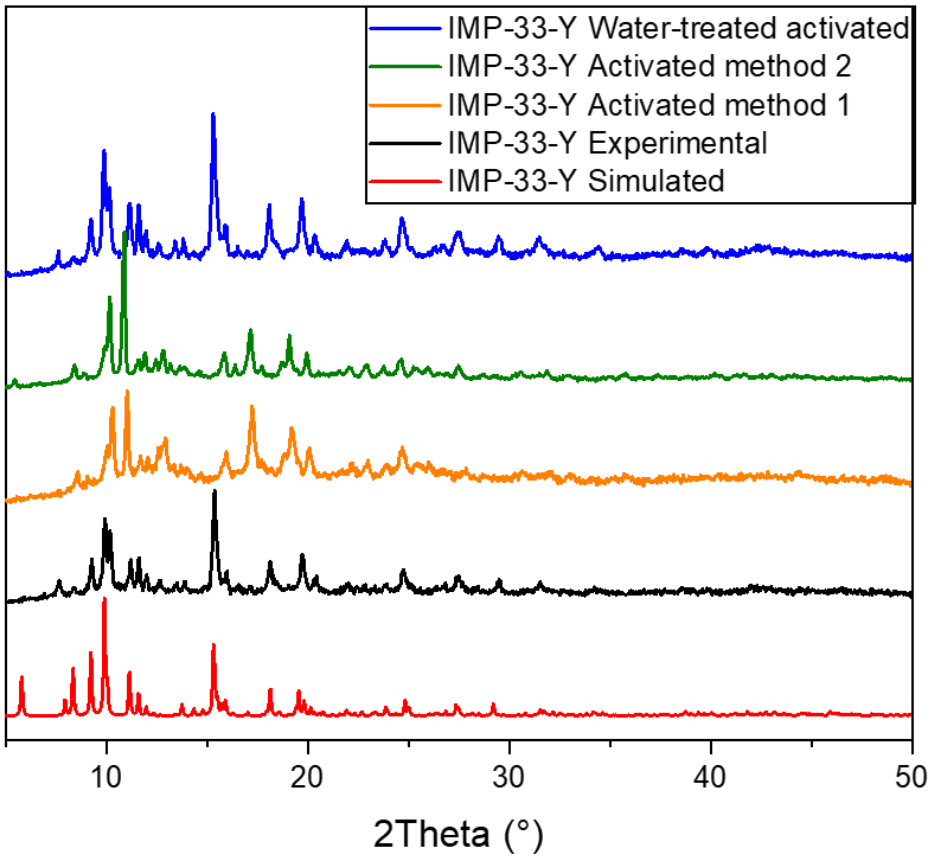

Figure 3.10 PXRD pattern of the simulated, experimental, activated (method 1 and method 2), and water-treated activated **IMP-33-Y**.

In order to visualise the topology of the framework better, the metal clusters and ligands can be reduced to simple nodes, and disordered $[Y(H_2O)_8]^{3+}$ and ammonium cations are omitted. The metal nodes (or SBUs) in **IMP-33-Y** comprise two yttrium cations, each of which is coordinated by two bidentate chelating carboxylate groups, two di-monodentate bridging carboxylate groups and two water molecules. This therefore gives a six-connected vertex (Figure 3.12a). The three deprotonated carboxylate groups in each ligand bind to different SBUs to give an overall $(\kappa^1\text{-}\kappa^1\text{-}\mu_1)^2\text{-}(\kappa^1\text{-}\kappa^1\text{-}\mu_2)\text{-}\mu_4$ coordination mode and a 3

connected node (Figure 3.12b). These 6- and 3-connected nodes join together to give a *flu*-3,6-*C*2/*c* topology, as shown in Figure 3.12d. and calculated by *TopCryst*.[342] Such topology remains rare in the literature, although some examples can be found in lanthanide MOFs with tridentate linkers.[343-345]

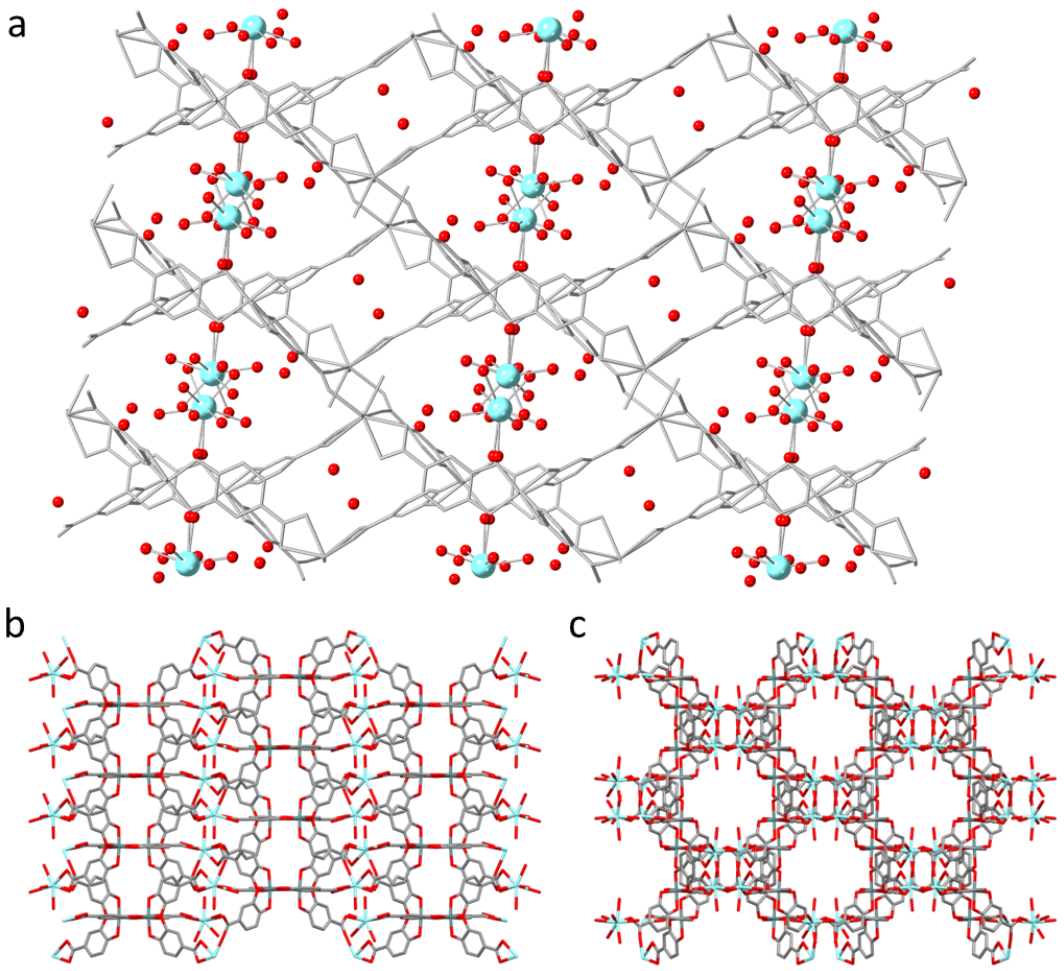

Figure 3.11 a) Packing diagram of **IMP-33-Y** along *b* axis showing pore space occupied by the disordered $[Y(H_2O)_8]^{3+}$ cations and non-coordinated water molecules (ammonium cations are not shown in the crystal data). Two $[Y(H_2O)_8]^{3+}$ cations are shown in each pore due to symmetric disorder, and only one $[Y(H_2O)_8]^{3+}$ cation is presented in each pore, resulting in an overall 50% occupancy in each position. The anionic frameworks are shown in grey colour; b, c) packing diagram of **IMP-33-Y** along *a* and *c* axis. C: grey, O: red, Y: pale blue, Ge: grey blue. H atoms are omitted for clarity. Highly disordered water molecules (11 per asymmetric unit) have been removed by the SQUEEZE routine of PLATON.[265]

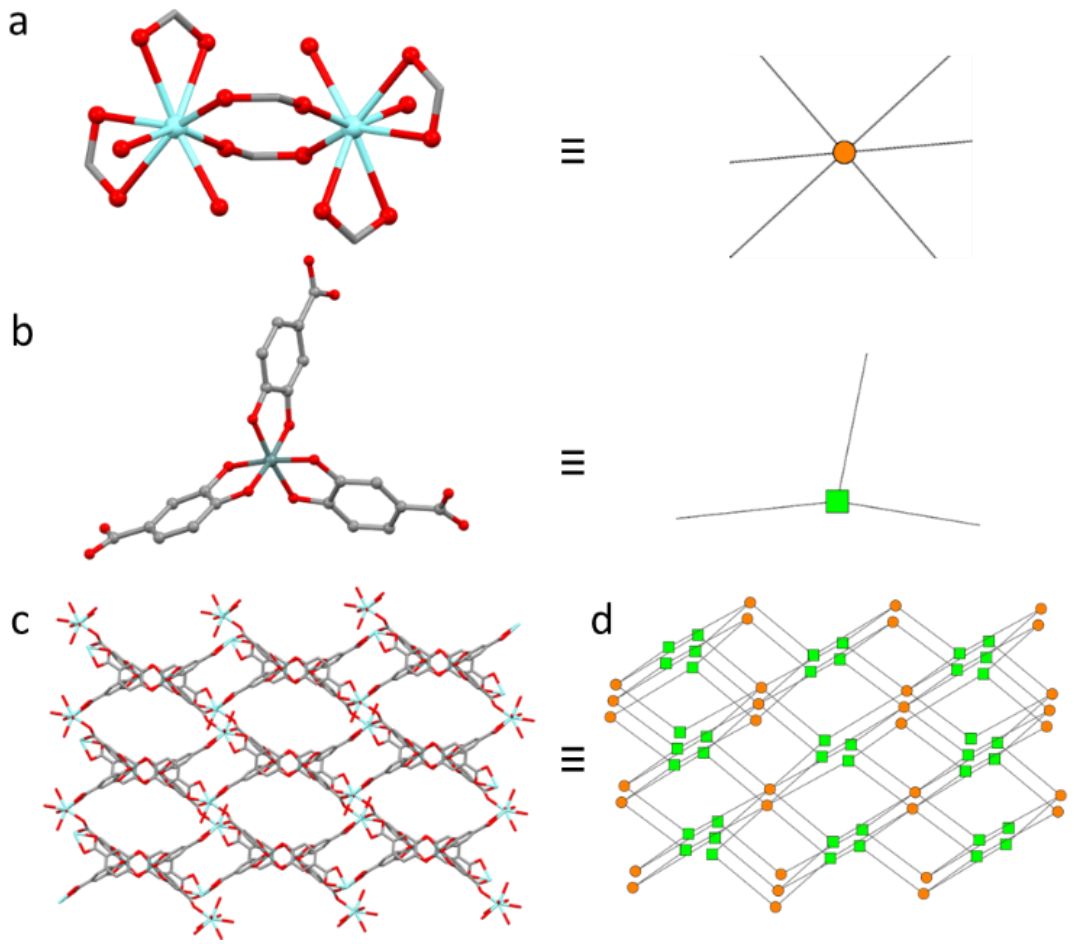

Figure 3.12 a) coordination environment of the 6-connected SBU; b) 3-connected ligand; c) packing diagram of **IMP-33-Y** (0 1 0); d) topology view of the framework (0 1 0). C: grey, O: red, Ge: grey blue, Y: pale blue. H atoms are omitted for clarity.

IMP-33-Y exhibits solvent-filled channels that extend in different directions, whilst the largest rhombic shape pore along (0 1 0) direction is observed with a size of approximately 16 × 7 $Å^2$ (diagonals). After theoretical removal of highly disordered non-coordinated solvent molecules, disordered Y^{3+} molecules and coordinated water molecules, it is predicted by *PLATON*[265] that the solvent-accessible void volume is 59.4% of the unit cell volume.

The activation of **IMP-33-Y** was then conducted through two methods. The first method (method 1) involved direct thermal activation of freshly prepared **IMP-33-Y** under vacuum at 60°C overnight. In the second solvent exchange method (method 2), **IMP-33-Y** was

soaked in acetone three times over a period of two days to exchange the non-coordinated solvent molecules, then the MOF was soaked in dichloromethane overnight and finally put under a dynamic vacuum at RT overnight. Both activations yield the same structure as revealed through PXRD measurement with some peak shifts compared to the freshly prepared MOF sample (Figure 3.10), which might be due to the structure change.

As **IMP-33-Y** remains crystalline after activation, N_2 sorption studies were conducted. However, the results indicate that the frameworks are non-porous, presumably due to the presence of Y^{3+} and triethylammonium cations in the void space which cannot be removed through activation, thus blocking the absorption of any gas molecules (Figure 3.11). It is then calculated by Mercury[275] (solvate analyser) that the void space for guest molecules (with the size of 2 Å) is 2.1% without the consideration of triethylammonium cations (due to disorder, not shown in the crystal structure). Considering the larger size of the N_2 molecules (3.6 Å, kinetic diameter), there is less space for N_2 molecules to be absorbed and this calculated result fits well with the gas uptake result. The measured BET surface area was 65.28 m^2/g, presumably due to the absorption of N_2 molecules on the surface of the sample. The activated **IMP-33-Y** is then soaked in water followed by PXRD measurement, and the resulting pattern indicates the regeneration of the MOF as the PXRD pattern is identical to the as-synthesized MOF.

TGA results of **IMP-33-Y** (air-dried crystals) under N_2 showed that approximately 16.0% weight loss occurred between 30-150°C (Figure 3.13). This loss is attributed to the loss of uncoordinated solvent molecules (calcd. ~16 water molecules). The weight loss (approx. 5.2%) between 150-300°C suggests the loss of coordinated water molecules (calcd. ~5 water molecules). Thus, the formular of the **IMP-33-Y** is calculated to be $[[Y_2(\mathbf{L3\text{-}Ge})_2(H_2O)_4][Y(H_2O)_8]\cdot(Et_3NH)\cdot 9H_2O]$. The framework remains stable until 300°C when it starts to decompose.

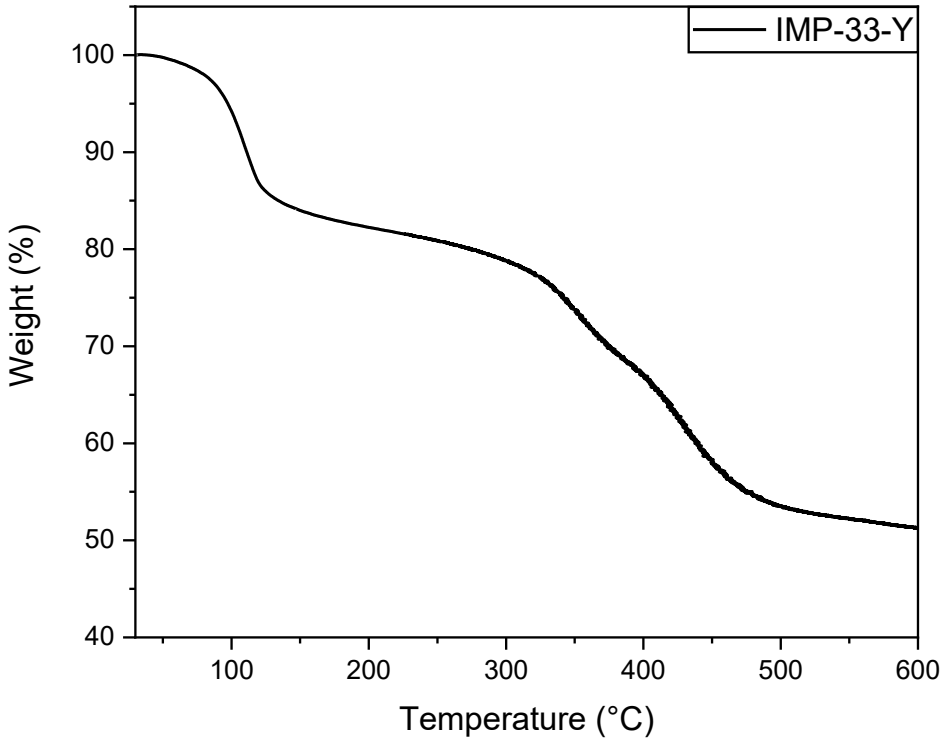

Figure 3.13 TGA curve for **IMP-33-Y**.

3.3.2 Lanthanide MOFs (IMP-33-Ln) Built from L3-Ge with *flu*-3,6-*C*2/*c* Topology

A series of Ln-MOFs (**IMP-33-Ln**) were obtained through the hydrothermal reaction of **20** with metal nitrate salts (Gd, Tb, Dy, Ho, Er, Tm, Yb or Lu, all trivalent). In a typical reaction, $Dy(NO_3)_3 \cdot 5H_2O$ (0.1 mmol) and **20** (0.05 mmol) were dissolved in a solvent combination of water (3 mL) and MeCN (1 mL) in a sealed glass vial, and this mixture was heated at 80°C for 1 day to yield colourless blade-shaped crystals. Crystals of **IMP-33-Ho** and **IMP-33-Er** were pale orange and pink respectively, while the other crystals were colourless.

Crystals of **IMP-33-Dy** were selected for SCXRD analysis to study the detailed structure. The crystals were analysed to be $[[Dy_2(\mathbf{L3\text{-}Ge})_2(H_2O)_4][(Dy(H_2O)_8]\cdot(Et_3NH)\cdot H_2O]$ (Figure 3.14) and the phase purity of the bulk crystals was confirmed through PXRD studies (Figure 3.15). Each asymmetric unit contains one deprotonated ligand anion, one Dy^{3+} cation coordinated by three ligand carboxylate groups and two water molecules, one disordered independent Dy^{3+} cation, and eight water molecules coordinating with the disordered Dy^{3+} cation ($[Dy(H_2O)_8]^{3+}$ take overall 50% occupancy due to symmetric

disorder), and half solvent water molecule, and each unit cell contains four of the formula units. There are only slight differences in the lattice parameters compared to **IMP-33-Y**, which may be caused by the difference in the metal cation size.

From a topological view, **IMP-33-Dy** exhibits an identical connection fashion to the Y analogue. The three carboxylate groups in **L3-Ge** bind to different metal nodes to give a 3-connected node. The coordination environment of the metal cluster is the same as **IMP-33-Y**, hence the metal node can be regarded as 6-connected. The combination of these two nodes results in a *flu*-3,6-*C*2/*c* topology. H-bond interactions are also observed between O atoms from the GeO_6 centre and water molecules from the $[Dy(H_2O)_8]^{3+}$ cation, as well as water molecules in the SBU and O atoms from carboxylate groups.

IMP-33-Dy exhibits void spaces in various directions for solvent molecules to fill, and the largest channel along (0 1 0) direction is estimated to be 16 × 7 $Å^2$ (diagonal). After theoretical removal of highly disordered non-coordinated solvent molecules and the disordered $[Dy(H_2O)_8]^{3+}$ cations, it is calculated by *PLATON*[265] that the solvent accessible void volume is 58.5% of the unit cell volume. However, it is expected that **IMP-33-Dy** are non-porous due to the presence of Dy^{3+} and ammonium cations in the void space (similar to **IMP-33-Y**) and which cannot be removed by any activation process as they provide overall balance of charge.

It was anticipated that all **IMP-33-Ln** would be isostructural due to their similar trivalent metal cations.[346] This was verified by PXRD analysis on freshly prepared **IMP-33-Ln**. It can be observed from Figure 3.16 that all these **IMP-33-Ln** have similar patterns, with peaks located at the same positions. GA results of **IMP-33-Ln** (air-dried crystals) under N_2 reveal that these frameworks remain stable up to about 300°C when they start to decompose. The weight loss between 30-150°C can be attributed to the loss of uncoordinated solvent molecules (approx. 14.6%). These results are consistent with **IMP-33-Y** which showed a similar weight loss curve (Figure 3.17), suggesting that **IMP-33-Ln** have similar water components.

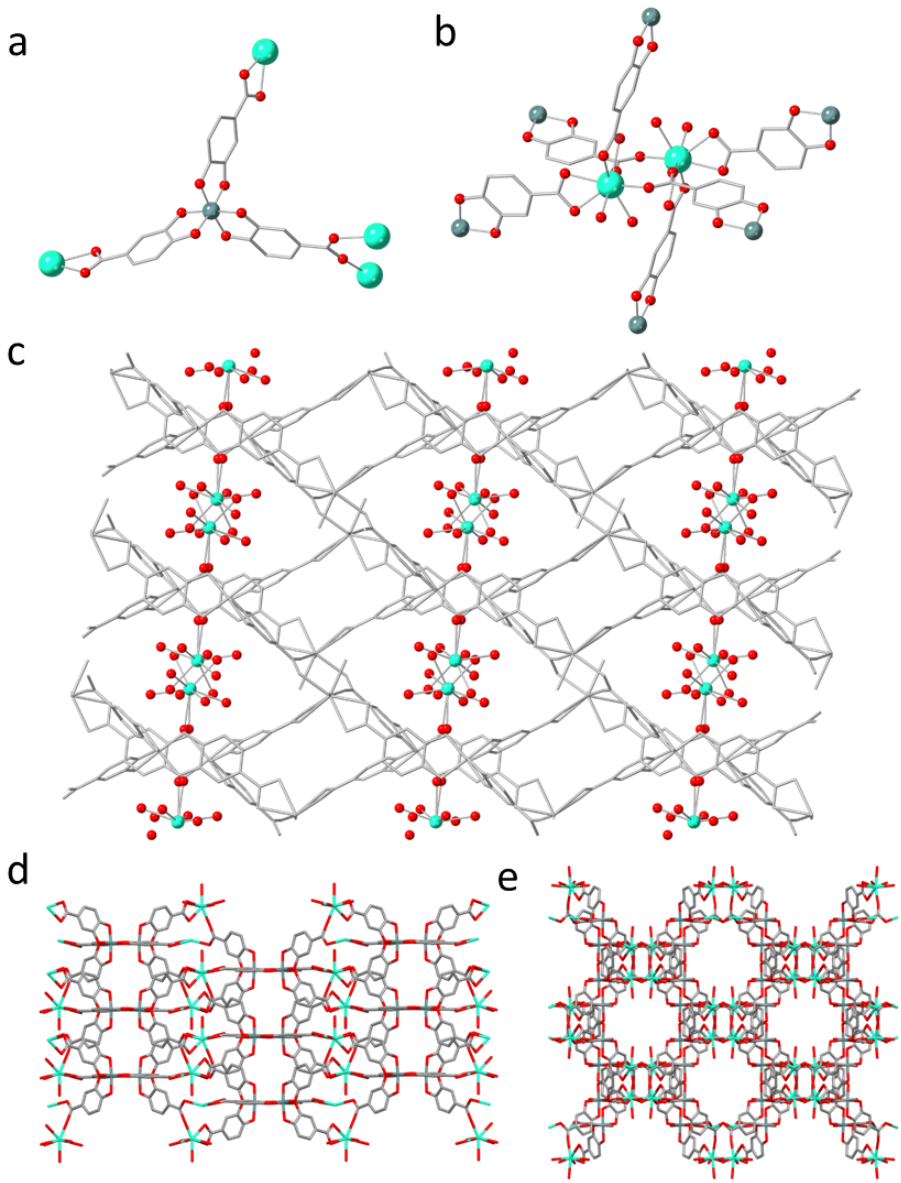

Figure 3.14 a) coordination environment of the tridentate Ge ligand; b) six connected SBU; c) packing diagram of **IMP-33-Dy** along (0 1 0) view showing pore spaces occupied by the disordered $[Dy(H_2O)_8]^{3+}$ cations. Two $[Dy(H_2O)_8]^{3+}$ cations are shown in each pore due to symmetric disorder, and only one $[Y(H_2O)_8]^{3+}$ cation is presented in each pore, resulting in an overall 50% occupancy in each position. The anionic frameworks are shown in grey colour; d,e) packing diagram of **IMP-33-Dy** along (1 0 0) and (0 0 1) view. C: grey, O: red, Ge: grey blue, Dy: green-blue. H atoms are omitted for clarity. Highly disordered water molecules (12 per asymmetric unit) have been removed by the SQUEEZE routine of PLATON.[265]

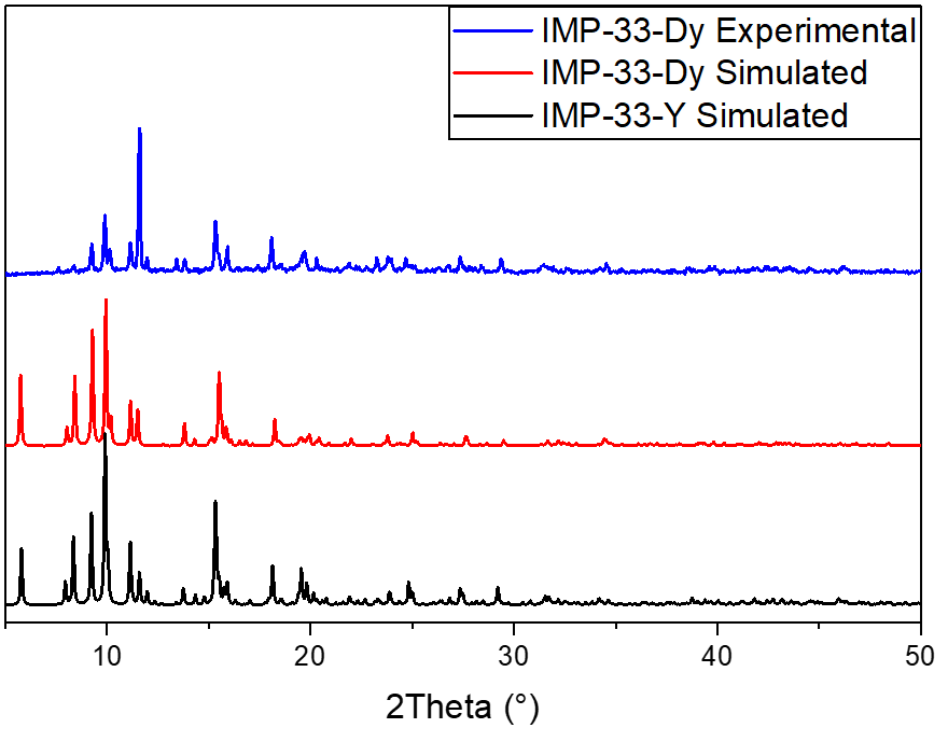

Figure 3.15 PXRD pattern of **IMP-33-Dy** (simulated and experimental) and **IMP-33-Y**.

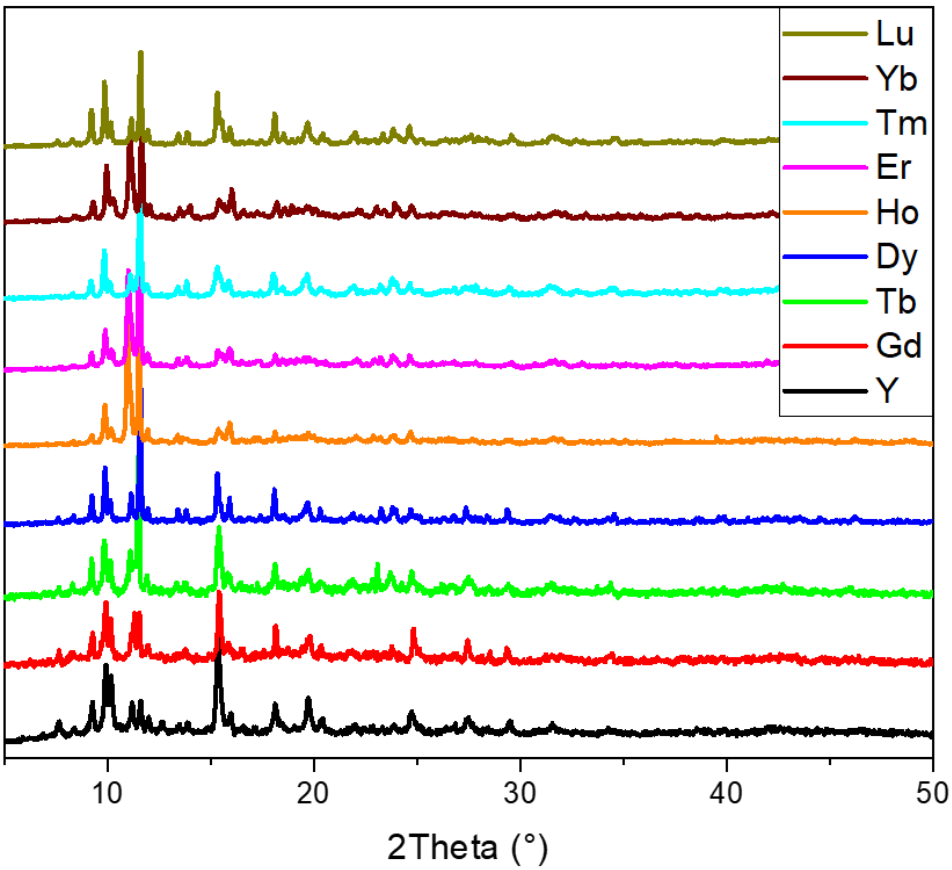

Figure 3.16 PXRD pattern of **IMP-33-Ln**.

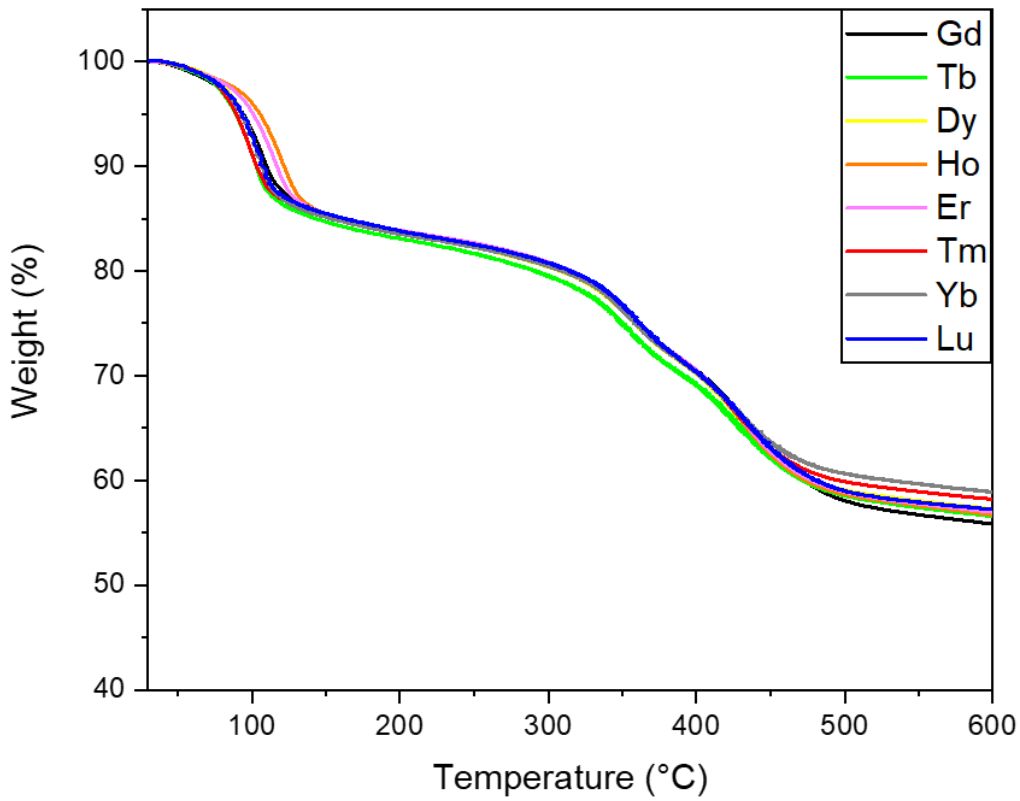

Figure 3.17 TGA results of **IMP-33-Ln**.

Although the single crystal data for the rest of the **IMP-33-Ln** MOFs were not obtained, DASH[347] software was used to calculate the lattice constants of some of these MOFs from their PXRD data. The unit cell parameters of **IMP-33-Tb** and **IMP-33-Lu** were obtained and listed in Table 3.1 below. It is clearly observed that these two MOFs have almost identical lattice parameters compared with **IMP-33-Y** and **IMP-33-Dy**, and evidence further supports the proposal that all these **IMP-33-Ln** MOFs are isostructural. Unfortunately, despite several attempts the expected structure cannot be obtained using this software, due to the low resolution of the PXRD data.

Data type	**IMP-33-Y**	**IMP-33-Dy**	**IMP-33-Tb**	**IMP-33-Lu**
Formula	$C_{42}H_{18}Y_3Ge_2O_{24}\cdot 17H_2O$	$C_{42}H_{18}Dy_3Ge_2O_{24}\cdot 13H_2O$	$C_{42}H_{18}Tb_3Ge_2O_{24}\cdot xH_2O$	$C_{42}H_{18}Lu_3Ge_2O_{24}\cdot xH_2O$
Formula weight	1624.74	1773.45	-	-
Crystal system	monoclinic	monoclinic	monoclinic	monoclinic
Space group	*C*2/*c*	*C*2/*c*	*C*2/*c*	*C*2/*c*
a/Å	19.9205(2)	19.5343(3)	19.4716	19.6063
b/Å	14.33510(10)	14.22670(10)	14.3469	14.5061
c/Å	30.7566(2)	30.9853(3)	30.9818	30.7236
β/°	97.0890(10)	96.9100(10)	96.445	96.852
V/Å^3	8715.79(12)	8548.53(17)	8600.27	8675.73
Data source	SCXRD	SCXRD	PXRD	PXRD

Table 3.1 Crystallographic data of **IMP-33-Y**, **IMP-33-Dy**, **IMP-33-Tb** and **IMP-33-Lu**

3.3.3 A Sc-MOF (IMP-34-Sc) Built from L3-Ge with *flu*-3,6-*C*2/*c* Topology

The reaction of **20** [$(Et_3NH)_2$(**L3-Ge**)] with $Sc(NO_3)_3 \cdot H_2O$ (1:2 molar ratio) in a mixture of water and MeCN (3 and 1 mL) at 80°C for 1 day afforded colourless prism-shaped crystals of **IMP-34-Sc**. The crystal was analysed by SCXRD studies to be [[Sc_3(**L3-Ge**)$_2(H_2O)_6$]·$(Et_3NH)(MeCN)_6(H_2O)_9$], and the phase purity of the bulk crystals was consistent with the calculated pattern from single crystal data. **IMP-34-Sc** crystallised in the monoclinic space group $P2_1$. Each asymmetric unit consists of four ligand anions, six Sc^{3+} cations, two triethylammonium cations, twelve coordinating water molecules, and each unit cell contains two asymmetric units. **IMP-34-Sc** comprises an anionic framework, and the negative charge is balanced by the triethylammonium cations in the framework. This was confirmed by the presence of cations in the crystal structure as well as the ^{1}H NMR studies of the digested MOF in aqueous NaOD showing the triethylammonium to **L3-Ge** ratio of 1:2. H-bond interactions are also observed from the GeO_6 centre with the ammonium cations and water molecules from the SBU (Figure 3.18), with distances ranging from 2.988 to 3.264 Å (N(H)···O-Ge and O(H)···O-Ge).

To investigate the topology of **IMP-34-Sc**, the SBU and ligand anions can be simplified to point nodes with a given coordination number. There are three Sc^{3+} cations in each metal cluster, the central Sc^{3+} cation (Sc1 or Sc3) is coordinated by six bridging di-monodentate carboxylate groups (each from a different ligand molecule), while the terminal two Sc^{3+} cations (Sc4, Sc6 or Sc2, Sc5) are each coordinated by three bridging di-monodentate carboxylate groups and three water molecules. Each Sc^{3+} cation adopts an octahedral geometry, with the adjacent and opposite O-Sc-O angles between 79.5(2)-103.4(3) and 164.1(2)-177.7(2)° respectively. Although there are two crystallographically different SBU (based on Sc1, Sc4, Sc6, and Sc2, Sc3, Sc5), they are structurally equivalent giving a 6-connected trinuclear [$Sc_3(CO_2)_6(H_2O)_6$] node. There are four types of crystallographically distinct Ge ligands (Ge1, Ge2, Ge3, Ge4), each of which binds to three different metal nodes in a $(\kappa^1\text{-}\kappa^1\text{-}\mu_2)^3\text{-}\mu_6$ coordination mode, thus these ligands can be considered equivalent and categorized as 3-connected. This combination of 3-connected ligands and

6-connected metal nodes results in a *flu*-3,6-*C*2/*c* topology (Figure 3.19). Interestingly this is the same topology as observed in **IMP-33-Y**, however the trimetallic metal node in **IMP-34-Sc** has a higher charge than the di-cationic metal node in **IMP-33-Y** resulting in a lower negative charge on the framework: $[Sc_3(\mathbf{L3\text{-}Ge})_2]^-$ vs $[Y_2(\mathbf{L3\text{-}Ge})_2]^{4-}$.

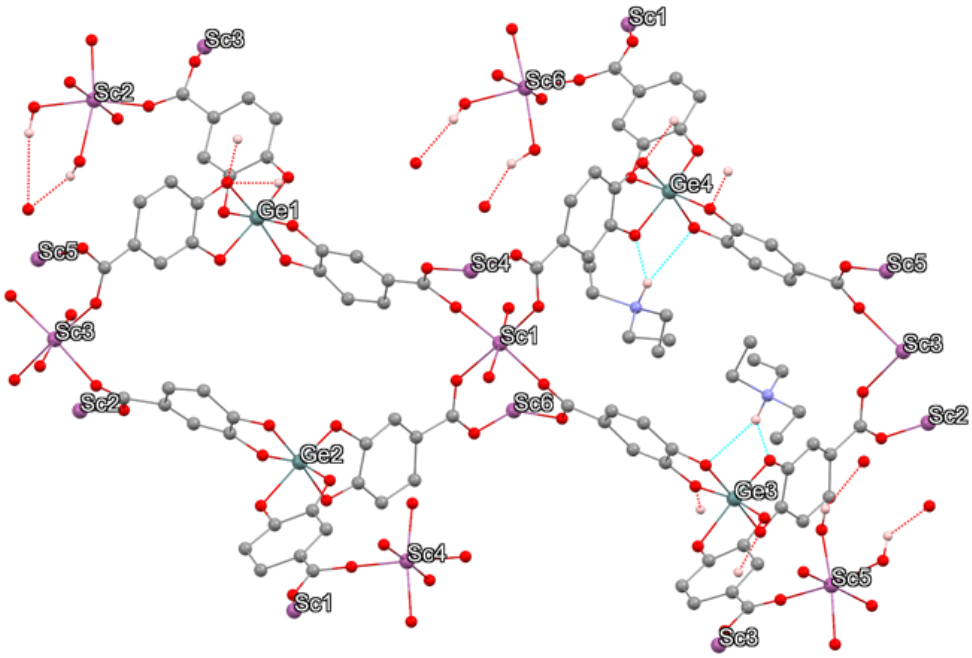

Figure 3.18 Asymmetric unit of **IMP-Sc-34** showing H-bonds (red and blue dotted line). C; grey, O: red, N: night blue, Ge: grey blue, Sc: pink, H: pale pink. Other H atoms are omitted for clarity.

IMP-34-Sc displays 3-D channels in various directions which are filled with solvent molecules. The largest channel is observed along the (0 1 0) direction and is approximately 12 × 8 $Å^2$ across the diagonals. After theoretical removal of highly disordered non-coordinated solvent molecules, coordinated water molecules and ammonium cations, according to *PLATON*[265] calculations the accessible void volume is 57.0% of the unit cell volume. However, **IMP-34-Sc** lost its crystallinity after activation at 60°C overnight, as observed in PXRD results. This can be attributed to the partial collapse of the frameworks, and further tests on gas sorption measurement were not conducted. This change can be mostly recovered by soaking the activated **IMP-34-Sc** in water, as indicated by the PXRD results (Figure 3.20).

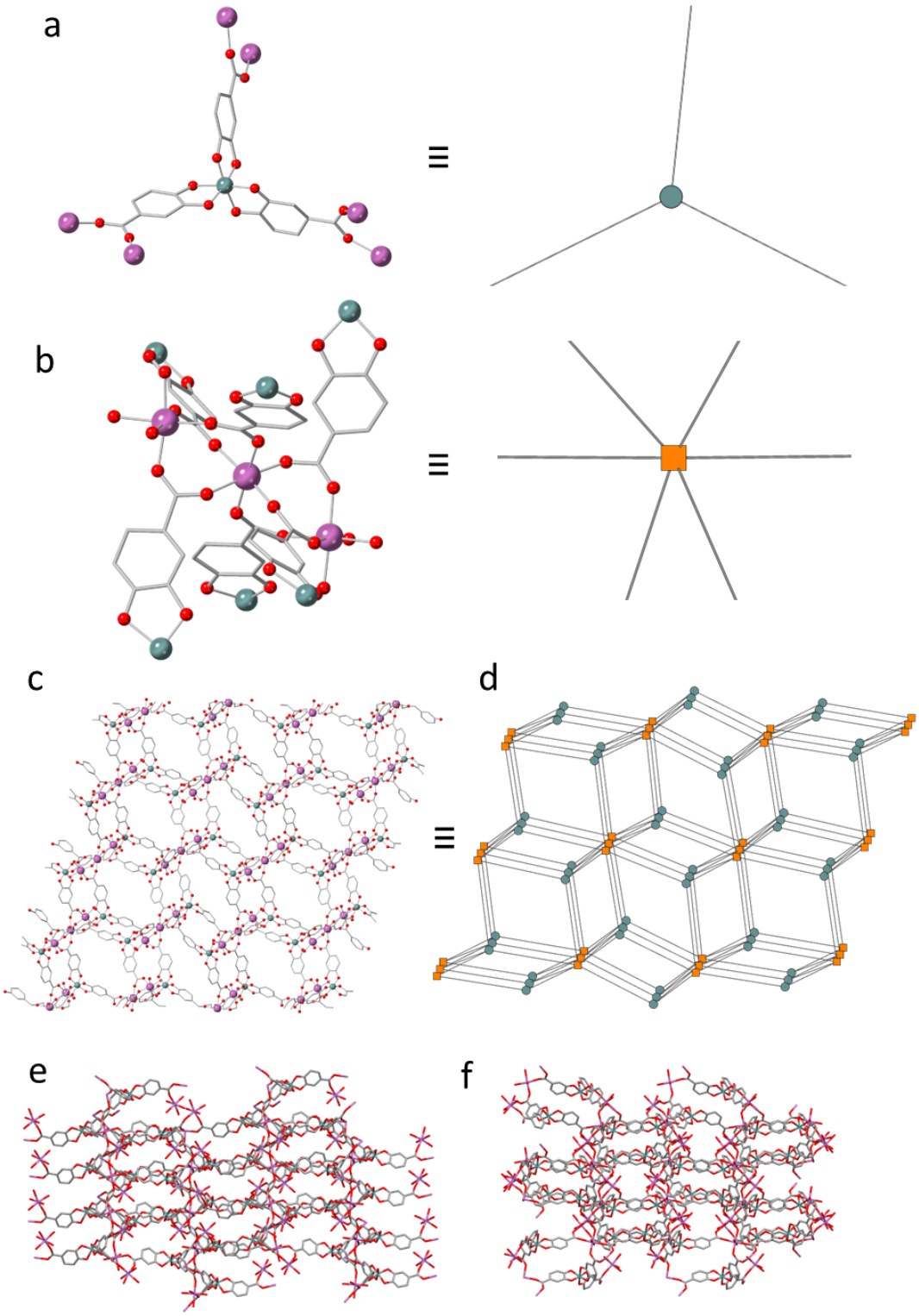

Figure 3.19 a) Structure of the tridentate ligand in **IMP-34-Sc**; b) hexadentate SBU node; c) packing diagram of **IMP-34-Sc** along (0 1 0) direction; d) framework topology; e, f) packing diagram along (1 0 0) and (0 0 1) direction. C: grey, O: red, Ge: grey blue, Sc: pink. H atoms are omitted for clarity.

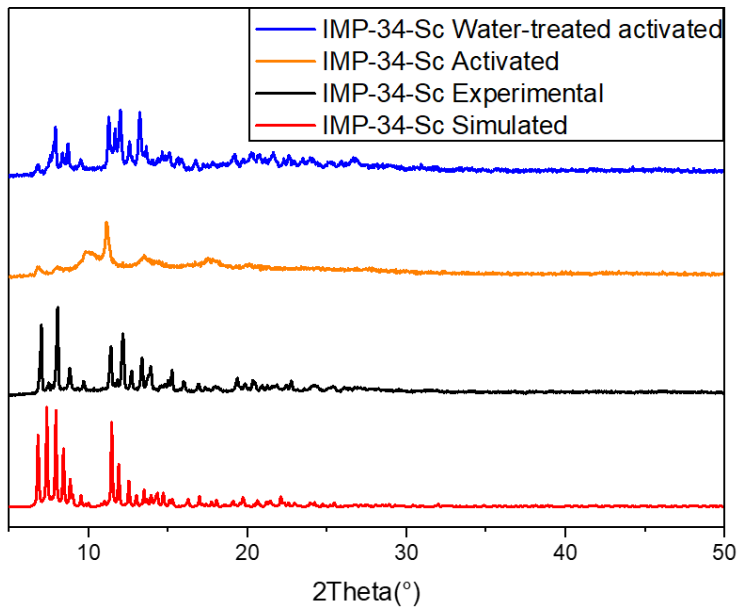

Figure 3.20 PXRD patterns of the simulated, experimental, thermal vacuum activated, and water-treated activated **IMP-34-Sc**.

TGA results of **IMP-34-Sc** (air-dried crystals) under N_2 showed approximately 11.6% weight loss occurred between 30-150°C (Figure 3.21), which is mainly attributed to the loss of uncoordinated solvent molecules (calcd. 10 water molecules). The weight loss between 150-300°C can be attributed to the loss of coordinated water molecules (calcd. 3.5 water molecules). The framework stays stable until 300°C when it starts to decompose.

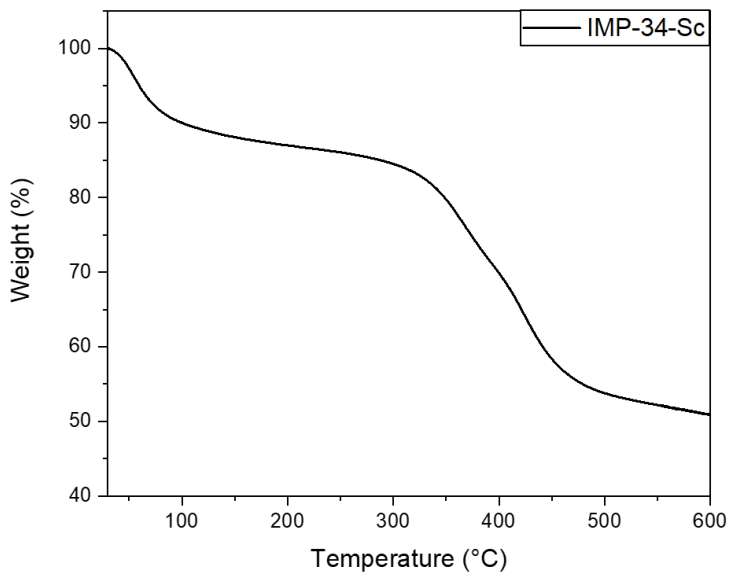

Figure 3.21 TGA curve of **IMP-34-Sc**

3.4 Other Attempted Syntheses

L1-type linkers are considered potential building blocks for MOF construction due to their terminal oxalate chelation points. Metal-oxalate complexes have been widely reported in the literature, and these structures range from 1D linear chain, 2D sheet to 3D framework structures by the variation of metal coordination mode or the incorporation of bridging ligands.[348-350] The introduction of the Si/Ge atom in the L1 linker anion may facilitate the formation of novel structures in MOF synthesis.

The reaction of compound **1** with $Mn(NO_3)_2{\cdot}4H_2O$ in water at 75°C for 12 h afforded colourless block crystals. However, these crystals were analysed to be $[Mn(C_2O_4)(H_2O)_2]_n$ by SCXRD, with no Si observed in the structure. This could be attributed to the hydrolysis of the linker thus liberating the oxalate groups. This is a known structure and it is still interesting, despite the absence of Si, displaying linear chains consisting of Mn^{2+} linked by oxalate groups (Figure 3.22).[351] Each Mn^{2+} cation is coordinated by two axial water molecules to exhibit an octahedral geometry.

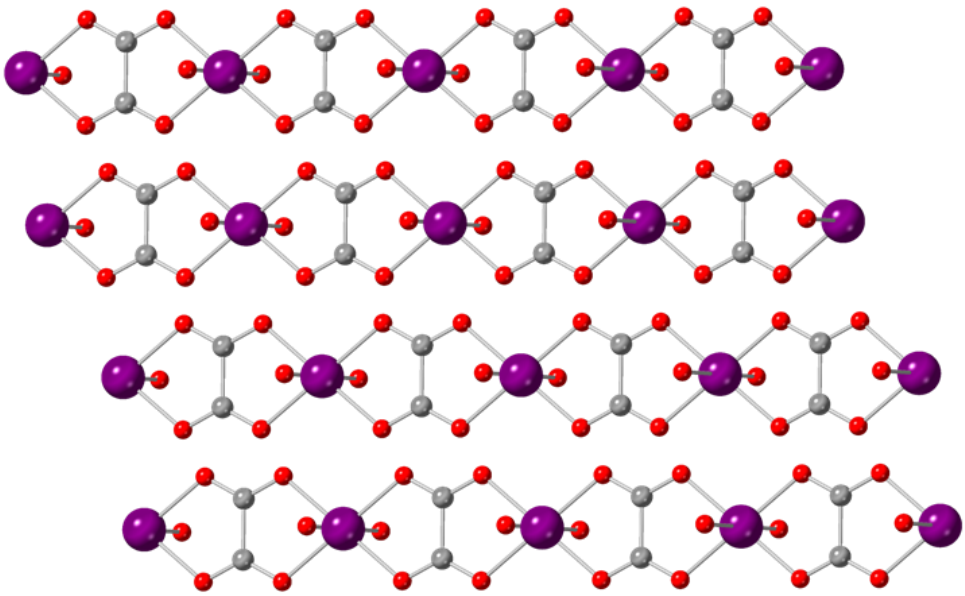

Figure 3.22 Crystal structure of $Mn(C_2O_4)(H_2O)_2$ along (1 1 0) view. C: grey, O: red, Mn: purple, H atoms are omitted for clarity. Figure redrawn using published crystal data from Gharamaleki and co-workers (CSD refcode: FOZHUX11).[351]

A mixture of **8** [$(Et_3NH)_2$(**L1-Ge**)] and $Zn(NO_3)_2 \cdot 6H_2O$ was dissolved in DMF and heated at 80°C for 1 day to afford colourless block crystals. However, PXRD results indicated that the pattern is similar to the pattern of [$ZnC_2O_4 \cdot 2H_2O$] (CSD refcode QQQBOD04, Figure 3.23). It is speculated that these block crystals have a similar structure to the Zn oxalate compound, and Ge is not present in the structure. This could arise from the breakdown of the Ge linker with the oxalate groups detaching from the Ge atom, leading to the formation of zinc oxalate.

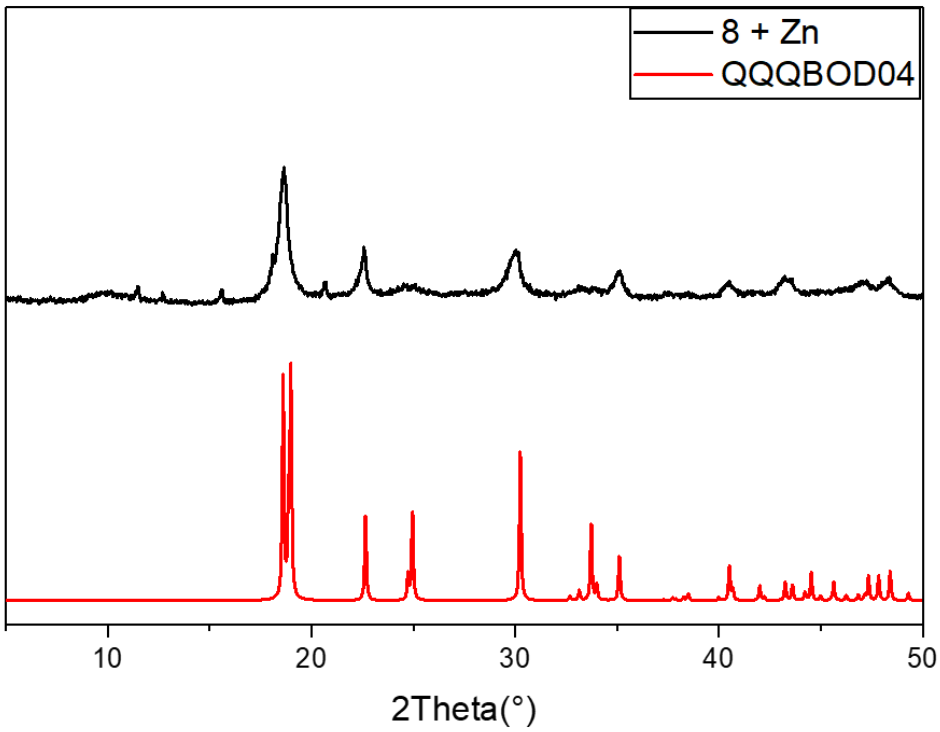

Figure 3.23 PXRD pattern the block crystal (**8** + **Zn**) and $ZnC_2O_4 \cdot 2H_2O$ (CSD refcode: QQQBOD04).[352]

In an attempt to synthesise **IMP-33-Y** using a water and MeCN ratio of 1:3, the solvent mixture turned green during heating. After standing at RT for 10 days, pale bluish-green cubic crystals were formed in the glass vial. The crystal was analysed by SCXRD to be [$Y(H_2O)_{10}$](**H_3L3-Ge**)$_4 \cdot (H_2O)_{69}$ (green crystal). Although there is no typical coordination bond formed between the Y^{3+} cation and linker anion, the structure is still of interest. It crystallized in the trigonal *R*-3*c* space group. Each asymmetric unit contains one-third of the formula, and there are 12 formula molecules present in a unit cell. Each linker anion

formed three intermolecular H-bonds with adjacent linker molecules through COOH groups, with O(H)···O distances ranging between 2.570 and 2.603 Å and O-H-O angles in a range of 149.48 and 171.24°. Additionally, eight linker molecules form the vertices of a cube to form a cubic cage structure (Figure 3.24). The Y^{3+} cations are located at the vertex among the eight neighbouring cages (lie outside the cubes) and form H-bond interactions

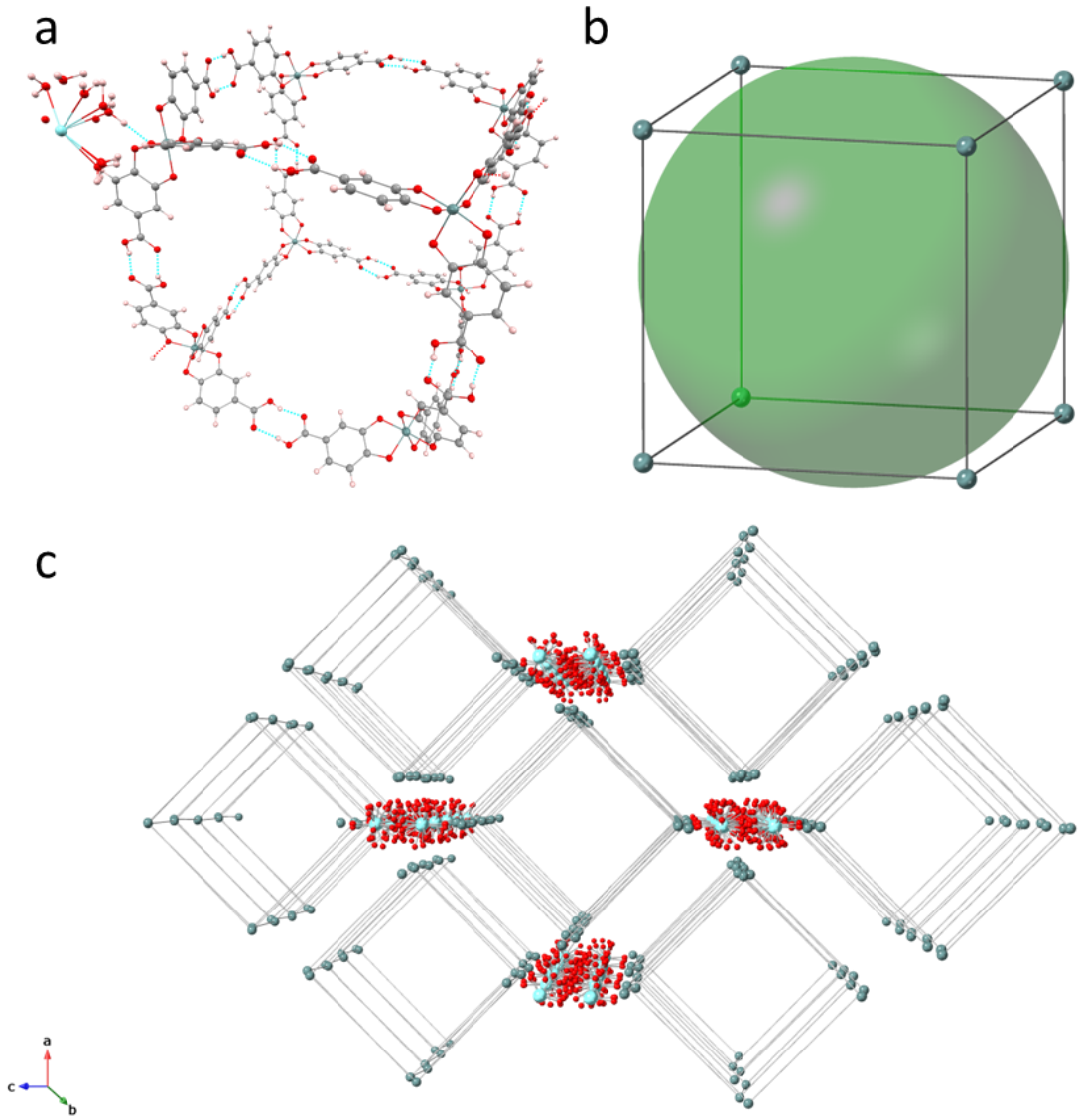

Figure 3.24 Crystal structure of the green crystals, a) cubic cage constructed from eight linker anions; b) simplified net showing large void space (green); c) packing diagram along (2 4 1) view. C: grey, O: red, Ge; grey blue, Y: pale blue, H: pale pink. H-bonds are shown in blue dotted lines.

from its coordinating water and O atoms to neighbouring GeO_6 centres. The largest pore was observed along the (2 4 1) direction with a pore size of ~21 × 21 $Å^2$. Such an arrangement generates an interesting H-bonded organic framework, in which the cubic cages are formed through carboxyl H-bonds dimer and linked by H-bonds through the coordinated water molecules from Y^{3+} cations. Similar cube structures containing different species such as H-bonded Metal-Organic cages,[353] covalent organic cages[354] have been reported in the literature.

It is predicted by *PLATON*[265] that the solvent-accessible void space is 69.2%. However, the green crystals suffer from structural instability, as indicated by PXRD results on an air-dried sample showing a loss of crystallinity (Figure 3.25), which could arise from the breakdown of the H-bonded system.

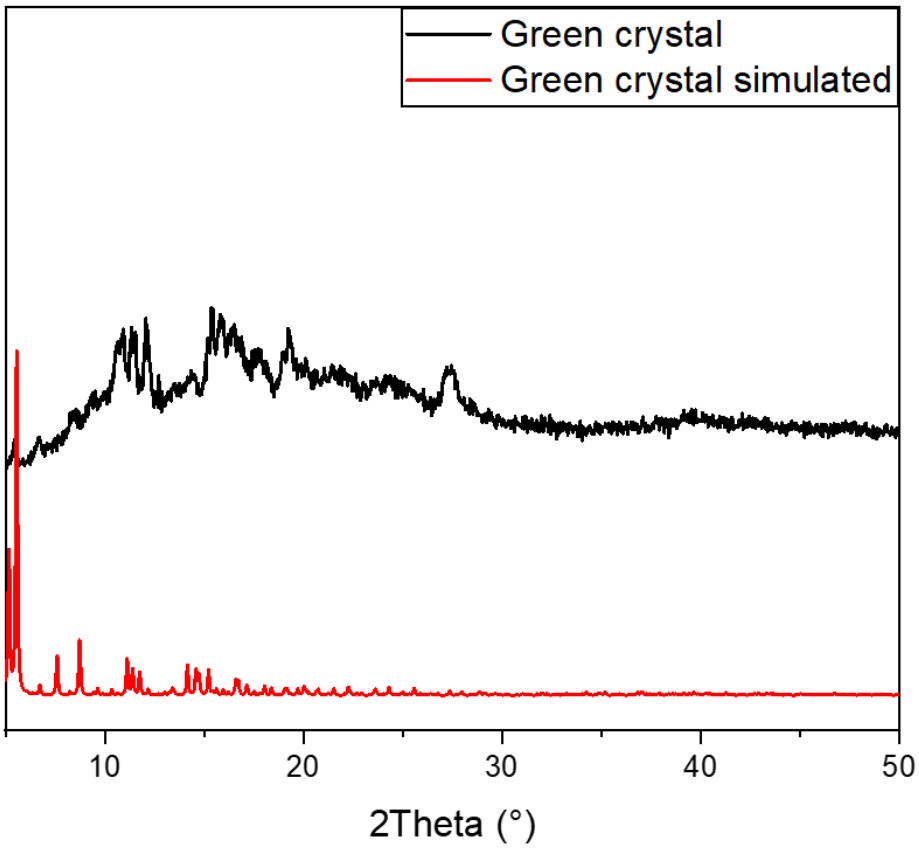

Figure 3.25 PXRD pattern of the air-dried green crystals (simulated and experimental results).

3.5 Conclusions

The hexacoordinate GeO_6 linker (compound **20**) has been demonstrated to be a suitable tridentate linker for MOF construction. Hydrothermal reactions of compound **20** with RE metal nitrates in a mixture of water and MeCN afforded a series of **IMP-33-RE** MOFs. **IMP-33-Y** was an anionic framework consisting of binuclear Y^{3+} nodes connected by six carboxylate groups and three-connected ligands with an octahedral GeO_6 centre. These nodes can be simplified to yield a *flu*-3,6-*C*2/*c* topology. The negative-charged framework was balanced by $[Y(H_2O)_8]^{3+}$ and triethylammonium cations in the void space, with the latter being confirmed through NMR studies. Activation of the **IMP-33-Y** led to a structural change on dehydration, and this change can be recovered by simply soaking the activated powder in water. The presence of Y^{3+} cations and ammonium cations in the void space excluded any large space for guest molecules to enter, resulting in a non-porous framework as indicated by gas sorption studies.

A series of Ln-MOFs were prepared using the same protocol as the **IMP-33-Y**. The detailed structure of the **IMP-33-Dy** was obtained through SCXRD studies, and the results confirmed that this MOF has almost the same lattice constant as **IMP-33-Y**. The connectivity remains the same, hence giving **IMP-33-Dy** a *flu*-3,6-*C*2/*c* topology. Other structures of **IMP-33-Ln** series were studied through PXRD measurements. The peak positions are identical compared to **IMP-33-Y** and **IMP-33-Dy**, hence all these MOFs are iso-structural.

The reaction of scandium nitrate with compound **20** afforded **IMP-34-Sc**. Crystallographic analysis revealed that this anionic framework was assembled from six-connected trinuclear Sc^{3+} nodes $[Sc_3(COO)_6(H_2O)_6]$ and the three-connected Ge ligands. The negatively charged framework was balanced by the ammonium cations in the framework, which was confirmed through SCXRD and NMR studies. Although the metal cluster was different from **IMP-33-Y**, the overall connectivity remains the same to give a *flu*-3,6-*C*2/*c* topology. Activation of **IMP-34-Sc** resulted in the partial collapse of the framework, but the framework can be

recovered by treatment with water.

The L1-type linker has been used in MOF synthesis. However, due to the poor stability of this type of linker, only metal oxalate salts were obtained. Future work on MOF synthesis with the L1-type linker should be carried out under milder conditions. Other L2- and L3-type linkers have been implemented in MOF synthesis as well, with different metal salts and solvent combinations, such as DMF, DMA, EtOH, MeOH etc., but the reactions always yielded unidentifiable dark amorphous precipitate. Such results could be attributed to the poor stability of the linker.

Ln-based MOFs are good candidates for chemical sensing, optical applications etc. In the next chapter, the photoluminescence properties of **IMP-33-Tb** will be investigated, and its sensing performance will be demonstrated.

Chapter 4: IMP-33-Tb for Metal Sensing

4.1 Introduction

Lanthanide-based MOFs have attracted much research interest stemming from the unique properties of Ln(III) ions. Such features originate from the presence of electron gradually filled f orbital across the Ln(III) ions with an electronic configuration of $[Xe]4f^n$ (n = 0 to 14, from La^{3+} to Lu^{3+}). The localized 4f electrons are well shielded by the outer $5s^2 5p^6$ shells, the untouched 4f electrons play an important role in contributing novel magnetic and optical properties to Ln^{3+} ions.[355] Benefiting directly from this, Gd^{3+} has a large magnetic moment resulting from the 7 unpaired electrons in the 4f orbital, which is the largest number of unpaired electron spins for an atom. This feature endows Gd^{3+} ions strong paramagnetic nature and it is recognized as a powerful candidate for MRI. Some Gd-MOF-based nanoparticles have demonstrated the potential to serve as MRI contrast agent.[356, 357]

Due to the highly localized nature of the 4f orbitals, there is almost no overlap between 4f orbital in Ln^{3+} ions and the ligand orbitals, resulting in the predominantly ionic bonding character between Ln^{3+} and ligand complex, and this feature can be observed from the irregular geometry and various coordination number (6 to 12, sometimes can be lower) in Ln-complexes compared with that in d-block metal complexes.[355, 358] The higher coordination number allows Ln^{3+} ions to bind to solvent molecules during MOF synthesis, and the solvent molecules can be subsequently removed through activation, leading to the exposure of OMS. The unsaturated OMS offers coordinating points for guest molecules to interact, thus supporting processes such as gas sorption/separation and heterogeneous catalysis. Apart from the OMS, the functional diversities of Ln-MOFs can be achieved from the decoration of functional groups in the organic linkers as well. Thus, all these factors contribute to the versatile functionalities of Ln-MOFs and this type of MOF has been used in applications in chemical sensing, catalytic reactions, gas separation, magnetic resonance imaging (MRI), optical applications etc.[359-365]

In particular, Ln-MOF as the sensing agent for the detection of chemicals has been widely studied due to their unique luminescent properties from the Ln^{3+} ions. Lanthanide luminescence is usually recognized in the process of converting incoming light (usually UV) to visible light or near-infrared (NIR).[105] All the Ln^{3+} ions can be excited to give characteristic emissions, except La^{3+} and Lu^{3+} due to the empty or fully filled 4f orbitals respectively. Normally the electronic 4f-4f transitions are Laporte forbidden, hence these

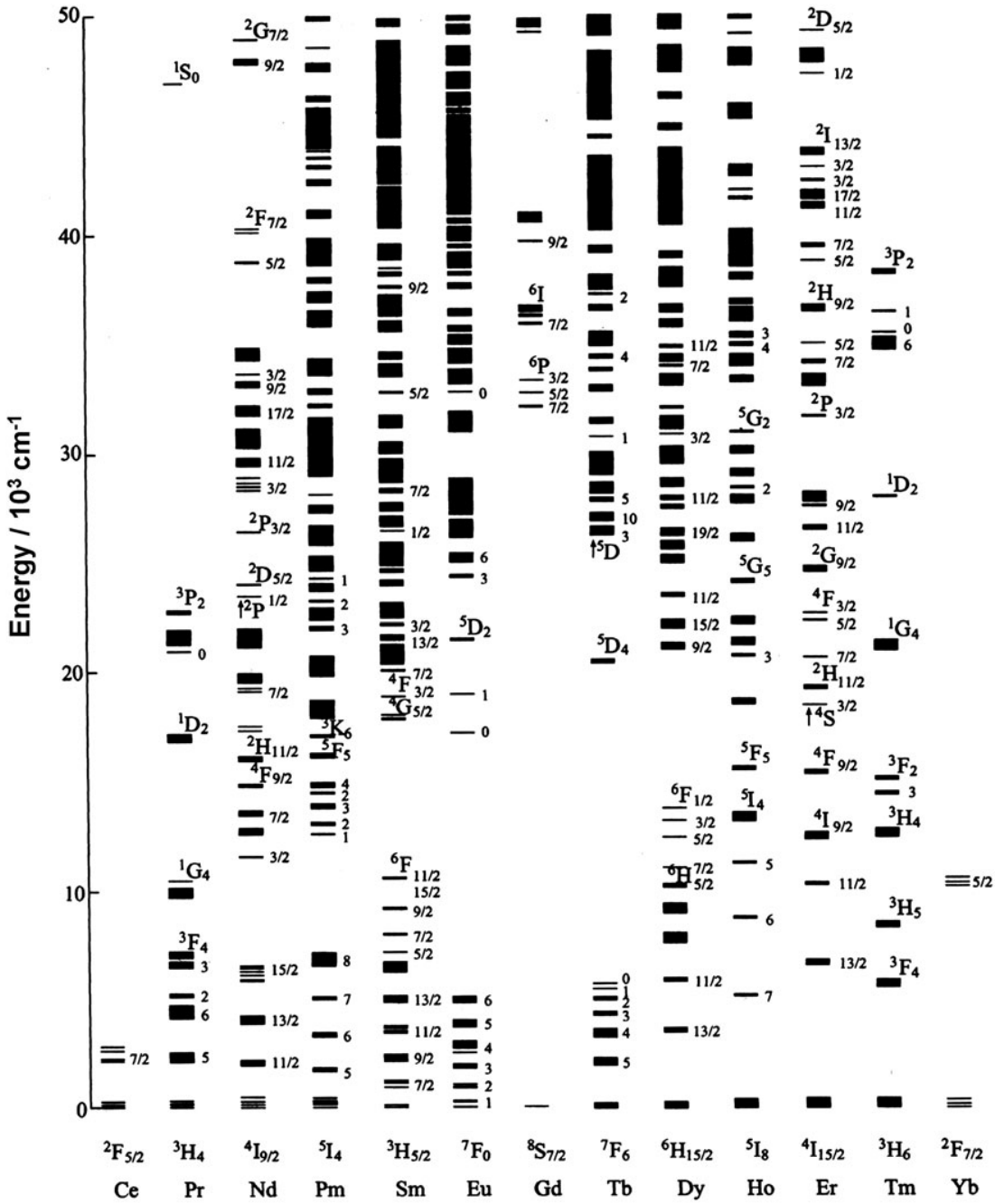

Figure 4.1 A summary of electronic excited-state energy levels for Ln^{3+} ions.[366]

Ln^{3+} ions can only be excited with a specific wavelength of light, depending on the energy gap between the ground and excitation state of each element (Figure 4.1). Considering the fact that the 4f electrons are well-shielded by the outer $5s^2 5p^6$ shells, the surrounding chemical environment has negligible effects on the energy level of the 4f electrons, hence the resulting long-lived narrow and sharp characteristic emissions can be easily recognized, even when these ions are present in a complex or material.[366] Emissions cover the range from UV to visible and NIR, as shown in Figure 4.2. Typically, Eu^{3+}, Sm^{3+}, Dy^{3+}, Tb^{3+} and Tm^{3+} emit red, orange, yellow, green and blue light under UV excitation respectively, while Pr^{3+}, Nd^{3+}, Ho^{3+}, Er^{3+} and Yb^{3+} display emissions in the NIR region.[360]

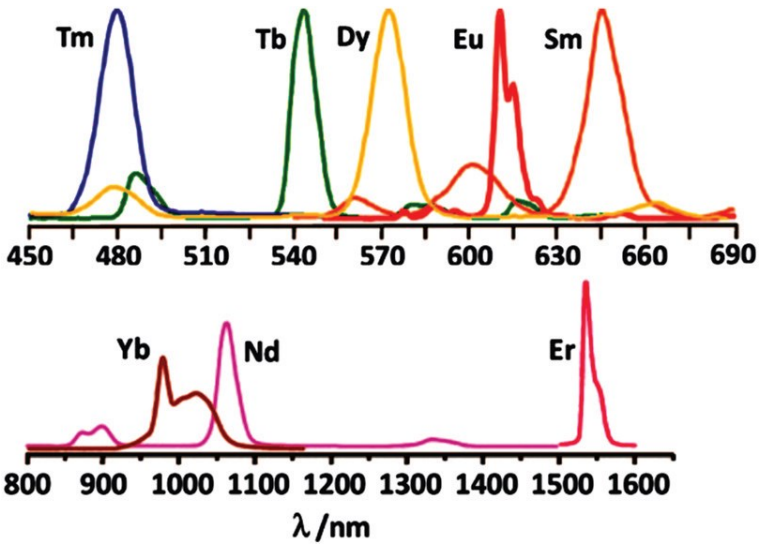

Figure 4.2 Luminescence spectra of some Ln^{3+} ions.[367]

Although the 4f electron in Ln^{3+} ions can be excited under specific wavelengths, the absorption efficiency is low, due to the shielded structure by the outer electrons.[368] Hence, these metal ions cannot be directly utilized in luminescent materials. One way to overcome this issue is to add an "antenna", in which the metal ion is coordinated by an organic ligand (also termed luminescence sensitization). The organic ligand acts as an energy acceptor to expand the energy absorption range. The energy absorption procedure usually involves three steps: Firstly, the organic ligand absorbs excitation light to temporarily 'store' the energy. Then the energy is transferred from the ligand to the Ln^{3+} ions through intramolecular energy transfer (known as the energy transfer (EnT) process). Finally, the

Ln^{3+} ions are excited and undergo energy release to emit light.

The choice of organic ligand needs to be rationally considered, as the energy level can have a huge impact on the EnT efficiency, thus further affecting the quantum yield and overall luminescence performance. As mentioned above, Ln^{3+} can only absorb photons with specific wavelengths. Additionally, the luminescence of Ln^{3+} ions can only occur from certain resonance levels, such as $^5D_4$ for Tb^{3+} (20,430 cm^{-1}) or $^5D_0$ for Eu^{3+} (17,250 cm^{-1}).[360, 369, 370] Energy is dissipated through a non-radiative process if the Ln^{3+} ions are excited to a non-resonance level. Hence the lowest triplet energy state of the ligand should be slightly above the resonance level of the Ln^{3+} ion (Figure 4.3). Energy back transfer (metal to ligand) occurs when the triplet energy state of the ligand is very close to the emission level of the Ln^{3+} ions, while a large energy gap between these two levels leads to a slower EnT process. Considering all these above, the ligand is then chosen with the energy gap between the singlet state and the triplet state to be 5000 cm^{-1}, and the gap between the triplet state of the ligand and the emissive level of the Ln^{3+} ions to be 2500-3000 cm^{-1}.[366] The organic ligand must be precisely tuned to maximize the energy transfer from the ligand to the metal ions and minimize the energy back transfer.[360, 368, 370]

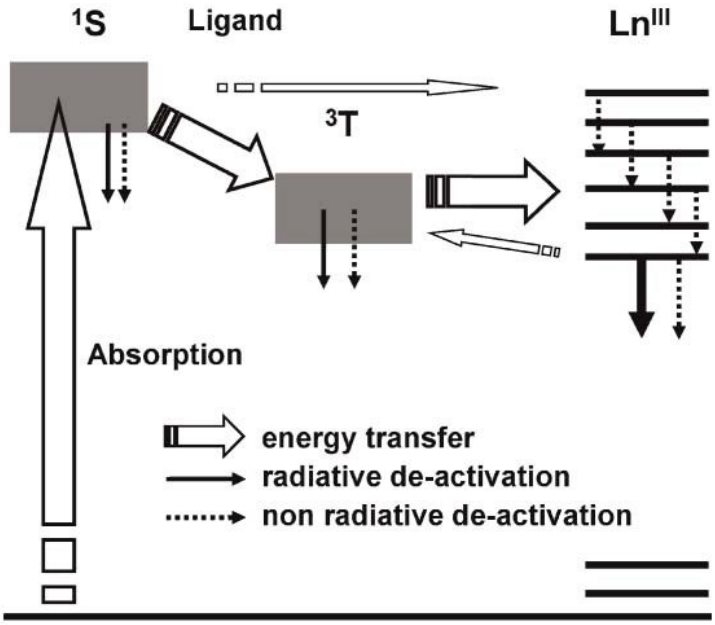

Figure 4.3 Simplified diagram showing the energy transfer process from ligand to metal ions during the sensitization process[368]

Terbium-based MOFs are widely applied as fluorescence sensing probes for the detection of a wide range of substances, due to their strong, characteristic green emission at around 544 nm. In these applications, luminescence quenching is widely utilized in the sensing process. Inorganic metal ions can be detected by Tb-MOF. For example, Gao *et al*. synthesized a Tb-MOF through the solvothermal reaction of 3,5-di(2',4'-dicarboxylphenyl) benzoic acid (H_5DBA) with terbium nitrate.[371] The resulting Tb-MOF is a microporous 3D framework, consisting of two DBA^{5-} ligand anions, four crystallographic independent Tb^{3+} cations, two hydroxyl groups, and three coordinating water molecules in each asymmetric unit (Figure 4.4). Upon excitation at 351 nm, this Tb-MOF exhibits characteristic emissions at 491, 546, 586 and 621 nm. Subsequently, this Tb-MOF was investigated on the detection of Fe^{3+}, $Cr_2O_7^{2-}$ and H_2O_2 in aqueous solution. The luminescence is significantly quenched when Fe^{3+} ions are presented in water, and the quench mechanism is attributed to the competitive absorption effect. Fe^{3+} ions act as a shield, absorbing excitation light in the range of 260 - 398 nm, thus suppressing the energy absorption process of the Tb-MOF. The same mechanism is also applied in sensing $Cr_2O_7^{2-}$ anions, which absorb excitation light as well to block the frameworks from absorbing energy to become excited. Additionally, this Tb-MOF can also be used for the detection of H_2O_2 in aqueous solution. The good linear relationship in the range between 0.1 and 300 μM suggests that this MOF has strong

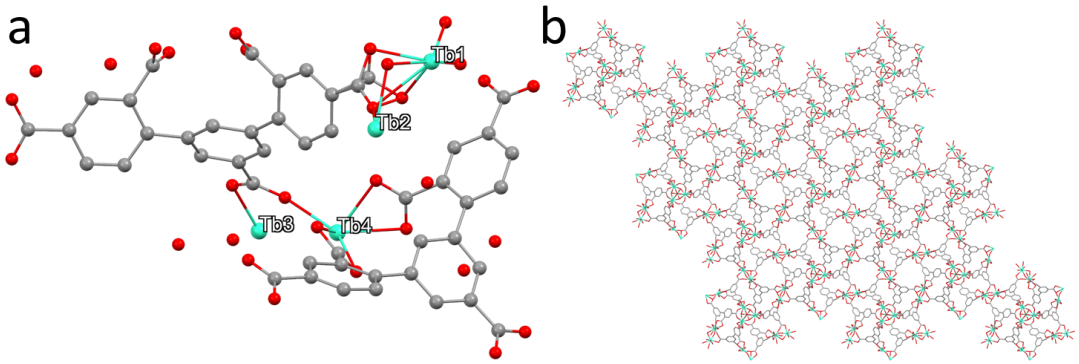

Figure 4.4 a) Asymmetric unit of the Tb-MOF consisting of four types of Tb^{3+} cations and two DBA^{5-} ligand anions; b) packing diagram of the Tb-MOF. C: grey, O: red, Tb: cyan. Figure drawn using published crystal data from Gao and co-workers.[371]

potential in H_2O_2 detecting applications. The quench process might involve the formation of H-bonds between the frameworks and H_2O_2 molecule, and such interactions affect the partial EnT from the ligand to Tb^{3+} ions, thus leading to the luminescence quench.

Apart from metal ions, organic molecules have also been detected by Tb-based MOFs. As illustrated by Zhang *et al*., a Tb-based MOF is synthesized to detect tetracycline (TC) which is often used to prevent inflammation in animals.[372] Solvothermal reaction of terbium nitrate and 5-(pyridine-4-ylmethoxy) isophthalic acid (H_2L) afforded colourless block crystals, and the crystal structure was then determined by SCXRD measurement and shown in Figure 4.5. This Tb-MOF also exhibits characteristic emission peaks at 491, 547, 589 and 623 nm upon excitation at 330 nm. The presence of TC in an aqueous solution can cause a decrease in the fluorescence intensity, and only after 2 mins the intensity reaches a constant value. The luminescence quench is caused by several factors. The absorption spectra of the TC significantly overlap with the excitation spectra of the Tb-MOF, indicating that TC molecules can absorb excitation light to suppress the energy absorption efficiency of the Tb-MOF. In addition, the interactions between -OH or $-NH_2$ groups in TC molecules and pyridine N atoms from the frameworks may affect the EnT process from ligand to Tb^{3+} ions. These cumulative effects of these interactions result in a low detection limit (184 nmol/L) towards TC in aqueous solution.

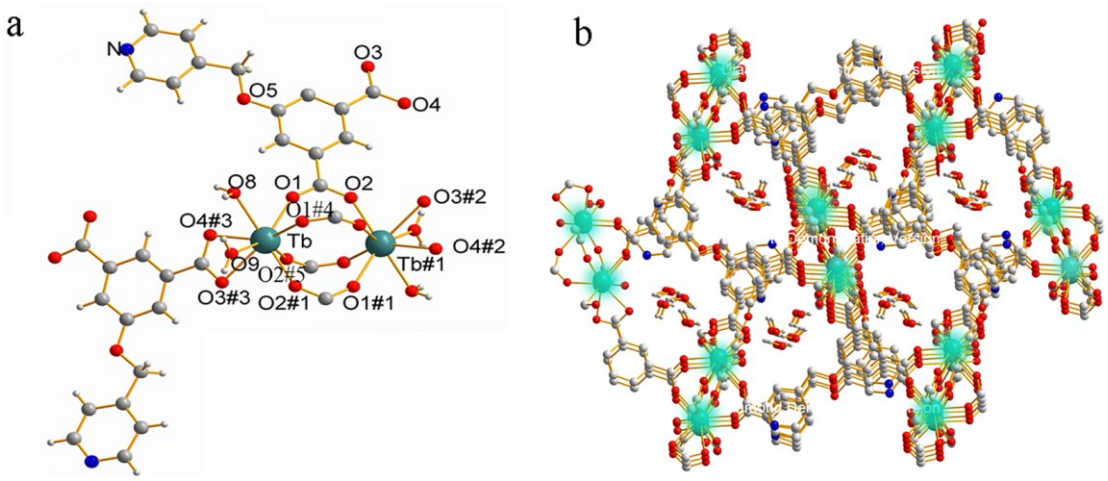

Figure 4.5 a) Crystal structure of the Tb SBU in the Tb-MOF; b) packing diagram.[372]

The collapse of the frameworks can also exhibit a luminescence turn-off effect, Xu *et al.* designed a Tb-based CP using adenosine monophosphate (AMP) and ciprofloxacin (CIP) as ligands.[373] The resulting Tb-CIP/AMP-CP exhibits strong characteristic green emissions from the Tb^{3+} ions, while this emission can be gradually quenched with the increasing concentration of Hg^{2+} ions. This complex has an outstanding performance for the detection of Hg^{2+} in aqueous solution, with a detection limit of 0.16 nM. The AMP ligand has a stronger affinity towards Hg^{2+} than Tb^{3+} ions, leading to the break of the coordination bond between the AMP ligand and Tb^{3+} ions (Figure 4.6). The water molecules are then coordinating with Tb^{3+} ions, causing O-H vibrational quench.

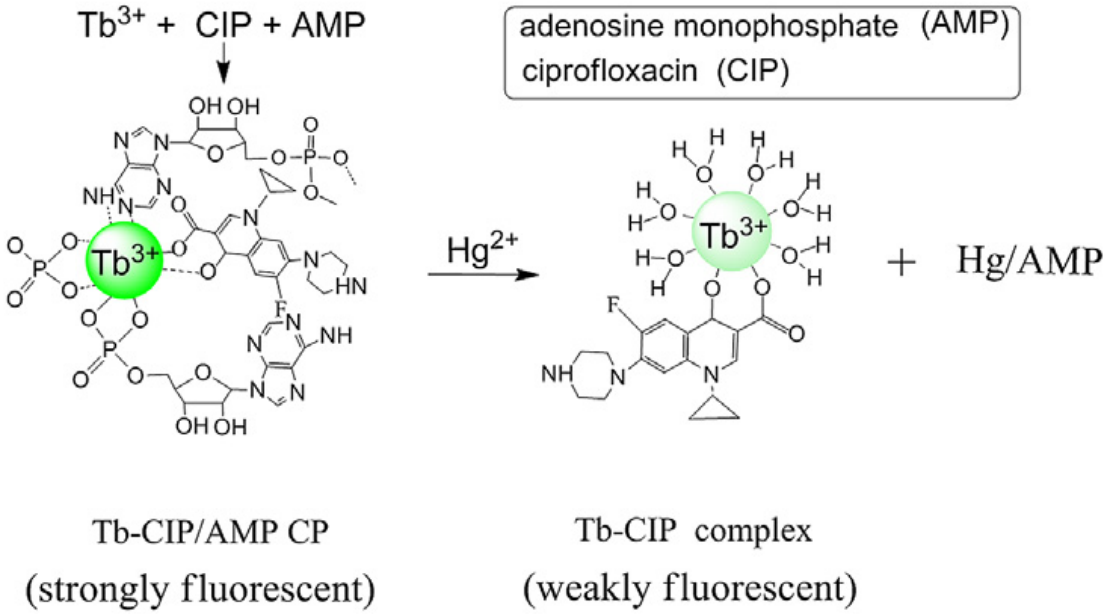

Figure 4.6 Chemical structure of the Tb-CIP/AMP-CP and sensing Hg^{2+} process.[373]

It is worth noting that luminescence behaviour can be enhanced by analytes as well, and this is often regarded as "turn-on" or "signal-on" effect.[374] For example, Chen *et al*. reported the synthesis of a Tb-MOF using dppa as the linker [H_4dppa = 5-(3'4'-dicarboxylphenoxy) isophthalic acid, Figure 4.7].[375] The crystals were obtained through hydrothermal method and were analysed to be [(Tb(dppa)(H_2O)$_2$)·dima·H_2O·0.5O] by SCXRD studies (dima = dimethylamine). This Tb-MOF was found to exhibit multi-responsive ability to detect Pb^{2+}, $Cr_2O_7^{2-}$, $B_4O_7^{2-}$, aniline, nitrobenzene and cefixime. There is a significant fluorescence enhancement when this Tb-MOF is treated with Pb^{2+} ion, and the enhancement mechanism

could be attributed to the interactions between organic ligand and Pb^{2+} ions, which facilitate the electron transfer to increase the overall luminescence intensity.

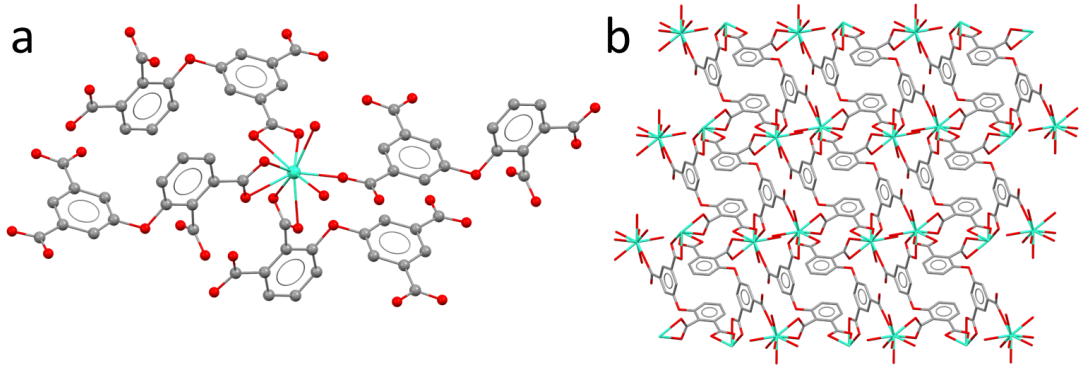

Figure 4.7 a) Coordination environment of the Tb^{3+} ions with dppa ligands, b) packing diagram of the Tb-MOF. C: grey, O: red, Tb: cyan. Figure drawn using published crystal data from Chen and co-workers.[375]

Tb-based MOFs can also be used in biology field, such as for the detection of bacterium. 2,6-Pyridine dicarboxylic acid (DPA) is recognized as a biomarker of Bacillus anthracis. Yang and co-workers synthesized a Tb-MOF using DHBDC (2,5-dihydroxy terephthalic acid) as the ligand.[376] The luminescence spectra of the Tb-MOF were recorded, with no characteristic emissions observed from Tb^{3+} ions. This phenomenon was attributed to the large energy gap between the first excited triplet state of the ligand and the resonance

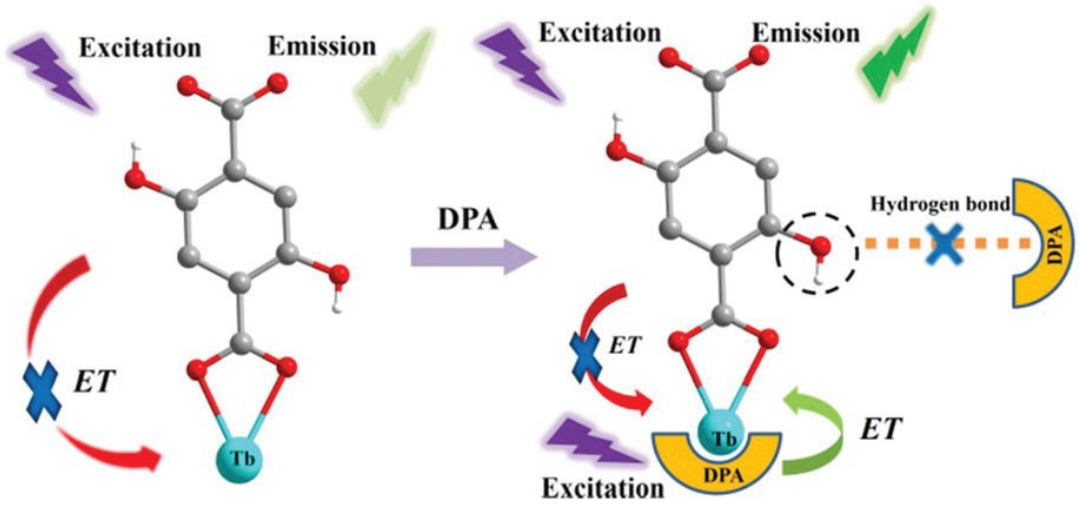

Figure 4.8 Proposed mechanism for the sensing of DPA by Tb-MOF.[376]

energy level of the Tb^{3+} ion, resulting in low EnT efficiency or even no EnT occurrence. When the DPA molecule is present, the characteristic emissions of the Tb^{3+} ions appear, showing a "turn-on" behaviour. In this process, the DPA molecule acts as an "antenna", transferring energy to Tb^{3+} ions through the coordination interactions between the Tb^{3+} ions and carboxylate groups from the DPA molecule (Figure 4.8), and the small energy difference between the triplet state of the DPA ligand and the $^5D_4$ level of Tb^{3+} ions allow for such an EnT process.

Pb^{2+} is undoubtedly considered toxic to humans. Due to its long biological half-life of 10 to 30 years,[377] lead will accumulate in the human body, causing serious health problems such as anaemia, cancer, neuro and reproductive system damage, even at lower concentrations.[378] Hence it is vital important to develop effective methods to detect Pb^{2+} in the environment to prevent human exposure to lead pollution. Traditional methods for metal detecting Pb^{2+} such as ICP-AES, XRF etc. can usually provide reliable results.[359] However, these measurements usually involve expensive equipment and complicated procedures.[371] Currently, fluorescence detection has been widely studied because these types of sensors have advantages such as simple operation procedure, high sensitivity towards the analyte, short response time and high selectivity when applied in complicated conditions.[359, 376] Tb-MOF-based fluorescence sensors distinguish from them due to its unique luminescence properties from Tb^{3+} ions, allowing the observation of change through naked eye, as well as the turnable functionalized ligands which can be decorated with various functional group to achieve high selectivity and sensitivity to environmental changes.[379]

The versatility of Tb-MOFs based sensors has been demonstrated in the preceding text. These examples highlight the importance of investigating the sensing performance of IMP-33-Tb towards Pb^{2+} ions in aqueous environment. In the following section, the sensing performance will be illustrated, and the potential sensing mechanism will be discussed.

4.2 Tb-MOF as a sensing agent to detect Pb^{2+}

4.2.1 Photoluminescence Properties of IMP-33-Tb

The solid-state photoluminescence properties of **IMP-33-Tb** were studied with a view to its role in the detection of metal cations. The sample was prepared by adding 3 mg finely ground **IMP-33-Tb** powder to 3 mL water in a glass vial, followed by treatment in an ultrasound bath for 20 mins. The suspension was then transferred to a cuvette to conduct photoluminescence measurements. Upon excitation at 330 nm, **IMP-33-Tb** displays characteristic luminescence emission peaks at 488 nm, 545 nm, 585 nm, and 621 nm, corresponding to the typical f-f transitions of the Tb^{3+} ions ($^5D_4 \rightarrow {}^7F_6$, $^5D_4 \rightarrow {}^7F_5$, $^5D_4 \rightarrow {}^7F_4$ and $^5D_4 \rightarrow {}^7F_3$ respectively, Figure 4.9). Quantum yield studies were also carried out and the result shows that the absolute QY of the **IMP-33-Tb** is 24.45%, a comparable value and higher than some Tb-MOFs.[361, 380, 381] Lifetime measurements were conducted as well, and the lifetime of the emission light at 545 nm was found to be 0.65 ms, which belongs to phosphorescence. This value is in good agreement with other Tb-based MOFs reported in the literature.[361, 382, 383]

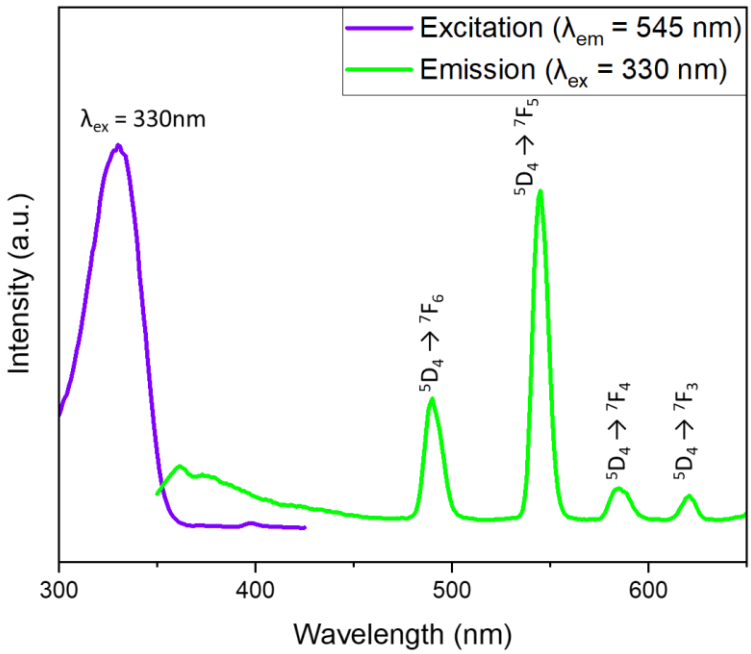

Figure 4.9 Excitation and emission spectra of **IMP-33-Tb**.

The sensing performance of **IMP-33-Tb** towards metal ions was then studied. Aqueous metal nitrate solutions (Na^+, Mg^{2+}, K^+, Ca^{2+}, Mn^{2+}, Co^{2+}, Ni^{2+}, Zn^{2+}, Sr^{2+}, Cd^{2+}, Cs^+, Pb^{2+}) were prepared separately with a concentration of 10 mM. Subsequently 3 mg **IMP-33-Tb** powder was added to the above solutions and the mixtures were sonicated for 20 mins. It can be seen from Figure 4.10 that there is a significant luminescence quench when **IMP-33-Tb** is added to the Pb^{2+} solution (about 90%, quench percentage = $[(I_0 - I)/I_o] \times 100\%$, I_0 and I are the luminescence intensity of the $^5D_4 \rightarrow {}^7F_5$ transitions (545 nm) of **IMP-33-Tb** before and after being treated with metal cations respectively), while other metal cations do not have significant effect on the overall intensity. This phenomenon suggests that **IMP-33-Tb** have the potential to be used as a sensor to detect Pb^{2+} ions in wastewater.

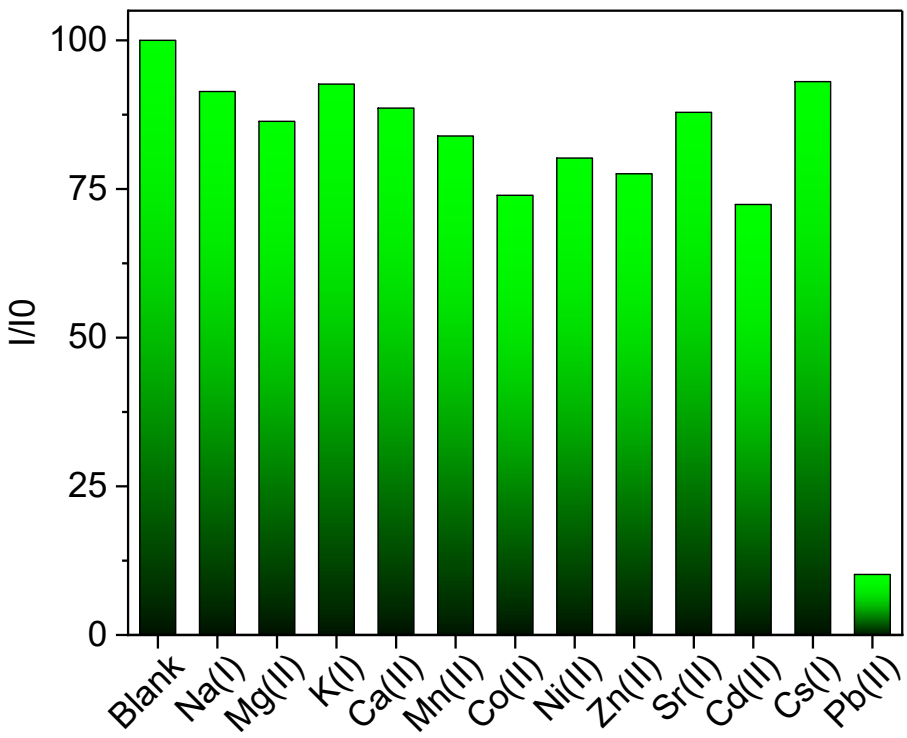

Figure 4.10 Relative luminescence intensity of **IMP-33-Tb** in solutions containing various metal cations (10 mM) at 545 nm.

4.2.2 IMP-33-Tb for Aqueous Pb^{2+} Sensing

Given the fact that the luminescence can be significantly quenched by Pb^{2+}, the sensing

performance and sensitivity of **IMP-33-Tb** towards different concentrations of Pb^{2+} ions were investigated. A series of Pb^{2+} solutions in different concentrations were prepared, and the MOF powders were dispersed into these solutions using the same method as stated above, followed by luminescence measurement. It can be observed from Figure 4.11 that with the increasing Pb^{2+} concentration, the light emission intensity gradually decreases.

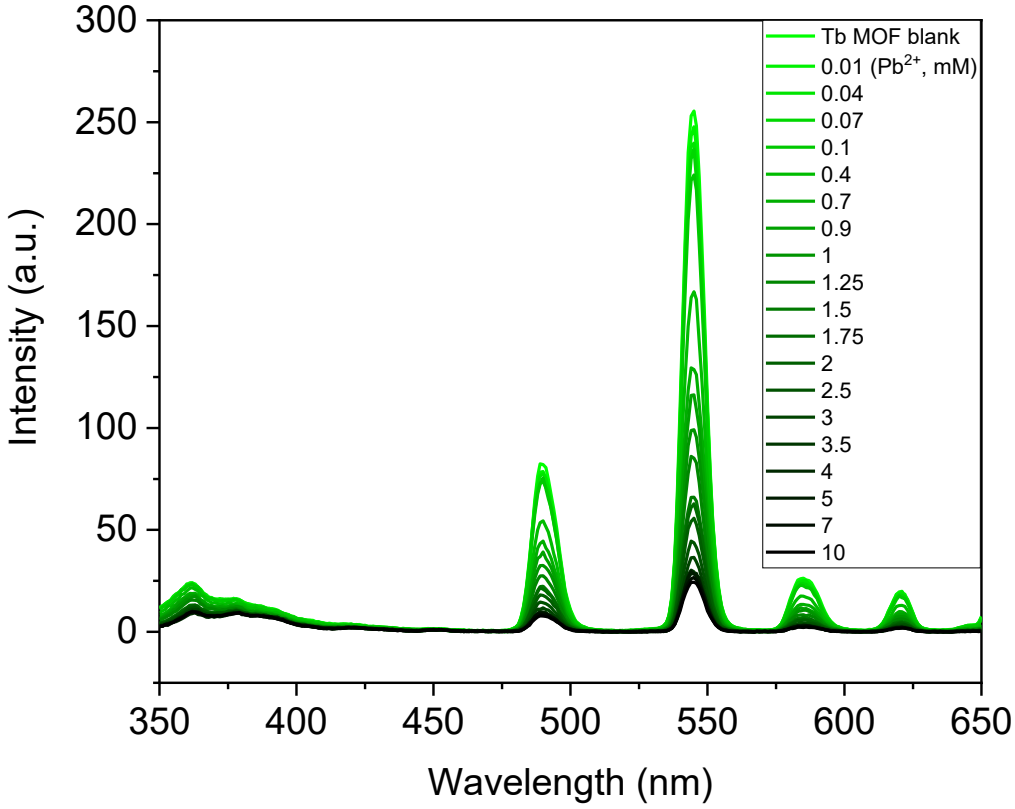

Figure 4.11 Luminescence intensity of **IMP-33-Tb** in Pb^{2+} solution with different concentrations.

To have a better understanding of the quench behaviour, quench efficiency was calculated by the Stern-Volmer (S-V) equation: $I_0/I = 1 + K_{SV}[Q]$, where K_{SV} is the quenching constant, and [Q] is the concentration of the Pb^{2+} ion.[361] The plot in Figure 4.12 shows that there is almost a linear relationship (R^2 = 0.994) between the relative intensity and the Pb^{2+} concentration, in the range between 10^{-2} to 4 mM. The calculated K_{SV} value is 1.80×10^3 M^{-1}, which is well within the expected range reported in other examples (Table 4.1 List of MOFs for Pb^{2+} sensing).

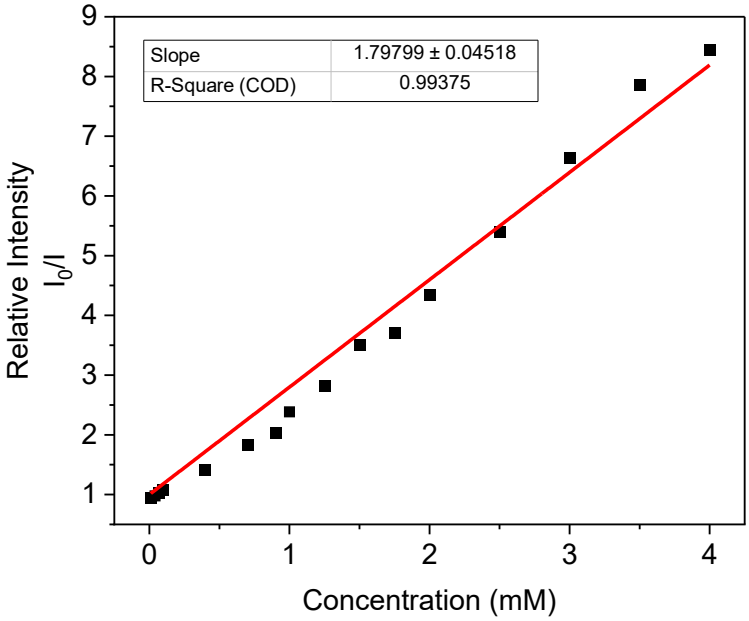

Figure 4.12 Linear relationship between the relative luminescence intensity and Pb^{2+} concentration at 545 nm.

MOF	K_{SV} / M^{-1}	Ref
$[Tb(5\text{-}HiBDC)(H_2O)_5]_n$[a]	1.75×10^4	359
NH_2-MIL-53(Cr)	7.48×10^3	384
$[Cu_2(bdc)_2(bpy)]$[b]	3.91×10^3	385
Ferrocene benzobisimidazole	4.13×10^4	386
Zn-TCPP-MOF[c]	1.60×10^5	387
$[Eu_2(FDC)_3DMA(H_2O)_3]\cdot DMA\cdot 4.5H_2O$[d]	2.97×10^3	378
LMOF-263	5.50×10^4	388
AUBM-3(La)	9.08×10^2	389
$[[Tb(dppa)(H_2O)_2]\cdot dima\cdot H_2O\cdot 0.5O]_n$[e]	8.69×10^3	375
IMP-33-Tb	1.80×10^3	This work

Table 4.1 List of MOFs for Pb^{2+} sensing, [a]5-HiH_2BDC = 5-hydroxy-iso-benzenedicarboxylic acid; [b]H_2bdc = benzene-1,4-dicarboxylic acid, bpy = 4,4'-bipyridine. [c]H_2TCPP = Meso-Tetra(4-carboxyphenyl) porphine. [d]H_2FDC = 9,9-dimethyl-2,7-fluorenedicarboxylic acid, DMA = dimethylacetamide. [e]H_4dppa = 5-(3'4'-dicarboxylphenoxy) isophthalic acid, dima = dimethylamine.

4.2.3 Mechanism Discussion

Based on this well-fitted linear relationship, the potential quench mechanism was then investigated. Different mechanisms are discussed in section 4.1 (*vide supra*). Most of the photoluminescence behaviour of Tb-based MOFs originates from the Tb^{3+} ions. Metal ion-based emission behaviour can be quenched through dynamic processes, in which the analytes suppress the EnT process through interactions with the framework. Another way to affect the EnT process is the competitive absorption mechanism, where the analytes absorb the emission lights from the MOF or act as a shield to prevent the MOF from absorbing excitation light.[374, 390] These two processes can both reduce the overall light emission intensity. UV-vis spectra were recorded to check if there is any competitive absorption mechanism. The result is shown in Figure 4.13, and it is evident that the absorption spectra of Pb^{2+} solution are non-overlapping with **IMP-33-Tb** at 330 and 545 nm, excluding the competitive absorption mechanism caused by the absorption of excitation light or emission light by Pb^{2+} ions. Luminescence lifetime is an intrinsic

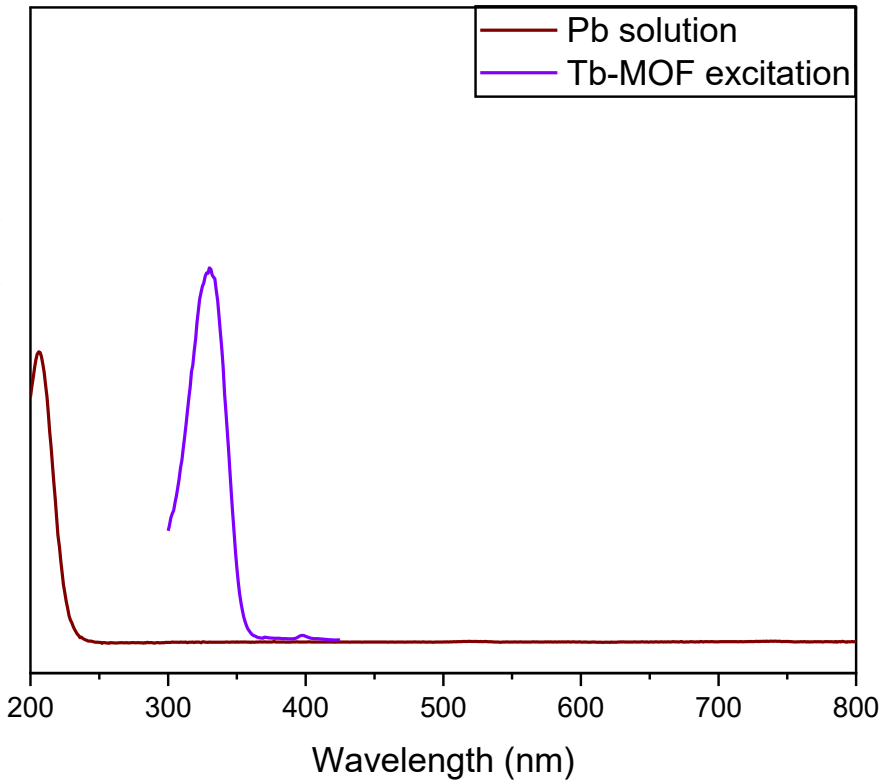

Figure 4.13 UV-vis absorption spectra of Pb^{2+} solution and **IMP-33-Tb** excitation spectra.

property that will change if the analyte is interacting with the framework. The lifetime of Pb^{2+} (0.1 mM) treated **IMP-33-Tb** (**Pb@IMP-33-Tb**) decreased from 0.65 ms to 0.55 ms, and this result suggests that Pb^{2+} ions affect the EnT process in the framework, which might originate from the interactions between Pb^{2+} ions phenolic O atoms as the GeO_6 centred framework is negatively charged.[359]

The process involved in this dynamic mechanism is reversible, thus the photoluminescent behaviour will recover with the removal of the analyte.[391] Pb@**IMP-33-Tb** was then washed with water three times, followed by luminescence measurement. It can be seen from Figure 4.14 that the intensity returns to about 100%, suggesting that there is no loss of MOF performance during the sensing process. PXRD measurement was also carried out to check the MOF structure (Figure 4.15), and the result indicates that **IMP-33-Tb** maintained its original structure after the sensing experiments. This result excludes the presence of a static quench mechanism because either the formation of a non-fluorescent complex or the collapse of the framework will lead to peak shift or loss of crystallinity.

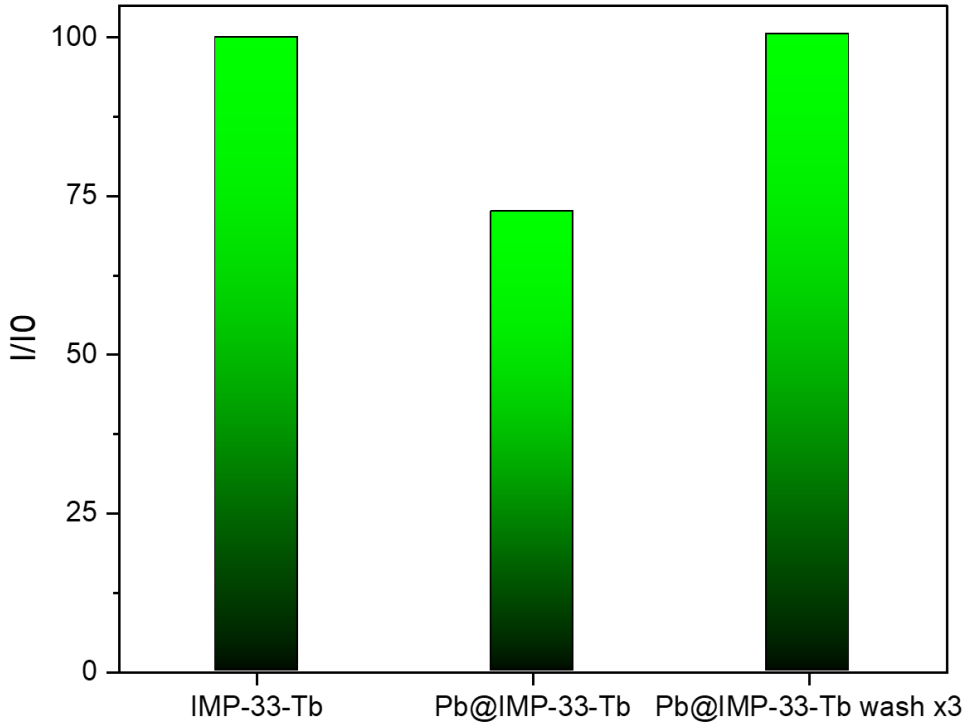

Figure 4.14 Relative luminescence intensity of freshly prepared **IMP-33-Tb**, Pb (0.1 mM) treated **IMP-33-Tb** (Pb@**IMP-33-Tb**) and washed Pb@**IMP-33-Tb** for three times.

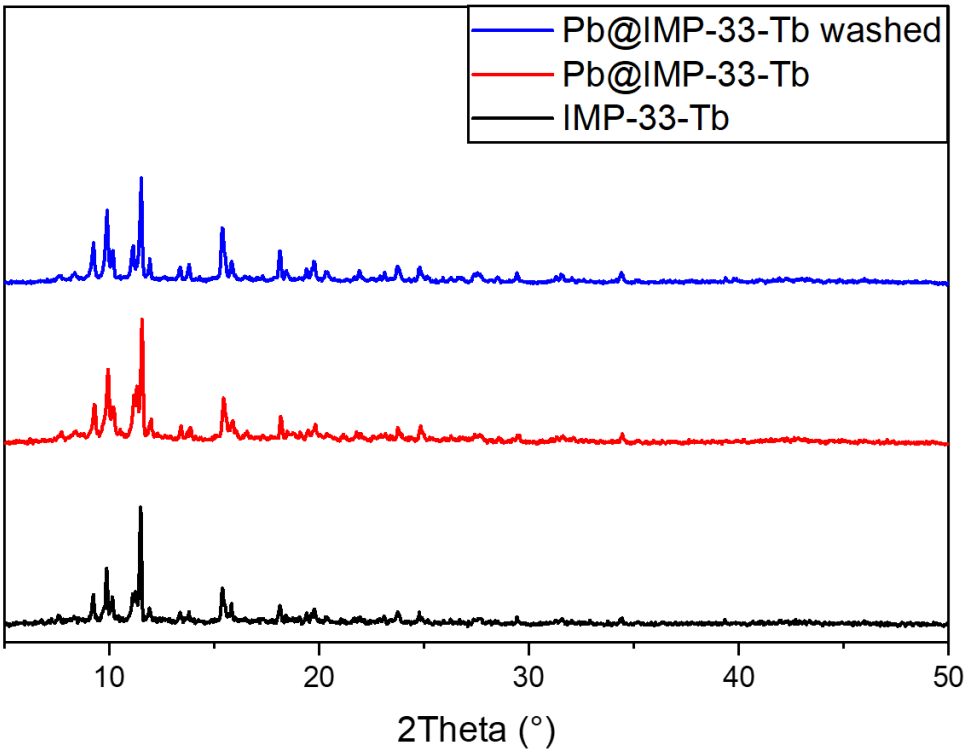

Figure 4.15 PXRD results of freshly prepared **IMP-33-Tb**, Pb treated **IMP-33-Tb** (Pb@**IMP-33-Tb**) and washed Pb@**IMP-33-Tb** for three times.

4.3 Conclusions

IMP-33-Tb has been characterized for its luminescence properties under UV excitation, and sensing performance towards Pb^{2+} ion. **IMP-33-Tb** exhibits characteristic emission with a bright green light upon excitation at 330 nm. The green light originates from the electron transition $^5D_4 \rightarrow {}^7F_5$, releasing energy to emit the light with a wavelength of 545 nm. The lifetime was measured to be 0.65 ms, and this value is consistent with phosphorescence occurring.

Then the sensing performances of **IMP-33-Tb** towards metal ions were studied. It was found that the Pb^{2+} ion can significantly quench the luminescent intensity, with a 90% decrease compared with the original intensity. The sensing sensitivity towards Pb^{2+} ions was also investigated, with a linear relationship between the relative intensity and Pb^{2+} concentration in the range between 0.01 to 4 mM. Such a relationship can be expressed by S-V equation, with a quench efficiency of 1.80×10^3 M^{-1}.

Possible quench mechanism at lower concentrations was determined through lifetime measurement, UV-vis and PXRD studies. The reduction in phosphorescence lifetime suggests that the presence of Pb^{2+} ions affects the EnT process in the framework, which might be due to the interactions between Pb^{2+} ions and phenolic O atoms, as the GeO_6 centre in the framework is negatively charged. The competitive absorption mechanism is excluded by UV-vis measurement, as there is no overlap between the absorption spectra of Pb^{2+} solution and **IMP-33-Tb**.

The overall intensity can be recovered by the removal of the Pb^{2+} ion, and this phenomenon suggests that there is no formation of non-fluorescent complexes or collapse of the framework. The overall structure integrity after sensing was also checked by PXRD studies. There was no evident change in the pattern after the MOF was treated with Pb^{2+} solution. It is believed that at lower concentrations there is no static quench mechanism involved in this quench process from these results. **IMP-33-Tb** have demonstrated the potential to be applied as a sensor to detect Pb^{2+} ions in aqueous environment.

Chapter 5: Conclusions

Previous reports have shown that MOFs constructed using hexacoordinated Si/Ge linkers, mainly SiF_6 and GeF_6 anions, can have promising gas sorption and separation applications. Although a smaller number of frameworks containing SiO_6/GeO_6 octahedral centres have been previously synthesized, these systems have not been widely explored. Current research on hexacoordinated Si/Ge compounds can be categorized into two areas; the first area comprises Si/Ge centres coordinated with oxalate acid type compounds; the second area is triscatechol-based silicate/germanates. In this work the incorporation of terminal carboxylate groups to these compounds has been investigated in order to facilitate their coordination with metal ions, thus enabling the generation of a novel series of MOFs.

Based on this hypothesis, three novel types of hexacoordinated Si/Ge connectors (**L1**, **L2**, **L3**, Figure 5.1) have been prepared. **L1** linkers feature three oxalate groups. As all these linkers are negatively charged, counter-cations are required to balance the charge. By varying the counter-cation (mostly ammonium type cations), different H-bonded contacts can be formed, and in some cases, the presence of multiple donors in the ammonium cations facilitate the formation of extended H-bonded networks, such as those observed in compounds **5**, **9**, **11**. **L1** linkers were shown to be not suitable for MOF synthesis due to poor stability. The water stability of **L1-Si** has limited its synthesis in situations where water is present in the metal salt reagents. Although the improved water stability of **L1-Ge** linkers

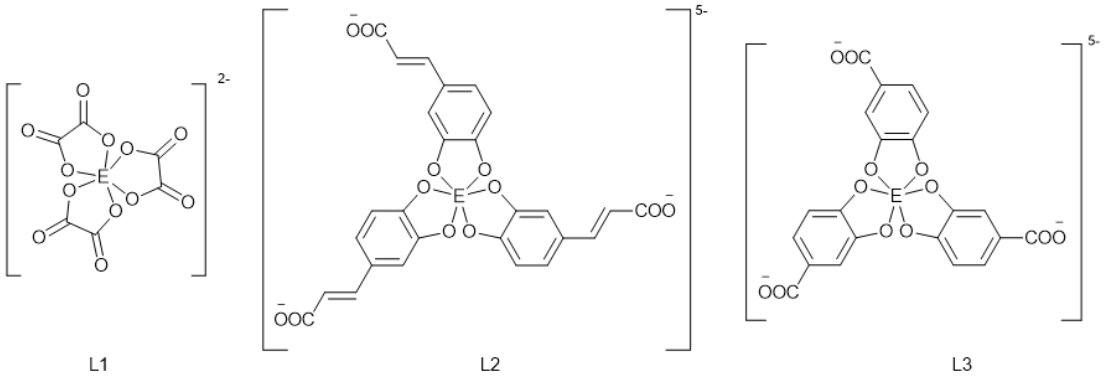

Figure 5.1 Structure of **L1**, **L2**, and **L3** type linkers. (E = Si/Ge)

allows such reactions, the oxalate groups tend to detach from the Ge centre and coordinate with metal cations to form metal oxalate salts. Further investigations need to be done to explore the stability of the linker in various solvent systems.

L2 linkers were synthesized based on triscatechol-type compounds, but with additional side arm and terminal COOH groups attaching to the phenyl ring. These compounds were successfully prepared and characterised by NMR, IR, and MS studies. Due to the non-crystalline nature of these connectors, detailed structures of these linkers were not able to be obtained, but these compounds are still potential trigonal building blocks. Additionally, the extended side arm allows the decoration with functional groups or extending the length for the synthesis of MOFs with various pore sizes.

L3 linkers have shorter side arms compared to **L2**, thus reducing the overall degree of flexibility leading to more rigid structures which tend to crystallise more easily. These linkers were prepared successfully and characterised by NMR, IR, and MS studies. The increased crystallinity was reflected through PXRD studies as well as the success of crystal growth of compounds **16** and **20**. However, the Si linkers undergo hydrolysis in water, thus care should be taken to eliminate the presence of water in the MOF synthesis process. The increased water stability of all Ge linkers allows their formation of MOFs with RE metal nitrate. A series of RE MOFs (**IMP-33-Ln** and **IMP-34-Sc**, Ln = Y, Gd, Tb, Dy, Ho, Er, Tm, Yb, Lu) were successfully prepared through the hydrothermal reaction of rare earth metal nitrate salts with **20** [$(Et_3NH)_2$(**L3-Ge**)]. **IMP-33-Y** comprises bimetallic SBU coordinating to six carboxylate groups and three connected ligands, and such arrangements generate a rare *flu*-3,6-*C*2/*c* topology. **IMP-33-Ln** has identical structures to **IMP-33-Y**, as confirmed through PXRD measurements as well as the single crystal study on **IMP-33-Dy**. **IMP-34-Sc** comprises anionic frameworks consisting of six-connected trimetallic SBUs and three connected ligands. Although the Sc-MOF has a different SBU, the overall connectivity remains the same to yield a *flu*-3,6-*C*2/*c* topology. The bimetallic SBU in **IMP-33-Ln** results in a higher anionic network charge of 4- vs 1- in **IMP-34-Sc**. These MOFs are the first examples containing GeO_6-based connectors.

IMP-33-Tb emits a bright green light under UV excitations, and the photoluminescence property was then studied. This Tb-MOF exhibits characteristic emissions at 488 nm, 545 nm, 585 nm, and 621 nm, corresponding to the typical f-f transitions of the Tb^{3+} ions ($^5D_4 \rightarrow {}^7F_6$, $^5D_4 \rightarrow {}^7F_5$, $^5D_4 \rightarrow {}^7F_4$ and $^5D_4 \rightarrow {}^7F_3$ respectively) upon excitation wavelength at 330 nm. Pb^{2+} is considered toxic to the human body and the environment, hence it is of great importance to develop sensitive sensors to detect Pb^{2+} in aqueous conditions. The sensing abilities of **IMP-33-Tb** towards metal cations were investigated, and the presence of Pb^{2+} ions in an aqueous solution can significantly quench the emission. There is a linear relationship between the luminescence intensity and the concentration of Pb^{2+} ions, with a quench efficiency of 1.80×10^3 M^{-1}. The quench mechanism was determined to be a dynamic quench mechanism through UV-vis, PL, and PXRD studies, and can be attributed to the interactions between the negatively charged framework and the Pb^{2+} ions, which affect the EnT process between the ligand and Tb^{3+} ion. The good sensing selectivity and sensitivity towards Pb^{2+} ions suggested that **IMP-33-Tb** could be used as a sensor for the detection of Pb^{2+} in aqueous solutions.

Chapter 6: Experimental

6.1 Materials and General Methods

All chemicals were commercially available (Sigma-Aldrich, Fluorochem, VWR, TCI, Alfa Aesar) unless specified, and were used without further purification. Anhydrous solvent was obtained under a nitrogen atmosphere from a PuresSolv multiple dispensing solvent drying system. All "water" or "H_2O" refer to deionized water. Reactions under N_2 were performed using standard Schlenk line techniques, and all glassware was dried in a 120 °C oven overnight before use. Linker and MOF samples were synthesized using Memmert UFE500 programmable oven or Grant Instruments QBH2 heating blocks. Mass spectra results were obtained by Dr Lisa Haigh and Ms Malgorzata Puchnarewicz using ESI methods. Thermogravimetric analysis (TGA) was carried out on a Perkin Elmer TGA 8000 instrument under a nitrogen flow (50 mL/min) over the range of 30-600 °C at a heating rate of 10 °C/min. Photoluminescence spectra were recorded on a Cary Eclipse Fluorescence Spectrophotometer and the slit width of both the source and detector for the excitation and the emission were kept at 5 nm to maintain consistency. All PL data were recorded using Hellma® absorption cuvette made from high performance quartz glass, with a spectral range of 200-2,500 nm, pathlength 10 mm, and a chamber volume of 3,500 µL. Infrared spectra were recorded on an Agilent Cary 630 FTIR Spectrometer. UV-vis spectrum was recorded on a Cary 5000 UV-Vis-NIR Spectrophotometer.

^{1}H, ^{13}C, and ^{29}Si NMR spectra were recorded on a Bruker spectrometer (^{1}H 400 MHz, ^{13}C 101 MHz, ^{29}Si 80 MHz). For MOF analysis, MOF samples were digested in 6% NaOD in D_2O. NMR results were analysed in MestReNova software. PXRD results were collected on a Bruker 2D Phaser machine with Cu-Kα radiation (1.51184 Å) between 5° and 50° (2θ). Data (*.raw*) were converted to *.csv* format for analysis using PowDLL Converter[392] software. SCXRD results were collected on an Oxford Diffraction Xcalibur 3 diffractometer (compound **5**, **6**, **7**, **9**, **11**, **12**, **16**, **25**) by Dr Andrew White at Imperial

College London, and a Rigaku 007HF or Rigaku FR-E+ diffractometer (all MOFs and compound **20**, **22, 23**, green crystals) by Dr Peter Horton at UK National Crystallography Service, Southampton. The topology of the MOFs was analysed by TopCryst[342] website. Simulated (calculated) powder patterns were generated by Mercury[275] software from single crystal data.

Hydrogen-bond distances are the distance between donor to acceptor, unless specified. Such as O(H)···O is the distance two O atoms.

6.2 L1 type linkers

Bis(tetraethylammonium) tris(oxalato)silicate $[Et_4N]_2$[L1-Si] (Compound 1)

Freshly prepared $Ag_2C_2O_4$ (4.60 g, excess, see Section 6.5) was added to dry acetone (300 mL) and the flask was covered with aluminium foil. Then $SiCl_4$ (0.58 mL, 5 mmol) and Et_4NBr (2.102 g, 10 mmol) were added and the solution was stirred for 1 h at room temperature. The solution was filtered and diethyl ether (~400 mL, anhydrous) was added to the filtrate, which resulted in the precipitation of the crude product. This solid was filtered under vacuum, redissolved in absolute ethanol. The solid residue was removed by filtration, and the filtrate was finally removed under vacuum at 40°C for 2 h to give a colourless crystalline product, mp. 248-252°C (decomp.). Yield: 2.41 g, 87%. ^{1}H NMR (400 MHz, D_6-DMSO): δ(ppm) = 3.21 (q, 8H, J = 8 Hz, C**H**$_2$), 1.17 (t, 12H, J = 8 Hz C**H**$_3$); ^{13}C NMR (101 MHz, D_6-DMSO): δ(ppm) = 160.16 (**C**=O), 51.88 (**C**H$_2$), 7.53 (**C**H$_3$); ^{29}Si NMR (80 MHz, D_6-DMSO): δ(ppm) = -174.09; IR (ATR): ν (cm^{-1}) = 1739, 1674, 1326, 1236, 907, 850, 823, 643, 621, 561, 466.

Bis(tetrabutylammonium) tris(oxalato)silicate $[Bu_4N]_2$[L1-Si] (Compound 2)

Freshly prepared $Ag_2C_2O_4$ (4.70 g, excess) was added to dry acetone (300 mL) and the flask was covered with aluminium foil. Then $SiCl_4$ (0.58 mL, 5 mmol) and n-Bu_4NBr (3.224 g, 10 mmol) were added and the solution was stirred for 1 h at room temperature. The solution was next filtered, and the filtrate was evaporated to dryness. The crude product was redissolved in absolute ethanol. The solid residue was removed by filtration, and the filtrate was removed under vacuum at 40°C for 2 h to give a colourless solid, mp. 105°C. Yield: 3.33 g, 86%. ^{1}H NMR (400 MHz, D_6-DMSO): δ(ppm) = 3.17 (m, 8H, NC**H**$_2$CH$_2$CH$_2$CH$_3$), 1.57 (m, 8H, NCH$_2$C**H**$_2$CH$_2$CH$_3$), 1.32 (m, 8H, NCH$_2$CH$_2$C**H**$_2$CH$_3$), 0.94 (t, 12H, J = 8 Hz NCH$_2$CH$_2$CH$_2$C**H**$_3$); ^{13}C NMR (101 MHz, D_6-DMSO): δ(ppm) = 160.14 (**C**=O), 57.97 (N**C**H$_2$CH$_2$CH$_2$CH$_3$), 23.52 (NCH$_2$**C**H$_2$CH$_2$CH$_3$), 19.68 (NCH$_2$CH$_2$**C**H$_2$CH$_3$), 13.98 (NCH$_2$CH$_2$CH$_2$**C**H$_3$); ^{29}Si NMR (80 MHz, D_6-DMSO): δ(ppm) = -174.08; IR (ATR): ν (cm^{-1}) = 2956, 1737, 1677, 1327, 1241, 906, 850, 827, 641, 617, 559, 492.

Bis(diethylammonium) tris(oxalato)silicate $[Et_2NH_2]_2$[L1-Si] (Compound 3)

All synthesis processes were carried under an atmosphere of dry N_2. Oxalic acid (1.351 g, 15 mmol) and $Si(OMe)_4$ (0.74 mL, 5 mmol) were added to dry THF (30 mL). Et_2NH (1.04 mL, 10 mmol) was then added to the stirred solution and the mixture was heated under reflux for 3 h. The supernatant was removed after the mixture was cooled down to room temperature and the oily residue was dried under vacuum to give white solid. Next, the solid was dissolved in boiling ethanol and then recrystallized by cooling down the solution to room temperature. The crystallized product was isolated by filtration, washed with diethyl ether before drying under vacuum at 40°C for 2 h to give a colourless product. Yield: 1.74 g, 79%. ^{1}H NMR (400 MHz, D_6-DMSO): δ(ppm) = 8.40 (br, 2H, N**H**$_2$), 2.93 (q, 4H, J = 8 Hz, C**H**$_2$), 1.16 (t, 6H, J = 8 Hz, C**H**$_3$); ^{13}C NMR (400 MHz, D_6-DMSO): δ(ppm) = 160.15 (**C**=O), 41.82 (**C**H$_2$), 11.48 (**C**H$_3$); ^{29}Si NMR (80 MHz, D_6-DMSO): δ(ppm) = -174.03; IR (ATR): ν (cm^{-1}) = 1742, 1705, 1673, 1325, 1236, 915, 853, 828, 640, 620, 553, 494, 470.

Bis(triethylammonium) tris(oxalato)silicate $[Et_3NH]_2$[L1-Si] (Compound 4)

All synthesis processes were carried under an atmosphere of dry N_2. Oxalic acid (1.351 g, 15 mmol) and $Si(OMe)_4$ (0.74 mL, 5 mmol) were added to dry THF (30 mL). Et_3N (1.39 mL, 10 mmol) was then added to the stirred solution and the mixture was heated under reflux for 3 h. The supernatant was removed after the mixture was cooled down to room temperature and the oily residue was dried under vacuum to give white solid. Next, the solid was dissolved in boiling ethanol and then recrystallized by cooling the solution to room temperature. The crystallized product was isolated by filtration, washed with diethyl ether before drying under vacuum at 40°C for 2 h to give a colourless product, mp. 110-112°C. Yield: 2.40 g, 96%. ^{1}H NMR (400 MHz, D_6-DMSO): δ(ppm) = 8.83 (br, 1H, N**H**), 3.10 (q, 6H, J = 8 Hz, C**H**$_2$), 1.17 (t, 9H, J = 8 Hz C**H**$_3$); ^{13}C NMR (101 MHz, D_6-DMSO): δ(ppm) = 160.15 (**C**=O), 46.22 (**C**H$_2$), 9.06 (**C**H$_3$); ^{29}Si NMR (80 MHz, D_6-DMSO): δ(ppm) = -174.04; MS (ESI-): calcd. (monoisotopic) for $[C_6O_{12}Si+H]^-$ m/z = 292.9237, found m/z = 292.9250; IR (ATR): ν (cm^{-1}) = 1737, 1675, 1332, 1247, 909, 852, 824, 640, 621, 554,

495, 472.

Tetramethylethylenediammonium tris(oxalato)silicate [H_2TMEDA][L1-Si] (Compound 5)

All synthesis was carried out under N_2. Methanol was dried using 3Å molecule sieve before use. To a stirred solution of methanol (25 mL) with oxalic acid (1.351 g, 5 mmol) $Si(OMe)_4$ (0.74 mL, 5 mmol) was added. N,N,N',N'-Tetramethylethylenediamine (0.75 mL, 5 mmol) was then added and the mixture was kept stirring under reflux for 3h. After cooling down to room temperature, the white precipitate was isolated by filtration, followed by washing with diethyl ether and finally dried under vacuum at 60°C for 3h. Yield: 1.89 g, 92%. ^{1}H NMR (400 MHz, D_6-DMSO): δ(ppm) = 9.52 (br, 2H, N**H**), 3.40 (d, 4H, C**H**$_2$), 2.83 (s, 12H, C**H**$_3$); ^{13}C NMR (101 MHz, D_6-DMSO): δ(ppm) = 160.16 (C=O), 51.42 (**C**H_2), 43.44 (**C**H_3); ^{29}Si NMR (80 MHz, D_6-DMSO): δ(ppm) = -173.99; MS (ESI-): calcd. (monoisotopic) for $[C_6O_{12}Si+H]^-$ m/z = 292.9237, found m/z = 292.9240; IR (ATR): ν (cm^{-1}) = 1740, 1674, 1323, 1248, 910, 852, 823, 643, 621, 556, 496, 466.

Single crystals of [H_2TMEDA][**L1-Si**] were obtained through the vapour diffusion method. 20 mg compound **5** was dissolved in 3 mL hot DMF and placed in a 7 mL glass vial, and this vial was placed in a 25 mL glass vial which contained 3 mL diethyl ether as an anti-solvent. Colourless needle crystals were formed in the inner vial after 3 days.

Tetramethylpropanediammonium tris(oxalato)silicate [H_2TMPDA][L1-Si] (Compound 6)

All synthesis was carried out under N_2. Methanol was dried using 3Å molecule sieve before use. To a stirred solution of methanol (25 mL) with oxalic acid (1.351 g, 5 mmol) $Si(OMe)_4$ (0.74 mL, 5 mmol) was added. N,N,N',N'-Tetramethylpropanediamine (0.84 mL, 5 mmol) was then added and the mixture was kept stirring under reflux for 3 h. After cooling down to room temperature, the white precipitate was isolated by filtration, followed by washing with diethyl ether and finally dried under vacuum at 60°C for 3h. Yield: 1.78 g, 83.9%. ^{1}H NMR (400 MHz, D_6-DMSO): δ(ppm) = 9.46 (br, 2H, N**H**), 3.08 (m, 4H, NC**H**$_2$), 2.80 (s,

12H, C**H**$_3$), 1.99 (tt, 2H, NCH$_2$C**H**$_2$); ^{13}C NMR (101 MHz, D$_6$-DMSO): δ(ppm) = 160.16 (C=O), 54.04 (N**C**H$_2$), 42.81 (**C**H$_3$), 19.81 (NCH$_2$**C**H$_2$); ^{29}Si NMR (80 MHz, D$_6$-DMSO): δ(ppm) = -173.99; IR (ATR): ν (cm^{-1}) = 1738, 1334, 1246, 1202, 910, 854, 820, 640, 551, 494, 459.

Single crystals of [H$_2$TMPDA][**L1-Si**] were obtained through the vapour diffusion method. 20 mg compound **6** was dissolved in 3 mL hot DMF and placed in a 7 mL glass vial, and this vial was placed in a 25 mL glass vial which contained 3 mL diethyl ether as an anti-solvent. Colourless block crystals were formed at the bottom of the inner vial after 3 days.

Tetramethylbutanediammonium tris(oxalato)silicate [H$_2$TMBDA] [L1-Si] (Compound 7)

All synthesis was carried out under N$_2$. Methanol was dried using 3Å molecule sieve before use. To a stirred solution of methanol (25 mL) with oxalic acid (1.351 g, 5 mmol) Si(OMe)$_4$ (0.74 mL, 5 mmol) was added. N,N,N',N'-Tetramethylbutanediamine (0.91 mL, 5 mmol) was then added and the mixture was kept stirring under reflux for 3h. After cooling down to room temperature, the white precipitate was isolated by filtration, followed by washing with diethyl ether and finally dried under vacuum at 60°C for 3 h. Yield: 1.83 g, 84%. ^{1}H NMR (400 MHz, D$_6$-DMSO): δ(ppm) = 8.78 (br, 2H, N**H**), 3.06 (m, 4H, NC**H**$_2$), 2.77 (s, 12H, C**H**$_3$), 1.63 (m, 4H, NCH$_2$C**H**$_2$); ^{13}C NMR (101 MHz, D$_6$-DMSO): δ(ppm) = 160.18 (**C**=O), 56.49 (N**C**H$_2$), 42.77 (**C**H$_3$), 21.37 (NCH$_2$**C**H$_2$); ^{29}Si NMR (80 MHz, D$_6$-DMSO): δ(ppm) = -174.01; IR (ATR): ν (cm^{-1}) = 1744, 1704, 1347, 1256, 909, 847, 820, 633, 554, 472.

Single crystals of [H$_2$TMBDA][**L1-Si**] were obtained through the vapour diffusion method. 30 mg compound **7** was dissolved in 3 mL hot DMF and placed in a 7 mL glass vial, and this vial was placed in a 25 mL glass vial which contained 3 mL diethyl ether as an anti-solvent. Colourless plate crystals were obtained at the bottom of the inner vial after 3 days.

Bis(triethylammonium) tris(oxalato)germanate [Et$_3$NH]$_2$[L1-Ge] (Compound 8)

All synthesis processes were carried under an atmosphere of dry N$_2$. Oxalic acid (1.351 g,

15 mmol) and $Ge(OMe)_4$ (0.74 mL, 5 mmol) were added to dried THF (30 mL). Et_3N (1.39 mL, 10 mmol) was then added to the stirred solution and the mixture was heated under reflux for 3 h. The supernatant was removed after the mixture was cooled down to room temperature and the oily residue was dried under vacuum. Next, the solid was dissolved in boiling ethanol and then recrystallized by cooling down the solution to room temperature. The precipitate was gravity filtered, washed with diethyl ether before drying under vacuum at 50°C for 2 h to give a colourless product. Yield: 1.68 g, 62%. ^{1}H NMR (400 MHz, D_6-DMSO): δ(ppm) = 9.06 (br, 1H, N**H**), 3.10 (q, 6H, J = 8 Hz, C**H**$_2$), 1.18 (t, 9H, J = 8 Hz C**H**$_3$); ^{13}C NMR (101 MHz, D_6-DMSO): δ(ppm) = 159.86 (**C**=O), 46.19 (**C**H_2), 9.10 (**C**H_3); MS (ESI-): calcd. (monoisotopic) for $[C_6O_{12}Ge+H]^-$ m/z = 338.8680, found m/z = 338.8694; IR (ATR): ν (cm^{-1}) = 1726, 1671, 1310, 1226, 1192, 892, 811, 595, 466.

Tetramethylethylenediammonium tris(oxalato)germanate [H_2TMEDA][L1-Ge] (Compound 9)

All synthesis was carried out under N_2. To a stirred solution of THF (25mL) with oxalic acid (1.351 g, 5 mmol) $Ge(OMe)_4$ (0.74 mL, 5 mmol) was added. N,N,N',N'-Tetramethylethylenediamine (0.75 mL, 5 mmol) was then added and the mixture was kept stirring under reflux for 3 h. After cooling to room temperature, the white precipitate was isolated by filtration, followed by washing with ethanol and diethyl ether before finally dried under vacuum at 50°C for 3 h. Yield: 1.63 g, 74%. ^{1}H NMR (400 MHz, D_6-DMSO): δ(ppm) = 9.43 (br, 2H, N**H**), 3.39 (m, 4H, C**H**$_2$), 2.83 (s, 12H, C**H**$_3$); ^{13}C NMR (101 MHz, D_6-DMSO): δ(ppm) = 159.87 (**C**=O), 51.39 (**C**H_2), 43.44 (**C**H_3); MS (ESI-): calcd. (monoisotopic) for $[C_6O_{12}Ge+H]^-$ m/z = 338.8680, found m/z = 338.8697; IR (ATR): ν (cm^{-1}) = 1728, 1315, 1232, 1195, 894, 817, 599, 468.

Single crystals of [H_2TMEDA][**L1-Ge**] were obtained by cooling an aqueous solution of the germanate salt. The linker (50 mg) was dissolved in 3 mL hot H_2O in a glass vial, and colourless block crystals were formed in few hours after the vial cooled to room temperature.

Tetramethylpropanediammonium tris(oxalato)germanate [H_2TMPDA][L1-Ge] (Compound 10)

All synthesis was carried out under N_2. To a stirred solution of THF (25 mL) with oxalic acid (1.351 g, 5 mmol) $Ge(OMe)_4$ (0.74 mL, 5 mmol) was added. N,N,N',N'-Tetramethylpropanediamine (0.84 mL, 5 mmol) was then added and the mixture was kept stirring under reflux for 3 h. After cooling down to room temperature, the white precipitate was isolated by filtration, followed by washing with ethanol and diethyl ether before finally dried under vacuum at 60°C for 3 h. Yield: 1.30 g, 54%. ^{1}H NMR (400 MHz, D_2O): δ(ppm) = 3.12 (m, 4H, NC**H**$_2$), 2.82 (s, 12H, C**H**$_3$), 2.03 (m, 2H, NCH$_2$C**H**$_2$); ^{13}C NMR (101 MHz, D_2O): δ(ppm) = 160.66 (C=O), 54.04 (N**C**H$_2$), 42.81 (**C**H$_3$), 19.76 (NCH$_2$**C**H$_2$); IR (ATR): ν (cm^{-1}) = 1736, 1631, 1310, 1219, 1183, 890, 813, 771, 595, 467.

Bispyridium tris(oxalato)germanate (H_2Bipy)[Ge(C_2O_4)$_3$] ([H_2Bipy][L1-Ge]) (Compound 11)

A mixture of germanium dioxide (0.031 g, 0.3 mmol), 4,4'-bipyridine (0.047 g, 0.3 mmol) and oxalic acid (0.081 g, 0.9 mmol) were placed in a PTFE autoclave and deionized water (10mL) was added. The mixture was sonicated to form a homogeneous suspension. Then the autoclave was placed in a programmable oven, slowly heated to 100°C over 10 h, held at 100°C for 72 h and gradually cooled to room temperature over 10 h. Colourless needle-shaped crystals were formed after the autoclave was left undisturbed for 1 week (See below Crystal 1). Yield: 0.16 g. ^{1}H NMR (400 MHz, D_2O): δ(ppm) = 8.83 (m, 2H, C3-**H**), 8.23 (m, 2H, C2-**H**); IR (ATR): ν (cm^{-1}) = 3093, 1720, 1630, 1590, 1480, 1333, 1245, 1187, 895, 704, 772, 599, 458.

The mother liquid was transferred to a glass vial and colourless tablets crystals (See below Crystal 2) were formed after leaving the vial in an open atmosphere for 3 days. ^{1}H NMR (400 MHz, D_2O): δ(ppm) = 8.89 (m, 2H, C3-**H**), 8.34 (m, 2H, C2-**H**); IR (ATR): ν (cm^{-1}) = 3074, 1736, 1598, 1486, 1312, 1233, 1200, 896, 810, 596, 466.

Crystal 1 Crystal 2

Bisguanidinium tris(oxalato)germanate $[Gu]_2[L1\text{-}Ge]$ (Compound 12)

A mixture of germanium dioxide (0.052 g, 0.5 mmol), guanidinium oxalate (0.457 g, 1 mmol) and oxalic acid (0.009 g, 0.5 mmol) was placed in a PTFE autoclave and deionized water (10 mL) was added. The mixture was sonicated to form a homogeneous suspension. Then the autoclave was placed in a programmable oven, slowly heated to 100°C over 10 h, held at 100°C for 72 h and gradually cooled to room temperature over 10 h. Colourless block-like needle crystals were formed after the solution was transferred into a 14 mL glass vial and left in the open air for 1 month.

6.3 L2 type linkers

Bis(triethylammonium) tris[3-(3,4-diolatophenyl)acrylic acid]silicate [$Et_3NH]_2$[L2-Si] (Compound 13)

All synthesis processes were carried under an atmosphere of dry N_2. Caffeic acid (2.702 g, 15 mmol) was dissolved in acetonitrile (20 mL). Et_3N (1.39 mL, 10 mmol) was added dropwise to the stirred solution, resulting in the formation of a yellow precipitate. $Si(OMe)_4$ (0.74 mL, 5 mmol) was then added and the mixture was stirred at room temperature for 48 h. The yellow precipitate was isolated by suction filtration, then washed with acetonitrile and diethyl ether before drying under vacuum at 40°C for 2 h to give a yellow powder, mp. >260°C (decomp.), colour change from pale yellow to grey at 160°C, then to purple at about 200°C. Yield: 2.67g, 70%. ^{1}H NMR (400 MHz, D_6-DMSO): δ(ppm) = 7.36 (d, 1H, J = 12 Hz, Ph-C**H**=CH), 6.61 (s, 1H, C2-**H**), 6.59 (s, 1H, C6-**H**), 6.25 (s, 1H, C5-**H**), 5.97 (d, 1H, J = 12 Hz, Ph-CH=C**H**), 2.93 (q, 6H, J = 8 Hz, C**H**$_2$CH$_3$), 1.10 (t, 9H, J = 8 Hz, CH$_2$C**H**$_3$); ^{13}C NMR (101 MHz, D_6-DMSO): δ(ppm) = 169.26 (**C**OOH), 156.71, 152.79, 147.31, 122.67, 121.35, 111.40, 109.20, 106.51, 46.16 (**C**H$_2$CH$_3$), 9.78 (CH$_2$**C**H$_3$); ^{29}Si NMR (80 MHz, D_6-DMSO): δ(ppm) = -138.37; MS (ESI-): calcd. (monoisotopic) for $[C_{27}H_{18}O_{12}Si+H]^-$ m/z = 563.0646, found m/z = 563.0655; IR (ATR): ν (cm^{-1}) = 1675, 1588, 1493, 1351, 1253, 1116, 835, 696, 581, 510.

Bis[dimethylethanol ammonium] tris[3-(3,4-diolatophenyl)acrylic acid]silicate [HDMAE]$_2$[L2-Si] (Compound 14)

All synthesis processes were carried under an atmosphere of dry N_2. Caffeic acid (2.702 g, 15 mmol) was dissolved in acetonitrile (20 mL). DMAE (1.39 mL, 10 mmol) was added dropwise to the stirred solution, followed by adding $Si(OMe)_4$ (0.74 mL, 5 mmol) to the mixture, which was then stirred at room temperature for 48 h. The product was isolated by adding diethyl ether (approx. 100 mL) and gravity filtered before drying under vacuum at 50°C for 3 h to give a yellow powder. Yield: 2.96 g, 83% ^{1}H NMR (400 MHz, D_6-DMSO): δ(ppm) = 7.36 (dd, 1H, J = 12 Hz, Ph-C**H**=CH), 6.62 (s, 1H, C2-**H**), 6.60 (s, 1H, C6-**H**),

6.26 (ddd, 1H, C5-**H**), 5.97 (m, 1H, J = 12 Hz, Ph-CH=C**H**), 3.62 (t, 2H, J = 8 Hz, $NCH_2C\mathbf{H}_2$), 2.87 (t, 2H, J = 8 Hz, $NC\mathbf{H}_2$), 2.58 (s, 6H, $C\mathbf{H}_3$); ^{13}C NMR (101 MHz, D_6-DMSO): δ(ppm) = 169.19 (**C**OOH), 156.68, 152.72, 147.39, 122.72, 121.50, 111.23, 109.28, 106.58, 60.00 ($NCH_2\mathbf{C}H_2$), 57.07 ($N\mathbf{C}H_2$), 44.30 ($\mathbf{C}H_3$); ^{29}Si NMR (80 MHz, D_6-DMSO): δ(ppm) = -138.53; IR (ATR): ν (cm^{-1}) = 1677, 1622, 1589, 1490, 1442, 1347, 1251, 1151, 1114, 965, 733, 690, 576, 504.

Bis(triethylammonium) tris[3-(3,4-diolatophenyl)acrylic acid]germanate

$[Et_3NH]_2$[L2-Ge] (Compound 15)

All synthesis processes were carried under an atmosphere of dry N_2. Caffeic acid (2.702 g, 15 mmol) was dissolved in acetonitrile (20 mL). Et_3N (1.39 mL, 10 mmol) was added dropwise to the stirred solution, resulting in the formation of a yellow precipitate. $Ge(OMe)_4$ (0.74 mL, 5 mmol) was then added and the mixture was stirred at room temperature for 48 h. The yellow precipitate was isolated by suction filtration, then washed with acetonitrile and diethyl ether before drying under vacuum at 40°C for 2 h to give a yellow powder. Yield: 3.37 g, 83%, ^1H NMR (400 MHz, D_6-DMSO): δ(ppm) = 7.35 (d, 1H, J = 12 Hz, Ph-C**H**=CH), 6.61 (s, 1H, C2-**H**), 6.59 (s, 1H, C6-**H**), 6.29 (s, 1H, C5-**H**), 5.94 (d, 1H, J = 12 Hz, Ph-CH=C**H**), 3.10 (q, 8H, J = 8 Hz, $C\mathbf{H}_2CH_3$), 1.16 (t, 9H, J = 8 Hz, $CH_2C\mathbf{H}_3$); ^{13}C NMR (101 MHz, D_6-DMSO): δ(ppm) = 169.26 (**C**OOH), 156.71, 152.79, 147.31, 122.67, 121.35, 111.40, 109.20, 106.51, 46.16 ($\mathbf{C}H_2CH_3$), 9.78 ($CH_2\mathbf{C}H_3$); ^{29}Si NMR (80 MHz, D_6-DMSO): δ(ppm) = -138.37; MS (ESI-): calcd. (monoisotopic) for $[C_{27}H_{18}O_{12}Ge+H]^-$ m/z = 609.0088, found m/z = 609.0099; IR (ATR): ν (cm^{-1}) = 1675, 1588, 1493, 1351, 1253, 1116, 835, 696, 581, 510.

6.4 L3 type linkers

Bis(triethylammonium) tris(3,4-diolato-benzoic acid)silicate $[Et_3NH]_2$[L3-Si] (Compound 16)

All synthesis processes were carried under an atmosphere of dry N_2. 3,4-Dihydroxybenzoic acid (2.312 g, 15 mmol) was dissolved in acetonitrile (20 mL). Et_3N (1.39 mL, 10 mmol) was added dropwise to the stirred solution, resulting in the formation of a white suspension. $Si(OMe)_4$ (0.74 mL, 5 mmol) was then added and the mixture was stirred at room temperature for 48 h. The white precipitate was isolated by suction filtration, then washed with acetonitrile and diethyl ether before drying under vacuum at 50°C for 3 h to give a white powder. Yield: 2.93 g, 85%. ^{1}H NMR (400 MHz, D_6-DMSO): δ(ppm) = 10.51 (br, 1H, COO**H**), 7.10 (dq, 1H, C6-**H**), 6.79 (t, 1H, C2-**H**), 6.26 (dt, 1H, C5-**H**), 3.10 (dt, 4H, C**H**$_2$CH$_3$), 1.16 (t, 6H, CH$_2$C**H**$_3$); ^{13}C NMR (101 MHz, D_6-DMSO): δ(ppm) = 168.99 (**C**OOH), 157.91, 151.83, 120.43, 117.74, 109.59, 108.69, 46.30 (**C**H$_2$CH$_3$), 9.12 (CH$_2$**C**H$_3$); ^{29}Si NMR (80 MHz, D_6-DMSO): δ(ppm) = -138.17; MS (ESI-): calcd. (monoisotopic) for $[C_{21}H_{12}O_{12}Si+H]^-$ m/z = 485.0182, found m/z = 485.0198; IR (ATR): ν (cm^{-1}) = 1656, 1498, 1444, 1269, 1118, 829, 774, 691, 663, 543.

Single crystals of $[Et_3NH]_2$[**L3-Si**] were obtained through vapour diffusion method. 16 mg product was dissolved in 0.5 mL hot DMF and placed in a 3.5 mL glass vial, and this vial was placed in a 14 mL glass vial which has 2.5 mL diethyl ether used as anti-solvent. Colourless tablets crystals were obtained at the bottom of the inner vial after all diethyl ether diffused into DMF.

Bis(diethylammonium) tris(3,4-diolato-benzoic acid)silicate $[Et_2NH_2]_2$[L3-Si] (Compound 17)

All synthesis processes were carried under an atmosphere of dry N_2. 3,4-Dihydroxybenzoic acid (2.312 g, 15 mmol) was dissolved in acetonitrile (20 mL). Et_2NH (1.03 mL, 10 mmol) was added dropwise to the stirred solution, resulting in the formation of a white suspension.

$Si(OMe)_4$ (0.74 mL, 5 mmol) was then added and the mixture was stirred at room temperature for 48 h. The white precipitate was isolated by suction filtration, then washed with acetonitrile and diethyl ether before drying under vacuum at 50°C for 3 h to give a white powder. Yield: 2.92 g, 85%. ^{1}H NMR (400 MHz, D_6-DMSO): δ(ppm) = 7.09 (dq, 1H, C6-**H**), 6.80 (t, 1H, C2-**H**), 6.26 (dt, 1H, C5-**H**), 2.94 (dt, 3H, C**H**$_2$), 1.15 (t, 4H, C**H**$_3$); ^{13}C NMR (101 MHz, D_6-DMSO): δ(ppm) = 168.99 (**C**OOH), 157.91, 151.83, 120.43, 117.74, 109.59, 108.69, 46.30 (**C**H_2CH_3), 9.12 (CH_2**C**H_3); ^{29}Si NMR (80 MHz, D_6-DMSO): δ(ppm) = -138.50; IR (ATR): ν (cm^{-1}) = 1665, 1592, 1496, 1442, 1262, 1113, 943, 826, 770, 535, 490.

Bis[dimethylethanol ammonium] tris(3,4-diolato-benzoic acid)silicate [HDMAE]$_2$[L3-Si] (Compound 18)

All synthesis processes were carried under an atmosphere of dry N_2. 3,4-Dihydroxybenzoic acid (2.312 g, 15 mmol) was dissolved in methanol (20 mL). DMAE (1.39 mL, 10 mmol) was added dropwise to the stirred solution, followed by adding $Si(OMe)_4$ (0.74 mL, 5 mmol) to the mixture, which was then stirred at room temperature for 48 h. The product was isolated by adding diethyl ether (approx. 100 mL) and gravity filtered before drying under vacuum at 50°C for 3 h to give a yellow powder. Yield: 2.08 g, 63%. ^{1}H NMR (400 MHz, D_6-DMSO): δ(ppm) = 7.12 (m, 1H, C6-**H**), 6.82 (rd, 1H, C2-**H**), 6.29 (m, 1H, C5-**H**), 3.63 (t, 2H, CH_2C**H**$_2$OH), 2.89 (t, 2H, C**H**$_2$$CH_2$OH), 2.59 (s, 6H, C**H**$_3$); ^{13}C NMR (101 MHz, D_6-DMSO): δ(ppm) = 169.09 (**C**OOH), 157.65, 151.68, 120.53, 118.11, 109.78, 108.82, 59.92 (CH_2**C**H_2OH), 56.96 (**C**H_2CH_2OH), 44.20 (**C**H_3); ^{29}Si NMR (80 MHz, D_6-DMSO): δ(ppm) = -138.44; IR (ATR): ν (cm^{-1}) = 1672, 1494, 1432, 1259, 1074, 942, 826, 689, 662, 536.

Bis[dimethylpropanol ammonium] tris(3,4-diolato-benzoic acid)silicate [HDMAP]$_2$[L3-Si] (Compound 19)

All synthesis processes were carried under an atmosphere of dry N_2. 3,4-Dihydroxybenzoic acid (2.312 g, 15 mmol) was dissolved in methanol (20 mL). DMAP (1.39 mL, 10 mmol)

was added dropwise to the stirred solution, followed by adding $Si(OMe)_4$ (0.74 mL, 5 mmol) to the mixture, which was then stirred at room temperature for 48 h. The product was isolated by adding diethyl ether (approx. 100 mL) and gravity filtered before drying under vacuum at 50°C for 3 h to give a grey powder. Yield: 1.93 g, 56%. ^{1}H NMR (400 MHz, D_6-DMSO): δ(ppm) = 7.11 (m, 1H, C6-**H**), 6.82 (rd, 1H, C2-**H**), 6.29 (m, 1H, C5-**H**), 3.44 (t, 2H, $CH_2CH_2C\mathbf{H}_2OH$), 2.84 (m, 2H, $C\mathbf{H}_2CH_2CH_2OH$), 2.56 (s, 6H, $C\mathbf{H}_3$), 1.70 (m, 2H, $CH_2C\mathbf{H}_2CH_2OH$); ^{13}C NMR (101 MHz, D_6-DMSO): δ(ppm) = 168.99 (COOH), 157.63, 151.65, 120.54, 118.08, 109.77, 108.85, 58.90 ($CH_2CH_2\mathbf{C}H_2OH$), 55.98 ($\mathbf{C}H_2CH_2CH_2OH$), 43.95 ($\mathbf{C}H_3$), 28.51 ($CH_2\mathbf{C}H_2CH_2OH$); ^{29}Si NMR (80 MHz, D_6-DMSO): δ(ppm) = -138.38; IR (ATR): ν (cm^{-1}) = 1681, 1494, 1432, 1258, 1075, 942, 827, 689, 662, 538.

Bis(triethylammonium) tris(3,4-diolato-benzoic acid)germanate $[Et_3NH]_2$[L3-Ge] (Compound 20)

All synthesis processes were carried under an atmosphere of dry N_2. 3,4-Dihydroxybenzoic acid (1.849 g, 12 mmol) was dissolved in acetonitrile (20 mL). Et_3N (1.12 mL, 8 mmol) was added dropwise to the stirred solution, resulting in the formation of a white suspension. $Ge(OMe)_4$ (0.59 mL, 4 mmol) was then added and the mixture was stirred at room temperature for 48 h. The white precipitate was isolated by suction filtration, then washed with acetonitrile and diethyl ether before drying under vacuum at 50°C for 3 h to give a white powder. Yield: 2.73g, 93%. ^{1}H NMR (400 MHz, D_6-DMSO): δ(ppm) = 11.59 (br, 1H, COO**H**), 7.06 (dd, 1H, C6-**H**), 6.85 (d, 1H, C2-**H**), 6.31 (d, 1H, C5-**H**), 3.10 (q, 4H, $C\mathbf{H}_2CH_3$), 1.16 (t, 6H, $CH_2C\mathbf{H}_3$),; ^{13}C NMR (101 MHz, D_6-DMSO): δ(ppm) = 168.94 (**C**OOH), 157.47, 151.38, 119.87, 117.35, 110.73, 109.79, 46.26 ($\mathbf{C}H_2CH_3$), 9.09 ($CH_2\mathbf{C}H_3$); MS (ESI-): calcd. for $[C_{21}H_{12}O_{12}Ge+H]^-$ m/z = 530.9624, found m/z = 530.9626; IR (ATR): ν (cm^{-1}) = 1657, 1494, 1439, 1264, 1118, 942, 813, 773, 648, 408.

Bis(diethylammonium) tris(3,4-diolato-benzoic acid)germanate $[Et_2NH_2]_2$[L3-Ge] (Compound 21)

All synthesis processes were carried under an atmosphere of dry N_2. 3,4-Dihydroxybenzoic

acid (1.849 g, 12 mmol) was dissolved in acetonitrile (20 mL). Et_2NH (0.83 mL, 8 mmol) was added dropwise to the stirred solution, resulting in the formation of a white suspension. $Ge(OMe)_4$ (0.59 mL, 4 mmol) was then added and the mixture was stirred at room temperature for 48 h. The white precipitate was isolated by suction filtration, then washed with acetonitrile and diethyl ether before drying under vacuum at 50°C for 3 h to give a white powder. Yield: 2.24g, 83%. ^{1}H NMR (400 MHz, D_6-DMSO): δ(ppm) = 11.69 (br, 1H, COO**H**), 8.23 (s, N**H**$_2$), 7.08 (dd, 1H, C6-**H**), 6.89 (d, 1H, C2-**H**), 6.33 (d, 1H, C5-**H**), 2.94 (q, 4H, C**H**$_2$), 1.15 (t, 6H, C**H**$_3$); ^{13}C NMR (101 MHz, D_6-DMSO): δ(ppm) = 168.89 (**C**OOH), 157.22, 151.12, 120.02, 117.56, 110.90, 109.94, 42.02 (**C**H$_2$), 11.51 (**C**H$_3$); IR (ATR): ν (cm^{-1}) = 1666, 1587, 1492, 1439, 1256, 1115, 942, 813, 769, 645, 412.

Bis(triethylammonium) tris(3,4-diolato-benzoic acid)titanium [Et$_3$NH]$_2$[L3-Ti] (Compound 22)

All synthesis processes were carried out under N_2. 3,4-Dihydroxybenzoic acid (1.3871 g, 9 mmol) was dissolved in acetonitrile (20 mL), followed by adding Et_3N (0.83 mL, 6 mmol) dropwise. After forming a white suspension, $Ti(OiPr)_4$ (0.91 mL, 3 mmol) was injected into the suspension with the suspension colour turned orange. The mixture was then kept stirred at 50°C for 24h. The orange solid was isolated by suction filtration followed by washing with diethyl ether before drying under vacuum at 50°C for 3 h. Yield: 1.88 g, 88.4%. ^{1}H NMR (400 MHz, D_6-DMSO): δ(ppm) = 11.59 (br, 3H, COO**H**), 8.85 (br. 2H, N**H**), 7.07 (dd, 3H, C6-**H**), 6.56 (d, 3H, C2-**H**), 6.03 (d, 3H, C5-**H**), 3.09 (q, 12H, C**H**$_2$), 1.17 (t, 18H, C**H**$_3$); ^{13}C NMR (101 MHz, D_6-DMSO): δ(ppm) = 169.03 (**C**OOH), 166.31, 159.99, 121.09, 118.29, 110.84, 110.01, 46.24 (**C**H$_2$CH$_3$), 9.22 (CH$_2$**C**H$_3$); MS (ESI-): calcd. for $[C_{21}H_{12}O_{12}Ti+H]^-$ m/z = 504.9892, found m/z = 504.9891; IR (ATR): ν (cm^{-1}) = 1694, 1657, 1483, 1428, 1252, 1173, 1118, 1075, 934, 813, 765, 740, 631, 503.

Crystal of [Et$_3$NH]$_2$[**L3-Ti**] was obtained through the vapour diffusion method by dissolving 6 mg L in 0.5 mL DMF in a small glass vial. Then the small glass vial was placed into a large glass vial which contained 2.5 mL Et_2O. After standing 3 days with all ether diffused into the small glass vial, dark brown plate-shaped crystals were obtained.

6.5 MOF synthesis

IMP-33-RE

A mixture of compound **20** (36.7 mg, 0.5 mmol) and metal nitrate (0.1 mmol, Y, Gd, Tb, Dy, Ho, Er, Tm, Yb, Lu, all trivalent) was placed in a 7 mL screw cap glass vial, followed by adding water (3 mL) and MeCN (1 mL). The mixture was then treated in an ultrasound bath for 5 mins to allow the reagent to completely dissolve, before placing in a heat block at 80°C for 24 h to afford colourless blade-shaped crystals. **IMP-33-Ho** and **IMP-33-Er** exhibited light orange and pink colours, respectively.

IMP-34-Sc

A mixture of compound **20** (36.7 mg, 0.5 mmol) and $Sc(NO_3)_3 \cdot H_2O$ (24.8 mg, 0.1 mmol) was placed in a 7 mL screw cap glass vial, followed by adding water (3 mL) and MeCN (1 mL). The mixture was then treated in an ultrasound bath for 5 mins to allow the reagent to completely dissolve, before placing in a heat block at 80°C for 24 h to afford colourless prism-shaped crystals.

6.5 Other compounds

$Ag_2C_2O_4$: Potassium oxalate monohydrate (18.42 g, 0.1 mol) and silver nitrate (33.97 g, 0.2 mol) were each separately dissolved in 100 mL water. The silver oxalate precipitate was formed by mixing the two solutions. This white precipitate was isolated by filtration and washed with water, followed by drying under vacuum at 60°C for 2 h. Yield: 29.16g, 96%. IR (ATR): ν (cm^{-1}) = 1560, 1381, 1299, 770, 518, 410. The product is stored in a brown glass bottle and the whole bottle is covered with aluminium foil to exclude light.

$Gu_2C_2O_4$: Firstly, guanidine carbonate (9.01 g, 50 mmol) and oxalic acid (4.57 g, 51 mmol) were each separately dissolved in 50 mL water. Guanidine oxalate was obtained by mixing these two solutions in a 250 mL round bottom flask and stirring for 10 mins. Most of the water (approx. 90%) was removed by rotary evaporation at 60°C and the residue was cooled to room temperature, resulting in the crystallization of the crude product. This colourless solid was washed with diethyl ether, before drying under vacuum at 60°C for 3 h. Yield: 9.94g, 95%.: ^{1}H NMR (400 MHz, D_2O): δ(ppm) = 4.71 (s, N**H**); ^{13}C NMR (101 MHz, D_2O): δ(ppm) = 173.22 (**C**=O), 157.87 (**C**-N); IR (ATR): ν (cm^{-1}) = 3120, 1653, 1577, 1309, 1131, 745, 531.

Piperazinium tris[benzene-1,2-diolato(2-)] titanium [$Ti(cat)_3 \cdot H_2pip \cdot 8H_2O$] (Compound 23)

A mixture of 3,4-dihydroxybenzoic acid (1.387 g, 9 mmol) and piperazine (0.258 g, 3 mmol) was added to a PTFE autoclave with 6 mL H_2O. Then $Ti(OiPr)_4$ (0.91 mL, 3 mmol) was added to the mixture before the autoclave was sealed and placed in an oven at 120°C for 3 days to afford single dark brown blade-shaped crystals.

4,5-Dihydroxyphthalic acid (Compound 24)[301]

The synthesis procedure was carried out under N_2. 4,5-Dimethoxyphthalic acid (0.452 g, 2 mmol) was added to CH_2Cl_2 (16 mL, degassed) at 0°C. BBr_3 (8.5 mL, 1 M in CH_2Cl_2) was then added and the mixture was stirred at room temperature for 1 day. Water (30 mL) was

added to the mixture and the organic phase was evaporated before adding EtOAc to extract (3 × 20 mL). The combined organic phase was washed with saturated brine and dried using $MgSO_4$ and the final product was obtained as a viscous liquid by evaporation of solvent under reduced pressure. ^{1}H NMR (400 MHz, D_6-DMSO): δ(ppm) = 12.82 (br, 1H, COO**H**), 9.79 (s, 1H, O**H**), 7.01 (s, 1H, C**H**); MS (ESI-): calcd. for $[C_8H_6O_6\text{-}H]^-$ m/z = 197.0092, found m/z = 197.0084.

The presence of 4,5-dihydroxyphthalic acid was also confirmed by ^{1}H NMR. However, the product was a mixture of product **24** and **25** and other minor impurities and the ratio of product **25** to **24** was about 2:1, calculated according to the integration of peak in ^{1}H NMR. Further purification of **24** was not carried out.

4,5-Dimethoxyphthalic acid (Compound 25)[298]

NaOH (35 mL, 7%) was added to a suspension of m-Meconin (3 g, 15.4 mmol) in 75 mL water, followed by adding $KMnO_4$ (2.687 g, 17 mmol) and the mixture was stirred at room temperature for 4 days. The mixture was then filtered through celite, and to the filtrate concentrated hydrochloric acid was added to acidify to pH 1. Then the mixture was extracted with EtOAc (3 × 40 mL) and the combined organic phase was washed with saturated brine and dried with $MgSO_4$. The crude product was obtained by removing the solvent under reduced pressure.

Purification: The crude product was suspended in an aqueous solution of $NaHCO_3$ (2.2 equiv.). The mixture was then sonicated until no bubbles were generated. The precipitate was removed by extracting into EtOAc and the left aqueous solution was acidified to pH 1 by adding hydrochloric acid. The final product was crystallized by the slow evaporation of water to give a light yellow solid. m. p. 169 - 173°C. Yield: 2.19 g, 63%. ^{1}H NMR (400 MHz, D_6-DMSO): δ(ppm) = 12.92 (br, 1H, COO**H**), 7.19 (s, 1H, C**H**), 3.84 (s, 3H, C**H**$_3$); ^{13}C NMR (101 MHz, D_6-DMSO): δ(ppm) = 168.84, 150.35, 126.27, 111.69, 56.25; IR (ATR): ν (cm^{-1}) = 1712, 1628, 1589, 1525, 1483, 1406, 1283, 1212, 1047, 840, 760, 649.

4,5-Dimethoxy-2-methyl benzaldehyde (Compound 26)[297]

3,4-Dimethoxytoluene (0.36 mL, 2.5 mmol) and dichloromethylmethyl ether (0.79 mL) were dissolved in dichloroethane (5 mL) at 0°C, followed by adding $SnCl_4$ (2.5 mL), and further dichloroethane (5 mL). The mixture was stirred at 0°C for 20 mins then at RT overnight. Then, the mixture was cooled to 0°C with an ice bath before HCl (3 M, 12.5 mL) was added. The mixture was then extracted into CH_2Cl_2 and the organic phase was finally evaporated to give compound **26** as a black solid. Yield: 0.43 g, 88%. Compound **25** can be purified through sublimation to give colourless powder. ^{1}H NMR (400 MHz, D_6-DMSO): δ(ppm) = 10.13 (s, 1H, C5-C**H**O), 7.33 (s, 1H, C4-**H**), 6.94 (s, 1H, C1-**H**), 3.85 (s, 3H, C3-OC**H**$_3$), 3.79 (s, 3H, C2-OC**H**$_3$), 2.58 (d, 3H, C6-C**H**$_3$),; ^{13}C NMR (101 MHz, D_6-DMSO): δ(ppm) = 191.38 (C5-**C**HO), 153.79 (**C**3), 147.48 (**C**2), 135.92 (**C**5), 127.00 (**C**6), 114.70 (**C**4), 112.21 (**C**1), 56.26 (C2-O**C**H$_3$), 55.97 (C3-O**C**H$_3$), 18.33 (C6-**C**H$_3$); IR (ATR): ν (cm^{-1}) = 1663, 1593, 1511, 1452, 1400, 1348, 1257, 1218, 1184, 1099, 995, 865, 834, 744, 667, 578, 481, 453, 414.

5,6-Dimethoxyphthalide (m-Meconin, Compound 27)[298]

Paraformaldehyde (8.378 g, 279 mmol) and 3,4-dimethoxybenzoic acid (5.465 g, 30 mmol) were added into a stirred solution of concentrated hydrochloric acid (180 mL, 37%) and the suspension was heated at 85°C for approximately 6 h until the solution became a clear brown solution. The solution was then cooled with an ice bath followed by slowly neutralizing with an aqueous ammonia solution (25%) until pH to 7-8. The light-brown precipitate was then isolated by suction filtration, followed by washing with water several times. The solid was then recrystallized from ethanol before drying under vacuum at 50°C for 3 h to give a light-yellow product. m.p. 152 - 154°C. Yield: 4.01g, 69%. ^{1}H NMR (400 MHz, D_6-DMSO): δ(ppm) = 7.25 (s, 1H, C5-**H**), 7.23 (s, 1H, C4-**H**), 5.27 (s, 1H, C3-C**H**$_2$), 3.88 (s, 3H, C6-C**H**$_3$), 3.84 (s, 3H, C5-C**H**$_3$); ^{13}C NMR (101 MHz, D_6-DMSO): δ(ppm) = 171.29, 155.01, 150.42, 142.24, 116.87, 106.12, 105.19, 69.64, 56.54, 56.33; IR (ATR): ν (cm^{-1}) = 1747, 1600, 1499, 1449, 1346, 1290, 1249, 1221, 1123, 1039, 995, 973, 856, 830, 762, 673, 594, 545, 455.

List of References

1. J. Liu, P. K. Thallapally, B. P. McGrail, D. R. Brown and J. Liu, *Chem. Soc. Rev.*, 2012, **41**, 2308-2322.
2. M. S. Denny Jr, J. C. Moreton, L. Benz and S. M. Cohen, *Nat. Rev. Mater.*, 2016, **1**, 16078.
3. Z. Chen, P. Li, R. Anderson, X. Wang, X. Zhang, L. Robison, L. R. Redfern, S. Moribe, T. Islamoglu and D. A. Gómez-Gualdrón, *Science*, 2020, **368**, 297-303.
4. M. Eddaoudi, J. Kim, N. Rosi, D. Vodak, J. Wachter, M. O'Keeffe and O. M. Yaghi, *Science*, 2002, **295**, 469-472.
5. M. Ding, R. W. Flaig, H. L. Jiang and O. M. Yaghi, *Chem. Soc. Rev.*, 2019, **48**, 2783-2828.
6. Y. Han, J. R. Li, Y. Xie and G. Guo, *Chem. Soc. Rev.*, 2014, **43**, 5952-5981.
7. B. F. Hoskins and R. Robson, *J. Am. Chem. Soc.*, 1989, **111**, 5962-5964.
8. A. K. Cheetham, G. Férey and T. Loiseau, *Angew. Chem. Int. Ed.*, 1999, **38**, 3268-3292.
9. B. F. Hoskins and R. Robson, *J. Am. Chem. Soc.*, 1990, **112**, 1546-1554.
10. K. Uemura, R. Matsuda and S. Kitagawa, *J. Solid State Chem.*, 2005, **178**, 2420-2429.
11. S. Kitagawa, M. Munakata and T. Tanimura, *Inorg. Chem.*, 1992, **31**, 1714-1717.
12. O. Yaghi and H. Li, *J. Am. Chem. Soc.*, 1995, **117**, 10401-10402.
13. O. M. Yaghi, G. Li and H. Li, *Nature*, 1995, **378**, 703-706.
14. M. Kondo, T. Yoshitomi, H. Matsuzaka, S. Kitagawa and K. Seki, *Angew. Chem. Int. Ed.*, 1997, **36**, 1725-1727.
15. H. Li, M. Eddaoudi, T. L. Groy and O. Yaghi, *J. Am. Chem. Soc.*, 1998, **120**, 8571-8572.
16. H. Li, M. Eddaoudi, M. O'Keeffe and O. M. Yaghi, *Nature*, 1999, **402**, 276.
17. S. S.-Y. Chui, S. M.-F. Lo, J. P. Charmant, A. G. Orpen and I. D. Williams, *Science*, 1999, **283**, 1148-1150.
18. R. Kitaura, K. Fujimoto, S. Noro, M. Kondo and S. Kitagawa, *Angew. Chem. Int. Ed.*, 2002, **41**, 133-135.
19. C. Serre, C. Mellot-Draznieks, S. Surblé, N. Audebrand, Y. Filinchuk and G. Férey, *Science*, 2007, **315**, 1828-1831.
20. C. Mellot-Draznieks, C. Serre, S. Surblé, N. Audebrand and G. Férey, *J. Am. Chem. Soc.*, 2005, **127**, 16273-16278.
21. C. Serre, F. Millange, C. Thouvenot, M. Noguès, G. Marsolier, D. Louër and G. Férey, *J. Am. Chem. Soc.*, 2002, **124**, 13519-13526.
22. S. Surble, C. Serre, C. Mellot-Draznieks, F. Millange and G. Ferey, *Chem. Commun.*, 2006, 284-286.
23. S. Horike, S. S. Nagarkar, T. Ogawa and S. Kitagawa, *Angew. Chem. Int. Ed.*, 2020, **59**, 6652-6664.
24. N. Ma and S. Horike, *Chem. Rev.*, 2022, **122**, 4163-4203.
25. S. Horike, D. Umeyama, M. Inukai, T. Itakura and S. Kitagawa, *J. Am. Chem. Soc.*, 2012, **134**, 7612-7615.
26. T. D. Bennett, J.-C. Tan, Y. Yue, E. Baxter, C. Ducati, N. J. Terrill, H. H.-M. Yeung, Z.

Zhou, W. Chen and S. Henke, *Nat. Commun.*, 2015, **6**, 8079.
27. D. Umeyama, S. Horike, M. Inukai, T. Itakura and S. Kitagawa, *J. Am. Chem. Soc.*, 2015, **137**, 864-870.
28. Y. Hirai, T. Nakanishi, Y. Kitagawa, K. Fushimi, T. Seki, H. Ito, H. Fueno, K. Tanaka, T. Satoh and Y. Hasegawa, *Inorg. Chem.*, 2015, **54**, 4364-4370.
29. J. Fonseca, T. Gong, L. Jiao and H.-L. Jiang, *J. Mater. Chem. A*, 2021, **9**, 10562-10611.
30. A. Kirchon, L. Feng, H. F. Drake, E. A. Joseph and H. C. Zhou, *Chem. Soc. Rev.*, 2018, **47**, 8611-8638.
31. K. Seki, M. Fujiwara, W, Mori, S. Takamizawa, U.S. Patent 5,862,796 (1999)
32. J. Lu, A. Mondal, B. Moulton and M. J. Zaworotko, *Angew. Chem. Int. Ed.*, 2001, **113**, 2171-2174.
33. L. Xie, S. Liu, C. Gao, R. Cao, J. Cao, C. Sun and Z. Su, *Inorg. Chem.*, 2007, **46**, 7782-7788.
34. L. J. Murray, M. Dinca, J. Yano, S. Chavan, S. Bordiga, C. M. Brown and J. R. Long, *J. Am. Chem. Soc.*, 2010, **132**, 7856-7857.
35. J. B. DeCoste, G. W. Peterson, H. Jasuja, T. G. Glover, Y.-g. Huang and K. S. Walton, *J. Mater. Chem. A*, 2013, **1**, 5642.
36. J. Zhang, L. Wojtas, R. W. Larsen, M. Eddaoudi and M. J. Zaworotko, *J. Am. Chem. Soc.*, 2009, **131**, 17040-17041.
37. T. F. Liu, D. Feng, Y. P. Chen, L. Zou, M. Bosch, S. Yuan, Z. Wei, S. Fordham, K. Wang and H. C. Zhou, *J. Am. Chem. Soc.*, 2015, **137**, 413-419.
38. O. M. Yaghi, M. O'Keeffe, N. W. Ockwig, H. K. Chae, M. Eddaoudi and J. Kim, *Nature*, 2003, **423**, 705-714.
39. W. Lu, Z. Wei, Z. Y. Gu, T. F. Liu, J. Park, J. Park, J. Tian, M. Zhang, Q. Zhang, T. Gentle, 3rd, M. Bosch and H. C. Zhou, *Chem. Soc. Rev.*, 2014, **43**, 5561-5593.
40. N. Stock and S. Biswas, *Chem. Rev.*, 2012, **112**, 933-969.
41. S. Diring, S. Furukawa, Y. Takashima, T. Tsuruoka and S. Kitagawa, *Chem. Mater.*, 2010, **22**, 4531-4538.
42. A. Schaate, P. Roy, A. Godt, J. Lippke, F. Waltz, M. Wiebcke and P. Behrens, *Chem. Eur. J.*, 2011, **17**, 6643-6651.
43. S. Yuan, L. Feng, K. Wang, J. Pang, M. Bosch, C. Lollar, Y. Sun, J. Qin, X. Yang, P. Zhang, Q. Wang, L. Zou, Y. Zhang, L. Zhang, Y. Fang, J. Li and H. C. Zhou, *Adv. Mater.*, 2018, **30**, e1704303.
44. C. O. Kappe, *Chem. Soc. Rev.*, 2008, **37**, 1127-1139.
45. J. Klinowski, F. A. Paz, P. Silva and J. Rocha, *Dalton Trans.*, 2011, **40**, 321-330.
46. J.-Y. Choi, J. Kim, S.-H. Jhung, H.-K. Kim, J.-S. Chang and H. K. Chae, *Bull. Korean Chem. Soc.*, 2006, **27**, 1523-1524.
47. S. H. Jhung, J. H. Lee, J. W. Yoon, C. Serre, G. Férey and J. S. Chang, *Adv. Mater.*, 2007, **19**, 121-124.
48. M. Schlesinger, S. Schulze, M. Hietschold and M. Mehring, *Microporous and Mesoporous Mater.*, 2010, **132**, 121-127.
49. T. Chalati, P. Horcajada, R. Gref, P. Couvreur and C. Serre, *J. Mater. Chem.*, 2011, **21**, 2220-2227.

50. U. Mueller, M. Schubert, F. Teich, H. Puetter, K. Schierle-Arndt and J. Pastré, *J. Mater. Chem.*, 2006, **16**, 626-636.
51. Y. Liu, Y. Wei, M. Liu, Y. Bai, X. Wang, S. Shang, J. Chen and Y. Liu, *Angew. Chem. Int. Ed.*, 2021, **60**, 2887-2891.
52. O. J. de Lima Neto, A. C. d. O. Frós, B. S. Barros, A. F. de Farias Monteiro and J. Kulesza, *New J. Chem.*, 2019, **43**, 5518-5524.
53. M. Hartmann, S. Kunz, D. Himsl, O. Tangermann, S. Ernst and A. Wagener, *Langmuir*, 2008, **24**, 8634-8642.
54. L. G. Qiu, Z. Q. Li, Y. Wu, W. Wang, T. Xu and X. Jiang, *Chem. Commun.*, 2008, 3642-3644.
55. W. J. Son, J. Kim, J. Kim and W. S. Ahn, *Chem. Commun.*, 2008, 6336-6338.
56. L. Aboutorabi and A. Morsali, *Inorg. Chim. Acta*, 2010, **363**, 2506-2511.
57. C. G. Carson, A. J. Brown, D. S. Sholl and S. Nair, *Cryst. Growth Des.*, 2011, **11**, 4505-4510.
58. B. Szczęśniak, S. Borysiuk, J. Choma and M. Jaroniec, *Mater. Horiz.*, 2020, **7**, 1457-1473.
59. A. P. Amrute, J. De Bellis, M. Felderhoff and F. Schüth, *Chem. Eng. J.*, 2021, **27**, 6819-6847.
60. A. Krusenbaum, S. Grätz, G. T. Tigineh, L. Borchardt and J. G. Kim, *Chem. Soc. Rev.*, 2022, **51**, 2873-2905.
61. T. Tsuzuki and P. G. McCormick, *J. Mater. Sci.*, 2004, **39**, 5143-5146.
62. T. K. Achar, A. Bose and P. Mal, *Beilstein J. Org. Chem.*, 2017, **13**, 1907-1931.
63. A. Pichon, A. Lazuen-Garay and S. L. James, *CrystEngComm*, 2006, **8**, 211-214.
64. J. Beamish-Cook, K. Shankland, C. A. Murray and P. Vaqueiro, *Cryst. Growth Des.*, 2021, **21**, 3047-3055.
65. D. Lv, Y. Chen, Y. Li, R. Shi, H. Wu, X. Sun, J. Xiao, H. Xi, Q. Xia and Z. Li, *J. Chem. Eng. Data*, 2017, **62**, 2030-2036.
66. K. Leng, Y. Sun, X. Li, S. Sun and W. Xu, *Cryst. Growth Des.*, 2016, **16**, 1168-1171.
67. Y. Chen, H. Wu, Z. Liu, X. Sun, Q. Xia and Z. Li, *Ind. Eng. Chem. Res.*, 2018, **57**, 703-709.
68. S. Głowniak, B. Szczęśniak, J. Choma and M. Jaroniec, *Mater. Today*, 2021, **46**, 109-124.
69. M. Taheri, I. D. Bernardo, A. Lowe, D. R. Nisbet and T. Tsuzuki, *Cryst. Growth Des.*, 2020, **20**, 2761-2773.
70. L. D. Salmi, M. J. Heikkilä, E. Puukilainen, T. Sajavaara, D. Grosso and M. Ritala, *Microporous and Mesoporous Mater.*, 2013, **182**, 147-154.
71. J. Troyano, C. Çamur, L. Garzón-Tovar, A. Carné-Sánchez, I. Imaz and D. Maspoch, *Acc. Chem. Res.*, 2020, **53**, 1206-1217.
72. M.-L. Hu, M. Y. Masoomi and A. Morsali, *Coord. Chem. Rev.*, 2019, **387**, 415-435.
73. A. Zuliani, M. C. Castillejos and N. Khiar, *Green Chem.*, 2023, **25**, 10596-10610.
74. M. Rubio-Martinez, C. Avci-Camur, A. W. Thornton, I. Imaz, D. Maspoch and M. R. Hill, *Chem. Soc. Rev.*, 2017, **46**, 3453-3480.
75. J. E. Mondloch, M. J. Katz, N. Planas, D. Semrouni, L. Gagliardi, J. T. Hupp and O. K.

Farha, *Chem. Commun.*, 2014, **50**, 8944-8946.
76. R. A. Dodson, A. G. Wong-Foy and A. J. Matzger, *Chem. Mater.*, 2018, **30**, 6559-6565.
77. G. Férey, C. Mellot-Draznieks, C. Serre, F. Millange, J. Dutour, S. Surblé and I. Margiolaki, *Science*, 2005, **309**, 2040-2042.
78. J. H. Cavka, S. Jakobsen, U. Olsbye, N. Guillou, C. Lamberti, S. Bordiga and K. P. Lillerud, *J. Am. Chem. Soc.*, 2008, **130**, 13850-13851.
79. J. E. Mondloch, O. Karagiaridi, O. K. Farha and J. T. Hupp, *CrystEngComm*, 2013, **15**, 9258.
80. J. Ma, A. P. Kalenak, A. G. Wong-Foy and A. J. Matzger, *Angew. Chem. Int. Ed.*, 2017, **56**, 14618-14621.
81. A. J. Howarth, A. W. Peters, N. A. Vermeulen, T. C. Wang, J. T. Hupp and O. K. Farha, *Chem. Mater.*, 2016, **29**, 26-39.
82. A. P. Nelson, O. K. Farha, K. L. Mulfort and J. T. Hupp, *J. Am. Chem. Soc.*, 2009, **131**, 458-460.
83. H. Furukawa, N. Ko, Y. B. Go, N. Aratani, S. B. Choi, E. Choi, A. Ö. Yazaydin, R. Q. Snurr, M. O'Keeffe and J. Kim, *Science*, 2010, **329**, 424-428.
84. T. K. Prasad and M. P. Suh, *Chem. Eur. J.*, 2012, **18**, 8673-8680.
85. L. Ma, A. Jin, Z. Xie and W. Lin, *Angew. Chem. Int. Ed.*, 2009, **48**, 9905-9908.
86. Y. Kalinovskyy, N. Cooper, M. Main, S. J. Holder and B. Blight, *Dalton Trans.*, 2017, **46**, 15704-15709.
87. E. J. Lee, J. Bae, K. M. Choi and N. C. Jeong, *ACS Appl. Mater. Interfaces*, 2019, **11**, 35155-35161.
88. D. Feng, Z. Y. Gu, J. R. Li, H. L. Jiang, Z. Wei and H. C. Zhou, *Angew. Chem. Int. Ed.*, 2012, **124**, 10453-10456.
89. J. E. Mondloch, W. Bury, D. Fairen-Jimenez, S. Kwon, E. J. DeMarco, M. H. Weston, A. A. Sarjeant, S. T. Nguyen, P. C. Stair and R. Q. Snurr, *J. Am. Chem. Soc.*, 2013, **135**, 10294-10297.
90. P. Deria, J. Yu, T. Smith and R. P. Balaraman, *J. Am. Chem. Soc.*, 2017, **139**, 5973-5983.
91. T. F. Liu, N. A. Vermeulen, A. J. Howarth, P. Li, A. A. Sarjeant, J. T. Hupp and O. K. Farha, *Eur. J. Inorg. Chem.*, 2016, **2016**, 4349-4352.
92. C. Gropp, S. Canossa, S. Wuttke, F. Gandara, Q. Li, L. Gagliardi and O. M. Yaghi, *ACS Cent. Sci.*, 2020, **6**, 1255-1273.
93. J. L. Rowsell, E. C. Spencer, J. Eckert, J. A. Howard and O. M. Yaghi, *Science*, 2005, **309**, 1350-1354.
94. K. K. Tanabe, Z. Wang and S. M. Cohen, *J. Am. Chem. Soc.*, 2008, **130**, 8508-8517.
95. Y. Inokuma, S. Yoshioka, J. Ariyoshi, T. Arai, Y. Hitora, K. Takada, S. Matsunaga, K. Rissanen and M. Fujita, *Nature*, 2013, **495**, 461-466.
96. H. Furukawa, F. Gandara, Y. B. Zhang, J. Jiang, W. L. Queen, M. R. Hudson and O. M. Yaghi, *J. Am. Chem. Soc.*, 2014, **136**, 4369-4381.
97. M. Dan-Hardi, C. Serre, T. Frot, L. Rozes, G. Maurin, C. Sanchez and G. Férey, *J. Am. Chem. Soc.*, 2009, **131**, 10857-10859.
98. C. Volkringer, T. Loiseau, N. Guillou, G. Ferey, E. Elkaim and A. Vimont, *Dalton Trans.*, 2009, 2241-2249.

99. B. Mu, F. Li, Y. Huang and K. S. Walton, *J. Mater. Chem.*, 2012, **22**, 10172.
100. S. Brunauer, P. H. Emmett and E. Teller, *J. Am. Chem. Soc.*, 1938, **60**, 309-319.
101. I. Langmuir, *J. Am. Chem. Soc.*, 1918, **40**, 1361-1403.
102. J. Rouquerol, F. Rouquerol, P. Llewellyn, G. Maurin and K. Sing, *Adsorption by powders and porous solids: principles, methodology and applications*, Academic press, 2013.
103. D. A. Gómez-Gualdrón, P. Z. Moghadam, J. T. Hupp, O. K. Farha and R. Q. Snurr, *J. Am. Chem. Soc.*, 2016, **138**, 215-224.
104. X. Zhang, Z. Chen, X. Liu, S. L. Hanna, X. Wang, R. Taheri-Ledari, A. Maleki, P. Li and O. K. Farha, *Chem. Soc. Rev.*, 2020, **49**, 7406-7427.
105. K. Müller-Buschbaum, F. Beuerle and C. Feldmann, *Microporous and Mesoporous Mater.*, 2015, **216**, 171-199.
106. M. Eddaoudi, D. B. Moler, H. Li, B. Chen, T. M. Reineke, M. O'keeffe and O. M. Yaghi, *Acc. Chem. Res.*, 2001, **34**, 319-330.
107. R. P. Davies, R. Less, P. D. Lickiss, K. Robertson and A. J. White, *Cryst. Growth Des.*, 2010, **10**, 4571-4581.
108. H.-R. Tian, C.-Y. Gao, Y. Yang, J. Ai, C. Liu, Z.-G. Xu and Z.-M. Sun, *New J. Chem.*, 2017, **41**, 1137-1141.
109. D. Wang, W. Yang, L. Li, X. Zhao, S. Feng and H. Liu, *J. Mater. Chem. A*, 2013, **1**, 13549.
110. Y. Yang, Z. Guo, X.-H. Chen and J. Liu, *J. Solid State Chem.*, 2019, **276**, 190-193.
111. F.-Q. Liu and T. D. Tilley, *Inorg. Chem.*, 1997, **36**, 5090-5096.
112. J. B. Lambert, Y. Zhao and C. L. Stern, *J. Phys. Org. Chem.*, 1997, **10**, 229-232.
113. J. B. Lambert, Z. Liu and C. Liu, *Organometallics*, 2008, **27**, 1464-1469.
114. R. J. L. R. P. Davies, P. D. Lickiss, K. Robertson, A. J. P. White, *Inorg. Chem.*, 2008, **47**, 9958-9964.
115. L. C. Delmas, A. J. P. White, D. Pugh, A. Evans, M. A. Isbell, J. Y. Y. Heng, P. D. Lickiss and R. P. Davies, *Chem. Commun.*, 2020, **56**, 7905-7908.
116. Y.-S. Xue, F.-Y. Jin, L. Zhou, M.-P. Liu, Y. Xu, H.-B. Du, M. Fang and X.-Z. You, *Cryst. Growth Des.*, 2012, **12**, 6158-6164.
117. Y.-F. Hui, C.-L. Kang, T. Tian, S. Dang, J. Ai, C. Liu, H.-R. Tian, Z.-M. Sun and C.-Y. Gao, *CrystEngComm*, 2017, **19**, 1564-1570.
118. L. C. Delmas, A. J. P. White, D. Pugh, P. N. Horton, S. J. Coles, P. D. Lickiss and R. P. Davies, *CrystEngComm*, 2018, **20**, 4541-4545.
119. D. Pugh, E. Ashworth, K. Robertson, L. C. Delmas, A. J. P. White, P. N. Horton, G. J. Tizzard, S. J. Coles, P. D. Lickiss and R. P. Davies, *Cryst. Growth Des.*, 2018, **19**, 487-497.
120. L. C. Delmas, P. N. Horton, A. J. P. White, S. J. Coles, P. D. Lickiss and R. P. Davies, *Polyhedron*, 2019, **157**, 25-32.
121. S. E. Wenzel, M. Fischer, F. Hoffmann and M. Froba, *Inorg. Chem.*, 2009, **48**, 6559-6565.
122. R. A. Driessen, F. B. Hulsbergen, W. J. Vermin and J. Reedijk, *Inorg. Chem.*, 1982, **21**, 3594-3597.

123. S. Subramanian and M. J. Zaworotko, *Angew. Chem. Int. Ed.*, 1995, **34**, 2127-2129.
124. S. Noro, S. Kitagawa, M. Kondo and K. Seki, *Angew. Chem. Int. Ed.*, 2000, **39**, 2081-2084.
125. T. Mahenthirarajah, Y. Li and P. Lightfoot, *Inorg. Chem.*, 2008, **47**, 9097-9102.
126. V. Bulicanu, K. S. Pedersen, M. Rouzieres, J. Bendix, P. Dechambenoit, R. Clerac and E. A. Hillard, *Chem. Commun.*, 2015, **51**, 17748-17751.
127. J. L. Manson, J. A. Schlueter, K. E. Garrett, P. A. Goddard, T. Lancaster, J. S. Moller, S. J. Blundell, A. J. Steele, I. Franke, F. L. Pratt, J. Singleton, J. Bendix, S. H. Lapidus, M. Uhlarz, O. Ayala-Valenzuela, R. D. McDonald, M. Gurak and C. Baines, *Chem. Commun.*, 2016, **52**, 12653-12656.
128. X.-Z. Zou, A.-S. Feng, Y.-Z. Liao, X.-Y. Xu, H.-Y. Wen, A. You, M. Mei and Y. Li, *Inorg. Chem. Commun.*, 2020, **118**, 108030.
129. Y. Zhang, W. Sun, B. Luan, J. Li, D. Luo, Y. Jiang, L. Wang and B. Chen, *Angew. Chem. Int. Ed.*, 2023, **62**, e202309925.
130. S.-i. Noro, R. Kitaura, M. Kondo, S. Kitagawa, T. Ishii, H. Matsuzaka and M. Yamashita, *J. Am. Chem. Soc.*, 2002, **124**, 2568-2583.
131. W. Liang, P. M. Bhatt, A. Shkurenko, K. Adil, G. Mouchaham, H. Aggarwal, A. Mallick, A. Jamal, Y. Belmabkhout and M. Eddaoudi, *Chem*, 2019, **5**, 950-963.
132. Z. Zhang, Q. Yang, X. Cui, L. Yang, Z. Bao, Q. Ren and H. Xing, *Angew. Chem. Int. Ed.*, 2017, **56**, 16282-16287.
133. J. Jia, A. J. Blake, N. R. Champness, P. Hubberstey, C. Wilson and M. Schroder, *Inorg. Chem.*, 2008, **47**, 8652-8664.
134. Z. Bao, D. Xie, G. Chang, H. Wu, L. Li, W. Zhou, H. Wang, Z. Zhang, H. Xing, Q. Yang, M. J. Zaworotko, Q. Ren and B. Chen, *J. Am. Chem. Soc.*, 2018, **140**, 4596-4603.
135. Y. Liu, H. Wu, L. Guo, W. Zhou, Z. Zhang, Q. Yang, Y. Yang, Q. Ren and Z. Bao, *Angew. Chem. Int. Ed.*, 2022, **61**, e202117609.
136. S. D. Burd, S. Ma, J. A. Perman, B. J. Sikora, R. Q. Snurr, P. K. Thallapally, J. Tian, L. Wojtas and M. J. Zaworotko, *J. Am. Chem. Soc.*, 2012, **134**, 3663-3666.
137. X. Cui, K. Chen, H. Xing, Q. Yang, R. Krishna, Z. Bao, H. Wu, W. Zhou, X. Dong and Y. Han, *Science*, 2016, **353**, 141-144.
138. X. Cui, Q. Yang, L. Yang, R. Krishna, Z. Zhang, Z. Bao, H. Wu, Q. Ren, W. Zhou, B. Chen and H. Xing, *Adv. Mater.*, 2017, **29**, 1606929.
139. X. Zhu, T. Ke, J. Zhou, Y. Song, Q. Xu, Z. Zhang, Z. Bao, Y. Yang, Q. Ren and Q. Yang, *J. Am. Chem. Soc.*, 2023, **145**, 9254-9263.
140. M.-J. Lin, A. Jouaiti, N. Kyritsakas and M. W. Hosseini, *CrystEngComm*, 2010, **12**, 67-69.
141. Y. Shen, K. Sugimoto, S. Yamashita, T. Yoshida, Y. Nakazawa, B. K. Breedlove, H. Zhang and M. Yamashita, *Chem. Commun.*, 2022, **58**, 3763-3766.
142. Q. Lin, C. Mao, A. Kong, X. Bu, X. Zhao and P. Feng, *J. Mater. Chem. A*, 2017, **5**, 21189-21195.
143. B. Manna, S. Sharma and S. Ghosh, *Crystals*, 2018, **8**, 37.
144. O. Alduhaish, R.-B. Lin, H. Wang, B. Li, H. D. Arman, T.-L. Hu and B. Chen, *Cryst. Growth Des.*, 2018, **18**, 4522-4527.

145. H.-M. Wen, C. Liao, L. Li, A. Alsalme, Z. Alothman, R. Krishna, H. Wu, W. Zhou, J. Hu and B. Chen, *J. Mater. Chem. A*, 2019, **7**, 3128-3134.
146. O. Shekhah, Y. Belmabkhout, K. Adil, P. M. Bhatt, A. J. Cairns and M. Eddaoudi, *Chem. Commun.*, 2015, **51**, 13595-13598.
147. L. Yang, X. Cui, Q. Yang, S. Qian, H. Wu, Z. Bao, Z. Zhang, Q. Ren, W. Zhou, B. Chen and H. Xing, *Adv. Mater.*, 2018, **30**, 1705374.
148. S. K. Elsaidi, M. H. Mohamed, C. M. Simon, E. Braun, T. Pham, K. A. Forrest, W. Xu, D. Banerjee, B. Space, M. J. Zaworotko and P. K. Thallapally, *Chem. Sci.*, 2017, **8**, 2373-2380.
149. E. A. Goreshnik, Y. I. Slyvka and M. G. Mys'kiv, *Inorg. Chim. Acta*, 2011, **377**, 177-180.
150. P. Nugent, Y. Belmabkhout, S. D. Burd, A. J. Cairns, R. Luebke, K. Forrest, T. Pham, S. Ma, B. Space, L. Wojtas, M. Eddaoudi and M. J. Zaworotko, *Nature*, 2013, **495**, 80-84.
151. H. Li, C. Liu, C. Chen, Z. Di, D. Yuan, J. Pang, W. Wei, M. Wu and M. Hong, *Angew. Chem. Int. Ed.*, 2021, **60**, 7547-7552.
152. N. Kumar, S. Mukherjee, N. C. Harvey-Reid, A. A. Bezrukov, K. Tan, V. Martins, M. Vandichel, T. Pham, L. M. van Wyk, K. Oyekan, A. Kumar, K. A. Forrest, K. M. Patil, L. J. Barbour, B. Space, Y. Huang, P. E. Kruger and M. J. Zaworotko, *Chem*, 2021, **7**, 3085-3098.
153. D. Sensharma, D. J. O'Hearn, A. Koochaki, A. A. Bezrukov, N. Kumar, B. H. Wilson, M. Vandichel and M. J. Zaworotko, *Angew. Chem. Int. Ed.*, 2022, **61**, e202116145.
154. S. Zou, Z. Di, Y. Liu, Z. Ji, H. Li, C. Chen and M. Wu, *Inorg. Chem. Commun.*, 2022, **137**, 109198.
155. S. Zou, Z. Di, H. Li, Y. Liu, Z. Ji, H. Li, C. Chen, M. Wu and M. Hong, *Inorg. Chem.*, 2022, **61**, 7530-7536.
156. J. J. Liu, Y. J. Hong, Y. F. Guan, M. J. Lin, C. C. Huang and W. X. Dai, *Dalton Trans.*, 2015, **44**, 653-658.
157. K. Uemura, A. Maeda, T. K. Maji, P. Kanoo and H. Kita, *Eur. J. Inorg. Chem.*, 2009, **2009**, 2329-2337.
158. Y. L. Yang, *Acta Cryst.*, 2012, **E68**, m209.
159. M.-C. Suen, Z.-K. Chan, J.-D. Chen, J.-C. Wang and C.-H. Hung, *Polyhedron*, 2006, **25**, 2325-2332.
160. S. Xiong, Y. He, R. Krishna, B. Chen and Z. Wang, *Cryst. Growth Des.*, 2013, **13**, 2670-2674.
161. E. M. Ketatni, N. Kyritsakas, P. Mobian and A. Jouaiti, *J. Mol. Struct.*, 2022, **1248**, 131466.
162. A. M. Tous-Granados and A. J. Hernandez-Maldonado, *Chem. Commun.*, 2023, **59**, 10020-10023.
163. M. J. Lin, A. Jouaiti, D. Pocic, N. Kyritsakas, J. M. Planeix and M. W. Hosseini, *Chem. Commun.*, 2010, **46**, 112-114.
164. M. Jiang, B. Li, X. Cui, Q. Yang, Z. Bao, Y. Yang, H. Wu, W. Zhou, B. Chen and H. Xing, *ACS Appl. Mater. Interfaces*, 2018, **10**, 16628-16635.

165. D. Sensharma, S. Vaesen, C. Healy, J. Hartmann, A. C. Kathalikkattil, P. Wix, F. Steuber, N. Zhu and W. Schmitt, *Eur. J. Inorg. Chem.*, 2018, **2018**, 1993-1997.
166. B. Li, X. Cui, D. O'Nolan, H. M. Wen, M. Jiang, R. Krishna, H. Wu, R. B. Lin, Y. S. Chen, D. Yuan, H. Xing, W. Zhou, Q. Ren, G. Qian, M. J. Zaworotko and B. Chen, *Adv. Mater.*, 2017, **29**, 1704210.
167. F. S. Keij, R. A. De Graaff, J. G. Haasnoot, J. Reedijk and E. Pedersen, *Inorg. Chim. Acta*, 1989, **156**, 65-70.
168. Y. Duan, Y. Huang, C. Wang, Q. Wang, K. Ge, Z. Lu, H. Wang, J. Duan, J. Bai and W. Jin, *Chem. Sci.*, 2023, **14**, 4605-4611.
169. H. Wang, Y. Duan, Y. Wang, Y. Huang, K. Ge, S. Wang, B. Zheng, Z. Wang, J. Bai and J. Duan, *ACS Appl. Mater. Interfaces*, 2022, **14**, 13550-13559.
170. Y.-P. Xia, C.-X. Wang, M.-H. Yu and X.-H. Bu, *Chin. Chem. Lett.*, 2021, **32**, 1153-1156.
171. L. Croitor, E. B. Coropceanu and M. S. Fonari, *CrystEngComm*, 2022, **24**, 6146-6154.
172. D. Kim, J. Han, O. S. Jung and Y. A. Lee, *RSC Adv.*, 2022, **12**, 25118-25122.
173. V. V. Ponomarova, V. V. Komarchuk, I. Boldog, H. Krautscheid and K. V. Domasevitch, *CrystEngComm*, 2013, **15**, 8280.
174. T. Ke, Q. Wang, X. Zhu, J. Hu, Z. Bao, Z. Zhang, Q. Ren and Q. Yang, *Chem. Eng. J.*, 2023, **472**, 144852.
175. A. B. Lago, A. Pino-Cuevas, R. Carballo and E. M. Vázquez-López, *CrystEngComm*, 2021, **23**, 153-162.
176. J. Klingele, B. Moubaraki, K. S. Murray, J. F. Boas and S. Brooker, *Eur. J. Inorg. Chem.*, 2005, **2005**, 1530-1541.
177. N. Li, Y. Hou and G.-G. Hou, *Inorg. Nano-Met. Chem.*, 2017, **47**, 1141-1144.
178. M.-C. Suen and J.-C. Wang, *Struct. Chem.*, 2006, **17**, 315-322.
179. M.-J. Lin, A. Jouaiti, N. Kyritsakas and M. W. Hosseini, *CrystEngComm*, 2011, **13**, 776-778.
180. A. Bajpai, M. Lusi and M. J. Zaworotko, *Chem. Commun.*, 2017, **53**, 3978-3981.
181. J. Lee, S. Park, D. Kim, Y.-A. Lee and O.-S. Jung, *Inorg. Chem. Front.*, 2020, **7**, 1546-1552.
182. T. Ke, Q. Wang, J. Shen, J. Zhou, Z. Bao, Q. Yang and Q. Ren, *Angew. Chem. Int. Ed.*, 2020, **59**, 12725-12730.
183. D.-Q. Qi, G.-G. Hou, X.-J. Wang, Y.-P. Zhang and J.-Z. You, *Synth. React. Inorg., Met.-Org., Nano-Met. Chem.*, 2014, **45**, 407-410.
184. M.-H. You, M.-H. Li and M.-J. Lin, *Cryst. Growth Des.*, 2022, **22**, 1384-1389.
185. T. G. Cherkasova, N. V. Pervukhina, N. V. Kuratieva, V. A. Sannikova, E. S. Tatarinova and E. V. Cherkasova, *Russ. J. Inorg. Chem.*, 2019, **64**, 1120-1126.
186. B. Q. Song, Q. Y. Yang, S. Q. Wang, M. Vandichel, A. Kumar, C. Crowley, N. Kumar, C. H. Deng, V. GasconPerez, M. Lusi, H. Wu, W. Zhou and M. J. Zaworotko, *J. Am. Chem. Soc.*, 2020, **142**, 6896-6901.
187. Q. Dong, X. Zhang, S. Liu, R. B. Lin, Y. Guo, Y. Ma, A. Yonezu, R. Krishna, G. Liu, J. Duan, R. Matsuda, W. Jin and B. Chen, *Angew. Chem. Int. Ed.*, 2020, **59**, 22756-22762.
188. Q. Dong, Y. Huang, K. Hyeon-Deuk, I. Y. Chang, J. Wan, C. Chen, J. Duan, W. Jin and S. Kitagawa, *Adv. Funct. Mater.*, 2022, **32**, 2203745.

189. M. Shivanna, K. I. Otake, B. Q. Song, L. M. van Wyk, Q. Y. Yang, N. Kumar, W. K. Feldmann, T. Pham, S. Suepaul, B. Space, L. J. Barbour, S. Kitagawa and M. J. Zaworotko, *Angew. Chem. Int. Ed.*, 2021, **60**, 20383-20390.
190. X.-Y. Tian, H.-L. Zhou, X. Fang, Z.-W. Mo, Y.-T. Xu, D.-D. Zhou and J.-P. Zhang, *CrystEngComm*, 2017, **19**, 6164-6169.
191. C. H. Springsteen, R. D. Sweeder and R. L. LaDuca, *Cryst. Growth Des.*, 2006, **6**, 2308-2314.
192. X.-W. Gu, E. Wu, J.-X. Wang, H.-M. Wen, B. Chen, B. Li and G. Qian, *Sci. Adv.*, 2023, **9**, eadh0135.
193. J. Wang, Y. Zhang, P. Zhang, J. Hu, R. B. Lin, Q. Deng, Z. Zeng, H. Xing, S. Deng and B. Chen, *J. Am. Chem. Soc.*, 2020, **142**, 9744-9751.
194. R. B. Lin, L. Li, H. Wu, H. Arman, B. Li, R. G. Lin, W. Zhou and B. Chen, *J. Am. Chem. Soc.*, 2017, **139**, 8022-8028.
195. P. Larpent, A. Jouaiti, N. Kyritsakas and M. W. Hosseini, *Chem. Commun.*, 2013, **49**, 4468-4470.
196. Y. Song, T. Ke, J. Shen, J. Li, X. Zhu, L. Yang, Z. Zhang, Z. Bao, Q. Ren and Q. Yang, *Sep. Purif. Technol.*, 2023, **323**, 124377.
197. H. S. Quah, V. Nalla, K. Zheng, C. A. Lee, X. Liu and J. J. Vittal, *Chem. Mater.*, 2017, **29**, 7424-7430.
198. S. Banerjee and P. Dastidar, *CrystEngComm*, 2013, **15**, 9415.
199. L. Li, R. Matsuda, I. Tanaka, H. Sato, P. Kanoo, H. J. Jeon, M. L. Foo, A. Wakamiya, Y. Murata and S. Kitagawa, *J. Am. Chem. Soc.*, 2014, **136**, 7543-7546.
200. S. Nazir, M. A. Rashid, M. Arif, A. Romerosa and A. C. Whitwood, *Inorg. Chim. Acta*, 2015, **427**, 198-202.
201. M. Lusi, P. B. Fechine, K. J. Chen, J. J. Perry IV and M. J. Zaworotko, *Chem. Commun.*, 2016, **52**, 4160.
202. M. J. Lin, A. Jouaiti, P. Grosshans, N. Kyritsakas and M. W. Hosseini, *Chem. Commun.*, 2011, **47**, 7635-7637.
203. O. Shekhah, Y. Belmabkhout, Z. Chen, V. Guillerm, A. Cairns, K. Adil and M. Eddaoudi, *Nat. Commun.*, 2014, **5**, 4228.
204. M.-J. Lin, A. Jouaiti, N. Kyritsakas and M. W. Hosseini, *CrystEngComm*, 2009, **11**, 189-191.
205. X. Wu, D. Li, L. Xu, Y.-F. Jiang, Y. Zhao and J. Zhao, *CrystEngComm*, 2023, **25**, 3222-3228.
206. H. Li, Q. Han, X. Chai, J. Wang and C. Yao, *Acta Cryst.*, 2012, **E68**, m405.
207. H. Casellas, A. Pevec, B. Kozlevčar, P. Gamez and J. Reedijk, *Polyhedron*, 2005, **24**, 1549-1554.
208. R. Gil-García, P. Gómez-Saiz, V. Díez-Gómez, G. Madariaga, M. Insausti, L. Lezama, J. V. Cuevas and J. García-Tojal, *Polyhedron*, 2014, **81**, 675-686.
209. C. Li, Z. Wei, M. Pan, H. Deng, J. Jiang and C. Su, *Chin. Chem. Lett.*, 2019, **30**, 1297-1301.
210. S. K. Elsaidi, M. H. Mohamed, T. Pham, T. Hussein, L. Wojtas, M. J. Zaworotko and B. Space, *Cryst. Growth Des.*, 2016, **16**, 1071-1080.

211. Z. Zhang, Q. Ding, S. B. Peh, D. Zhao, J. Cui, X. Cui and H. Xing, *Chem. Commun.*, 2020, **56**, 7726-7729.
212. H. Gong, C. Y. Chuah, Y. Yang and T.-H. Bae, *J. Ind. Eng. Chem.*, 2018, **60**, 279-285.
213. H. Gong, T. H. Nguyen, R. Wang and T.-H. Bae, *J. Membr. Sci.*, 2015, **495**, 169-175.
214. Y. Li, H. Li, S. Zou, Y. Liu, H. Li, Z. Ji, Z. Di, C. Chen and M. Wu, *Cryst. Growth Des.*, 2023, **23**, 2264-2271.
215. Z. Zhang, X. Cui, L. Yang, J. Cui, Z. Bao, Q. Yang and H. Xing, *Ind. Eng. Chem. Res.*, 2018, **57**, 7266-7274.
216. L. Yang, X. Cui, Y. Zhang, Q. Yang and H. Xing, *J. Mater. Chem. A*, 2018, **6**, 24452-24458.
217. K. Geng, T. He, R. Liu, S. Dalapati, K. T. Tan, Z. Li, S. Tao, Y. Gong, Q. Jiang and D. Jiang, *Chem. Rev.*, 2020, **120**, 8814-8933.
218. X. Lian, L. Xu, M. Chen, C. E. Wu, W. Li, B. Huang and Y. Cui, *J. Nanosci. Nanotechnol.*, 2019, **19**, 3059-3078.
219. S. Mukherjee, N. Sikdar, D. O'Nolan, D. M. Franz, V. Gascón, A. Kumar, N. Kumar, H. S. Scott, D. G. Madden and P. E. Kruger, *Sci. Adv.*, 2019, **5**, eaax9171.
220. P. Kanoo, S. K. Reddy, G. Kumari, R. Haldar, C. Narayana, S. Balasubramanian and T. K. Maji, *Chem. Commun.*, 2012, **48**, 8487-8489.
221. S. R. Caskey, A. G. Wong-Foy and A. J. Matzger, *J. Am. Chem. Soc.*, 2008, **130**, 10870-10871.
222. H. Li, L. Li, R. B. Lin, G. Ramirez, W. Zhou, R. Krishna, Z. Zhang, S. Xiang and B. Chen, *ACS Sustainable Chem. Eng.*, 2019, **7**, 4897-4902.
223. C. Gu, Z. Yu, J. Liu and D. S. Sholl, *ACS Appl. Mater. Interfaces*, 2021, **13**, 11039-11049.
224. S. K. Elsaidi, M. H. Mohamed, A. S. Helal, M. Galanek, T. Pham, S. Suepaul, B. Space, D. Hopkinson, P. K. Thallapally and J. Li, *Nat. Commun.*, 2020, **11**, 3103.
225. G. Han, Y. Gong, H. Huang, D. Cao, X. Chen, D. Liu and C. Zhong, *ACS Appl. Mater. Interfaces*, 2018, **10**, 32128-32132.
226. E. Adatoz, A. K. Avci and S. Keskin, *Sep. Purif. Technol.*, 2015, **152**, 207-237.
227. V. Chernikova, O. Shekhah, Y. Belmabkhout and M. Eddaoudi, *ACS Appl. Nano Mater.*, 2020, **3**, 6432-6439.
228. J. Roeser, D. Prill, M. J. Bojdys, P. Fayon, A. Trewin, A. N. Fitch, M. U. Schmidt and A. Thomas, *Nat. Chem.*, 2017, **9**, 977-982.
229. O. Yahiaoui, A. N. Fitch, F. Hoffmann, M. Fröba, A. Thomas and J. Roeser, *J. Am. Chem. Soc.*, 2018, **140**, 5330-5333.
230. S. Ashraf, Y. Zuo, S. Li, C. Liu, H. Wang, X. Feng, P. Li and B. Wang, *Chem. Eur. J.*, 2019, **25**, 13479-13483.
231. S. Ashraf, C. Liu, S. Li, I. U. Haq, M. Mehmood, P. Li and B. Wang, *ACS Appl. Mater. Interfaces*, 2020, **12**, 40372-40380.
232. G. Xiong, B.-B. Wang, L.-X. You, B.-Y. Ren, Y.-K. He, F. Ding, I. Dragutan, V. Dragutan and Y.-G. Sun, *J. Mater. Chem. A*, 2019, **7**, 393-404.
233. H. Luo, G. S. H. Poon Ho, C. Li, J. Huang, Z.-L. Xu and Y. Kim, *Ind. Eng. Chem. Res.*, 2023, **62**, 15790-15797.

234. C. Li, D. D. Wang, G. S. H. Poon Ho, Z. Zhang, J. Huang, K. T. Bang, C. Y. Lau, S. Y. Leu, Y. Wang and Y. Kim, *J. Am. Chem. Soc.*, 2023, **145**, 24603-24614.
235. I. I. Seifullina, E. E. Martsinko, E. A. Chebanenko, V. V. D'yakonenko, S. V. Shishkina and O. V. Pirozhok, *J. Struct. Chem.*, 2018, **59**, 154-159.
236. A. G. Pesaroglo, E. E. Martsinko, L. K. Minacheva, I. I. Seifullina and V. S. Sergienko, *Russ. J. Inorg. Chem.*, 2010, **55**, 1366-1372.
237. R. B. Lin, Y. He, P. Li, H. Wang, W. Zhou and B. Chen, *Chem. Soc. Rev.*, 2019, **48**, 1362-1389.
238. B. Chen, Z. Wang, Y. Wang, Y. Li, J. Zhao and L. Xie, *Cryst. Growth Des.*, 2021, **21**, 6173-6182.
239. Y. Wu, X. Mao, M. Zhang, X. Zhao, R. Xue, S. Di, W. Huang, L. Wang, Y. Li and Y. Li, *Adv. Mater.*, 2021, **33**, e2106079.
240. Y. H. Luo, X. T. He, D. L. Hong, C. Chen, F. H. Chen, J. Jiao, L. H. Zhai, L. H. Guo and B. W. Sun, *Adv. Funct. Mater.*, 2018, **28**, 1804822.
241. M. Simard, D. Su and J. D. Wuest, *J. Am. Chem. Soc.*, 1991, **113**, 4696-4698.
242. W. Yang, A. Greenaway, X. Lin, R. Matsuda, A. J. Blake, C. Wilson, W. Lewis, P. Hubberstey, S. Kitagawa and N. R. Champness, *J. Am. Chem. Soc.*, 2010, **132**, 14457-14469.
243. Y. He, S. Xiang and B. Chen, *J. Am. Chem. Soc.*, 2011, **133**, 14570-14573.
244. L. Chen, B. Zhang, L. Chen, H. Liu, Y. Hu and S. Qiao, *Mater. Adv.*, 2022, **3**, 3680-3708.
245. J. F. Feng, X. Y. Yan, Z. Y. Ji, T. F. Liu and R. Cao, *ACS Appl. Mater. Interfaces*, 2020, **12**, 29854-29860.
246. I. Hisaki, C. Xin, K. Takahashi and T. Nakamura, *Angew. Chem. Int. Ed.*, 2019, **58**, 11160-11170.
247. J. Jiang, Y. Zhao and O. M. Yaghi, *J. Am. Chem. Soc.*, 2016, **138**, 3255-3265.
248. Z. J. Lin, S. A. R. Mahammed, T. F. Liu and R. Cao, *ACS Cent. Sci.*, 2022, **8**, 1589-1608.
249. B. Wang, R. B. Lin, Z. Zhang, S. Xiang and B. Chen, *J. Am. Chem. Soc.*, 2020, **142**, 14399-14416.
250. P. Li, Y. He, J. Guang, L. Weng, J. C. Zhao, S. Xiang and B. Chen, *J. Am. Chem. Soc.*, 2014, **136**, 547-549.
251. H. Wang, Z. Bao, H. Wu, R. B. Lin, W. Zhou, T. L. Hu, B. Li, J. C. Zhao and B. Chen, *Chem. Commun.*, 2017, **53**, 11150-11153.
252. S. Feng, Y. Shang, Z. Wang, Z. Kang, R. Wang, J. Jiang, L. Fan, W. Fan, Z. Liu, G. Kong, Y. Feng, S. Hu, H. Guo and D. Sun, *Angew. Chem. Int. Ed.*, 2020, **59**, 3840-3845.
253. P. Li, Y. He, Y. Zhao, L. Weng, H. Wang, R. Krishna, H. Wu, W. Zhou, M. O'Keeffe, Y. Han and B. Chen, *Angew. Chem. Int. Ed.*, 2015, **54**, 574-577.
254. H. Wang, B. Li, H. Wu, T. L. Hu, Z. Yao, W. Zhou, S. Xiang and B. Chen, *J. Am. Chem. Soc.*, 2015, **137**, 9963-9970.
255. T. Li, B.-T. Liu, Z.-B. Fang, Q. Yin, R. Wang and T.-F. Liu, *J. Mater. Chem. A*, 2021, **9**, 4687-4691.
256. T. H. Chen, I. Popov, W. Kaveevivitchai, Y. C. Chuang, Y. S. Chen, O. Daugulis, A. J.

Jacobson and O. S. Miljanic, *Nat. Commun.*, 2014, **5**, 5131.
257. Y. Zhou, B. Liu, X. Sun, J. Li, G. Li, Q. Huo and Y. Liu, *Cryst. Growth Des.*, 2017, **17**, 6653-6659.
258. J.-H. Fournier, T. Maris, J. D. Wuest, W. Guo and E. Galoppini, *J. Am. Chem. Soc.*, 2003, **125**, 1002-1006.
259. X. Z. Luo, X. J. Jia, J. H. Deng, J. L. Zhong, H. J. Liu, K. J. Wang and D. C. Zhong, *J. Am. Chem. Soc.*, 2013, **135**, 11684-11687.
260. P. Li, O. Alduhaish, H. D. Arman, H. Wang, K. Alfooty and B. Chen, *Cryst. Growth Des.*, 2014, **14**, 3634-3638.
261. K. E. Maly, W. Buck and L. N. Dawe, *CrystEngComm*, 2017, **19**, 6401-6405.
262. M. A. Little and A. I. Cooper, *Adv. Funct. Mater.*, 2020, **30**, 1909842.
263. C. R. Groom, I. J. Bruno, M. P. Lightfoot and S. C. Ward, *Acta Cryst.*, 2016, **72**, 171-179.
264. I. Hisaki, S. Nakagawa, N. Tohnai and M. Miyata, *Angew. Chem. Int. Ed.*, 2015, **54**, 3008-3012.
265. A. L. Spek, *J. Appl. Crystallogr.*, 2003, **36**, 7-13.
266. I. Hisaki, N. Ikenaka, E. Gomez, B. Cohen, N. Tohnai and A. Douhal, *Chem. Eur. J.*, 2017, **23**, 11611-11619.
267. S. A. Boer, P.-X. Wang, M. J. MacLachlan and N. G. White, *Cryst. Growth Des.*, 2019, **19**, 4829-4835.
268. X. Song, Y. Wang, C. Wang, D. Wang, G. Zhuang, K. O. Kirlikovali, P. Li and O. K. Farha, *J. Am. Chem. Soc.*, 2022, **144**, 10663-10687.
269. D. W. Kang, M. Kang, H. Kim, J. H. Choe, D. W. Kim, J. R. Park, W. R. Lee, D. Moon and C. S. Hong, *Angew. Chem. Int. Ed.*, 2019, **58**, 16152-16155.
270. X. Zheng, N. Xiao, Z. Long, L. Wang, F. Ye, J. Fang, L. Shen and X. Xiao, *Synth. Met.*, 2020, **263**, 116365.
271. A. F. Benton and G. L. Cunningham, *J. Am. Chem. Soc.*, 1935, **57**, 2227-2234.
272. K. J. Balkus, I. S. Gabrielova and S. G. Bott, *Inorg. Chem.*, 1995, **34**, 5776-5780.
273. J. Cella, J. Cargioli and E. Williams, *J. Organomet. Chem*, 1980, **186**, 13-17.
274. O. Seiler, C. Burschka, M. Penka and R. Tacke, *Z. Anorg. Allg. Chem.*, 2002, **628**, 2427-2434.
275. C. F. Macrae, I. Sovago, S. J. Cottrell, P. T. Galek, P. McCabe, E. Pidcock, M. Platings, G. P. Shields, J. S. Stevens and M. Towler, *J. Appl. Cryst.*, 2020, **53**, 226-235.
276. B. Spingler, S. Schnidrig, T. Todorova and F. Wild, *CrystEngComm*, 2012, **14**, 751-757.
277. I. Richter, M. Penka and R. Tacke, *Inorg. Chem.*, 2002, **41**, 3950-3955.
278. R. Tacke, R. Bertermann, C. Burschka and S. Dragota, *Z. Anorg. Allg. Chem.*, 2004, **630**, 2006-2012.
279. L. Cunha-Silva, F.-N. Shi, F. A. Almeida Paz, M. J. Hardie, J. Klinowski, T. Trindade and J. Rocha, *Inorg. Chim. Acta*, 2009, **362**, 263-270.
280. M. A. Pereira Gonçalves and M. Ramos Silva, *J. Mol. Struct.*, 2020, **1200**, 127102.
281. I. Brekalo, D. E. Deliz, L. J. Barbour, M. D. Ward, T. Friscic and K. T. Holman, *Angew. Chem. Int. Ed.*, 2020, **59**, 1997-2002.
282. P. K. Sawinski, M. Meven, U. Englert and R. Dronskowski, *Cryst. Growth Des.*, 2013,

13, 1730-1735.
283. R. Tacke, A. Stewart, J. Becht, C. Burschka and I. Richter, *Can. J. Chem.*, 2000, **78**, 1380-1387.
284. Calculated based on VdW radii using the Cavities routine of CrystalMaker®: a crystal and molecular structures program for Mac and Windows. CrystalMaker Software Ltd, Oxford, England (www.crystalmaker.com)
285. J. J. Flynn and F. P. Boer, *J. Am. Chem. Soc.*, 1969, **91**, 5756-5761.
286. P. Bindu, B. Varghese and M. N. S. Rao, *Phosphorus, Sulfur Silicon Relat. Elem.*, 2003, **178**, 2373-2386.
287. G. E. Tilburey, T. J. Blundell, S. P. Argent and C. C. Perry, *Dalton Trans.*, 2019, **48**, 15470-15479.
288. B. A. Borgias, S. R. Cooper, Y. B. Koh and K. N. Raymond, *Inorg. Chem.*, 1984, **23**, 1009-1016.
289. A. D. Tinoco, E. V. Eames, C. D. Incarvito and A. M. Valentine, *Inorg. Chem.*, 2008, **47**, 8380-8390.
290. S. H. Johnson, C. E. Jackson and J. M. Zadrozny, *Inorg. Chem.*, 2020, **59**, 7479-7486.
291. G.-L. Dong, L. Wang, W.-H. Fang and L. Zhang, *Inorg. Chem. Commun.*, 2018, **93**, 61-64.
292. M. Liu, Y.-B. He, W. Lv, C. Zhang, H. Du, B. Li, Q.-H. Yang and F. Kang, *J. Power Sources*, 2014, **268**, 882-886.
293. O. Rossin, *Monatshefte für Chemie*, 1891, **12**, 486-500.
294. M. Freund, *Justus Liebigs Annalen der Chemie*, 1892, **271**, 311-408.
295. D. S. Pratt and G. A. Perkins, *J. Am. Chem. Soc.*, 1918, **40**, 219-236.
296. G. A. Olah, L. Ohannesian and M. Arvanaghi, *Chem. Rev.*, 1987, **87**, 671-686.
297. M.-G. Baudart and L. F. Hennequin, *J. Antibiot.*, 1993, **46**, 1458-1470.
298. A. G. Griesbeck, B. Öngel and M. Atar, *J. Phys. Org. Chem.*, 2017, **30**, e3741.
299. O. K. Farha, I. Eryazici, N. C. Jeong, B. G. Hauser, C. E. Wilmer, A. A. Sarjeant, R. Q. Snurr, S. T. Nguyen, A. O. Yazaydin and J. T. Hupp, *J. Am. Chem. Soc.*, 2012, **134**, 15016-15021.
300. M. Ghiaci and J. Asghari, *Synth. Commun.*, 1999, **29**, 973-979.
301. T. Ma, T. Kojima and Y. Matsuda, *Bull. Chem. Soc. Jpn.*, 2000, **73**, 747-748.
302. A. Soni, A. Dutt, V. Sattigeri and I. A. Cliffe, *Synth. Commun.*, 2011, **41**, 1852-1857.
303. L. X. Sosa-Vargas, I. Chambrier, C. J. MacDonald, S. J. Coles, G. J. Tizzard, A. N. Cammidge and M. J. Cook, *J. Porphyr. Phthalocyanines*, 2013, **17**, 511-521.
304. H. S. Lu, W. K. Han, X. Yan, C. J. Chen, T. Niu and Z. G. Gu, *Angew. Chem. Int. Ed.*, 2021, **60**, 17881-17886.
305. M. Nanjo, M. Goto and Y. Nakashima, *Inorg. Chim. Acta*, 2021, **528**, 120608.
306. Z. Zhang, B. Tan, P. Wang, X. Cui and H. Xing, *AIChE J.*, 2020, **66**, e16236.
307. І. Сейфулліна, О. Марцинко, О. Чебаненко, В. Дьяконенко, С. Шишкіна and О. Пєсарогло, *Voprosy Khimii i Khimicheskoi Tekhnologii*, 2020, **6**, 159-164.
308. X. Ren, Q. Pan, J. Liu, Y. Li, F. Wang, J. Li, Y. Xu and L. Li, *CrystEngComm*, 2014, **16**, 9545-9554.
309. M. S. Denning and J. M. Goicoechea, *Dalton Trans.*, 2008, 5882-5885.

310. F. Gándara, M. E. Medina, N. Snejko, B. Gómez-Lor, M. Iglesias, E. Gutiérrez-Puebla and M. A. Monge, *Inorg. Chem.*, 2008, **47**, 6791-6795.
311. N. N. Julius, A. Choudhury and C. N. R. Rao, *J. Solid State Chem.*, 2003, **170**, 124-129.
312. Q. Shen, C. J. Gómez-García, W. Sun, X. Lai, H. Pang and H. Ma, *Green Chem.*, 2021, **23**, 3104-3114.
313. S. R. Batten, S. M. Neville and D. R. Turner, *Coordination polymers: design, analysis and application*, Royal Society of Chemistry, 2008.
314. A. M. Spokoyny, D. Kim, A. Sumrein and C. A. Mirkin, *Chem. Soc. Rev.*, 2009, **38**, 1218-1227.
315. Y. Jiang, Y. Hu, B. Luan, L. Wang, R. Krishna, H. Ni, X. Hu and Y. Zhang, *Nat. Commun.*, 2023, **14**, 401.
316. F. Saraci, V. Quezada-Novoa, P. R. Donnarumma and A. J. Howarth, *Chem. Soc. Rev.*, 2020, **49**, 7949-7977.
317. M. O. Barsukova, S. A. Sapchenko, D. N. Dybtsev and V. P. Fedin, *Russ. Chem. Rev.*, 2018, **87**, 1139-1167.
318. J. W. Zhang, P. Qu, M. C. Hu, S. N. Li, Y. C. Jiang and Q. G. Zhai, *Inorg. Chem.*, 2019, **58**, 16792-16799.
319. H. J. Lv, J. W. Zhang, Y. C. Jiang, S. N. Li, M. C. Hu and Q. G. Zhai, *Inorg. Chem.*, 2022, **61**, 3553-3562.
320. P. Wang, L. Zhang, Z. Zhu, S. Wu, L. Shan, Y. Fan, L. Wang, X. Chen and J. Xu, *Inorg. Chim. Acta*, 2020, **501**, 119304.
321. S. A. Cotton, P. R. Raithby, A. Shield and J. M. Harrowfield, *Coord. Chem. Rev.*, 2022, **455**, 214366.
322. O. Yassine, O. Shekhah, A. H. Assen, Y. Belmabkhout, K. N. Salama and M. Eddaoudi, *Angew. Chem. Int. Ed.*, 2016, **55**, 15879-15883.
323. K. Liu, X. Li, D. Ma, Y. Han, B. Li, Z. Shi, Z. Li and L. Wang, *Mater. Chem. Front.*, 2017, **1**, 1982-1988.
324. E. Echenique-Errandonea, J. M. Perez, S. Rojas, J. Cepeda, J. M. Seco, I. Fernandez and A. Rodriguez-Dieguez, *Dalton Trans.*, 2021, **50**, 11720-11724.
325. L.-F. Chen, J. Zhang, G.-Q. Ren, L. Zhao-Ji, Y.-Y. Qin, P.-X. Yin, J.-K. Cheng and Y.-G. Yao, *CrystEngComm*, 2008, **10**, 1088.
326. F. Gándara, E. Gutiérrez-Puebla, M. Iglesias, N. Snejko and M. Á. Monge, *Cryst. Growth Des.*, 2009, **10**, 128-134.
327. X.-J. Zheng, L.-P. Jin and S. Gao, *Inorg. Chem.*, 2004, **43**, 1600-1602.
328. Y. Guo, L. Zhang, N. Muhammad, Y. Xu, Y. Zhou, F. Tang and S. Yang, *Inorg. Chem.*, 2018, **57**, 995-1003.
329. R. G. AbdulHalim, P. M. Bhatt, Y. Belmabkhout, A. Shkurenko, K. Adil, L. J. Barbour and M. Eddaoudi, *J. Am. Chem. Soc.*, 2017, **139**, 10715-10722.
330. L. Feng, Y. Wang, K. Zhang, K. Y. Wang, W. Fan, X. Wang, J. A. Powell, B. Guo, F. Dai, L. Zhang, R. Wang, D. Sun and H. C. Zhou, *Angew. Chem. Int. Ed.*, 2019, **58**, 16682-16690.
331. G. M. Farinola and R. Ragni, *Chem. Soc. Rev.*, 2011, **40**, 3467-3482.

332. X. Rao, Q. Huang, X. Yang, Y. Cui, Y. Yang, C. Wu, B. Chen and G. Qian, *J. Mater. Chem.*, 2012, **22**, 3210.
333. G. Bai, Z. Yang, H. Lin, W. Jie and J. Hao, *Nanoscale*, 2018, **10**, 9261-9267.
334. D. Medina-Velazquez, U. Caldiño, A. Morales-Ramirez, J. Reyes-Miranda, R. Lopez, R. Escudero, R. Ruiz-Guerrero and M. M. Perez, *Opt. Mater.*, 2019, **87**, 3-10.
335. Y.-M. Wang, X.-T. Tian, H. Zhang, Z.-R. Yang and X.-B. Yin, *ACS Appl. Mater. Interfaces*, 2018, **10**, 22445-22452.
336. H. Zhang, H. Liu, W. Jiang and S.-S. Zhao, *Dyes Pigm.*, 2019, **171**, 107665.
337. K. A. White, D. A. Chengelis, M. Zeller, S. J. Geib, J. Szakos, S. Petoud and N. L. Rosi, *Chem. Commun.*, 2009, 4506-4508.
338. K. A. White, D. A. Chengelis, K. A. Gogick, J. Stehman, N. L. Rosi and S. Petoud, *J. Am. Chem. Soc.*, 2009, **131**, 18069-18071.
339. W. J. Rieter, K. M. Taylor, H. An, W. Lin and W. Lin, *J. Am. Chem. Soc.*, 2006, **128**, 9024-9025.
340. M. Ferrari, *Nat. Rev. Cancer*, 2005, **5**, 161-171.
341. W. J. Rieter, K. M. Pott, K. M. Taylor and W. Lin, *J. Am. Chem. Soc.*, 2008, **130**, 11584-11585.
342. A. P. Shevchenko, A. A. Shabalin, I. Y. Karpukhin and V. A. Blatov, *Sci. Technol. Adv. Mater.*, 2022, **2**, 250-265.
343. D. Wang, L. Sun, C. Hao, Y. Yan and Z. Liang, *RSC Adv.*, 2016, **6**, 57828-57834.
344. C. Zhang, Y. Yan, Q. Pan, L. Sun, H. He, Y. Liu, Z. Liang and J. Li, *Dalton Trans.*, 2015, **44**, 13340-13346.
345. S. Su, S. Wang, X. Song, S. Song, C. Qin, M. Zhu, Z. Hao, S. Zhao and H. Zhang, *Dalton Trans.*, 2012, **41**, 4772-4779.
346. Á. Monge, F. Gándara, E. Gutiérrez-Puebla and N. Snejko, *CrystEngComm*, 2011, **13**, 5031-5044.
347. W. I. F. David, K. Shankland, J. van de Streek, E. Pidcock, W. D. S. Motherwell and J. C. Cole, *J. Appl. Cryst.*, 2006, **39**, 910-915.
348. A. T. Royappa, A. D. Royappa, R. F. Moral, A. L. Rheingold, R. J. Papoular, D. M. Blum, T. Q. Duong, J. R. Stepherson, O. D. Vu and B. Chen, *Polyhedron*, 2016, **119**, 563-574.
349. T. Wu, D. Luo, C. Duan, Z. Shi, Y. Chen and Z. Lin, *Inorg. Chem. Commun.*, 2014, **41**, 54-57.
350. R.-Q. Zhong, R.-Q. Zou, D. S. Pandey, T. Kiyobayashi and Q. Xu, *Inorg. Chem. Commun.*, 2008, **11**, 951-953.
351. J. Soleimannejad, H. Aghabozorg, S. Hooshmand, M. Ghadermazi and J. Attar Gharamaleki, *Acta Cryst.*, 2007, **63**, m2389-m2390.
352. G. Giester, *Z. Kristallogr.*, 1997, **212**, 720-723.
353. D. F. Sava, V. C. Kravtsov, J. Eckert, J. F. Eubank, F. Nouar and M. Eddaoudi, *J. Am. Chem. Soc.*, 2009, **131**, 10394-10396.
354. S. Ivanova, E. Köster, J. J. Holstein, N. Keller, G. H. Clever, T. Bein and F. Beuerle, *Angew. Chem. Int. Ed.*, 2021, **60**, 17455-17463.
355. S. O. Parreiras, J. M. Gallego and D. Ecija, *Chem. Commun.*, 2023, **59**, 8878-8893.

356. M. Wastie and K. Latief, *Br. J. Radiol*, 2004, **77**, 146-147.
357. W. Hatakeyama, T. J. Sanchez, M. D. Rowe, N. J. Serkova, M. W. Liberatore and S. G. Boyes, *ACS Appl. Mater. Interfaces*, 2011, **3**, 1502-1510.
358. Y. Zhang, S. Liu, Z.-S. Zhao, Z. Wang, R. Zhang, L. Liu and Z.-B. Han, *Inorg. Chem. Front.*, 2021, **8**, 590-619.
359. G. Ji, J. Liu, X. Gao, W. Sun, J. Wang, S. Zhao and Z. Liu, *J. Mater. Chem. A*, 2017, **5**, 10200-10205.
360. S. N. Zhao, G. Wang, D. Poelman and P. Van Der Voort, *Materials*, 2018, **11**, 572.
361. X. Lu, Y. Tang, G. Yang and Y.-Y. Wang, *J. Mater. Chem. C*, 2023, **11**, 2328-2335.
362. G. A. Pereira, J. A. Peters, F. A. Almeida Paz, J. Rocha and C. F. Geraldes, *Inorg. Chem.*, 2010, **49**, 2969-2974.
363. Y. Ling, J. Jiao, M. Zhang, H. Liu, D. Bai, Y. Feng and Y. He, *CrystEngComm*, 2016, **18**, 6254-6261.
364. M. Tian, J. Zheng, J. Xue, X. Pan, D. Zhou, Q. Yao, Y. Li, W. Duan, J. Su and X. Huang, *Dalton Trans.*, 2021, **50**, 17785-17791.
365. M. Runowski, D. Marcinkowski, K. Soler-Carracedo, A. Gorczyński, E. Ewert, P. Woźny and I. R. Martín, *ACS Appl. Mater. Interfaces*, 2023, **15**, 3244-3252.
366. S. V. Eliseeva and J. C. Bunzli, *Chem. Soc. Rev.*, 2010, **39**, 189-227.
367. J.-C. G. Bünzli, *Chem. Rev.*, 2010, **110**, 2729-2755.
368. J. C. Bunzli and C. Piguet, *Chem. Soc. Rev.*, 2005, **34**, 1048-1077.
369. Y. Cui, Y. Yue, G. Qian and B. Chen, *Chem. Rev.*, 2012, **112**, 1126-1162.
370. Y. Cui, B. Chen and G. Qian, *Coord. Chem. Rev.*, 2014, **273-274**, 76-86.
371. H. M. Chai, G. Q. Zhang, C. X. Jiao, Y. X. Ren and L. J. Gao, *ACS Omega*, 2020, **5**, 33039-33046.
372. X. Liu, Q. Ma, X. Feng, R. Li and X. Zhang, *Microchem. J.*, 2021, **170**, 106714.
373. B. Liu, Y. Huang, X. Zhu, Y. Hao, Y. Ding, W. Wei, Q. Wang, P. Qu and M. Xu, *Anal. Chim. Acta*, 2016, **912**, 139-145.
374. Y. Liu, X.-Y. Xie, C. Cheng, Z.-S. Shao and H.-S. Wang, *J. Mater. Chem. C*, 2019, **7**, 10743-10763.
375. X.-L. Chen, L. Shang, L. Liu, H. Yang, H.-L. Cui and J.-J. Wang, *Dyes Pigm.*, 2021, **196**, 109809.
376. X. Y. Zhao, H. Yang, W. Y. Zhao, J. Wang and Q. S. Yang, *Dalton Trans.*, 2021, **50**, 1300-1306.
377. H. Zhu, J. Yuan, X. Tan, W. Zhang, M. Fang and X. Wang, *Environ. Sci.: Nano.*, 2019, **6**, 261-272.
378. L. Li, Q. Chen, Z. Niu, X. Zhou, T. Yang and W. Huang, *J. Mater. Chem. C*, 2016, **4**, 1900-1905.
379. Y. Zhao, X. Zhai, L. Shao, L. Li, Y. Liu, X. Zhang, J. Liu, F. Meng and Y. Fu, *J. Mater. Chem. C*, 2021, **9**, 15840-15847.
380. Y. Li, C. Jiang, X. Chen, Y. Jiang and C. Yao, *ACS Appl. Mater. Interfaces*, 2022, **14**, 8343-8352.
381. I. A. Garduño-Wilches, G. Alarcón-Flores, A. Carro-Gastélum, S. Carmona-Téllez, M. A. Aguilar-Frutis and S. Loera-Serna, *Nano-Struct. Nano-Objects*, 2021, **26**, 100736.

382. G. He, H. Peng, T. Liu, M. Yang, Y. Zhang and Y. Fang, *J. Mater. Chem.*, 2009, **19**, 7347.
383. H. W. Yang, P. Xu, X. G. Wang, X. J. Zhao and E. C. Yang, *Z. Anorg. Allg. Chem.*, 2019, **646**, 23-29.
384. H. Guo, D. Wang, J. Chen, W. Weng, M. Huang and Z. Zheng, *Chem. Eng. J.*, 2016, **289**, 479-485.
385. E. Moradi, R. Rahimi and V. Safarifard, *J. Solid State Chem.*, 2020, **288**, 121397.
386. F. Zapata, A. Caballero, A. Espinosa, A. Tarraga and P. Molina, *Dalton Trans.*, 2010, **39**, 5429-5431.
387. Q. Wang, W. Ke, H. Lou, Y. Han and J. Wan, *Dyes Pigm.*, 2021, **196**, 109802.
388. N. D. Rudd, H. Wang, E. M. Fuentes-Fernandez, S. J. Teat, F. Chen, G. Hall, Y. J. Chabal and J. Li, *ACS Appl. Mater. Interfaces*, 2016, **8**, 30294-30303.
389. M. E. Mahmoud, Z. Moussa, T. Prakasam, L. Li, M. G. Abiad, D. Patra and M. Hmadeh, *J. Solid State Chem.*, 2020, **281**, 121031.
390. B. Yan, *Inorg. Chem. Front.*, 2021, **8**, 201-233.
391. X. H. Zhou, L. Li, H. H. Li, A. Li, T. Yang and W. Huang, *Dalton Trans.*, 2013, **42**, 12403-12409.
392. N. Kourkoumelis, *Powder Diffr.*, 2013, **28**, 137-148.

Supplementary Information

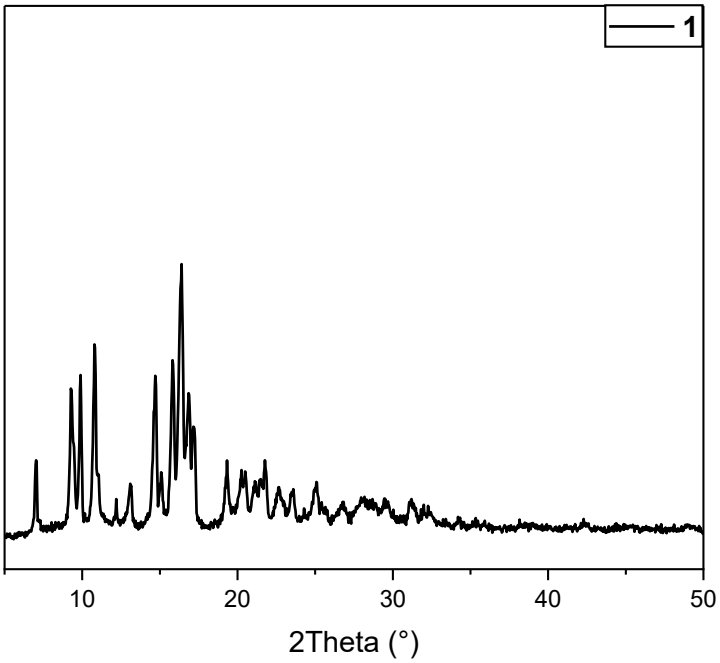

PXRD pattern of compound **1** [$(Et_4N)_2$(**L1-Si**)].

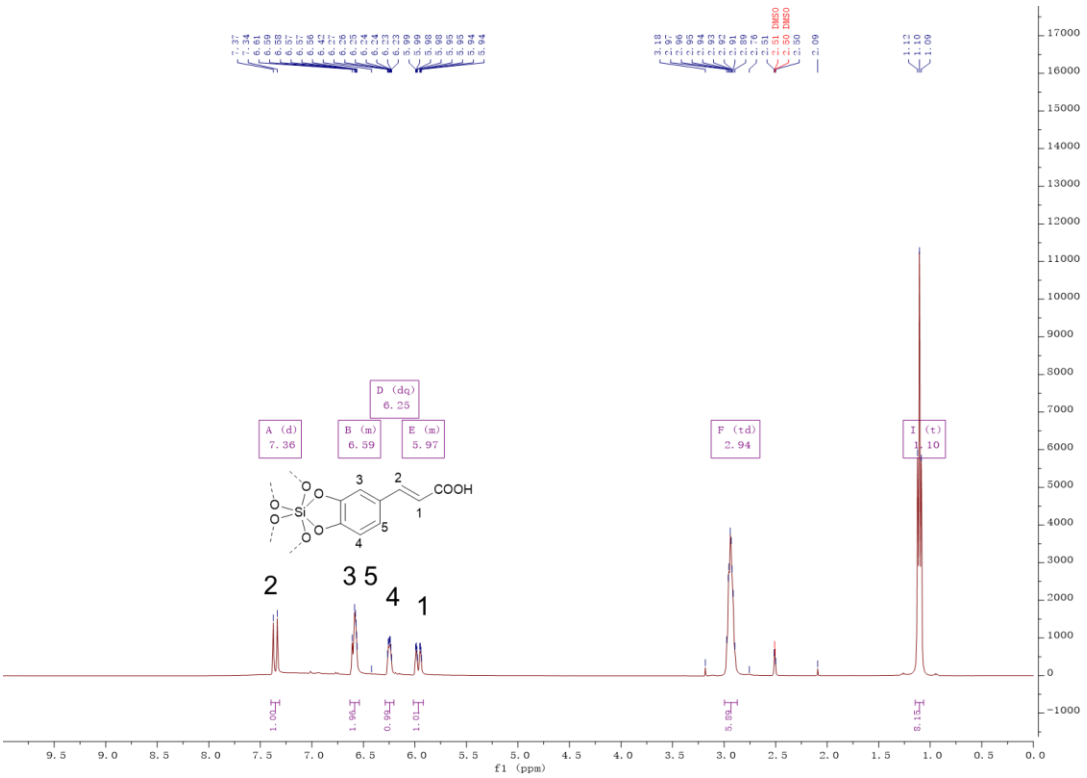

^{1}H NMR spectra of compound **13** (in DMSO-D_6)

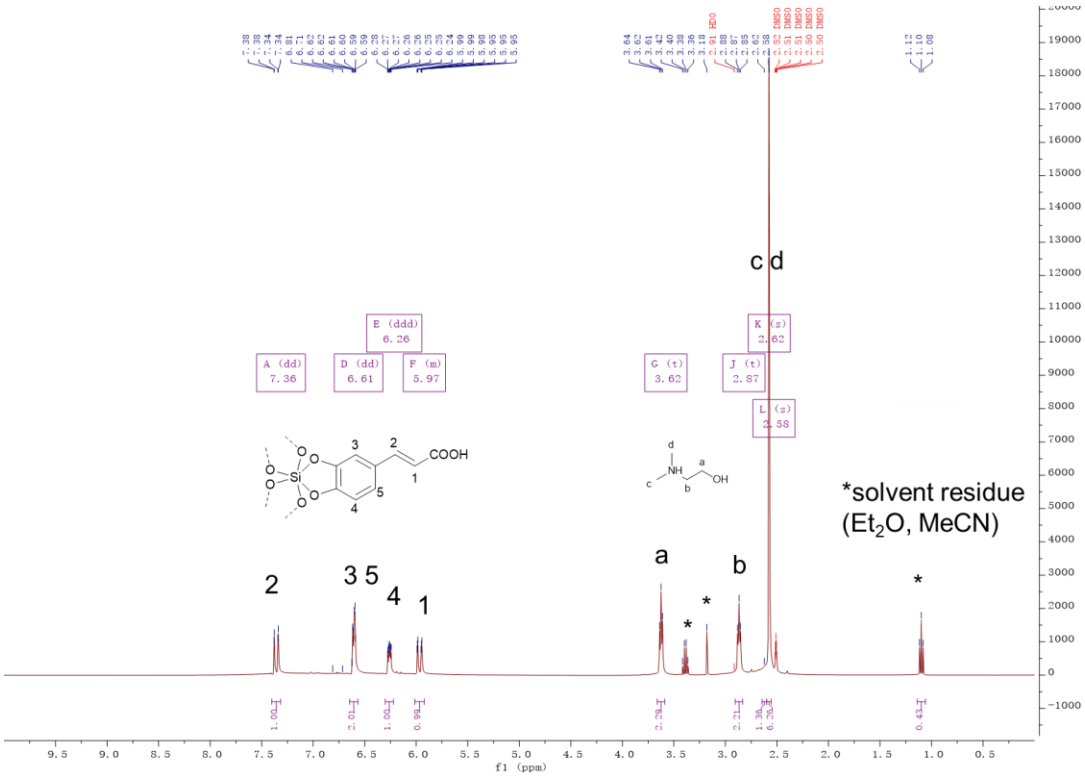

^{1}H NMR spectra of compound **14** (in DMSO-D$_6$)

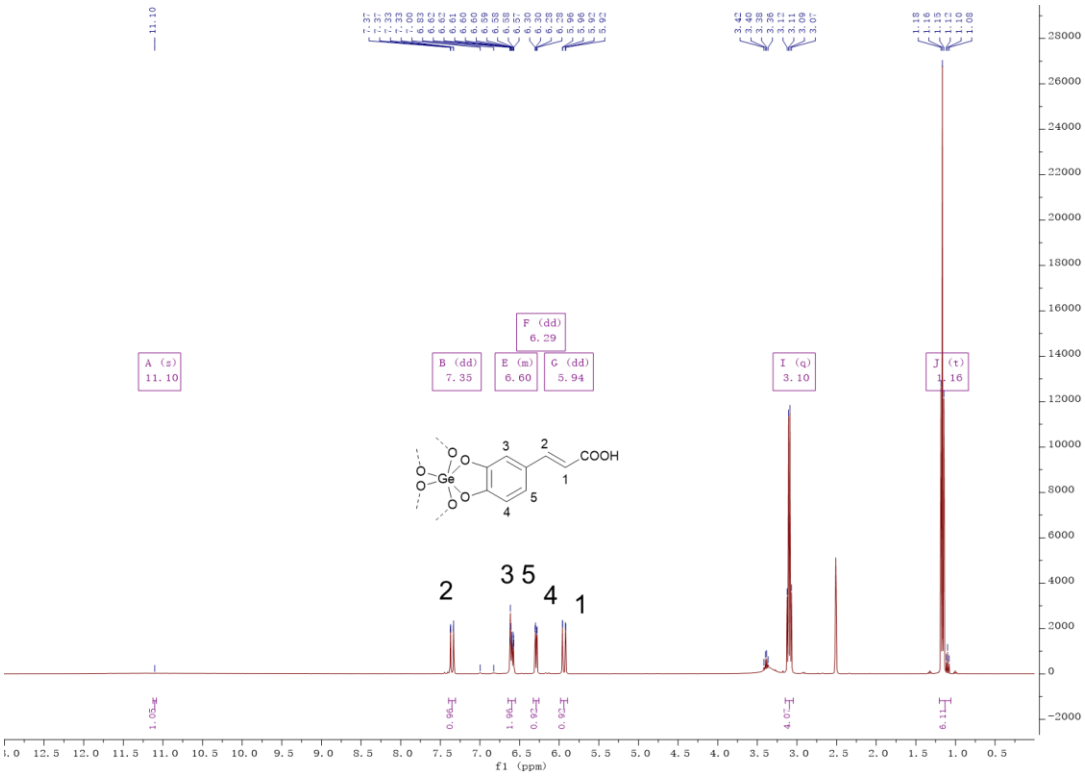

^{1}H NMR spectra of compound **15** (in DMSO-D$_6$)

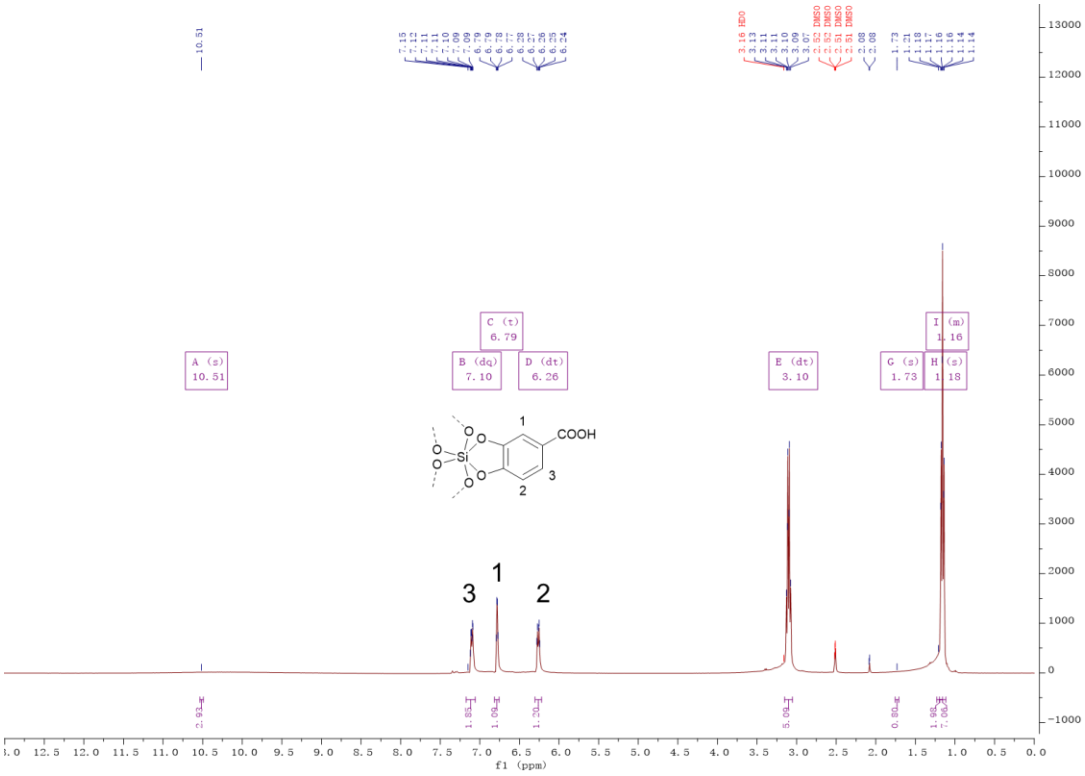

^{1}H NMR spectra of compound **16** (in DMSO-D_6)

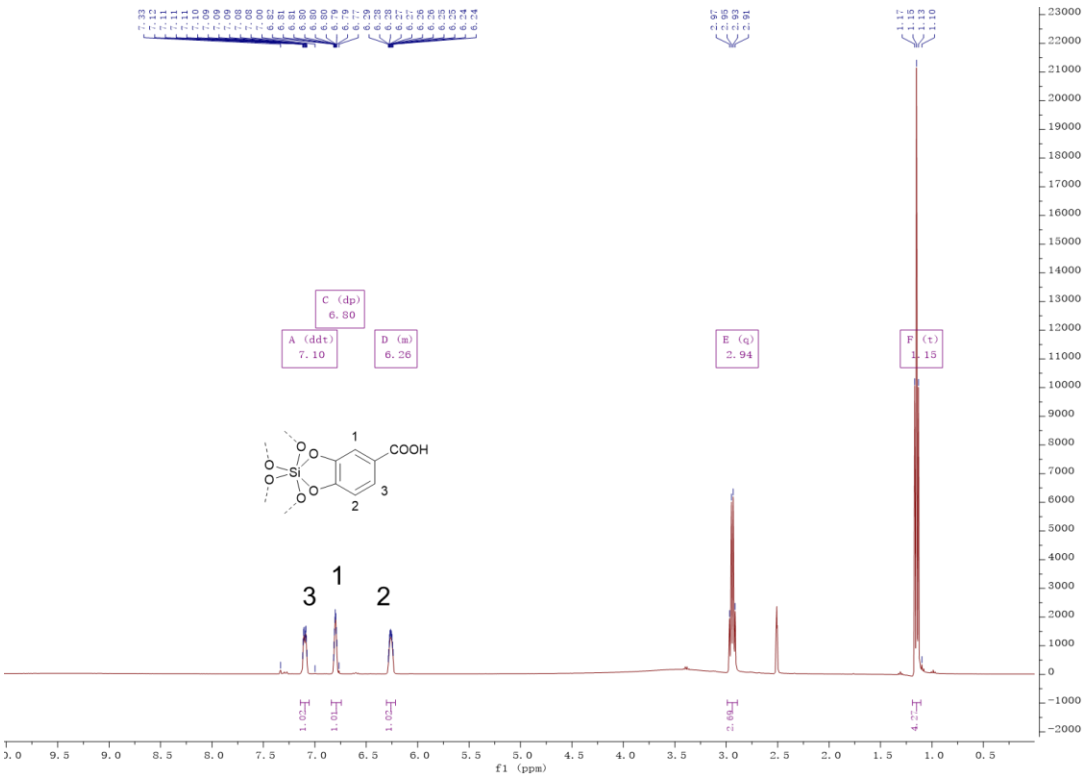

^{1}H NMR spectra of compound **17** (in DMSO-D_6)

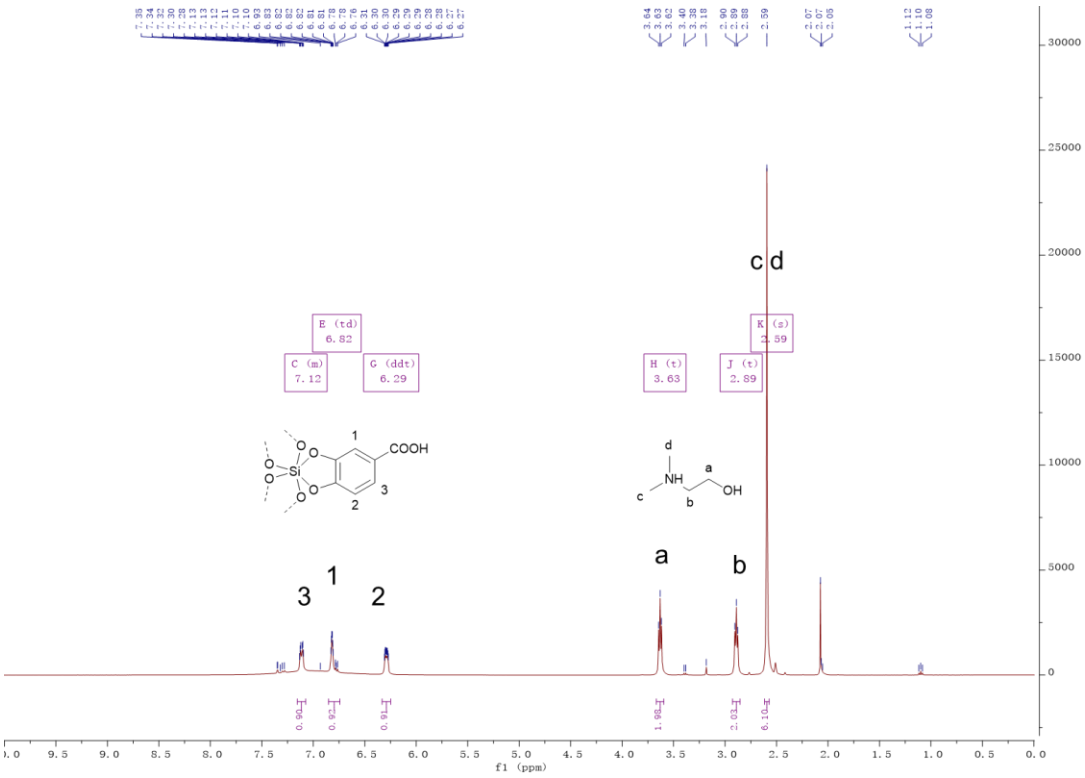

^{1}H NMR spectra of compound **18** (in DMSO-D_6)

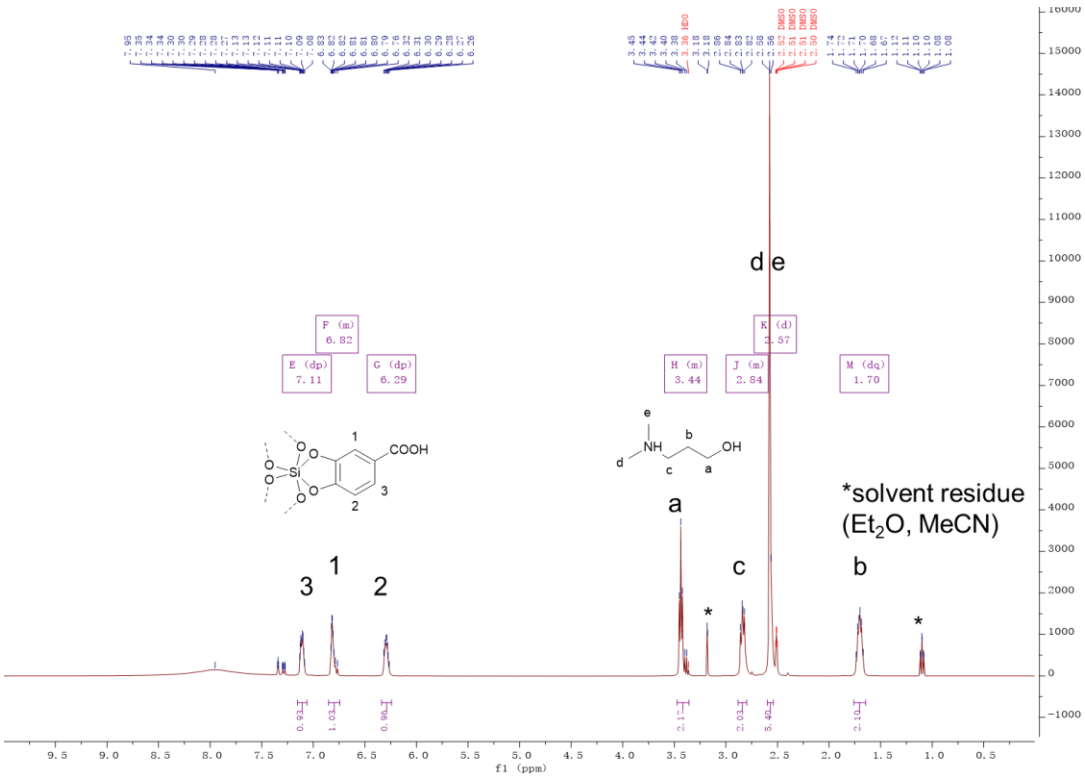

^{1}H NMR spectra of compound **19** (in DMSO-D_6)

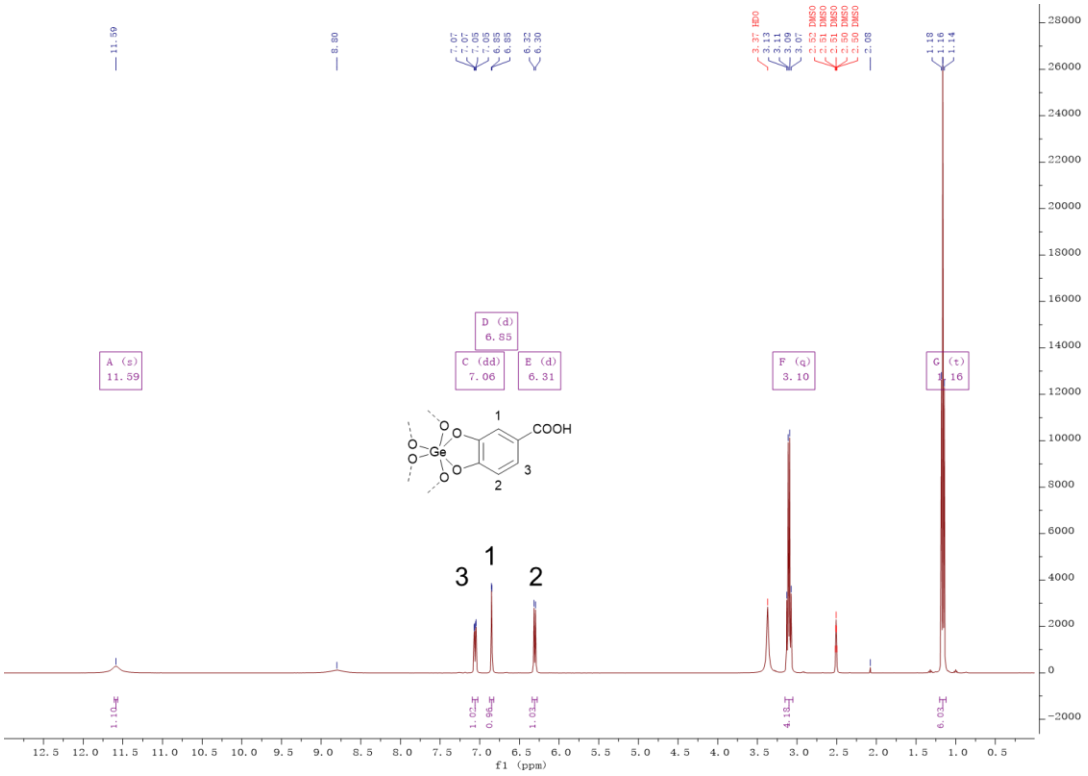

^{1}H NMR spectra of compound **20** (in DMSO-D_6)

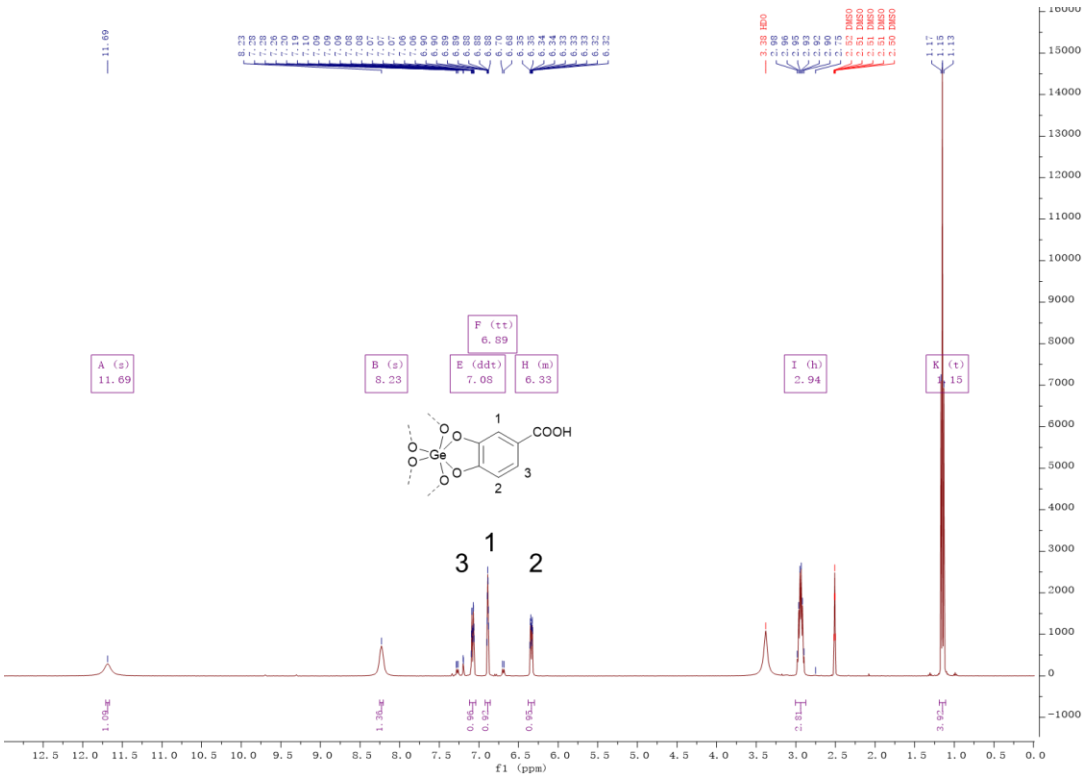

^{1}H NMR spectra of compound **21** (in DMSO-D_6)

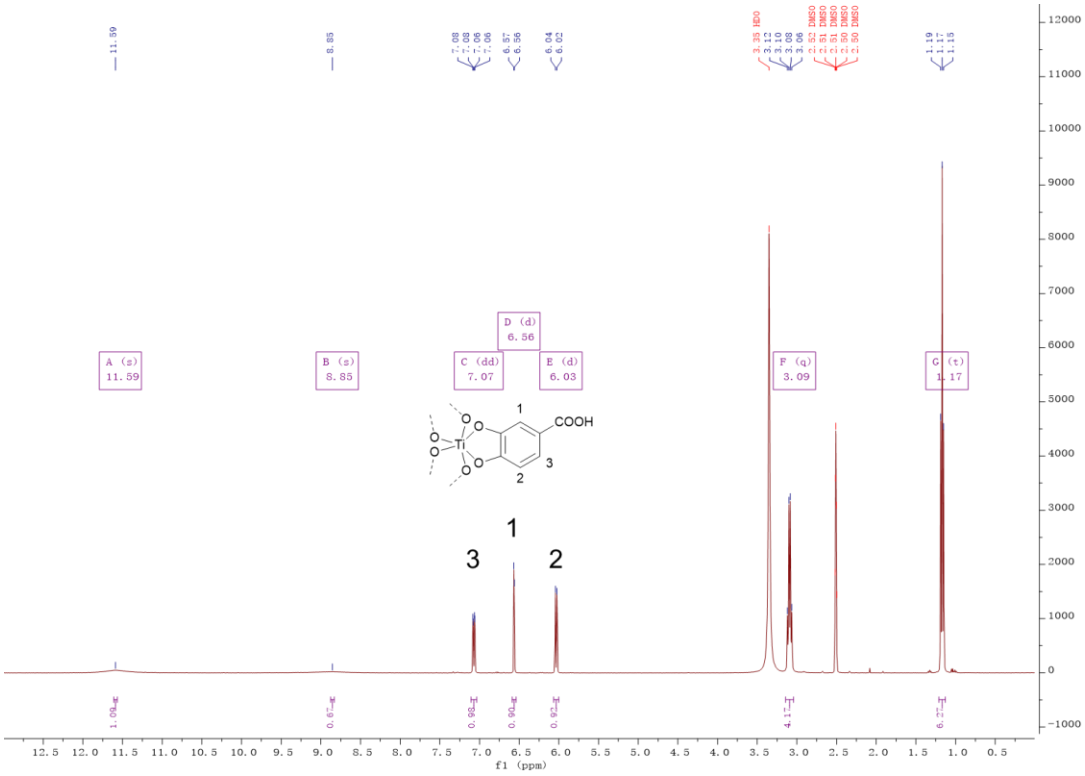

^{1}H NMR spectra of compound **22** (in DMSO-D_6)

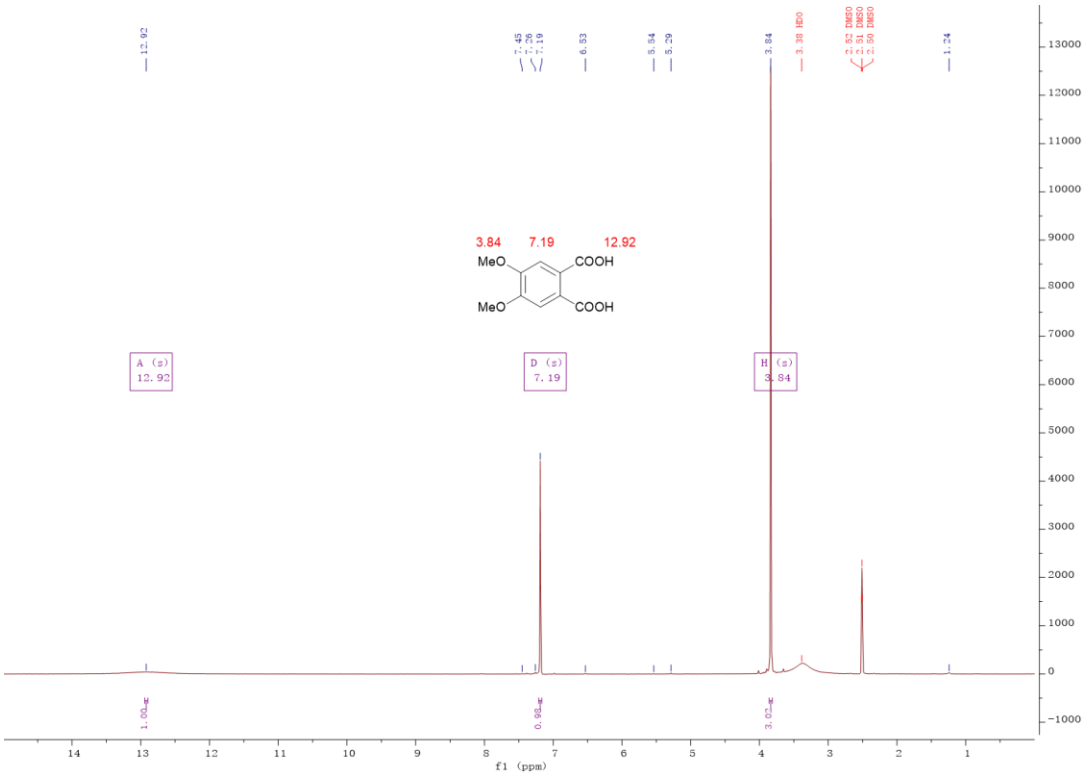

^{1}H NMR spectra of compound **25** (in DMSO-D_6)

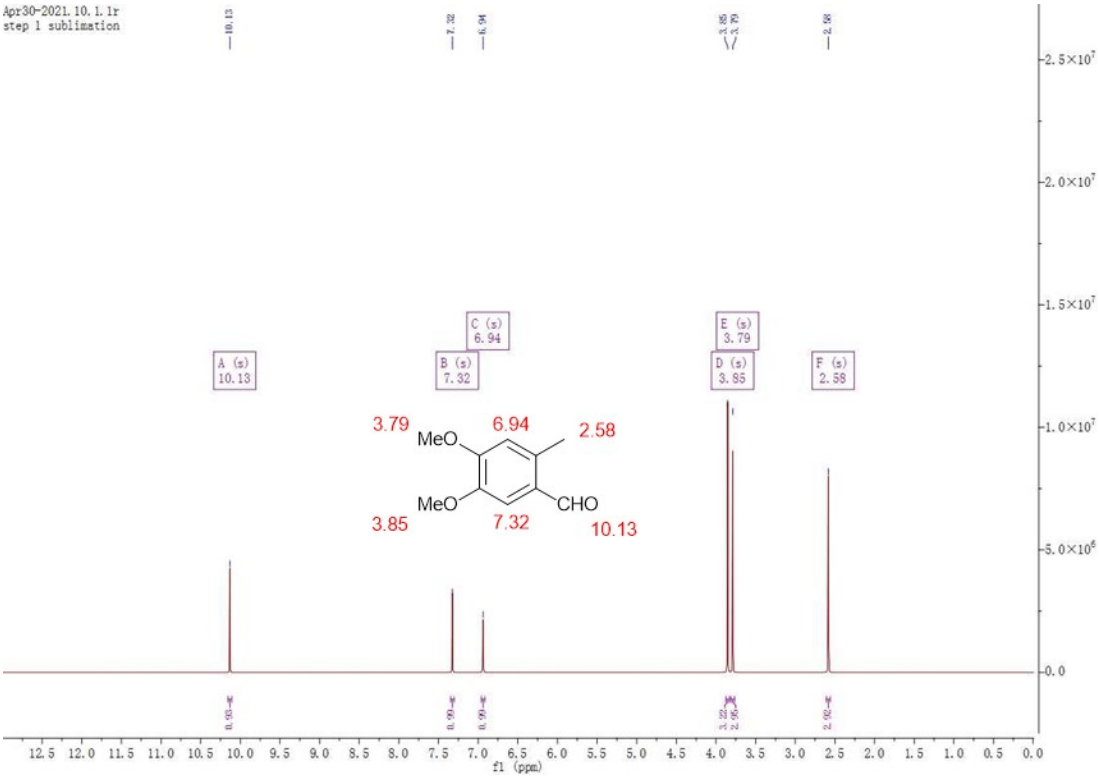

^{1}H NMR spectra of compound **26** (in DMSO-D_6)

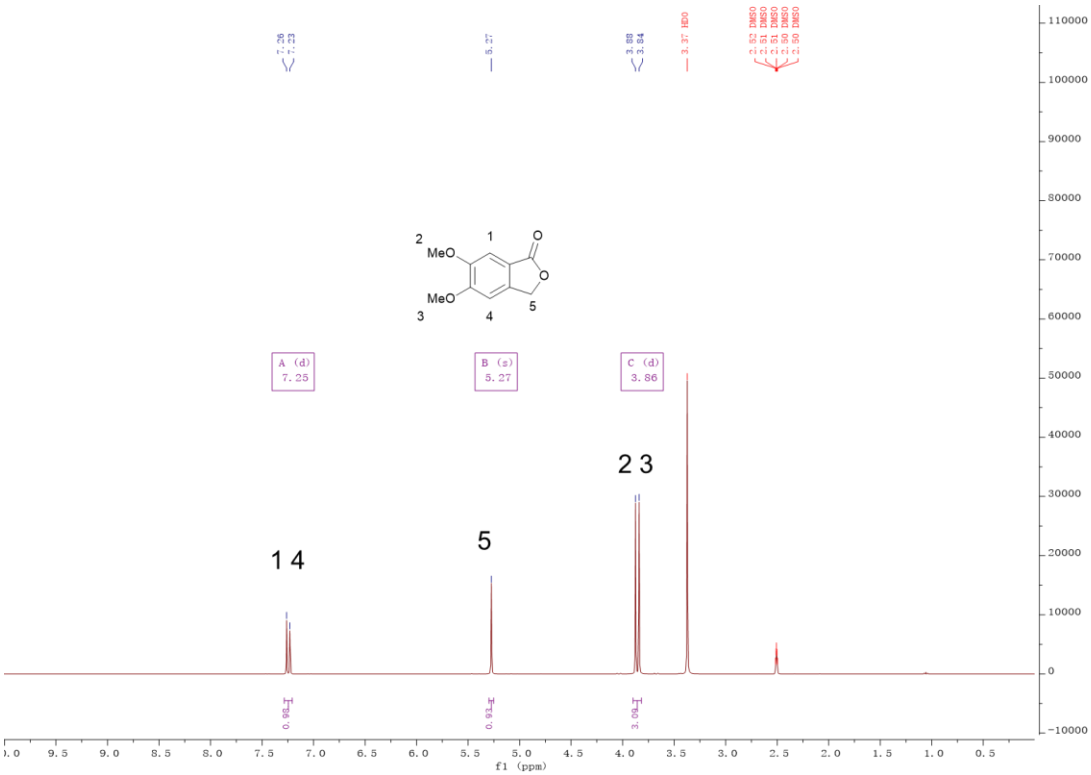

^{1}H NMR spectra of compound **27** (in DMSO-D_6)

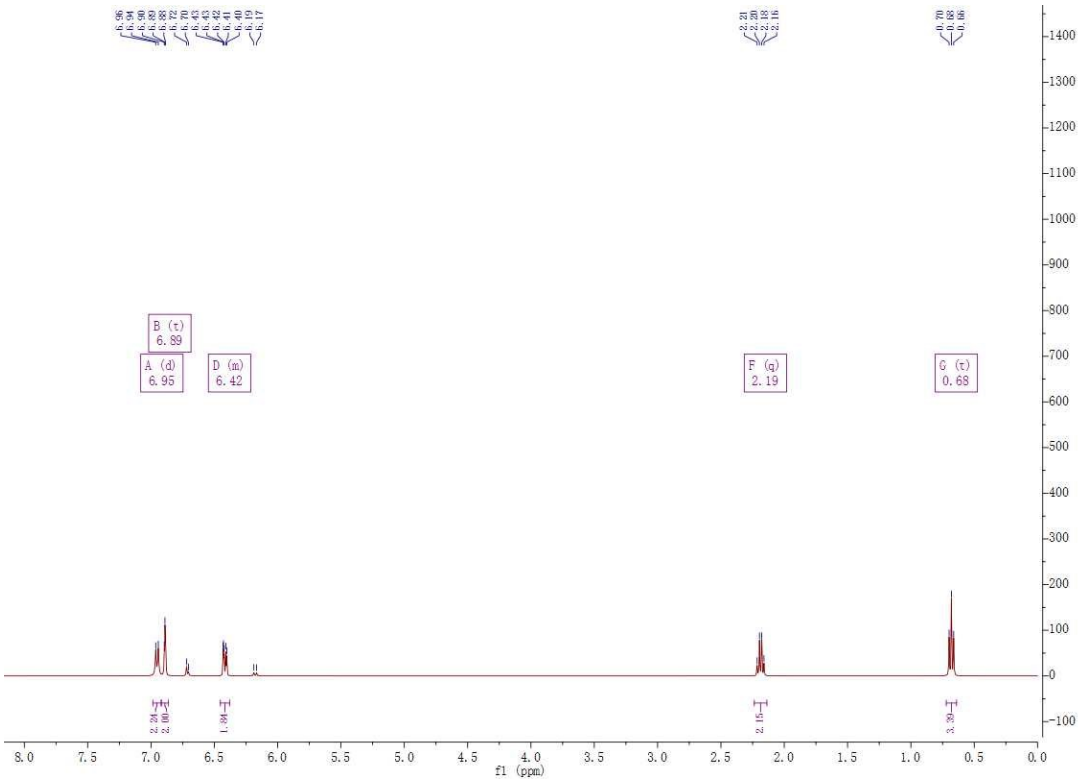

^{1}H NMR of digested **IMP-33-Y** (NaOD in D_2O)

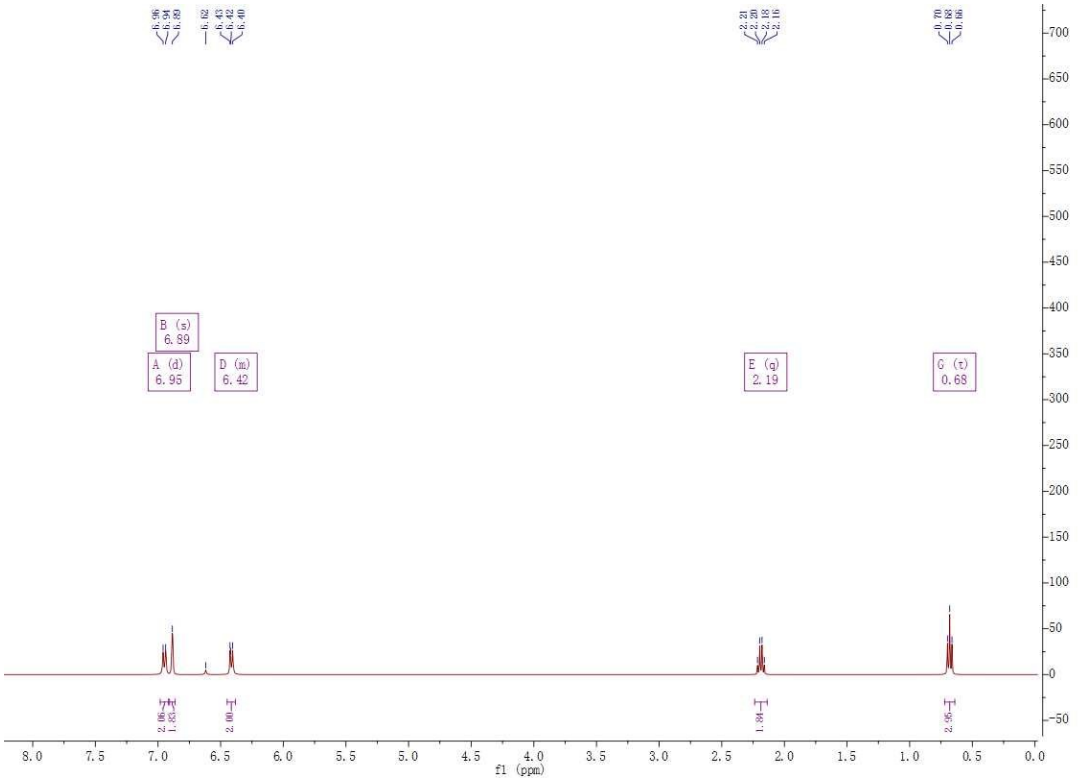

^{1}H NMR spectra of **IMP-34-Sc** (NaOD in D_2O)

Crystallography data

Compound **5**	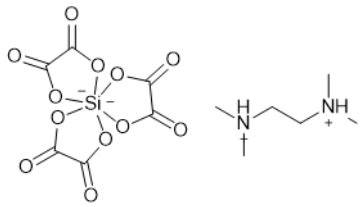
Identification code	RD2021
Formula	C6 O12 Si, C6 H18 N2
Formula weigh	410.37
Temperature	173(2) K
Diffractometer, wavelength	Agilent Xcalibur 3 E, 0.71073 Å
Crystal system, space group	Monoclinic, *C*2/*c*
Unit cell dimensions	a = 15.9360(10) Å, α = 90° b = 8.0111(4) Å, β = 111.531(8)° c = 14.4195(11) Å, γ = 90°
Volume, Z	1712.4(2) $Å^3$, 4
Density (calculated)	1.592 mg/m^3
Absorption coefficient	0.208 mm^{-1}
F(000)	856
Crystal colour / morphology	Yellow needles
Crystal size	0.486 × 0.367 × 0.189 mm^3
Θ range for data collection	2.748 to 27.907°
Index ranges	-20<=h<=16, -10<=k<=7, -17<=l<=15
Reflns collected / unique	2914 / 1712 [$R_{(int)}$ = 0.0200]
Reflns observed [F>4σ(F)]	1439
Absorption correction	Analytical
Max. and min. transmission	0.975 and 0.936
Refinement method	Full-matrix least-squares on F^2
Data / restraints / parameters	1712 / 1 / 129
Goodness-of-fit on F^2	1.031
Final R indices [F>4σ(F)]	R_1 = 0.0338, wR_2 = 0.0806
R indices (all data)	R_1 = 0.0427, wR_2 = 0.0853
Largest diff. peak, hole	0.262, -0.400 $eÅ^{-3}$
Mean and maximum shift/error	0.000 and 0.001

Compound **6**	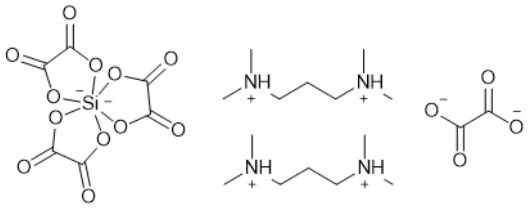
Identification code	RD2107
Formula	C6 O12 Si, 2(C7 H20 N2), C2 O4
Formula weigh	644.67
Temperature	173(2) K
Diffractometer, wavelength	Agilent Xcalibur 3 E, 0.71073 Å
Crystal system, space group	Triclinic, *P*-1
Unit cell dimensions	a = 9.7444(3) Å, α = 64.650(4)° b = 13.1227(5) Å, β = 70.783(3)° c = 14.4174(5) Å, γ = 89.769(3)°
Volume, Z	1552.85(11) $Å^3$, 2
Density (calculated)	1.379 mg/m^3
Absorption coefficient	0.153 mm^{-1}
F(000)	684
Crystal colour / morphology	Colourless blocks
Crystal size	0.446 × 0.218 × 0.110 mm^3
Θ range for data collection	2.600 to 28.254°
Index ranges	-12<=h<=12, -16<=k<=16, -18<=l<=19
Reflns collected / unique	20947 / 6589 [$R_{(int)}$ = 0.0208]
Reflns observed [F>4σ(F)]	5462
Absorption correction	Analytical
Max. and min. transmission	0.985 and 0.949
Refinement method	Full-matrix least-squares on F^2
Data / restraints / parameters	6589 / 4 / 412
Goodness-of-fit on F^2	1.021
Final R indices [F>4σ(F)]	R_1 = 0.0370, wR_2 = 0.0874
R indices (all data)	R_1 = 0.0478, wR_2 = 0.0935
Largest diff. peak, hole	0.332, -0.323 $eÅ^{-3}$
Mean and maximum shift/error	0.000 and 0.001

Compound **7**	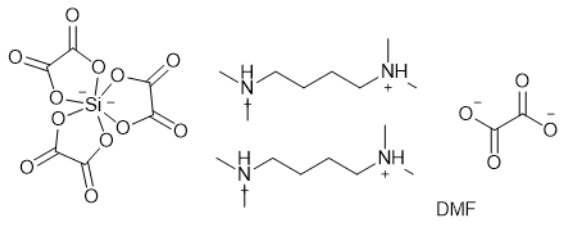
Identification code	RD2110
Formula	C6 O12 Si, 2(C8 H22 N2), C2 O4, C3 H7 N O
Formula weigh	745.82
Temperature	373(2) K
Diffractometer, wavelength	Agilent Xcalibur 3 E, 0.71073 Å
Crystal system, space group	Monoclinic, $P2_1/n$
Unit cell dimensions	a = 10.5320(2) Å, α = 90° b = 22.5800(4) Å, β = 96.0606(18)° c = 15.5839(3) Å, γ = 90°
Volume, Z	3685.32(12) Å^3, 4
Density (calculated)	1.344 mg/m^3
Absorption coefficient	0.141 mm^{-1}
F(000)	1592
Crystal colour / morphology	Colourless plates
Crystal size	0.581 × 0.307 × 0.151 mm^3
Θ range for data collection	2.405 to 28.374°
Index ranges	-14<=h<=13, -30<=k<=29, -20<=l<=20
Reflns collected / unique	49443 / 8303 [$R_{(int)}$ = 0.0368]
Reflns observed [F>4σ(F)]	6462
Absorption correction	Analytical
Max. and min. transmission	0.982 and 0.953
Refinement method	Full-matrix least-squares on F^2
Data / restraints / parameters	8303 / 38 / 500
Goodness-of-fit on F^2	1.018
Final R indices [F>4σ(F)]	R_1 = 0.0404, wR_2 = 0.0848
R indices (all data)	R_1 = 0.0597, wR_2 = 0.0934
Largest diff. peak, hole	0.229, -0.282 eÅ^{-3}
Mean and maximum shift/error	0.000 and 0.003

Compound **9**	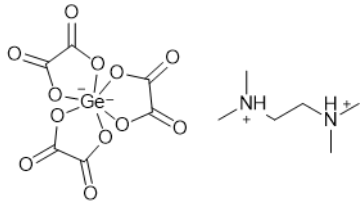
Identification code	RD2102
Formula	C6 Ge O12, C6 H18 N2
Formula weigh	454.87
Temperature	173(2) K
Diffractometer, wavelength	Agilent Xcalibur PX Ultra A, 1.54184 Å
Crystal system, space group	Monoclinic, *C*2/*c*
Unit cell dimensions	a = 15.9823(3) Å, α = 90° b = 8.04505(12) Å, β = 111.711(2)° c = 14.5077(3) Å, γ = 90°
Volume, Z	1733.05(6) $Å^3$, 4
Density (calculated)	1.743 mg/m^3
Absorption coefficient	3.064 mm^{-1}
F(000)	928
Crystal colour / morphology	Colourless blocks
Crystal size	0.442 × 0.294 × 0.244 mm^3
Θ range for data collection	5.960 to 73.481°
Index ranges	-18<=h<=19, -9<=k<=9, -13<=l<=17
Reflns collected / unique	4794 / 1701 [$R_{(int)}$ = 0.0209]
Reflns observed [F>4σ(F)]	1615
Absorption correction	Analytical
Max. and min. transmission	0.627 and 0.487
Refinement method	Full-matrix least-squares on F^2
Data / restraints / parameters	1701 / 1 / 130
Goodness-of-fit on F^2	1.079
Final R indices [F>4σ(F)]	R_1 = 0.0225, wR_2 = 0.0579
R indices (all data)	R_1 = 0.0244, wR_2 = 0.0593
Largest diff. peak, hole	0.309, -0.367 $eÅ^{-3}$
Mean and maximum shift/error	0.000 and 0.000

Compound **11**	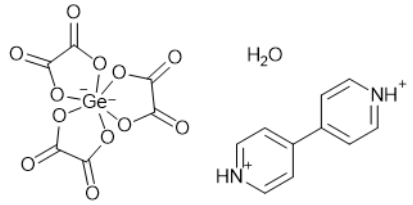
Identification code	RD2103
Formula	C6 Ge O12, C10 H10 N2, H2 O
Formula weigh	512.87
Temperature	173(2) K
Diffractometer, wavelength	Agilent Xcalibur 3 E, 0.71073 Å
Crystal system, space group	Monoclinic, $P2_1/c$
Unit cell dimensions	a = 8.0261(3) Å, α = 90° b = 17.9810(6) Å, β = 96.617(3)° c = 13.1577(4) Å, γ = 90°
Volume, Z	1886.23(11) Å^3, 4
Density (calculated)	1.806 mg/m^3
Absorption coefficient	1.704 mm^{-1}
F(000)	1032
Crystal colour / morphology	Colourless tablets
Crystal size	0.528 × 0.406 × 0.213 mm^3
Θ range for data collection	2.555 to 28.324°
Index ranges	-10<=h<=6, -23<=k<=21, -16<=l<=17
Reflns collected / unique	6759 / 3781 [$R_{(int)}$ = 0.0318]
Reflns observed [F>4σ(F)]	3098
Absorption correction	Analytical
Max. and min. transmission	0.740 and 0.568
Refinement method	Full-matrix least-squares on F^2
Data / restraints / parameters	3781 / 4 / 306
Goodness-of-fit on F^2	1.026
Final R indices [F>4σ(F)]	R_1 = 0.0347, wR_2 = 0.0757
R indices (all data)	R_1 = 0.0471, wR_2 = 0.0810
Largest diff. peak, hole	0.299, -0.386 eÅ^{-3}
Mean and maximum shift/error	0.000 and 0.001

Compound **12**	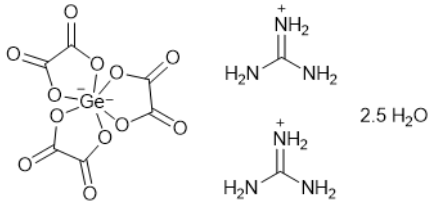
Identification code	RD2134
Formula	C21 H12 O12 Si, 2(C6 H16 N), 3(C3 H7 N O)
Formula weigh	501.86
Temperature	173(2) K
Diffractometer, wavelength	Agilent Xcalibur 3 E, 0.71073 Å
Crystal system, space group	Monoclinic, $P2_1/n$
Unit cell dimensions	a = 10.92864(11) Å, α = 90° b = 24.6794(2) Å, β = 91.3677(9)° c = 19.98783(17) Å, γ = 90°
Volume, Z	5389.42(8) Å^3, 12
Density (calculated)	1.856 mg/m^3
Absorption coefficient	1.797 mm^{-1}
F(000)	3060
Crystal colour / morphology	Colourless block-like needles
Crystal size	0.509 × 0.285 × 0.206 mm^3
Θ range for data collection	2.623 to 28.332°
Index ranges	-14<=h<=14, -32<=k<=32, -26<=l<=26
Reflns collected / unique	205178 / 12752 [$R_{(int)}$ = 0.0380]
Reflns observed [F>4σ(F)]	10344
Absorption correction	Semi-empirical from equivalents
Max. and min. transmission	1.00000 and 0.72147
Refinement method	Full-matrix least-squares on F^2
Data / restraints / parameters	12752 / 0 / 708
Goodness-of-fit on F^2	1.042
Final R indices [F>4σ(F)]	R_1 = 0.0357, wR_2 = 0.0856
R indices (all data)	R_1 = 0.0505, wR_2 = 0.0929
Largest diff. peak, hole	0.717, -0.412 eÅ^{-3}
Mean and maximum shift/error	0.000 and 0.001

Compound **16**	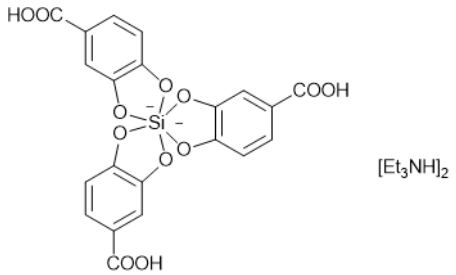
Identification code	RD2022
Formula	C21 H12 O12 Si, 2(C6 H16 N), 3(C3 H7 N O)
Formula weigh	908.08
Temperature	173(2) K
Diffractometer, wavelength	Agilent Xcalibur 3 E, 0.71073 Å
Crystal system, space group	Triclinic, *P*-1
Unit cell dimensions	a = 9.8788(4) Å, α = 95.373(4)° b = 14.7468(7) Å, β = 90.577(4)° c = 16.5789(8) Å, γ = 97.219(4)°
Volume, Z	2384.97(19) $Å^3$, 2
Density (calculated)	1.265 mg/m^3
Absorption coefficient	0.119 mm^{-1}
F(000)	972
Crystal colour / morphology	Colourless tablets
Crystal size	0.309 × 0.275 × 0.066 mm^3
Θ range for data collection	2.353 to 28.269°
Index ranges	-13<=h<=11, -12<=k<=19, -19<=l<=14
Reflns collected / unique	13899 / 9373 [$R_{(int)}$ = 0.0308]
Reflns observed [F>4σ(F)]	4837
Absorption correction	Analytical
Max. and min. transmission	0.993 and 0.973
Refinement method	Full-matrix least-squares on F^2
Data / restraints / parameters	9373 / 302 / 505
Goodness-of-fit on F^2	1.115
Final R indices [F>4σ(F)]	R_1 = 0.1042, wR_2 = 0.3102
R indices (all data)	R_1 = 0.1626, wR_2 = 0.3578
Largest diff. peak, hole	0.768, -0.375 $eÅ^{-3}$
Mean and maximum shift/error	0.000 and 0.002

Compound **20**	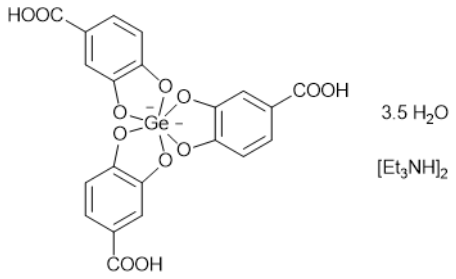
Identification code	2023NCS0004
Formula	$C_{33}H_{51}GeN_2O_{15.5}$
$D_{calc.}$/ g cm^{-3}	1.455
μ/mm^{-1}	1.788
Formula Weight	796.34
Colour / Shape	Colourless, blade-shaped
Size/mm^3	0.180×0.050×0.025
T/K	100(2)
Crystal System, Space group	Monoclinic, $P2_1/c$
Unit cell dimensions	a = 33.0723(2) Å, α = 90° b = 14.02040(10) Å, β = 96.1050(10)° c = 15.76820(10) Å, γ = 90°
V/Å^3	7270.04(8)
Z, Z'	8, 2
Radiation type, Wavelength/Å	Cu K_a, 1.54178
Θ_{min}/°, Θ_{max}/°	2.687, 70.070
Measured Refl's.	156877
Indep't Refl's	13796
Refl's I≥2 s(I)	12419
R_{int}	0.0505
Parameters	967
Restraints	10
Largest Peak	1.405
Deepest Hole	-0.874
GooF	1.031
wR_2 (all data)	0.1460
wR_2	0.1416
R_1 (all data)	0.0524
R_1	0.0485

Compound **22**	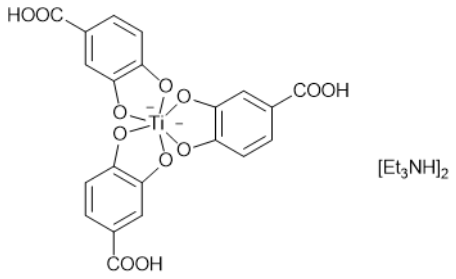
Identification code	2023NCS0133
Formula	$C_{33}H_{44}N_2O_{12}Ti$
$D_{calc.}$/ g cm^{-3}	1.425
μ/mm^{-1}	2.773
Formula Weight	708.60
Colour, Shape	dark brown, plate-shaped
Size/mm^3	0.060×0.040×0.015
T/K	100(2)
Crystal System, Space Group	Monoclinic, $C2/c$
Unit cell dimensions	a = 14.7870(9) Å, α = 90° b = 11.2636(4) Å, β = 113.819(8)° c = 21.6696(15) Å, γ = 90°
V/Å^3	3301.8(4)
Z	4
Z'	0.5
Radiation type, Wavelength/Å	Cu K$_a$, 1.54178
Θ_{min}/°, Θ_{max}/°	4.461, 75.250
Measured Refl's.	6064
Indep't Refl's	6064
Refl's I≥2 s(I)	4973
Parameters	363
Restraints	713
Largest Peak	0.358
Deepest Hole	-0.385
GooF	1.048
wR_2 (all data)	0.1793
wR_2	0.1671
R_1 (all data)	0.0912
R_1	0.0734

Compound **23**	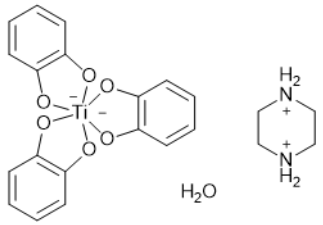
Identification code	2022NCS0612
Formula	$C_{22}H_{26}N_2O_7Ti$
$D_{calc.}$/ g cm^{-3}	1.464
μ/mm^{-1}	3.753
Formula Weight	478.328
Colour, Shape	dark brown, blade-shaped
Size/mm^3	0.280×0.160×0.040
T/K	100(2)
Crystal System, Space Group	Triclinic, P-1
Unit cell dimensions	a = 10.3771(3) Å, α = 94.673(2)° b = 10.3813(2) Å, β = 100.929(2)° c = 10.6564(3) Å, γ = 100.929(2)°
V/Å^3	1084.94(5)
Z	2
Z'	1
Radiation type, Wavelength/Å	Cu K$_a$, 1.54178
Θ_{min}/°, Θ_{max}/°	4.31, 70.06
Measured Refl's.	20144
Indep't Refl's	4084
Refl's I≥2 s(I)	3683
R_{int}	0.0411
Parameters	292
Restraints	2
Largest Peak	0.9539
Deepest Hole	-0.4094
GooF	1.0317
wR_2 (all data)	0.1634
wR_2	0.1598
R_1 (all data)	0.0582
R_1	0.0544

Compound **25**	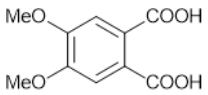
Identification code	RD2114
Formula	C10 H10 O6
Formula weigh	226.18
Temperature	173(2) K
Diffractometer, wavelength	Agilent Xcalibur PX Ultra A, 1.54184 Å
Crystal system, space group	Monoclinic, $P2_1/c$
Unit cell dimensions	a = 9.7816(4)Å, α = 90° b = 14.2660(5) Å, β = 90.487(4)° c = 7.1020(3) Å, γ = 90°
Volume, Z	991.00(7) $Å^3$, 4
Density (calculated)	1.516 mg/m^3
Absorption coefficient	1.102 mm^{-1}
F(000)	472
Crystal colour / morphology	Colourless block-like needles
Crystal size	0.395 × 0.202 × 0.163 mm^3
Θ range for data collection	4.521 to 73.547°
Index ranges	-11<=h<=12, -17<=k<=17, -8<=l<=8
Reflns collected / unique	14140 / 1974 [$R_{(int)}$ = 0.0439]
Reflns observed [F>4σ(F)]	1555
Absorption correction	Analytical
Max. and min. transmission	0.867 and 0.732
Refinement method	Full-matrix least-squares on F^2
Data / restraints / parameters	1974 / 2 / 1551974 / 2 / 155
Goodness-of-fit on F^2	1.058
Final R indices [F>4σ(F)]	R_1 = 0.0445, wR_2 = 0.1148
R indices (all data)	R_1 = 0.0574, wR_2 = 0.1285
Largest diff. peak, hole	0.327, -0.1910.327, -0.191 $eÅ^{-3}$
Mean and maximum shift/error	0.000 and 0.001

IMP-33-Y	See Figure 3.12
Identification code	2021NCS0370
Formula	$C_{42}H_{52}Ge_2O_{41}Y_3$
$D_{calc.}$/ g cm^{-3}	1.238
μ/mm^{-1}	4.018
Formula Weight	1624.74
Colour, Shape	Colourless, blade-shaped
Size/mm^3	0.220×0.100×0.020
T/K	100(2)
Crystal System, Space Group	Monoclinic, $C2/c$
a/Å	19.9205(2)
b/Å	14.33510(10)
c/Å	30.7566(2)
a/°	90
b/°	97.0890(10)
g/°	90
V/Å^3	8715.79(12)
Z	4
Z'	0.5
Radiation type, Wavelength/Å	Cu K$_a$, 1.54178
Θ_{min}/°	2.896
Θ_{max}/°	68.273
Measured Refl's.	27185
Indep't Refl's	27185
Refl's I≥2 s(I)	26231
Parameters	429
Restraints	656
Largest Peak	1.812
Deepest Hole	-1.551
GooF	1.041
wR_2 (all data)	0.1842
wR_2	0.1831
R_1 (all data)	0.0670
R_1	0.0658

IMP-33-Dy	See Figure 3.14
Identification code	2022NCS0180
Formula	$C_{42}H_{44}Dy_3Ge_2O_{37}$
$D_{calc.}$/ g cm^{-3}	1.378
μ/mm^{-1}	15.185
Formula Weight	1773.45
Colour, Shape	Colourless, blade-shaped
Size/mm^3	0.180×0.060×0.010
T/K	100(2)
Crystal System, Space Group	monoclinic, $C2/c$
a/Å	19.5343(3)
b/Å	14.22670(10)
c/Å	30.9853(3)
a/°	90
b/°	96.9100(10)
g/°	90
V/Å^3	8548.53(17)
Z	4
Z'	0.5
Radiation type, Wavelength/Å	Cu K$_a$, 1.54178
Θ_{min}/°	2.873
Θ_{max}/°	70.051
Measured Refl's.	13640
Indep't Refl's	13640
Refl's I≥2 s(I)	13100
Parameters	405
Restraints	377
Largest Peak	1.722
Deepest Hole	-1.668
GooF	1.025
wR_2 (all data)	0.1511
wR_2	0.1498
R_1 (all data)	0.0574
R_1	0.0558

IMP-34-Sc	See Figure 3.19
Identification code	2022NCS0357
Formula	$C_{60}H_{82}Ge_2N_7O_{39}Sc_3$
$D_{calc.}$/ g cm^{-3}	1.408
μ/mm^{-1}	1.014
Formula Weight	1805.38
Colour, Shape	Colourless, prism-shaped
Size/mm^3	0.120×0.100×0.080
T/K	100(2)
Crystal System, Space Group	Monoclinic, $P2_1$
Flack Parameter	0.499(8)
Hooft Parameter	0.081(2)
a/Å	25.1090(8)
b/Å	13.1102(2)
c/Å	27.1137(6)
a/°	90
b/°	107.410(3)
g/°	90
V/Å^3	8516.5(4)
Z, Z'	4, 2
Radiation type, Wavelength/Å	Mo K_a, 0.71075
Θ_{min}/°, Θ_{max}/°	2.076, 28.701
Measured Refl's.	203984
Indep't Refl's	43773
Refl's I≥2 s(I)	37435
R_{int}	0.0791
Parameters	1534
Restraints	5139
Largest Peak	1.366
Deepest Hole	-1.124
GooF	1.076
wR_2 (all data)	0.1823
wR_2	0.1767
R_1 (all data)	0.0793
R_1	0.0683

Green crystal	See Figure 3.24
Identification code	2021NCS0461
Formula	$C_{84}Ge_4H_{206}O_{127}Y$
$D_{calc.}$/ g cm^{-3}	0.948
μ/mm^{-1}	1.533
Formula Weight	3627.75
Colour, Shape	pale bluish green, cube-shaped
Size/mm^3	0.200×0.200×0.200
T/K	100(2)
Crystal System, Space Group	Trigonal, R-3c
a/Å	31.79180(10)
b/Å	31.79180(10)
c/Å	87.0708(2)
a/°	90
b/°	90
g/°	120
V/Å^3	76213.7(5)
Z	12
Z'	0.333333
Radiation type, Wavelength/Å	Cu K$_a$, 1.54178
Θ_{min}/°	3.170
Θ_{max}/°	68.229
Measured Refl's.	459288
Indep't Refl's	15487
Refl's I≥2 s(I)	14232
R_{int}	0.0222
Parameters	473
Restraints	112
Largest Peak	0.464
Deepest Hole	-0.773
GooF	1.091
wR_2 (all data)	0.1751
wR_2	0.1720
R_1 (all data)	0.0506
R_1	0.0485

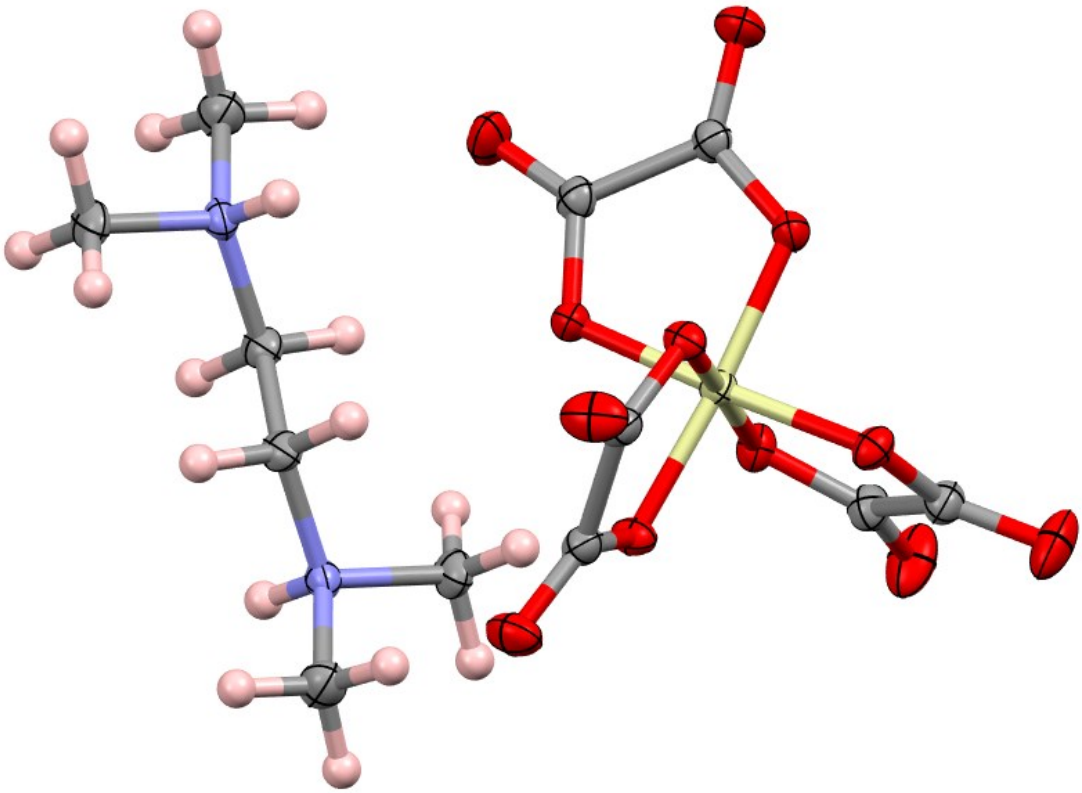

Crystal structure of Compound **5** (50% probability ellipsoids)

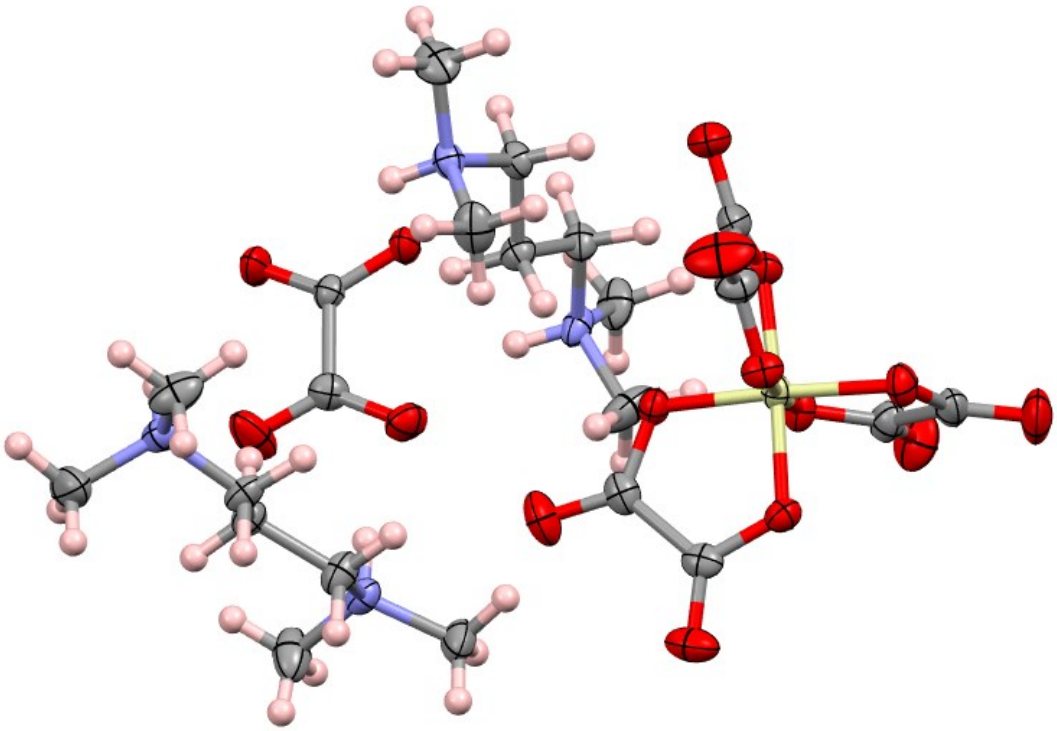

Crystal structure of Compound **6** (50% probability ellipsoids)

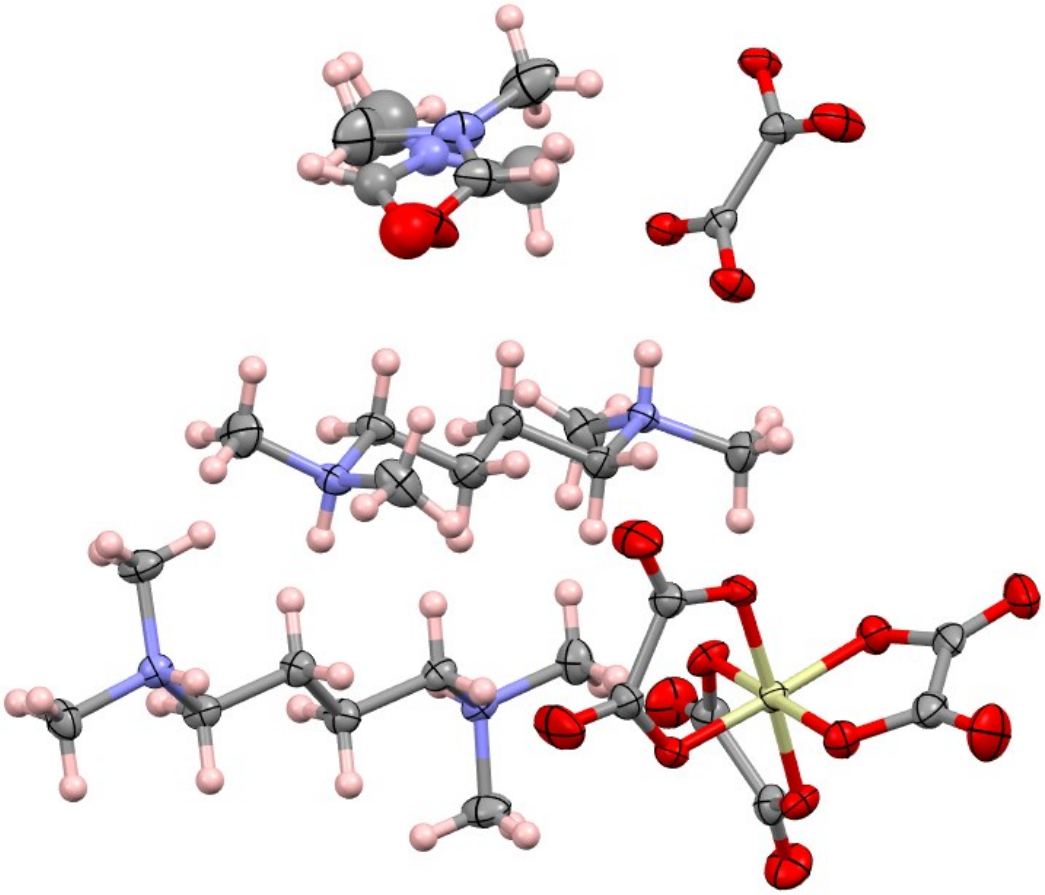

Crystal structure of Compound **7** (50% probability ellipsoids)

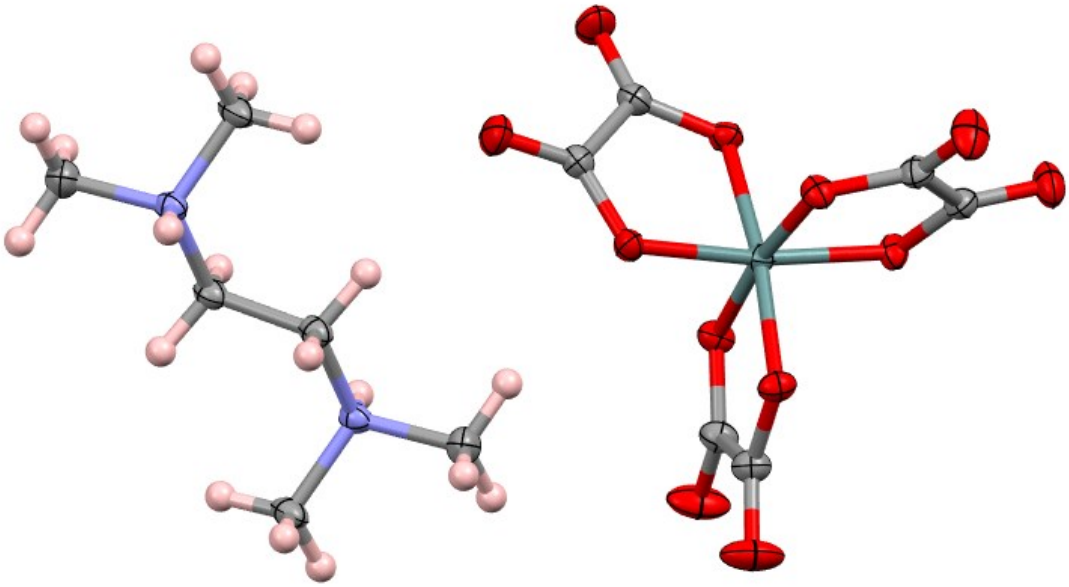

Crystal structure of Compound **9** (50% probability ellipsoids)

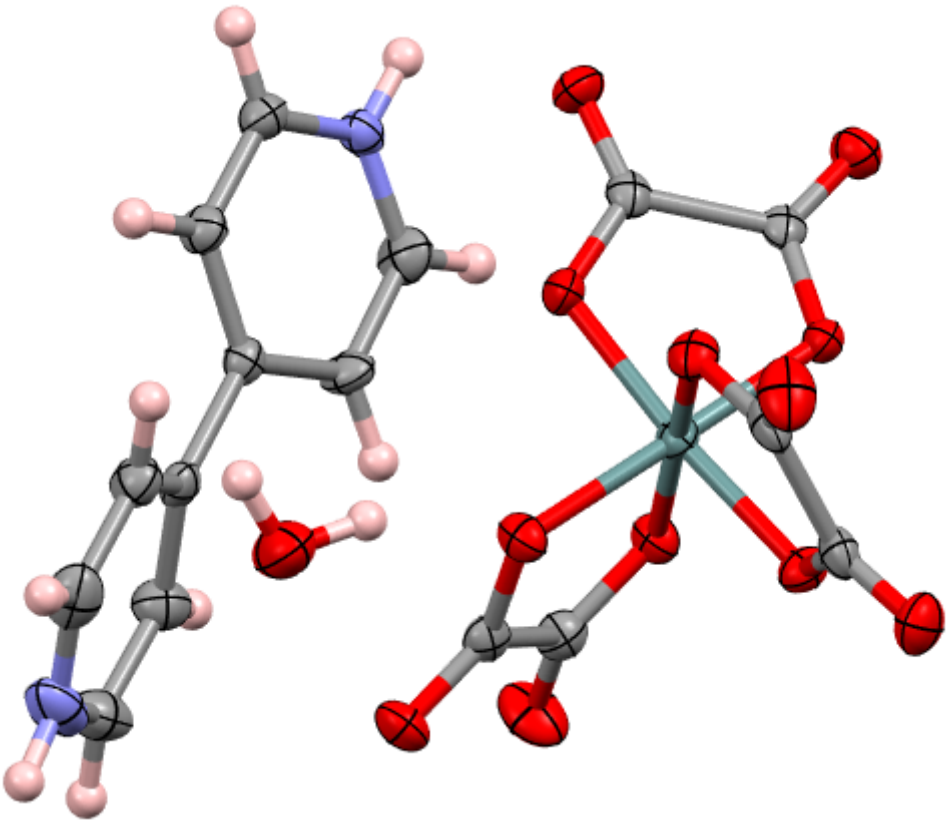

Crystal structure of Compound **11** (50% probability ellipsoids)

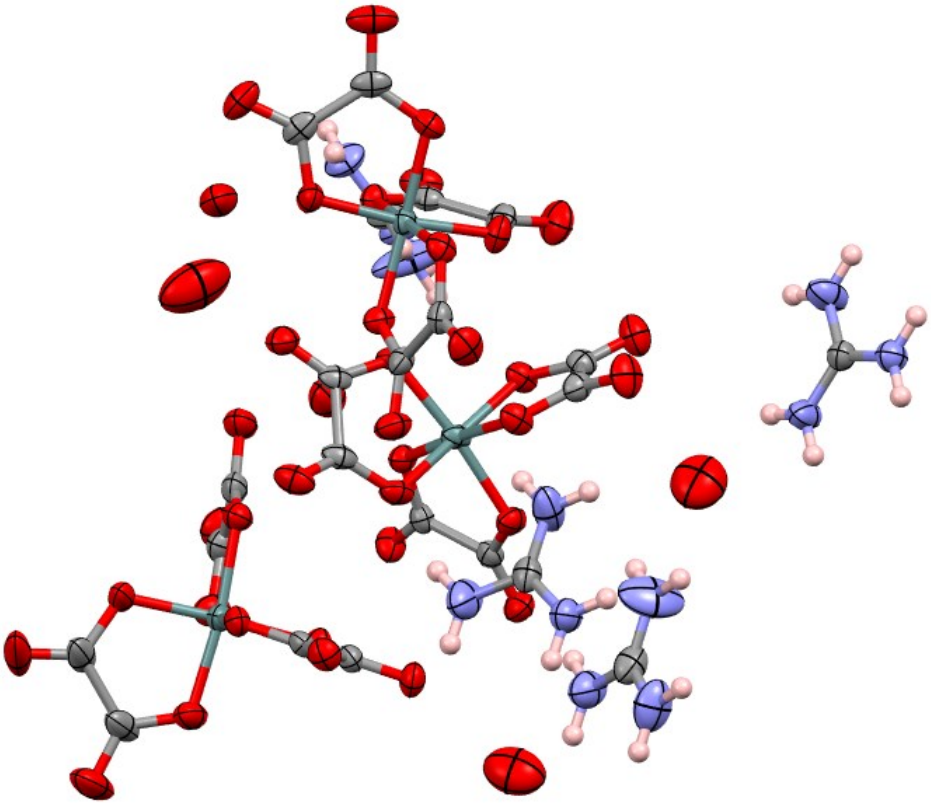

Crystal structure of Compound **12** (50% probability ellipsoids)

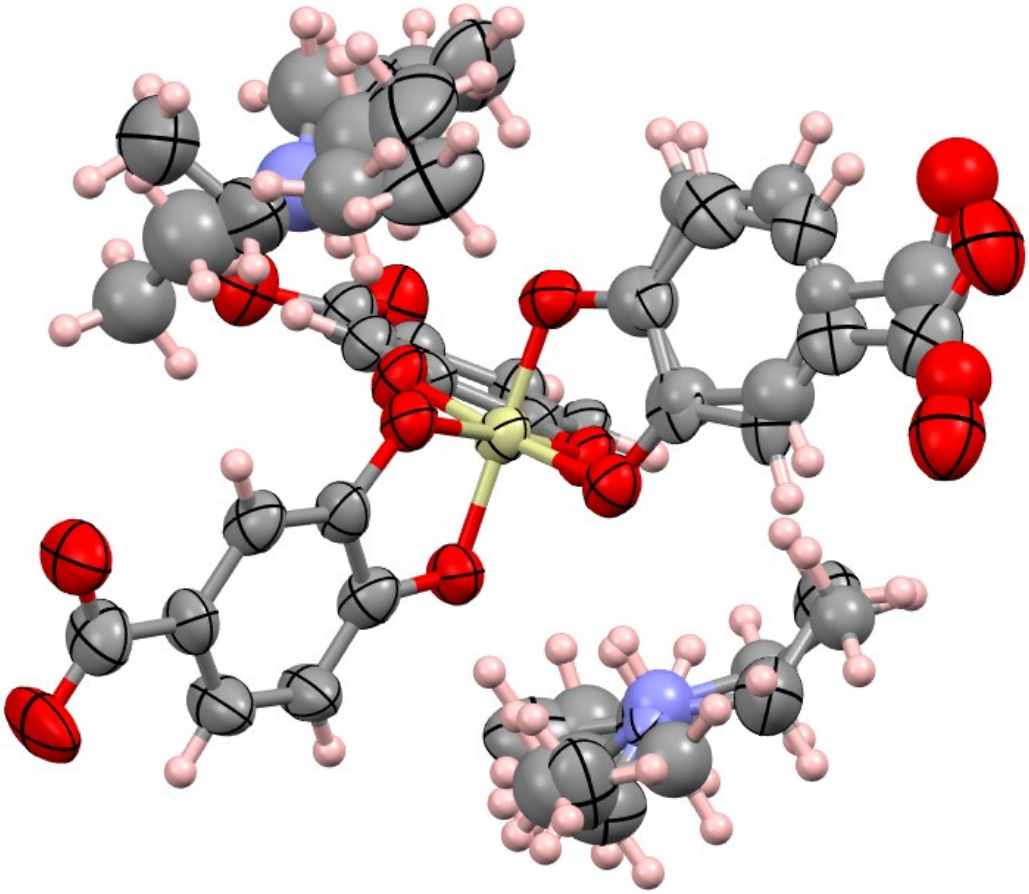

Crystal structure of Compound **16** (50% probability ellipsoids)

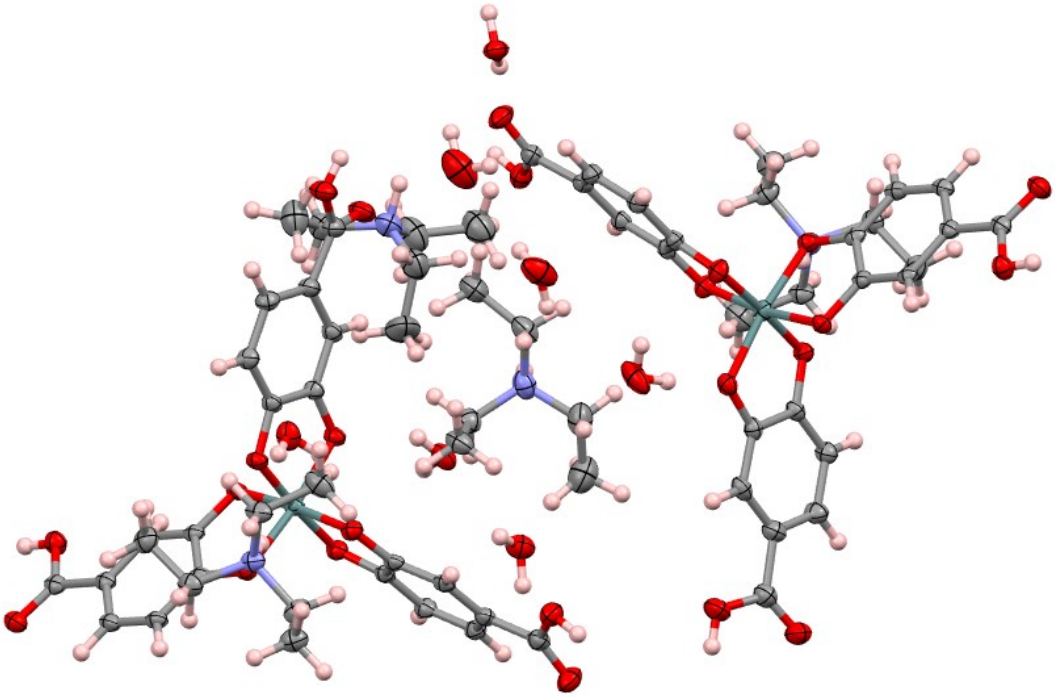

Crystal structure of Compound **20** (50% probability ellipsoids)

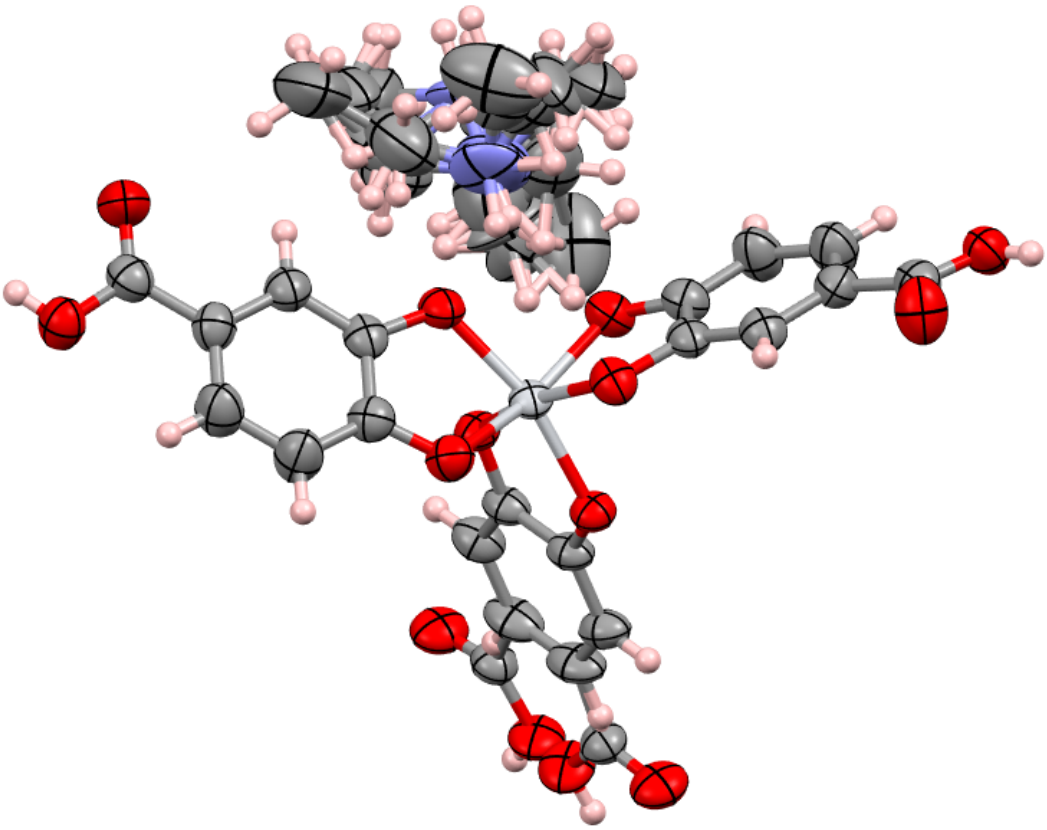

Crystal structure of Compound **22** (50% probability ellipsoids)

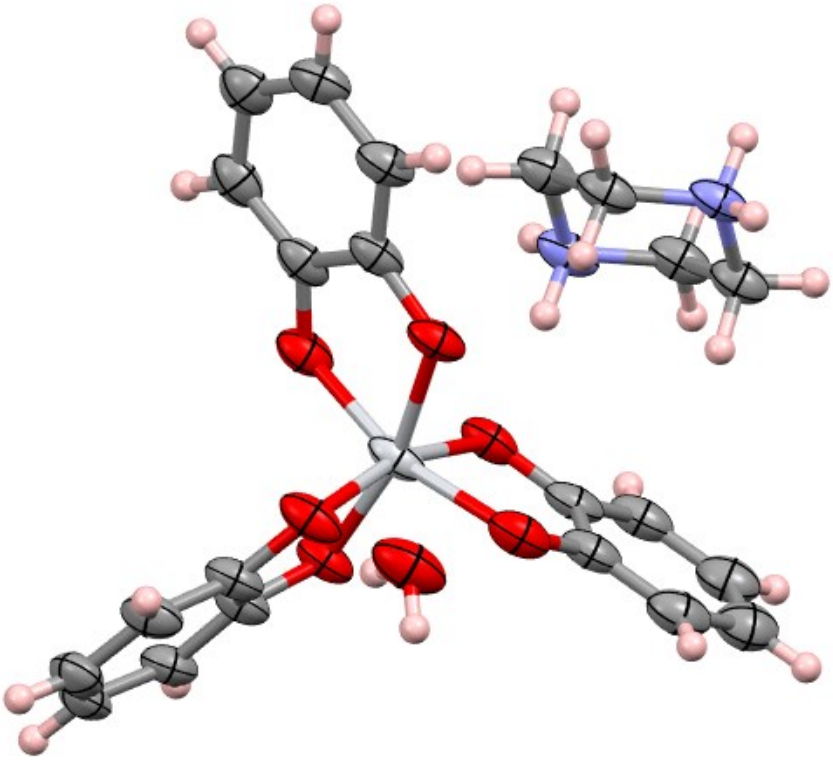

Crystal structure of Compound **23** (50% probability ellipsoids)

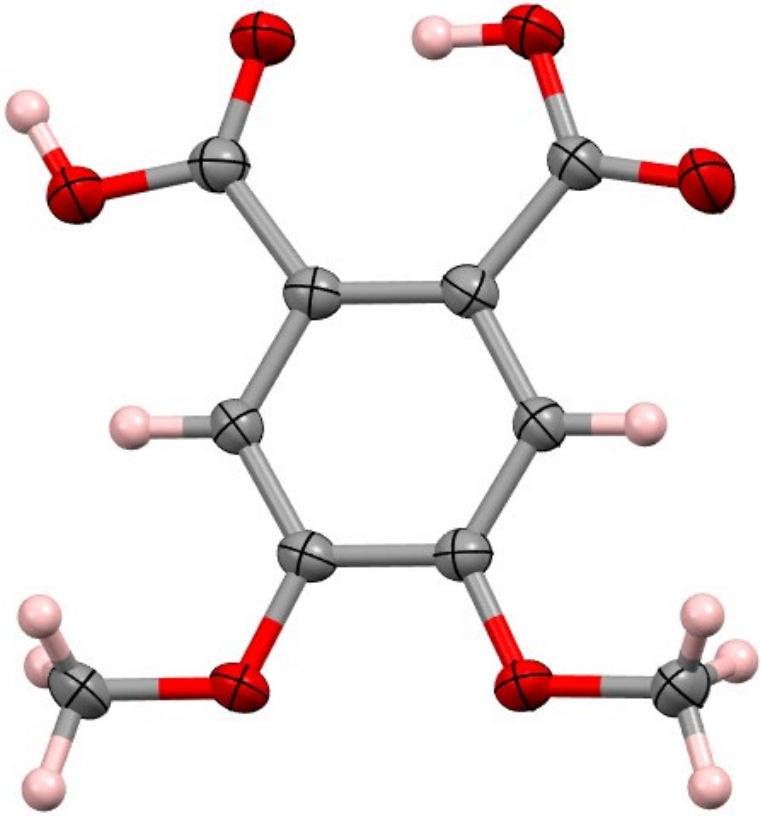

Crystal structure of Compound **25** (50% probability ellipsoids)

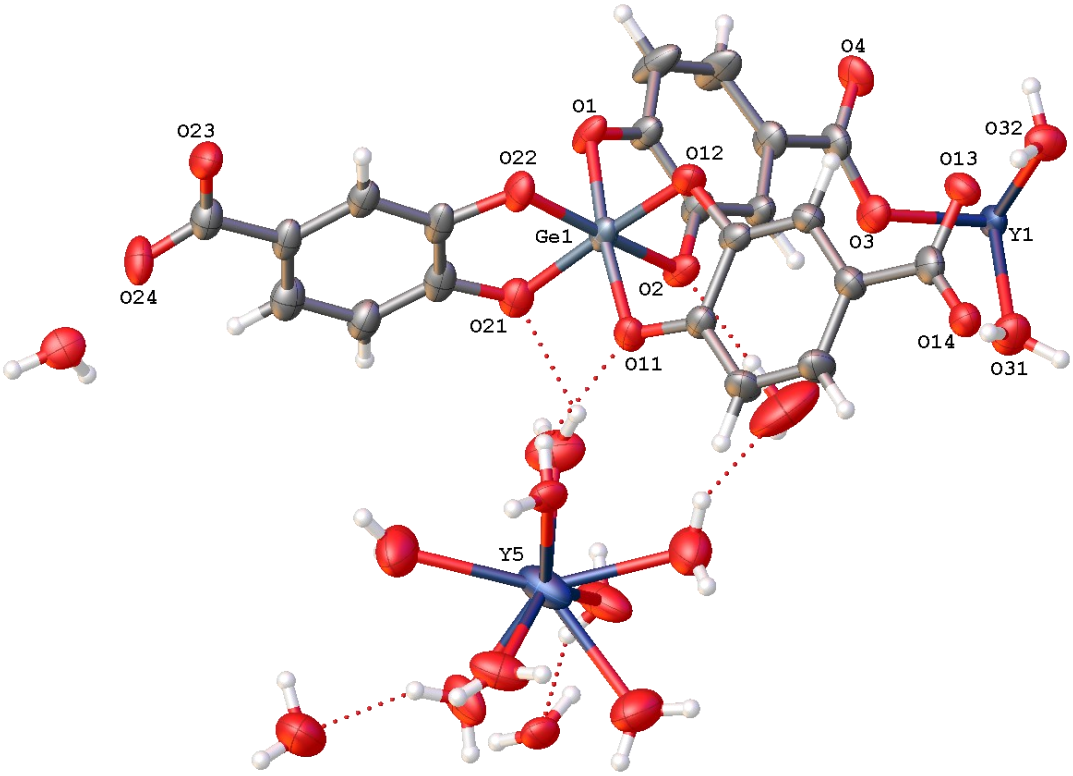

Crystal structure of **IMP-33-Y** (50% probability ellipsoids)

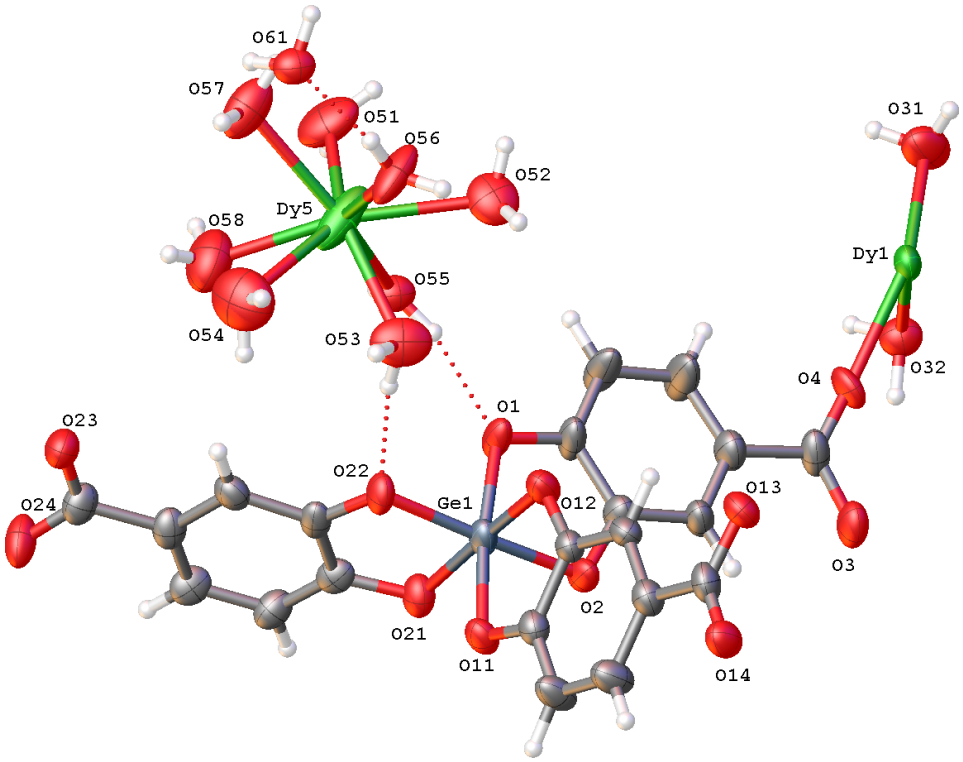

Crystal structure of Compound **IMP-33-Dy** (50% probability ellipsoids)

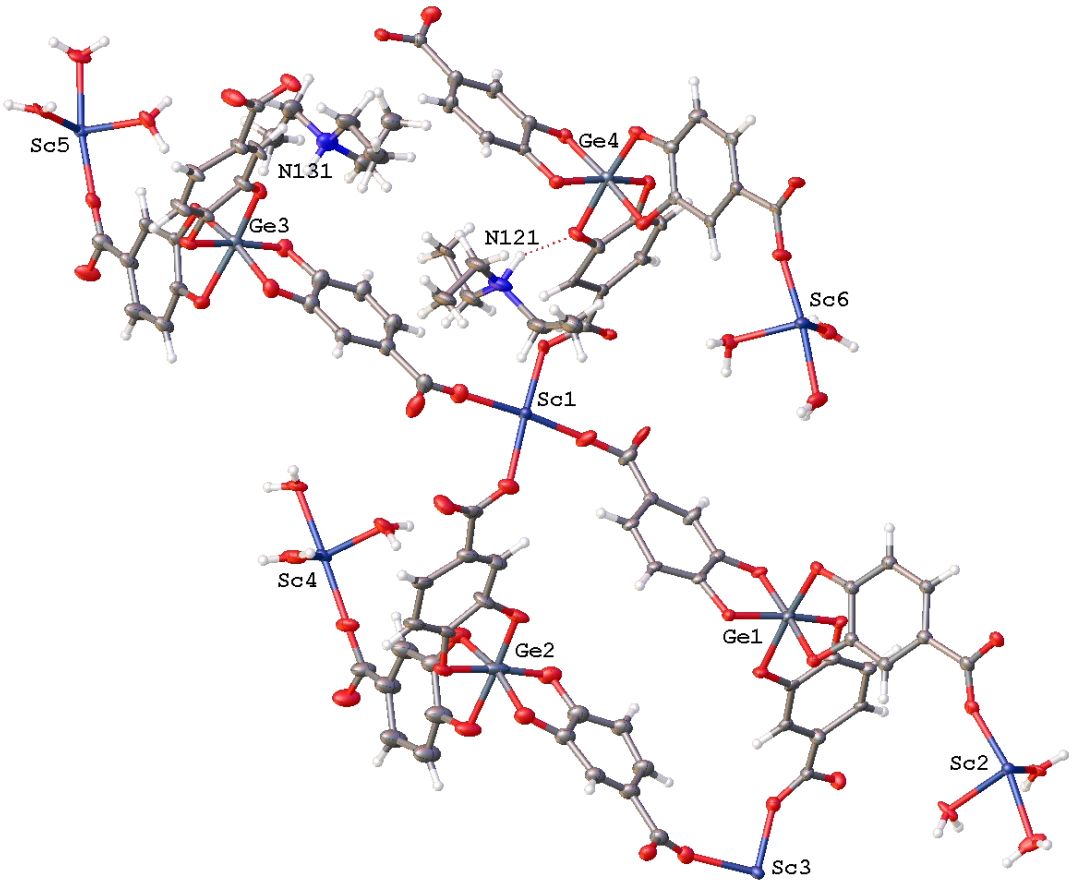

Crystal structure of Compound **IMP-34-Sc** (50% probability ellipsoids)

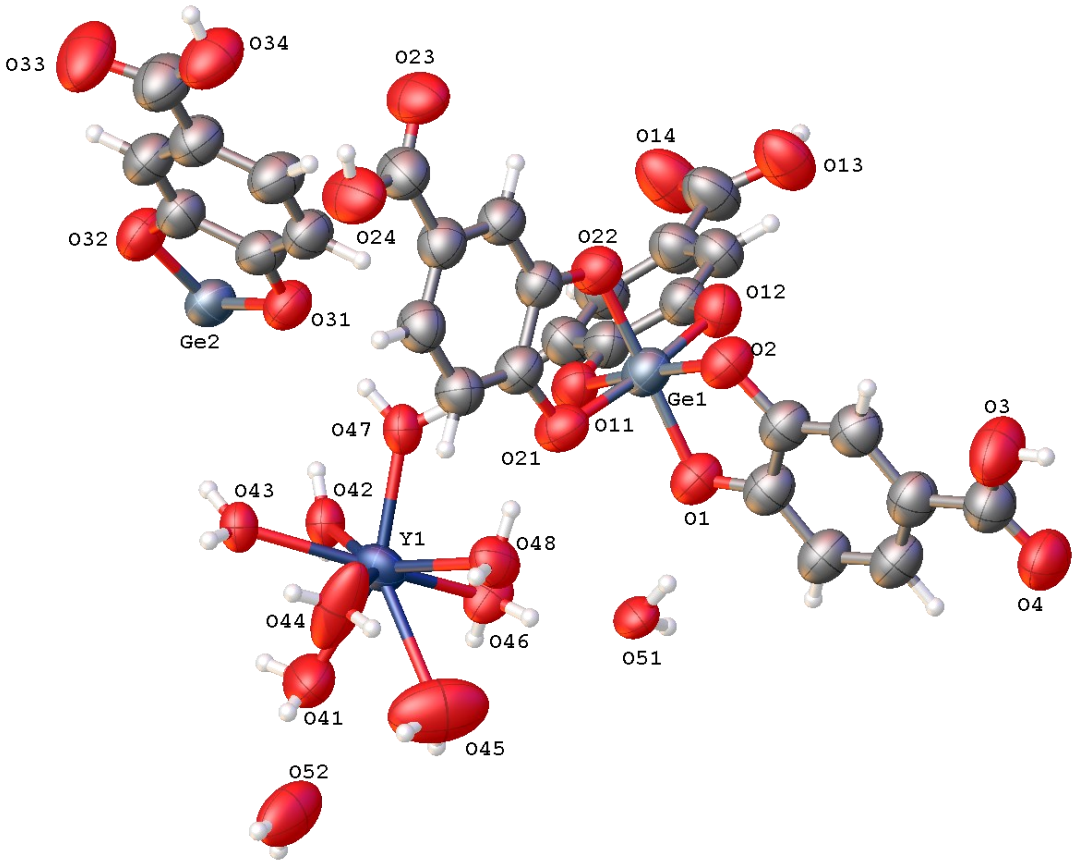

Crystal structure of green crystal (50% probability ellipsoids)

Copyright Permissions

Order Date	03-Apr-2024	Type of Use	Republish in a thesis/dissertation
Order License ID	1468807-1	Publisher	ROYAL SOCIETY OF CHEMISTRY
ISSN	1460-4744	Portion	Chart/graph/table/figure

LICENSED CONTENT

Publication Title	Chemical Society reviews	Publication Type	e-Journal
Article Title	Tuning the structure and function of metal-organic frameworks via linker design.	Start Page	5561
		End Page	5593
Author/Editor	Royal Society of Chemistry (Great Britain)	Issue	16
		Volume	43
Date	01/01/1972	URL	http://www.rsc.org/csr
Language	English		
Country	United Kingdom of Great Britain and Northern Ireland		
Rightsholder	Royal Society of Chemistry		

REQUEST DETAILS

Portion Type	Chart/graph/table/figure	Distribution	Worldwide
Number of Charts / Graphs / Tables / Figures Requested	1	Translation	Original language of publication
		Copies for the Disabled?	No
Format (select all that apply)	Electronic	Minor Editing Privileges?	No
Who Will Republish the Content?	Academic institution	Incidental Promotional Use?	No
Duration of Use	Current edition and up to 5 years	Currency	GBP
Lifetime Unit Quantity	Up to 499		
Rights Requested	Main product		

NEW WORK DETAILS

Title	Hexacoordinate Si/Ge Compounds and their Application in Metal-Organic Frameworks	Institution Name	Imperial College London
		Expected Presentation Date	2024-05-31
Instructor Name	Shouyi Tian		

ADDITIONAL DETAILS

Order Reference Number	N/A	The Requesting Person / Organization to Appear on the License	Shouyi Tian

REQUESTED CONTENT DETAILS

Title, Description or Numeric Reference of the Portion(s)	Tuning the structure and function of metal-organic frameworks via linker design.	Title of the Article / Chapter the Portion Is From	Tuning the structure and function of metal-organic frameworks via linker design.
Editor of Portion(s)	Lu, Weigang; Wei, Zhangwen; Gu, Zhi-Yuan; Liu, Tian-Fu; Park, Jinhee; Park, Jihye; Tian, Jian; Zhang, Muwei; Zhang, Qiang; Gentle III, Thomas; Bosch, Mathieu; Zhou, Hong-Cai	Author of Portion(s)	Lu, Weigang; Wei, Zhangwen; Gu, Zhi-Yuan; Liu, Tian-Fu; Park, Jinhee; Park, Jihye; Tian, Jian; Zhang, Muwei; Zhang, Qiang; Gentle III, Thomas; Bosch, Mathieu; Zhou, Hong-Cai
Volume / Edition	43 / ONLINE	Issue, if Republishing an Article From a Serial	16
Page or Page Range of Portion	5561-5593	Publication Date of Portion	2014-08-21

Licence for Figure 1.8

ACS Publications
Most Trusted. Most Cited. Most Read.

Structural Diversity in Metal–Organic Frameworks Built from Rigid Tetrahedral [Si(p-C6H4CO2)4]4– Struts

Author: Robert P. Davies, Rob Less, Paul D. Lickiss, et al

Publication: Crystal Growth and Design

Publisher: American Chemical Society

Date: Oct 1, 2010

Copyright © 2010, American Chemical Society

PERMISSION/LICENSE IS GRANTED FOR YOUR ORDER AT NO CHARGE

This type of permission/license, instead of the standard Terms and Conditions, is sent to you because no fee is being charged for your order. Please note the following:

- Permission is granted for your request in both print and electronic formats, and translations.
- If figures and/or tables were requested, they may be adapted or used in part.
- Please print this page for your records and send a copy of it to your publisher/graduate school.
- Appropriate credit for the requested material should be given as follows: "Reprinted (adapted) with permission from {COMPLETE REFERENCE CITATION}. Copyright {YEAR} American Chemical Society." Insert appropriate information in place of the capitalized words.
- One-time permission is granted only for the use specified in your RightsLink request. No additional uses are granted (such as derivative works or other editions). For any uses, please submit a new request.

If credit is given to another source for the material you requested from RightsLink, permission must be obtained from that source.

BACK CLOSE WINDOW

Licence for Figure 1.11

Order Date	03-Apr-2024	Type of Use	Republish in a thesis/dissertation
Order License ID	1468810-1	Publisher	ROYAL SOCIETY OF CHEMISTRY
ISSN	1364-548X	Portion	Chart/graph/table/figure

LICENSED CONTENT

Publication Title	Chemical communications	Rightsholder	Royal Society of Chemistry
Article Title	Molecular tectonics: tubular crystals with controllable channel size and orientation.	Publication Type	e-Journal
		Start Page	112
		End Page	114
Author/Editor	Royal Society of Chemistry (Great Britain)	Issue	1
Date	01/01/1996	Volume	46
Language	English		
Country	United Kingdom of Great Britain and Northern Ireland		

REQUEST DETAILS

Portion Type	Chart/graph/table/figure	Distribution	Worldwide
Number of Charts / Graphs / Tables / Figures Requested	1	Translation	Original language of publication
		Copies for the Disabled?	No
Format (select all that apply)	Electronic	Minor Editing Privileges?	No
Who Will Republish the Content?	Academic institution	Incidental Promotional Use?	No
Duration of Use	Current edition and up to 5 years	Currency	GBP
Lifetime Unit Quantity	Up to 499		
Rights Requested	Main product		

NEW WORK DETAILS

Title	Hexacoordinate Si/Ge Compounds and their Application in Metal-Organic Frameworks	Institution Name	Imperial College London
		Expected Presentation Date	2024-05-31
Instructor Name	Shouyi Tian		

ADDITIONAL DETAILS

Order Reference Number	N/A	The Requesting Person / Organization to Appear on the License	Shouyi Tian

REQUESTED CONTENT DETAILS

Title, Description or Numeric Reference of the Portion(s)	Molecular tectonics: tubular crystals with controllable channel size and orientation.	Title of the Article / Chapter the Portion Is From	Molecular tectonics: tubular crystals with controllable channel size and orientation.
Editor of Portion(s)	Lin, Mei-Jin; Jouaiti, Abdelaziz; Pocic, David; Kyritsakas, Nathalie; Planeix, Jean-Marc; Hosseini, Mir Wais	Author of Portion(s)	Lin, Mei-Jin; Jouaiti, Abdelaziz; Pocic, David; Kyritsakas, Nathalie; Planeix, Jean-Marc; Hosseini, Mir Wais
Volume / Edition	46	Issue, if Republishing an Article From a Serial	1
Page or Page Range of Portion	112-114		
		Publication Date of Portion	2010-01-07

Order Date	03-Apr-2024	Type of Use	Republish in a thesis/dissertation
Order License ID	1468811-1	Publisher	ROYAL SOCIETY OF CHEMISTRY
ISSN	1466-8033	Portion	Chart/graph/table/figure

LICENSED CONTENT

Publication Title	CrystEngComm	Publication Type	e-Journal
Article Title	Molecular tectonics: chaining cages into a 1-D coordination networkCCDC reference number 746134. For crystallographic data in CIF or other electronic format see DOI: 10.1039/b917864c	Start Page	67
		End Page	69
		Issue	1
		Volume	12
		URL	http://www.rsc.org/Publishing/Journals/ce/index.asp
Author/Editor	Royal Society of Chemistry (Great Britain)		
Date	01/01/1999		
Language	English		
Country	United Kingdom of Great Britain and Northern Ireland		
Rightsholder	Royal Society of Chemistry		

REQUEST DETAILS

Portion Type	Chart/graph/table/figure	Distribution	Worldwide
Number of Charts / Graphs / Tables / Figures Requested	1	Translation	Original language of publication
		Copies for the Disabled?	No
Format (select all that apply)	Electronic	Minor Editing Privileges?	No
Who Will Republish the Content?	Academic institution	Incidental Promotional Use?	No
Duration of Use	Current edition and up to 5 years	Currency	GBP
Lifetime Unit Quantity	Up to 499		
Rights Requested	Main product		

NEW WORK DETAILS

Title	Hexacoordinate Si/Ge Compounds and their Application in Metal-Organic Frameworks	Institution Name	Imperial College London
		Expected Presentation Date	2024-05-31
Instructor Name	Shouyi Tian		

ADDITIONAL DETAILS

Order Reference Number	N/A	The Requesting Person / Organization to Appear on the License	Shouyi Tian

REQUESTED CONTENT DETAILS

Title, Description or Numeric Reference of the Portion(s)	Molecular tectonics: chaining cages into a 1-D coordination network	Title of the Article / Chapter the Portion Is From	Molecular tectonics: chaining cages into a 1-D coordination network
Editor of Portion(s)	Lin, Mei-Jin; Jouaiti, Abdelaziz; Kyritsakas, Nathalie; Hosseini, Mir Wais	Author of Portion(s)	Lin, Mei-Jin; Jouaiti, Abdelaziz; Kyritsakas, Nathalie; Hosseini, Mir Wais
Volume / Edition	12	Issue, if Republishing an Article From a Serial	1
Page or Page Range of Portion	67-69		
		Publication Date of Portion	2010-01-01

Licence for Figure 1.16

3D Anionic Silicate Covalent Organic Framework with srs Topology

Author: Oussama Yahiaoui, Andrew N. Fitch, Frank Hoffmann, et al

Publication: Journal of the American Chemical Society

Publisher: American Chemical Society

Date: Apr 1, 2018

Copyright © 2018, American Chemical Society

PERMISSION/LICENSE IS GRANTED FOR YOUR ORDER AT NO CHARGE

This type of permission/license, instead of the standard Terms and Conditions, is sent to you because no fee is being charged for your order. Please note the following:

- Permission is granted for your request in both print and electronic formats, and translations.
- If figures and/or tables were requested, they may be adapted or used in part.
- Please print this page for your records and send a copy of it to your publisher/graduate school.
- Appropriate credit for the requested material should be given as follows: "Reprinted (adapted) with permission from {COMPLETE REFERENCE CITATION}. Copyright {YEAR} American Chemical Society." Insert appropriate information in place of the capitalized words.
- One-time permission is granted only for the use specified in your RightsLink request. No additional uses are granted (such as derivative works or other editions). For any uses, please submit a new request.

If credit is given to another source for the material you requested from RightsLink, permission must be obtained from that source.

BACK CLOSE WINDOW

Licence for Figure 1.21

Versatile Platform of Ion Conducting 2D Anionic Germanate Covalent Organic Frameworks with Potential for Capturing Toxic Acidic Gases

Author: Shumaila Ashraf, Caixia Liu, Shuai Li, et al

Publication: Applied Materials

Publisher: American Chemical Society

Date: Sep 1, 2020

Copyright © 2020, American Chemical Society

PERMISSION/LICENSE IS GRANTED FOR YOUR ORDER AT NO CHARGE

This type of permission/license, instead of the standard Terms and Conditions, is sent to you because no fee is being charged for your order. Please note the following:

- Permission is granted for your request in both print and electronic formats, and translations.
- If figures and/or tables were requested, they may be adapted or used in part.
- Please print this page for your records and send a copy of it to your publisher/graduate school.
- Appropriate credit for the requested material should be given as follows: "Reprinted (adapted) with permission from {COMPLETE REFERENCE CITATION}. Copyright {YEAR} American Chemical Society." Insert appropriate information in place of the capitalized words.
- One-time permission is granted only for the use specified in your RightsLink request. No additional uses are granted (such as derivative works or other editions). For any uses, please submit a new request.

If credit is given to another source for the material you requested from RightsLink, permission must be obtained from that source.

BACK CLOSE WINDOW

Licence for Figure 1.22

Order Date	03-Apr-2024	Type of Use	Republish in a thesis/dissertation
Order License ID	1468815-1	Publisher	ROYAL SOCIETY OF CHEMISTRY
ISSN	1460-4744	Portion	Chart/graph/table/figure

LICENSED CONTENT

Publication Title	Chemical Society reviews	Publication Type	e-Journal
Article Title	Multifunctional porous hydrogen-bonded organic framework materials.	Start Page	1362
		End Page	1389
Author/Editor	Royal Society of Chemistry (Great Britain)	Issue	5
		Volume	48
Date	01/01/1972	URL	http://www.rsc.org/csr
Language	English		
Country	United Kingdom of Great Britain and Northern Ireland		
Rightsholder	Royal Society of Chemistry		

REQUEST DETAILS

Portion Type	Chart/graph/table/figure	Distribution	Worldwide
Number of Charts / Graphs / Tables / Figures Requested	1	Translation	Original language of publication
		Copies for the Disabled?	No
Format (select all that apply)	Electronic	Minor Editing Privileges?	No
Who Will Republish the Content?	Academic institution	Incidental Promotional Use?	No
Duration of Use	Current edition and up to 5 years	Currency	GBP
Lifetime Unit Quantity	Up to 499		
Rights Requested	Main product		

NEW WORK DETAILS

Title	Hexacoordinate Si/Ge Compounds and their Application in Metal-Organic Frameworks	Institution Name	Imperial College London
		Expected Presentation Date	2024-05-31
Instructor Name	Shouyi Tian		

ADDITIONAL DETAILS

Order Reference Number	N/A	The Requesting Person / Organization to Appear on the License	Shouyi Tian

REQUESTED CONTENT DETAILS

Title, Description or Numeric Reference of the Portion(s)	Multifunctional porous hydrogen-bonded organic framework materials.	Title of the Article / Chapter the Portion Is From	Multifunctional porous hydrogen-bonded organic framework materials.
Editor of Portion(s)	Chen, Banglin; He, Yabing; Li, Peng; Lin, Rui-Biao; Wang, Hailong; Zhou, Wei	Author of Portion(s)	Chen, Banglin; He, Yabing; Li, Peng; Lin, Rui-Biao; Wang, Hailong; Zhou, Wei
Volume / Edition	48 / ONLINE	Issue, if Republishing an Article From a Serial	5
Page or Page Range of Portion	1362-1389	Publication Date of Portion	2019-03-04

Licence for Figure 2.1

License Number	5761070016232
License date	Apr 02, 2024

Printable Details

Licensed Content

Licensed Content Publisher	John Wiley and Sons
Licensed Content Publication	Angewandte Chemie International Edition
Licensed Content Title	A C3-Symmetric Macrocycle-Based, Hydrogen-Bonded, Multiporous Hexagonal Network as a Motif of Porous Molecular Crystals
Licensed Content Author	Mikiji Miyata, Norimitsu Tohnai, Shoichi Nakagawa, et al
Licensed Content Date	Jan 28, 2015
Licensed Content Volume	54
Licensed Content Issue	10
Licensed Content Pages	5

Order Details

Type of use	Dissertation/Thesis
Requestor type	Author of this Wiley article
Format	Electronic
Portion	Figure/table
Number of figures/tables	2
Will you be translating?	No

About Your Work

Title of new work	Hexacoordinate Si/Ge Compounds and their Application in Metal-Organic Frameworks
Institution name	Imperial College London
Expected presentation date	May 2024

Additional Data

Portions	Figure 1, Figure 3

Licence for Figure 2.3

License Number	5761070358595
License date	Apr 02, 2024

Printable Details

Licensed Content

Licensed Content Publisher	John Wiley and Sons
Licensed Content Publication	Chemistry - A European Journal
Licensed Content Title	Hexaazatriphenylene-Based Hydrogen-Bonded Organic Framework with Permanent Porosity and Single-Crystallinity
Licensed Content Author	Abderrazzak Douhal, Norimitsu Tohnai, Boiko Cohen, et al
Licensed Content Date	Aug 9, 2017
Licensed Content Volume	23
Licensed Content Issue	48
Licensed Content Pages	9

Order Details

Type of use	Dissertation/Thesis
Requestor type	Author of this Wiley article
Format	Electronic
Portion	Figure/table
Number of figures/tables	1
Will you be translating?	No

About Your Work

Title of new work	Hexacoordinate Si/Ge Compounds and their Application in Metal-Organic Frameworks
Institution name	Imperial College London
Expected presentation date	May 2024

Additional Data

Portions	Figure 2

Licence for Figure 2.4

License Number	5761340608249
License date	Apr 03, 2024

Printable Details

Licensed Content

Licensed Content Publisher	John Wiley and Sons
Licensed Content Publication	Angewandte Chemie International Edition
Licensed Content Title	A Hydrogen-Bonded Organic Framework (HOF) with Type IV NH3 Adsorption Behavior
Licensed Content Author	Chang Seop Hong, Dohyun Moon, Woo Ram Lee, et al
Licensed Content Date	Sep 25, 2019
Licensed Content Volume	58
Licensed Content Issue	45
Licensed Content Pages	4

Order Details

Type of use	Dissertation/Thesis
Requestor type	Author of this Wiley article
Format	Electronic
Portion	Figure/table
Number of figures/tables	1
Will you be translating?	No

About Your Work

Title of new work	Hexacoordinate Si/Ge Compounds and their Application in Metal-Organic Frameworks
Institution name	Imperial College London
Expected presentation date	May 2024

Additional Data

Portions	Figure 1

Licence for Figure 2.6

License Number	5761861277304
License date	Apr 04, 2024
Licensed Content Publisher	Elsevier
Licensed Content Publication	Synthetic Metals
Licensed Content Title	Hydrogen bonded-directed pure organic frameworks based on TTF-tetrabenzoic acid and bipyridine base
Licensed Content Author	Xuemei Zheng,Ning Xiao,Zaihao Long,Lejia Wang,Fenxia Ye,Jianghua Fang,Liangjun Shen,Xunwen Xiao
Licensed Content Date	May 1, 2020
Licensed Content Volume	263
Licensed Content Issue	n/a
Licensed Content Pages	1
Start Page	116365
End Page	
Type of Use	reuse in a thesis/dissertation
Portion	figures/tables/illustrations
Number of figures/tables/illustrations	1
Format	electronic
Are you the author of this Elsevier article?	No
Will you be translating?	No
Title of new work	Hexacoordinate Si/Ge Compounds and their Application in Metal-Organic Frameworks
Institution name	Imperial College London
Expected presentation date	May 2024
Portions	Figure 3

Licence for Figure 2.7

ACS Publications
Most Trusted. Most Cited. Most Read.

Topology-Guided Design for Sc-soc-MOFs and Their Enhanced Storage and Separation for CO2 and C2-Hydrocarbons

Author: Jian-Wei Zhang, Peng Qu, Man-Cheng Hu, et al
Publication: Inorganic Chemistry
Publisher: American Chemical Society
Date: Dec 1, 2019

Copyright © 2019, American Chemical Society

PERMISSION/LICENSE IS GRANTED FOR YOUR ORDER AT NO CHARGE

This type of permission/license, instead of the standard Terms and Conditions, is sent to you because no fee is being charged for your order. Please note the following:

- Permission is granted for your request in both print and electronic formats, and translations.
- If figures and/or tables were requested, they may be adapted or used in part.
- Please print this page for your records and send a copy of it to your publisher/graduate school.
- Appropriate credit for the requested material should be given as follows: "Reprinted (adapted) with permission from {COMPLETE REFERENCE CITATION}. Copyright {YEAR} American Chemical Society." Insert appropriate information in place of the capitalized words.
- One-time permission is granted only for the use specified in your RightsLink request. No additional uses are granted (such as derivative works or other editions). For any uses, please submit a new request.

If credit is given to another source for the material you requested from RightsLink, permission must be obtained from that source.

BACK CLOSE WINDOW

Licence for Figure 3.2

ACS Publications
Most Trusted. Most Cited. Most Read.

Micropore Regulation in Ultrastable [Sc3O]-Organic Frameworks for Acetylene Storage and Purification

Author: Hong-Juan Lv, Jian-Wei Zhang, Yu-Cheng Jiang, et al
Publication: Inorganic Chemistry
Publisher: American Chemical Society
Date: Feb 1, 2022

Copyright © 2022, American Chemical Society

PERMISSION/LICENSE IS GRANTED FOR YOUR ORDER AT NO CHARGE

This type of permission/license, instead of the standard Terms and Conditions, is sent to you because no fee is being charged for your order. Please note the following:

- Permission is granted for your request in both print and electronic formats, and translations.
- If figures and/or tables were requested, they may be adapted or used in part.
- Please print this page for your records and send a copy of it to your publisher/graduate school.
- Appropriate credit for the requested material should be given as follows: "Reprinted (adapted) with permission from {COMPLETE REFERENCE CITATION}. Copyright {YEAR} American Chemical Society." Insert appropriate information in place of the capitalized words.
- One-time permission is granted only for the use specified in your RightsLink request. No additional uses are granted (such as derivative works or other editions). For any uses, please submit a new request.

If credit is given to another source for the material you requested from RightsLink, permission must be obtained from that source.

BACK CLOSE WINDOW

Licence for Figure 3.3

1. Materials Chemistry Frontiers

Billing Status: Open

Article: A microporous yttrium metal–organic framework of an unusual nia topology for high adsorption selectivity of C2H2 and CO2 over CH4 at room temperature

Order License ID	1469032-1	**Type of Use**	Republish in a thesis/dissertation
Order detail status	Completed	**Publisher**	Royal Society of Chemistry
Project Name	1	**Portion**	Image/photo/illustration
ISSN	2052-1537		

0.00 GBP
Republication Permission

LICENSED CONTENT

Publication Title	Materials Chemistry Frontiers	**Rightsholder**	Royal Society of Chemistry
Article Title	A microporous yttrium metal–organic framework of an unusual nia topology for high adsorption selectivity of C2H2 and CO2 over CH4 at room temperature	**Publication Type**	e-Journal
		Start Page	1982
		End Page	1988
Author/Editor	Zhongguo hua xue hui (Beijing, China), Royal Society of Chemistry (Great Britain)	**Issue**	10
		Volume	1
Date	01/01/2016		
Language	English		
Country	United Kingdom of Great Britain and Northern Ireland		

REQUEST DETAILS

Portion Type	Image/photo/illustration	**Distribution**	Worldwide
Number of Images / Photos / Illustrations	1	**Translation**	Original language of publication
		Copies for the Disabled?	No
Format (select all that apply)	Electronic	**Minor Editing Privileges?**	No
Who Will Republish the Content?	Academic institution	**Incidental Promotional Use?**	No
Duration of Use	Current edition and up to 5 years	**Currency**	GBP
Lifetime Unit Quantity	Up to 499		
Rights Requested	Main product		

NEW WORK DETAILS

Title	Hexacoordinate Si/Ge Compounds and their Application in Metal-Organic Frameworks	**Institution Name**	Imperial College London
		Expected Presentation Date	2024-05-31
Instructor Name	Shouyi Tian		

ADDITIONAL DETAILS

The Requesting Person / Organization to Appear on the License	Shouyi Tian

REQUESTED CONTENT DETAILS

Title, Description or Numeric Reference of the Portion(s)	A microporous yttrium metal–organic framework of an unusual nia topology for high adsorption selectivity of C2H2 and CO2 over CH4 at room temperature	**Title of the Article / Chapter the Portion Is From**	A microporous yttrium metal–organic framework of an unusual nia topology for high adsorption selectivity of C2H2 and CO2 over CH4 at room temperature
Editor of Portion(s)	Liu, Kang; Li, Xu; Ma, Dingxuan; Han, Yi; Li, Baiyan; Shi, Zhan; Li, Zhenjiang; Wang, Lei	**Author of Portion(s)**	Liu, Kang; Li, Xu; Ma, Dingxuan; Han, Yi; Li, Baiyan; Shi, Zhan; Li, Zhenjiang; Wang, Lei
Volume / Edition	1	**Issue, if Republishing an Article From a Serial**	10
Page or Page Range of Portion	1982-1988	**Publication Date of Portion**	2017-10-01

Licence for Figure 3.5

1. Dalton transactions

Billing Status: Open

Article: A novel yttrium-based metal–organic framework for the efficient solvent-free catalytic synthesis of cyanohydrin silyl ethers

Order License ID	1469036-1	**Type of Use**	Republish in a thesis/dissertation
Order detail status	Completed	**Publisher**	ROYAL SOCIETY OF CHEMISTRY
Project Name	1	**Portion**	Image/photo/illustration
ISSN	1477-9234		

0.00 GBP
Republication Permission

LICENSED CONTENT

Publication Title	Dalton transactions	**Rightsholder**	Royal Society of Chemistry
Article Title	A novel yttrium-based metal–organic framework for the efficient solvent-free catalytic synthesis of cyanohydrin silyl ethers	**Publication Type**	e-Journal
		Start Page	11720
		End Page	11724
Author/Editor	Royal Society of Chemistry (Great Britain)	**Issue**	34
		Volume	50
Date	01/01/2003		
Language	English		
Country	United Kingdom of Great Britain and Northern Ireland		

REQUEST DETAILS

Portion Type	Image/photo/illustration	**Distribution**	Worldwide
Number of Images / Photos / Illustrations	1	**Translation**	Original language of publication
		Copies for the Disabled?	No
Format (select all that apply)	Electronic	**Minor Editing Privileges?**	No
Who Will Republish the Content?	Academic institution	**Incidental Promotional Use?**	No
Duration of Use	Current edition and up to 5 years	**Currency**	GBP
Lifetime Unit Quantity	Up to 499		
Rights Requested	Main product		

NEW WORK DETAILS

Title	Hexacoordinate Si/Ge Compounds and their Application in Metal-Organic Frameworks	**Institution Name**	Imperial College London
		Expected Presentation Date	2024-05-31
Instructor Name	Shouyi Tian		

ADDITIONAL DETAILS

The Requesting Person / Organization to Appear on the License	Shouyi Tian

REQUESTED CONTENT DETAILS

Title, Description or Numeric Reference of the Portion(s)	A novel yttrium-based metal–organic framework for the efficient solvent-free catalytic synthesis of cyanohydrin silyl ethers	**Title of the Article / Chapter the Portion Is From**	A novel yttrium-based metal–organic framework for the efficient solvent-free catalytic synthesis of cyanohydrin silyl ethers
Editor of Portion(s)	Echenique-Errandonea, Estitxu; Pérez, Juana M.; Rojas, Sara; Cepeda, Javier; Seco, José M.; Fernández, Ignacio; Rodríguez-Diéguez, Antonio	**Author of Portion(s)**	Echenique-Errandonea, Estitxu; Pérez, Juana M.; Rojas, Sara; Cepeda, Javier; Seco, José M.; Fernández, Ignacio; Rodríguez-Diéguez, Antonio
Volume / Edition	50	**Issue, if Republishing an Article From a Serial**	34
Page or Page Range of Portion	11720-11724	**Publication Date of Portion**	2021-09-14

Licence for Figure 3.6

1. Journal of materials chemistry

Billing Status: Open

Article: Color tunable and white light emitting Tb3+ and Eu3+ doped lanthanide metal–organic framework materials

Order License ID	1469044-1	Type of Use	Republish in a thesis/dissertation
Order detail status	Completed	Publisher	ROYAL SOCIETY OF CHEMISTRY,
Project Name	1	Portion	Image/photo/illustration
ISSN	1364-5501		

0.00 GBP
Republication Permission

LICENSED CONTENT

Publication Title	Journal of materials chemistry	Rightsholder	Royal Society of Chemistry
Article Title	Color tunable and white light emitting Tb3+ and Eu3+ doped lanthanide metal–organic framework materials	Publication Type	e-Journal
		Start Page	3210
		Issue	7
Author/Editor	Royal Society of Chemistry (Great Britain)	Volume	22
Date	01/01/1991	URL	http://firstsearch.oclc.org
Language	English		
Country	United Kingdom of Great Britain and Northern Ireland		

REQUEST DETAILS

Portion Type	Image/photo/illustration	Distribution	Worldwide
Number of Images / Photos / Illustrations	1	Translation	Original language of publication
		Copies for the Disabled?	No
Format (select all that apply)	Electronic	Minor Editing Privileges?	No
Who Will Republish the Content?	Academic institution	Incidental Promotional Use?	No
Duration of Use	Current edition and up to 5 years	Currency	GBP
Lifetime Unit Quantity	Up to 499		
Rights Requested	Main product		

NEW WORK DETAILS

Title	Hexacoordinate Si/Ge Compounds and their Application in Metal-Organic Frameworks	Institution Name	Imperial College London
		Expected Presentation Date	2024-05-31
Instructor Name	Shouyi Tian		

ADDITIONAL DETAILS

The Requesting Person / Organization to Appear on the License	Shouyi Tian

REQUESTED CONTENT DETAILS

Title, Description or Numeric Reference of the Portion(s)	Color tunable and white light emitting Tb3+ and Eu3+ doped lanthanide metal–organic framework materials	Title of the Article / Chapter the Portion Is From	Color tunable and white light emitting Tb3+ and Eu3+ doped lanthanide metal–organic framework materials
Editor of Portion(s)	Rao, Xingtang; Huang, Qian; Yang, Xiuli; Cui, Yuanjing; Yang, Yu; Wu, Chuande; Chen, Banglin; Qian, Guodong	Author of Portion(s)	Rao, Xingtang; Huang, Qian; Yang, Xiuli; Cui, Yuanjing; Yang, Yu; Wu, Chuande; Chen, Banglin; Qian, Guodong
Volume / Edition	22	Issue, if Republishing an Article From a Serial	7
Page or Page Range of Portion	3210		
		Publication Date of Portion	2012-01-24

Licence for Figure 3.7

ACS Publications
Most Trusted. Most Cited. Most Read.

Near-Infrared Luminescent Lanthanide MOF Barcodes

Author: Kiley A. White, Demetra A. Chengelis, Kristy A. Gogick, et al
Publication: Journal of the American Chemical Society
Publisher: American Chemical Society
Date: Dec 1, 2009

Copyright © 2009, American Chemical Society

PERMISSION/LICENSE IS GRANTED FOR YOUR ORDER AT NO CHARGE

This type of permission/license, instead of the standard Terms and Conditions, is sent to you because no fee is being charged for your order. Please note the following:

- Permission is granted for your request in both print and electronic formats, and translations.
- If figures and/or tables were requested, they may be adapted or used in part.
- Please print this page for your records and send a copy of it to your publisher/graduate school.
- Appropriate credit for the requested material should be given as follows: "Reprinted (adapted) with permission from {COMPLETE REFERENCE CITATION}. Copyright {YEAR} American Chemical Society." Insert appropriate information in place of the capitalized words.
- One-time permission is granted only for the use specified in your RightsLink request. No additional uses are granted (such as derivative works or other editions). For any uses, please submit a new request.

If credit is given to another source for the material you requested from RightsLink, permission must be obtained from that source.

BACK CLOSE WINDOW

Licence for Figure 3.8

ACS Publications
Most Trusted. Most Cited. Most Read.

Nanoscale Coordination Polymers for Platinum-Based Anticancer Drug Delivery

Author: William J. Rieter, Kimberly M. Pott, Kathryn M. L. Taylor, et al
Publication: Journal of the American Chemical Society
Publisher: American Chemical Society
Date: Sep 1, 2008

Copyright © 2008, American Chemical Society

PERMISSION/LICENSE IS GRANTED FOR YOUR ORDER AT NO CHARGE

This type of permission/license, instead of the standard Terms and Conditions, is sent to you because no fee is being charged for your order. Please note the following:

- Permission is granted for your request in both print and electronic formats, and translations.
- If figures and/or tables were requested, they may be adapted or used in part.
- Please print this page for your records and send a copy of it to your publisher/graduate school.
- Appropriate credit for the requested material should be given as follows: "Reprinted (adapted) with permission from {COMPLETE REFERENCE CITATION}. Copyright {YEAR} American Chemical Society." Insert appropriate information in place of the capitalized words.
- One-time permission is granted only for the use specified in your RightsLink request. No additional uses are granted (such as derivative works or other editions). For any uses, please submit a new request.

If credit is given to another source for the material you requested from RightsLink, permission must be obtained from that source.

BACK | CLOSE WINDOW

Licence for Figure 3.9

1. Chemical Society reviews

Billing Status: Open

Article: Lanthanide luminescence for functional materials and bio-sciences.

Order License ID	1512131-1	Type of Use	Republish in a thesis/dissertation
Order detail status	Completed	Publisher	ROYAL SOCIETY OF CHEMISTRY
Project Name	1	Portion	Image/photo/illustration
ISSN	1460-4744		

0.00 GBP
Republication Permission

LICENSED CONTENT

Publication Title	Chemical Society reviews	Publication Type	e-Journal
Article Title	Lanthanide luminescence for functional materials and bio-sciences.	Start Page	189
		End Page	227
Author / Editor	Royal Society of Chemistry (Great Britain)	Issue	1
		Volume	39
Date	01/01/1972	URL	http://www.rsc.org/csr
Language	English		
Country	United Kingdom of Great Britain and Northern Ireland		
Rightsholder	Royal Society of Chemistry		

REQUEST DETAILS

Portion Type	Image/photo/illustration	Distribution	Worldwide
Number of Images / Photos / Illustrations	1	Translation	Original language of publication
		Copies for the Disabled?	No
Format (select all that apply)	Electronic	Minor Editing Privileges?	No
Who Will Republish the Content?	Academic institution	Incidental Promotional Use?	No
Duration of Use	Current edition and up to 5 years	Currency	GBP
Lifetime Unit Quantity	Up to 499		
Rights Requested	Main product		

NEW WORK DETAILS

Title	Hexacoordinate Si/Ge Compounds and their Application in Metal-Organic Frameworks	Institution Name	Imperial College London
		Expected Presentation Date	2024-08-02
Instructor Name	Shouyi Tian		

ADDITIONAL DETAILS

The Requesting Person / Organization to Appear on the License	Shouyi Tian

REQUESTED CONTENT DETAILS

Title, Description or Numeric Reference of the Portion(s)	Figure 1	Title of the Article / Chapter the Portion Is From	Lanthanide luminescence for functional materials and bio-sciences.
Editor of Portion(s)	Eliseeva, Svetlana V.; Bünzli, Jean-Claude G.	Author of Portion(s)	Eliseeva, Svetlana V.; Bünzli, Jean-Claude G.
Volume / Edition	39 / ONLINE		
Page or Page Range of Portion	189-227	Issue, if Republishing an Article From a Serial	1
		Publication Date of Portion	2010-01-01

Licence for Figure 4.1

ACS Publications
Most Trusted. Most Cited. Most Read.

Lanthanide Luminescence for Biomedical Analyses and Imaging

Author: Jean-Claude G. Bünzli
Publication: Chemical Reviews
Publisher: American Chemical Society
Date: May 1, 2010

Copyright © 2010, American Chemical Society

PERMISSION/LICENSE IS GRANTED FOR YOUR ORDER AT NO CHARGE

This type of permission/license, instead of the standard Terms and Conditions, is sent to you because no fee is being charged for your order. Please note the following:

- Permission is granted for your request in both print and electronic formats, and translations.
- If figures and/or tables were requested, they may be adapted or used in part.
- Please print this page for your records and send a copy of it to your publisher/graduate school.
- Appropriate credit for the requested material should be given as follows: "Reprinted (adapted) with permission from {COMPLETE REFERENCE CITATION}. Copyright {YEAR} American Chemical Society." Insert appropriate information in place of the capitalized words.
- One-time permission is granted only for the use specified in your RightsLink request. No additional uses are granted (such as derivative works or other editions). For any uses, please submit a new request.

If credit is given to another source for the material you requested from RightsLink, permission must be obtained from that source.

BACK CLOSE WINDOW

Licence for Figure 4.2

1. Chemical Society reviews

Billing Status: Open

Article: Taking advantage of luminescent lanthanide ions.

Order License ID	1469052-1	Type of Use	Republish in a thesis/dissertation
Order detail status	Completed	Publisher	ROYAL SOCIETY OF CHEMISTRY
Project Name	1	Portion	Image/photo/illustration
ISSN	1460-4744		

0.00 GBP
Republication Permission

LICENSED CONTENT

Publication Title	Chemical Society reviews	Publication Type	e-Journal
Article Title	Taking advantage of luminescent lanthanide ions.	Start Page	1048
		End Page	1077
Author/Editor	Royal Society of Chemistry (Great Britain)	Issue	12
		Volume	34
Date	01/01/1972	URL	http://www.rsc.org/csr
Language	English		
Country	United Kingdom of Great Britain and Northern Ireland		
Rightsholder	Royal Society of Chemistry		

REQUEST DETAILS

Portion Type	Image/photo/illustration	Distribution	Worldwide
Number of Images / Photos / Illustrations	1	Translation	Original language of publication
		Copies for the Disabled?	No
Format (select all that apply)	Electronic	Minor Editing Privileges?	No
Who Will Republish the Content?	Academic institution	Incidental Promotional Use?	No
Duration of Use	Current edition and up to 5 years	Currency	GBP
Lifetime Unit Quantity	Up to 499		
Rights Requested	Main product		

NEW WORK DETAILS

Title	Hexacoordinate Si/Ge Compounds and their Application in Metal-Organic Frameworks	Institution Name	Imperial College London
		Expected Presentation Date	2024-05-31
Instructor Name	Shouyi Tian		

ADDITIONAL DETAILS

The Requesting Person / Organization to Appear on the License	Shouyi Tian

REQUESTED CONTENT DETAILS

Title, Description or Numeric Reference of the Portion(s)	Taking advantage of luminescent lanthanide ions.	Title of the Article / Chapter the Portion Is From	Taking advantage of luminescent lanthanide ions.
Editor of Portion(s)	Bünzli, Jean-Claude G.; Piguet, Claude	Author of Portion(s)	Bünzli, Jean-Claude G.; Piguet, Claude
Volume / Edition	34 / ONLINE	Issue, if Republishing an Article From a Serial	12
Page or Page Range of Portion	1048-1077		
		Publication Date of Portion	2005-12-01

Licence for Figure 4.3

License Number	5761380489167
License date	Apr 03, 2024

Printable Details

Licensed Content

Licensed Content Publisher	Elsevier
Licensed Content Publication	Microchemical Journal
Licensed Content Title	A recycled Tb-MOF fluorescent sensing material for highly sensitive and selective detection of tetracycline in milk
Licensed Content Author	Xinfang Liu,Qinqin Ma,Xun Feng,Rongfang Li,Xiaoyu Zhang
Licensed Content Date	Nov 1, 2021
Licensed Content Volume	170
Licensed Content Issue	n/a
Licensed Content Pages	1

Order Details

Type of Use	reuse in a thesis/dissertation
Portion	figures/tables/illustrations
Number of figures/tables/illustrations	1
Format	electronic
Are you the author of this Elsevier article?	No
Will you be translating?	No

About Your Work

Title of new work	Hexacoordinate Si/Ge Compounds and their Application in Metal-Organic Frameworks
Institution name	Imperial College London
Expected presentation date	May 2024

Additional Data

Portions	Figure 1

Licence for Figure 4.5

License Number	5761380689801
License date	Apr 03, 2024

Printable Details

Licensed Content

Licensed Content Publisher	Elsevier
Licensed Content Publication	Analytica Chimica Acta
Licensed Content Title	Smart lanthanide coordination polymer fluorescence probe for mercury(II) determination
Licensed Content Author	Baoxia Liu,Yankai Huang,Xu Zhu,Yuanqiang Hao,Yujie Ding,Wei Wei,Qi Wang,Peng Qu,Maotian Xu
Licensed Content Date	Mar 17, 2016
Licensed Content Volume	912
Licensed Content Issue	n/a
Licensed Content Pages	7

Order Details

Type of Use	reuse in a thesis/dissertation
Portion	figures/tables/illustrations
Number of figures/tables/illustrations	1
Format	electronic
Are you the author of this Elsevier article?	No
Will you be translating?	No

About Your Work

Title of new work	Hexacoordinate Si/Ge Compounds and their Application in Metal-Organic Frameworks
Institution name	Imperial College London
Expected presentation date	May 2024

Additional Data

Portions	Scheme 1

Licence for Figure 4.6

1. Dalton transactions

Billing Status: Open

Article: A weak luminescent Tb-MOF-based "turn-on" sensor for highly selective and sensitive sensing of anthrax biomarker

Order License ID	1469084-1	**Type of Use**	Republish in a thesis/dissertation
Order detail status	Completed	**Publisher**	ROYAL SOCIETY OF CHEMISTRY
Project Name	1	**Portion**	Image/photo/illustration
ISSN	1477-9234		

0.00 GBP
Republication Permission

LICENSED CONTENT

Publication Title	Dalton transactions	**Rightsholder**	Royal Society of Chemistry
Article Title	A weak luminescent Tb-MOF-based "turn-on" sensor for highly selective and sensitive sensing of anthrax biomarker	**Publication Type**	e-Journal
		Start Page	1300
Author/Editor	Royal Society of Chemistry (Great Britain)	**End Page**	1306
		Issue	4
Date	01/01/2003	**Volume**	50
Language	English		
Country	United Kingdom of Great Britain and Northern Ireland		

REQUEST DETAILS

Portion Type	Image/photo/illustration	**Distribution**	Worldwide
Number of Images / Photos / Illustrations	1	**Translation**	Original language of publication
		Copies for the Disabled?	No
Format (select all that apply)	Electronic	**Minor Editing Privileges?**	No
Who Will Republish the Content?	Academic institution	**Incidental Promotional Use?**	No
Duration of Use	Current edition and up to 5 years	**Currency**	GBP
Lifetime Unit Quantity	Up to 499		
Rights Requested	Main product		

NEW WORK DETAILS

Title	Hexacoordinate Si/Ge Compounds and their Application in Metal-Organic Frameworks	**Institution Name**	Imperial College London
		Expected Presentation Date	2024-05-31
Instructor Name	Shouyi Tian		

ADDITIONAL DETAILS

The Requesting Person / Organization to Appear on the License	Shouyi Tian

REQUESTED CONTENT DETAILS

Title, Description or Numeric Reference of the Portion(s)	A weak luminescent Tb-MOF-based "turn-on" sensor for highly selective and sensitive sensing of anthrax biomarker	**Title of the Article / Chapter the Portion Is From**	A weak luminescent Tb-MOF-based "turn-on" sensor for highly selective and sensitive sensing of anthrax biomarker
Editor of Portion(s)	Zhao, Xiao-yang; Yang, Hui; Zhao, Wenyuan; Wang, Jia; Yang, Qishan	**Author of Portion(s)**	Zhao, Xiao-yang; Yang, Hui; Zhao, Wenyuan; Wang, Jia; Yang, Qishan
Volume / Edition	50	**Issue, if Republishing an Article From a Serial**	4
Page or Page Range of Portion	1300-1306		
		Publication Date of Portion	2021-02-02

Licence for Figure 4.8